Author:
Rowe, Andre J

Title:
Macroevolution and function in giant theropod dinosaurs

Macroevolution and function in giant theropod dinosaurs

By

Andre Jordan Rowe
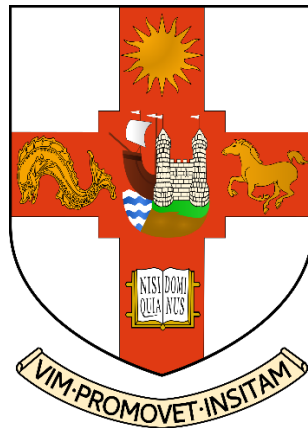
School of Earth Sciences

University of Bristol

A dissertation submitted to the University of Bristol in accordance with the requirements for award of the degree of Doctor of Philosophy in the Faculty of Science

November 2022

Word count: 37,856

ABSTRACT

Theropods are among the most well-studied groups of non-avian dinosaurs, known for their ancestral carnivory, hollow bones, and three-toed limbs. They are the largest bipedal animals to have ever existed. Several theropod lineages independently achieved gigantic body sizes at different times in geologic history. They include the tyrannosauroids, megalosauroids, and allosauroids. In this thesis, I quantify the effects of large body size on theropod dinosaur feeding biomechanics by analysing 3D models of theropod dinosaur skulls using the finite element method. First, I create and compare 3D models from computed tomography (CT) scans and surface scans of extant diapsid skulls and perform finite element analysis (FEA) under identical loading parameters to discern how scanning methods influence FE results, as my dinosaur models were generated from a mixture of CT scans and surface scans. It was found that once surface scanned models are solidified, they output stress and strain distributions and model deformations comparable to their CT scanned counterparts, though differing by notable stress and strain magnitudes in some cases. Secondly, I examine tyrannosauroids, as the animals varied greatly in their body size distribution and possess a relatively well-understood fossil record. I use FEA to test whether skull shape becomes more or less resistant to feeding induced forces as taxa body size increases. It was found that large-bodied tyrannosauroids experienced higher absolute stresses compared to small-bodied relatives. Lastly, I examine 3D models of theropod dinosaur skulls across several clades including the Megalosauroidea, Allosauroidea, and Abelisauroidea using FEA. My results indicate that tyrannosauroid skulls were more adept at absorbing high stresses associated with strong bite forces and gigantic body sizes, and the general trend of skull strengthening with large body size is most notable in tyrannosauroids and mostly absent in smaller basal theropod dinosaurs.

DECDICATION AND ACKNOWLEDGMENTS

First, I must thank Emily Rayfield for all her help over the years I was in the UK, especially with COVID-19 and the difficulties it brought. I still vividly remember us meeting at the SVP conference in Albuquerque, knowing immediately that I wanted to work with you at Bristol, and excitedly telling Eric Snively about it. I also remember you emailing me asking how PhD applications were going and helping get a tuition waiver for me. You were watching out for me before I even moved to the UK, and I will never forget that.

I must also thank all the great friends I made in the UK, including the Palaeobiology Research Group. My favourite place to go in Bristol will always be The Gryphon, where I have had genuinely enlightening conversations about the UK, my dinosaurs, metal music, and everything in between. That establishment was a necessity for my PhD days and helped me maintain my sanity – thanks for that, John Ashby. My friends back in Wisconsin were always available when I needed them, too. Alex Diamantopoulos and Trevor Rewolinski, I appreciate you both.

Perhaps most importantly, thanks to my parents Tracy Schley and Jack Rowe and grandparents Tom and Dolly Schley for their unconditional love and support. I would not be the man I am without them. Thank you for pushing me to pursue my dreams.

AUTHOR'S DELCARATION

I declare that the work in this dissertation was carried out in accordance with the requirements of the University's Regulations and Code of Practice for Research Degree Programmes and that it has not been submitted for any other academic award. Except where indicated by specific reference in the text, the work is the candidate's own work. Work done in collaboration with, or with the assistance of, others, is indicated as such. Any views expressed in the dissertation are those of the author.

SIGNED: .... DATE:.........................

TABLE OF CONTENTS

LIST OF FIGURES

LIST OF TABLES

CHAPTER 1

Introduction

1.1. Theropoda

Theropoda is an ancestrally carnivorous group of dinosaurs whose members are distinguished by three-toed limbs and hollow bones (Holtz, 1998). They are among the most highly studied group of fossil taxa, owing to public and scientific interest. The group was first recorded in the Carnian stage of the Late Triassic (231.4 million years ago) (Martínez et al. 2011) and eventually gave rise to the largest terrestrial carnivores to have ever lived, including *Tyrannosaurus rex* (Osborn 1905, 1906), *Tarbosaurus bataar* (Maleev 1955), *Allosaurus jimmadseni* (Chure & Loewen 2020), and *Torvosaurus tanneri* (Galton & Jensen 1979) (Figure 1.1). . While members of the group are typically recognized as the apex predators of Mesozoic ecosystems, certain members including the therizinosaurs independently evolved to become herbivorous, potentially to exploit new resources and avoid competing with carnivorous theropods (Senter & Robins 2010; Zanno 2010).
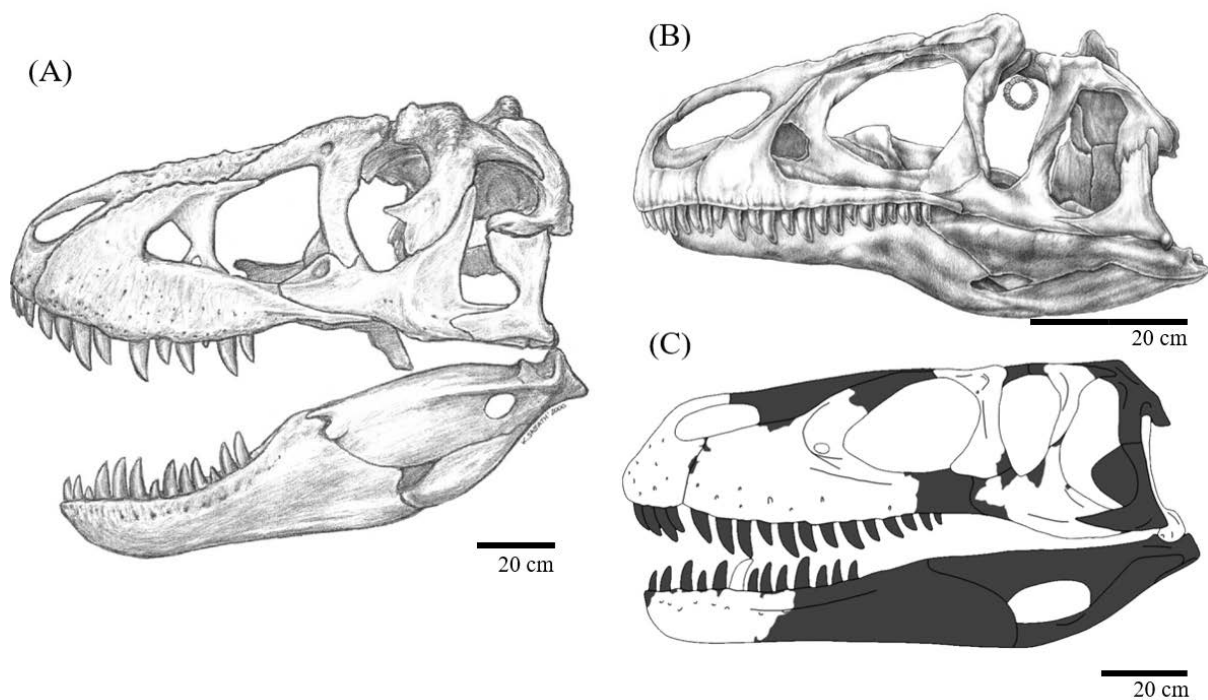
Figure 1.1. Lateral skull diagrams of several large theropod dinosaur skulls. Grey areas indicate missing elements, which are typically filled in museum replicas. (A) *Tarbosaurus*

bataar (Hurum & Sabbath 2003); (B) *Allosaurus jimmadseni* (Chure & Loewen 2020); (C)

Torvosaurus tanneri (Wikimedia Commons user IJReid, based on Britt 1991).

Possibly the earliest theropod dinosaurs are the herrerasaurids of Argentina, which were first recorded from the Late Carnian of the Triassic (Rogers et al. 1993). While they are sometimes considered to be among the earliest theropod representatives (Rauhut 2003; Bittencourt & Kellner 2004), other cladistic analyses have placed them as basal saurischians (Langer & Benton 2006; Irmis et al. 2007). The earliest non-ambiguous theropods are the small, gracile coelophysoids (Schwartz & Gillette 1994). The most common coelophysid is *Coelophysis bauri*, which measured up to 3 metres in length and attained a mass of 15 kg in gracile individuals (Paul 1988) and 25 kg in more robust individuals (Paul 2010). It lived in the Rhaetian stage of the Late Triassic (204-201 Ma ago) (Holtz 2012). Though *Coelophysis* has a well-preserved fossil record with many individuals, it is not included further as coelophysoids retained a light build and small skulls, and this thesis focuses on feeding in large-bodied theropod lineages. The coelophysoids along with several early theropod clades such as Dilophosauridae form the Neotheropoda (Marsh & Rowe 2020; Spiekman et al. 2021). *Dilophosaurus* is notable for being one of the earliest large theropods as well as possessing a distinctive head crest (Welles 1984). Its implications for skull function are currently unknown. The Middle Jurassic theropod *Monolophosaurus* possesses a similar head crest (Brusatte et al. 2010). Both genera are included in this thesis and the influence of the head crest on skull function is considered.

The ceratosaurs appeared around the Hettangian stage of the Early Jurassic (201-199 Ma ago) and include the iconic *Ceratosaurus* (Marsh 1884) and *Carnotaurus* (Cerroni et al. 2020), known for their cranial ornamentation, prominent horns, and diminutive forelimbs in derived taxa. Ceratosauria is divided into two subgroups, the Ceratosauridae and Abelisauroidea (Rauhut & Carrano 2016). The abelisaurs are noted for their skulls which

were tall and short in length. They were widespread geographically, including the Madagascan *Majungasaurus*, which was present during the Cretaceous-Paleogene mass extinction event (Longrich et al. 2017). Abelisauria also includes the Noasauridae, notable for the unusual *Masiakasaurus*, a theropod possessing a downturned jaw, with long procumbent teeth (Carrano et al. 2011). Overall, the group displays a wide range of cranial morphologies that have yet to biomechanically tested in 3D.

Tetanuran theropods are a clade defined as those dinosaurs more closely related to modern birds than to *Ceratosaurus* (Carrano et al. 2012). They encompass the majority of non-avian theropod diversity and likely diverged from the Ceratosauria during the Late Triassic (Sereno et al. 1994). Basal tetanurans were the first theropods to reach truly massive size, with both megalosauroid and allosauroid taxa reaching over 1 tonne. These are two of the theropod lineages which are notable for their rapid acquisition of gigantism. The Coelurosauria, the theropods more closely related to modern birds than the carnosaurs, first appeared in the Middle Jurassic and includes the proceratosaurid tyrannosauroid *Proceratosaurus* (Rauhut et al. 2010). Coelurosauria is notable as it contains both modern birds, and the Tyrannosauridae, one of the largest-bodied and most successful theropod clades, which persisted until the Cretaceous-Paleogene extinction (Hendrickx et al. 2015).

1.2. Tyrannosauroidea

Tyrannosauroids are among the largest and most iconic fossil taxa to have ever been described by science. They are a group of coelurosaurian theropods that first appeared in the Oxfordian stage of the Late Jurassic (160 Ma ago) (Figure 1.2). The earliest tyrannosauroid, *Guanlong wucaii*, is notable for its relatively small body size, distinctive cranial crest, and three-fingered forelimbs (Xu et al. 2006). The basal tyrannosauroid *Dilong paradoxus* possesses a similar suite of characteristics, though it lacks the cranial crest of *Guanlong* (Xu

et al. 2004). Derived tyrannosaurids, such as *Alioramus altai* (Brusatte et al. 2009) and *Raptorex kriegsteini* (Sereno et al. 2009) retain the slenderer body plans of the more ancestral tyrannosauroids, though some specimens including *Raptorex* had not yet reached adolescence (Fowler et al. 2011). *Tyrannosaurus rex* is known to have acquired its characteristically wide, deeply set jaws through ontogeny (Carr 1999, 2020). It is currently unknown how slenderer bodied tyrannosaurine tyrannosaurids such as *Raptorex* would have appeared at adulthood. However, the adult form of the alioramini *Qianzhousaurus sinensis* suggests that *Alioramus* maintained its slender features into adulthood, possibly to maintain a physiology which would be better suited for the pursuit of smaller, faster prey and allowing it to avoid competition with larger tyrannosaurids (Foster et al. 2022).

Derived tyrannosaurids of Maastrichtian Late Cretaceous North America are the most massive bipeds to have ever lived (Erickson et al. 2004; Cullen et al. 2020). This includes *Tyrannosaurus*, *Daspletosaurus* (Russell 1970; Carr et al. 2017), and *Albertosaurus* (Osborn 1905; Russell 1970). The more generalized tyrannosauroid *Bistahieversor sealeyi* was one of the earlier tyrannosauroids to acquire gigantic body size (Carr & Williamson 2010). It is also characterized by its deep snout and large olfactory bulbs (McKeown et al. 2020) which are characters noted in *Tyrannosaurus* (Snively et al. 2006; Zelenitsky et al. 2008).

Tyrannosaurus rex is often regarded as a model organism in vertebrate palaeobiological studies due to the availability of multiple nearly complete specimens (Brusatte & Carr 2016). Many individuals of *T. rex*, including the iconic FMNH PR 2081 (Larson 2008) and MOR 555, already have existing 3D data, making them readily available candidates for studies of the relationship between body size and functional morphology in a single theropod clade. The relatively complete tyrannosauroid fossil record and diverse range of body sizes and cranial morphologies make them ideal for comparative biomechanical studies. While cranial biomechanical studies involving *T. rex* have been published previously

(Rayfield 2004; Cost et al. 2019; Rowe & Snively 2021), they have never been performed in the context of theropod dinosaur body size comparisons.
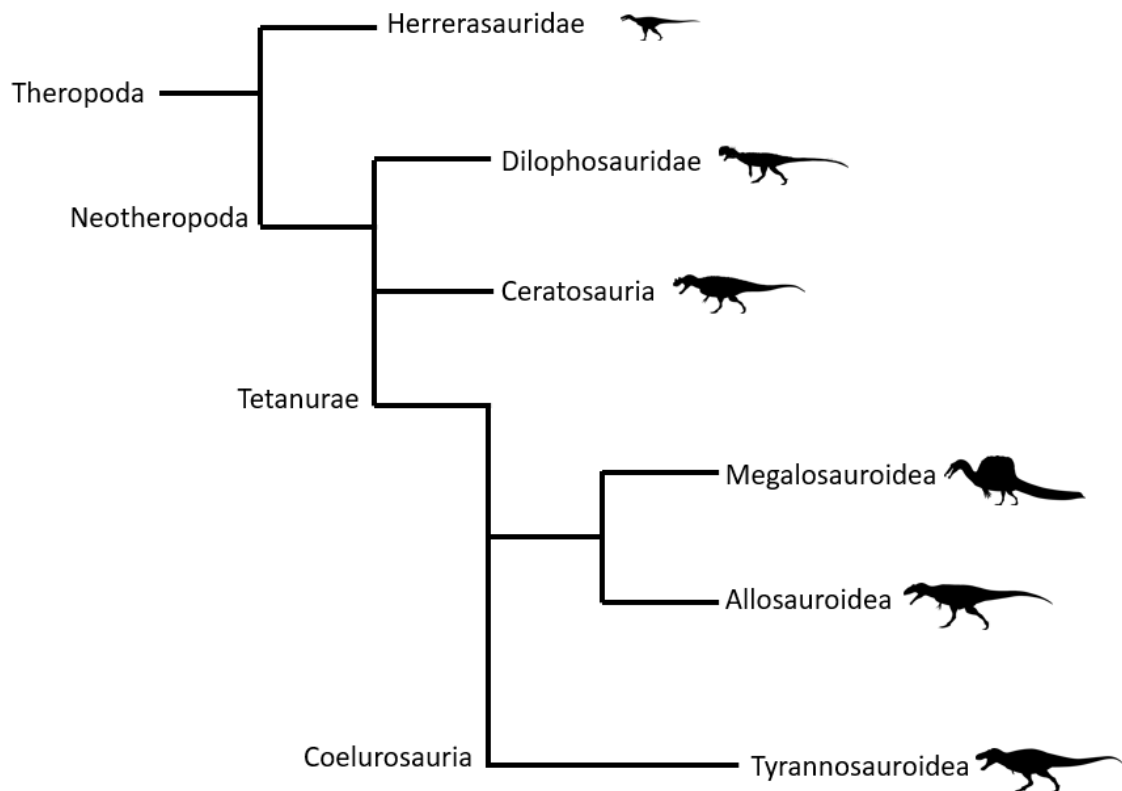
Figure 1.2. Cladogram of major theropod groups. This cladogram is modified from Brusatte et al. 2014. Dinosaur silhouette images are from PhyloPic.

1.3. Megalosauroidea

Considered synonymous with Spinosauroidea, Megalosauroidea contains some of the largest terrestrial carnivores to have ever existed, including some of the only semi-aquatic dinosaurs known thus far (Arden et al. 2019; Ibrahim et al. 2020; Fabbri et al. 2022), though this conclusion has been questioned (Henderson 2018; Hone & Holtz 2021). The clade contains several giant theropod genera including *Spinosaurus*, *Torvosaurus* (Galton & Jensen

1979), and *Suchomimus tenerensis* (Sereno et al. 1988), all possessing nearly complete cranial material with some filler elements, making it possible to study their feeding mechanics relative to tyrannosauroids and allosauroids.

The first megalosaurids appeared in the Middle Jurassic and were among the first major radiations of carnivorous dinosaurs (Benson et al. 2010). The megalosaurid type species, *Megalosaurus bucklandii* (Mantell 1827), found in the Bathonian stage of the Middle Jurassic (166 Ma ago), was the first genus of non-avian dinosaur to be validly named and described. However, the lack of cranial material makes it a poor specimen for biomechanical analysis. *Torvosaurus gurneyi* (Hendrickx & Mateus 2014) is a megalosaurid noted as one of the largest terrestrial carnivores of the Jurassic. It possessed an elongated, narrow snout, with three front teeth oriented outward. The reconstructed skull has never been biomechanically tested.

Spinosaurids are notable for their proposed semi-aquatic lifestyles, possessing the largest biped skeletons in terms of overall length (Glut 1982), and long crocodilian-like rostra (Cuff & Rayfield 2013). Several genera have enough cranial material recovered for biomechanical testing, including *Spinosaurus aegypticus* (dal Sasso et al. 2005), *Baryonyx walkeri* (Charig & Milner 1986), and *Suchomimus tenerensis* (Taquet & Russell 1998). Despite their proposed semi-aquatic lifestyles, remains of terrestrial prey have been found preserved in the guts of *Baryonyx* (Charig & Milner 1997), which may be evidence of predation or scavenging behaviour. Similarly, an Early Cretaceous pterosaur was found with a spinosaurid tooth embedded in its cervical vertebrae (Buffetaut et al. 2004). Thus, it is worthwhile to compare their feeding biomechanics with other giant theropods, even if their diet was mostly piscivorous.

1.4. Allosauroidea

Allosauroids, along with the megalosauroids, were among the apex predatory

dinosaur clades that were active through the Middle Jurassic to the Late Cretaceous. From the

Middle Jurassic onward, both clades comprised almost all large-bodied predators until they

were replaced by the tyrannosaurids of terminal Cretaceous ecosystems (Benson et al. 2010).

The group includes the well-studied North American *Allosaurus* (Marsh 1877), as well as the

massive *Acrocanthosaurus* and *Giganotosaurus* (Figure 1.2), two of the largest dinosaurs

recorded.

The group generally has long, narrow skulls with large orbits and some cranial

ornamentation, particularly in *Allosaurus* and *Neovenator*. Their limbs attained proportions

like those in other giant theropods, including the tyrannosauroids (Bybee et al. 2006), and all

genera maintained a similar centre of mass (Bates et al. 2012). The group is united by several

cranial similarities, including a small mandibular fenestra and short quadrate bone (Sereno et

al. 1996). Their narrow skulls and serrated teeth were equipped for slicing flesh off prey,

rather than puncturing flesh and bone as the large tyrannosaurids did (Rayfield 2005). Their

variation in cranial morphology, relatively well-understood fossil record, and large body size

trends make them ideal for studies of feeding biomechanics.

1.5. Gigantism in theropod dinosaurs

The trend towards large body size in metazoan lineages is often referred to as Cope's

rule. It is named after the famous American palaeontologist Edward Drinker Cope, who was

among the first to publish on the phenomenon, though it was more implicit rather than

concisely stated (Cope 1887, 1896). It has been documented extensively in both dinosaurs

(Hone et al. 2005; Sookias et al. 2012; Benson et al. 2014; Benson et al. 2018;) (Figure 1.6)

and mammals (Damuth 1993; Alroy 1998; Raia et al. 2012; Heim et al. 2015). Notably, it

does not occur in all animal groups, such as insects (Waller & Svensson 2017), certain extant

turtles (Moen 2006) and Mesozoic birds (Butler & Goswami 2008) (Figure 1.3). Because of these exceptions, it is regarded as a generalization in animal macroevolution rather than a law (Stanley 1973).
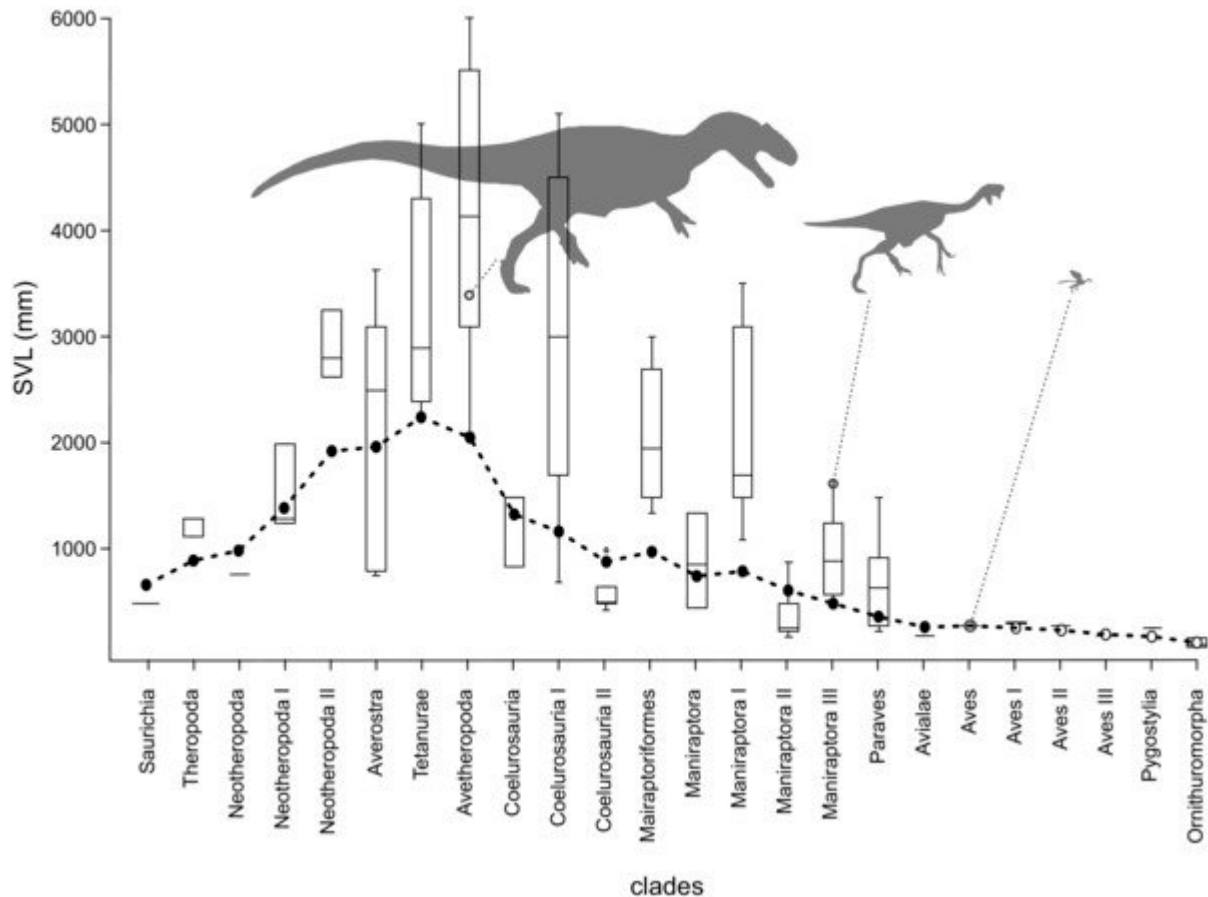
Figure 1.3. A box and whisker plot of body size acquisition in various theropod clades over geologic time. SVL (mm) refers to snout-vent length, the measurement from the top of the snout to the cloacal slit in reptile taxa. This plot is from Dececchi & Larsson 2013.

Body size is a critical aspect of an organism's biology, being the primary determinant of ecological opportunities, as well as the physiological and morphological determinants of the animal (Lindstedt & Calder, III 1981). It is accepted that very large animals are functionally unlike their smaller counterparts: they are more likely to be apex predators in their ecosystems, to tolerate a greater range of environmental conditions, to maintain internal homeostasis more effectively, to be less vulnerable as adults to lethal predation, and to be compete more successfully for mates (Brown & Maurer 1986; Hone et al. 2005). However,

they also require higher caloric intake, have lower fecundity, and are generally more prone to extinction (Holliday 2005). Large body size is therefore functionally distinct from small and medium sized animals (Ripple et al. 2017), and an ecologically important condition that is both enabled by resources and compelled by natural selection (Vermeij 2016).

Theropods are important in functional studies concerning body size, as they are the largest known bipedal animals in Earth's history. Despite absent postcranial material in certain theropod skeletons, body size and mass estimates have been recorded for a wide variety of genera (Therrien & Henderson 2007). At least three phylogenetically disparate theropod lineages independently acquired massive body size from the Middle Cretaceous. This includes the tyrannosaurs, spinosaurs, and carcharodontosaurs. These lineages were notably widespread geographically during their evolutionary transition to gigantic size, and it remains unknown what external drivers may have influenced their trend toward gigantism. Because theropod dinosaurs were the largest bipeds, the functional consequences of their gigantism is a key topic of interest in palaeobiology.

While the resultant locomotory abilities of gigantism in theropods has been researched previously (Hutchinson & Garcia 2002; Hutchinson 2006; Bishop et al. 2021), little work has evaluated and compared feeding biomechanics in various giant theropods. Given the availability of cranial material in a wide range of giant bipeds, and the advanced methods by which we can infer their functional morphology, the central aim of the thesis is to evaluate the effects of large body size on feeding ability.

1.6. Feeding biomechanics in theropods

Early functional studies of dinosaurs were observational rather than experimental, often relying on analogues to large extant mammals and flightless birds (Bakker 1986; Paul 1988). However, advancements in computational methods in recent decades (Lautenschlager 2016)

have allowed for testing and falsification of hypotheses concerning subjects such as locomotion and feeding. Feeding biomechanics are a key functional aspect of dinosaur biology that has seen received much attention. Studies of feeding mechanics have investigated the slashing bite of allosauroids (Rayfield et al. 2001) compared to the crushing bite of tyrannosauroids (Cost et al. 2019), the maximum gape of theropod dinosaurs (Lautenschlager 2015), and cranial muscle attachment sites (Button et al. 2016). Quantitative macroevolutionary trends in theropod feeding have more recently received attention but at the moment these studies are restricted to 2D structural analysis (Rayfield 2011; Ma et al. 2022) or phylogenetic comparative methods of lever arm trends (Sakamoto 2022). Thus, there is much potential to explore this, especially as there are now better methods for capturing 3D large datasets, as well as more efficient processors and software.

Methods that have been used in recent decades to study dinosaur feeding include the engineering technique finite element analysis (FEA) (Ross 2005; Rayfield 2007) and multibody dynamics (MDA). MDA is a computational method used to infer dynamic behaviour of interconnected rigid and/or flexible bodies, with their relative motion restricted by joints. It has become an important tool in designing and simulating complex mechanical systems (Shabana, 1997; Amirouche 2006), including those seen in the biological sciences (Sherman et al. 2011). The availability and sophistication of MDA software has resulted in its application to studies of fossil taxa regarding feeding behaviour. Given the completeness of their cranial material and the existence of CT scan data, theropod taxa including *Allosaurus* (Snively et al. 2013) and *Tyrannosaurus* (Bates & Falkingham 2012) have been common subjects in MDA studies, which have examined their feeding biomechanics. However, due to the complexity of MDA, the time it takes to conduct experiments, and the costs involved, FEA is chosen as our preferred method of analysing dinosaur feeding mechanics.

FEA is a technique that was originally developed for use in architecture and various engineering disciplines including heat transfer and fluid dynamics (Bathe 2006; Zienkiewicz et al. 2013). It is a method of quantifying and visualizing stress and strain in solid structures. It is now often used in functional morphology studies of extant (Moreno et al. 2008; Porro et al. 2011) and extinct (Rayfield et al. 2001; Rayfield 2005, 2011; Pierce et al. 2009) vertebrate taxa. While it is used to infer feeding mechanics from cranial elements of fossils and bones, it has seen use in studies of vertebrate appendages as well (Arbour & Snively 2009; Manning et al. 2009). This makes it ideal in studies of fossil taxa, as it is non-invasive, non-destructive, and FE tests are easily replicable.

FEA can be applied to both 2D and 3D structures. While 2D models are easier to produce, 3D models are generally considered to be more informative in biomechanical studies. This can be challenging in studies involving giant fossils and mounted museum specimens, as CT scans can be difficult and costly to produce. As an alternative to CT scanning, white light and laser surface scanning can work as a viable means of producing quality 3D models for biomechanical testing. While surface scanned models have been commonly used in geometric morphometric studies, their use in FEA has been somewhat limited.**1.7. Computed tomography**

One of the defining aspects of modern palaeobiological studies is the digitization of fossil specimens. Digitization is advantageous for several reasons, including the ability to preserve data in online repositories such as MorphoSource, the non-invasiveness of scanning, and the ability to share 3D data easily (Cunningham et al. 2014).

Computed tomography (CT) scanning has seen extensive use in the medical field for decades. It uses x-ray images taken from different angles to capture the internal geometry of solid structures. This has made it a staple in palaeontological studies involving visualization

of fossil specimens, given that the method allows for the digital removal of surrounding rock

matrix from fossils in Avizo and Mimics. This makes CT scanning invaluable for scientific

descriptions (Carlson et al. 2003; Rowe et al. 2016), morphological studies (Polly et al. 2016)

and biomechanical inquiries (Lautenschlager et al. 2016).

Because this thesis focuses on giant theropod skull biomechanics, CT scanning certain

specimens is almost impossible. Certain giant theropod skulls have already been CT scanned,

and their 3D data is incorporated in this study, including the adult tyrannosaurid

Tyrannosaurus rex (FMNH PR 2081) and the tyrannosauroid *Bistahieversor sealeyi*

(NMMNH P-27469). Other giant theropod taxa such as *Acrocanthosaurus atokensis* and

Suchomimus tenerensis, which are integral to addressing functional hypotheses of gigantism

in theropod clades, must be surface scanned.

1.8. Surface scanning

Surface scanning is a viable alternative to CT scanning. While CT scanning is ideal

for its ability to capture the internal features of solid structures, it has its disadvantages,

including higher costs, the inability to scan mounted museum specimens (Figure 1.5), and

time spent segmenting the data in downstream software. Surface scanning has the advantages

of portability and cheaper costs, though it does not capture internal details of solid structures,

requiring additional time to fill out internal structures, such as cranial bones, for

biomechanical studies; however, this is less of a problem when scanning replica skulls

(Figure 1.4). Surface scans can also miss out on more intricate details of cranial material,

such as small teeth and rugose bone textures, which makes CT scans ideal generally when

attempting to digitize smaller objects.
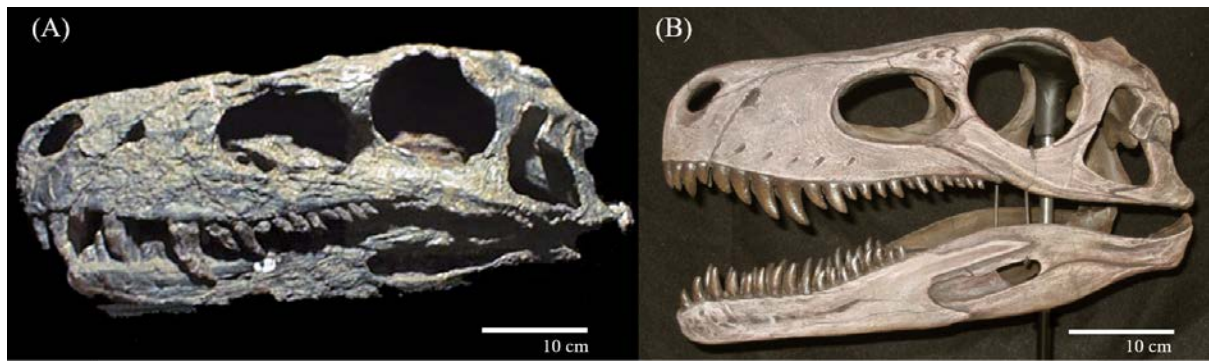
Figure 1.4. An example of real dinosaur skull material versus a replica skull to illustrate potential differences in 3D models during scanning. (A) *Herrerasaurus ischigualastensis* skull (photo by University of California Museum of Paleontology); (B) *Herrerasaurus ischigualastensis* replica skull mount (photo by P. Sereno).

There are different types of surface scans often used in biological and palaeontological studies, including photogrammetry, laser-based 3D surface scanning, and white light surface scanning (Falkingham et al. 2020). Photogrammetry has been utilized often in palaeontological studies due to its cheap costs since it only requires a camera and specific software. Typically, photographs taken with a digital camera are aligned, camera positions are calculated, and a point cloud is produced (Falkingham et al. 2012). It has been particularly common in studies of ichnofossils such as footprints (Breithaupt et al. 2004; Belvedere et al. 2013; Castanera et al. 2013), likely due to its ease of use in the field when compared to white light or laser surface scanning.

3D laser-based scanning is similarly popular, particularly in archaeology and anthropology as a means of creating a digital archive of important museum specimens (Kuzminsky & Gardiner 2012). It is methodically similar to white light scanning as it collects surface data of the desired object using a handheld scanner. However, these scanners typically use four laser beams to capture data points that form polygons, which form the geometric structure of the

object (Weber & Bookstein 2011). The white light surface scanning method used in this thesis does not use lasers, though the workflow is nearly identical otherwise (Figure 1.6).

Figure 1.5. The large, mounted *Acrocanthosaurus atokensis* skeleton replica (NCSM 14345) at the Dinosaur Discovery Museum, Kenosha, WI. This specimen would have been impossible to CT scan without dismounting the skull and acquiring a CT scanner large enough to accommodate the skull's size. As an alternative, it was scanned using an Artec Space Spider surface scanner and a ladder for assistance. Photo by A. Rowe.
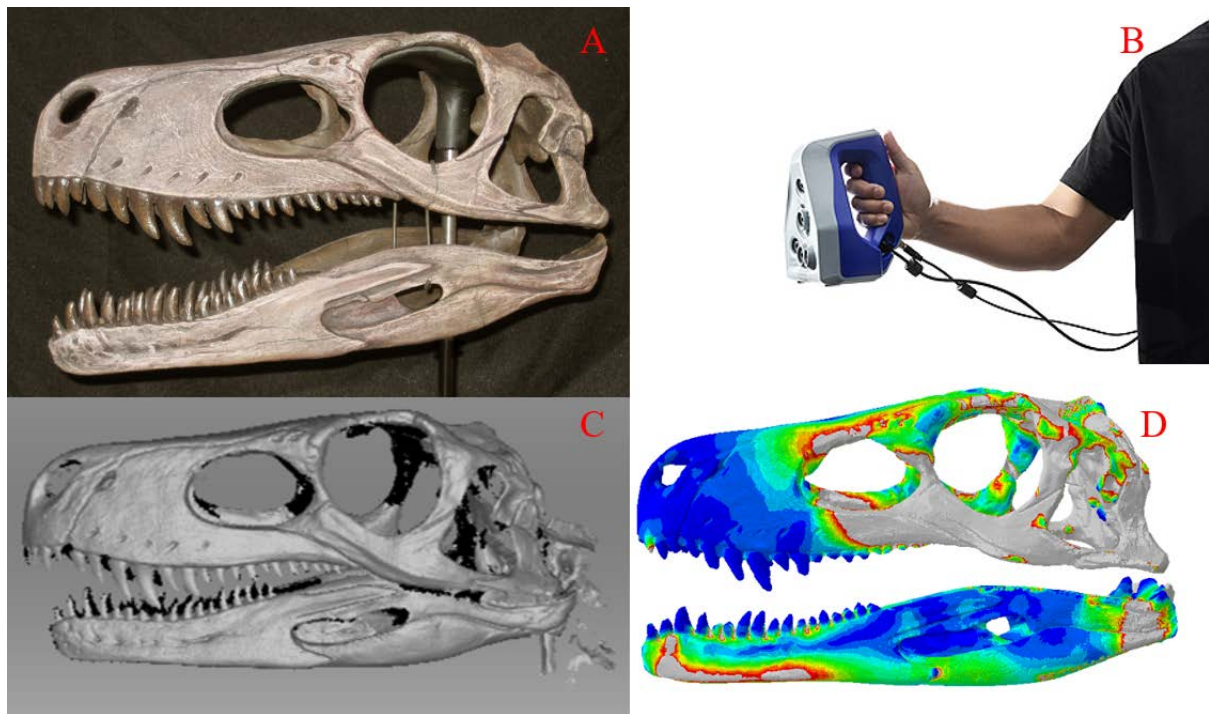
Figure 1.6. Surface scanning workflow adopted in this thesis. (A) *Herrerasaurus ischigualastensis* reconstructed skull (Photo by P. Sereno); (B) Artec Space Spider surface scanner used to scan dinosaur skulls; (C) *Herrerasaurus* 3D model in Artec Studio 14 Professional after reconstruction; (D) *Herrerasaurus* cranial FE results in Abaqus/CAE 6.14-1.

1.9. Aims and hypotheses

The ultimate aim of the thesis is to quantify and visualize skull function in a wide variety of giant theropods and better understand the influence of gigantism on feeding ability. Theropods were a diverse group of dinosaurs that possess a rich fossil record of cranial material, and the availability of scanning technology, engineering software, and coding techniques allows us to better understand trends in the evolution of the world's largest bipeds.

This is broken into three interrelated studies, as outlined below**.**

Aim 1. Access to museum collections containing dinosaur skulls and the availability of 3D model data online and from other researchers allows me to amass a large collection of

digitized theropod skulls. These skulls are a mix of CT scans and surface scans, which must be accounted for in biomechanical studies utilizing both types of scans. Therefore, one of the major aims of the thesis is to better understand what differences may arise in FE results when testing 3D models created via different scanning methods. I compare the stress and strain in 3D models loaded under identical parameters and using CT scans and surface scans of the same skulls. This is done quantitatively by analysing von Mises stress and maximum strain values, and qualitatively by visually comparing patterns of stress and strain in both types of models. I use three different extant reptile taxa from the University of Bristol's collections. This includes a Nile crocodile, a monitor lizard, and a green sea turtle. The crania and mandibles of each animal is scanned separately, resulting in 12 3D models in total. I test two main hypotheses in chapter 2.

Null hypotheses (1). 3D stress and strain magnitudes and patterns of stress for both the CT scanned models and surface scanned models will be identical when they are analysed with identical boundary conditions and material properties.

Alternative hypotheses (2). 3D stress and strain magnitudes and patterns of stress will vary between CT scanned models and surface scanned models when they are analysed with identical boundary conditions and material properties. I predict that surface scanned models experience lower stress and strain due to possessing filled internal geometries that are reconstructed in model editing software during the model creation process, while CT scanned models possess geometrically accurate interiors containing more hollow space (for example, nasal passages).

Aim 2. The wide variety of tyrannosauroid cranial and mandibular material enables an investigation of cranial biomechanics within a single dinosaur clade. My primary goal is to quantify stress and strain occurrences during feeding throughout tyrannosauroid evolution

and to plot differences in skull shape between individuals. Given the relatively well-described tyrannosauroid fossil record, CT scans and surface scans of tyrannosauroid taxa are subject to FEA and their feeding biomechanics are studied. Additionally, 3D models are scaled to the identical sizes by equalizing surface area to that of adult *T. rex* FMNH PR 2081. I test two main hypotheses in chapter 3.

Hypothesis (1). Larger tyrannosaurid taxa such as *Tyrannosaurus rex* and *Daspletosaurus torosus* experience higher absolute stresses and strain due to their large size and increased muscle mass. Despite this, they were able to accommodate high forces because the mandible was so much larger and could adequately absorb high stresses with minimal chance of breakage. This was one of the conclusions noted in Rowe & Snively 2021, though the total specimen pool was smaller, and it pertained only to the mandibles at different growth stages. A similar phenomenon is observed in giant pliosaurs (McHenry 2009; Foffa et al. 2014), wherein the large adults experience higher stresses than small individuals.

Hypothesis (2). When surface area values for cranial and mandibular models are equalized, the smaller-bodied tyrannosaur specimens (*Raptorex kriegsteini, Alioramus altai,* and *Albertosaurus sarcophagus*) experience higher stress and strain relative to the larger-bodied taxa (*Tyrannosaurus* rex, *Daspletosaurus torosus*, and *Bistahieversor sealeyi*) due to the more robust cranial osteology characterized in the allometry of tyrannosaurs and the minimum skull length of 1.4 m (Carr 2020). This was another conclusion noted in Rowe & Snively 2021.

Aim 3. The existing cranial material of other large theropod clades allows me to study their feeding biomechanics and compare them between groups and across the Theropoda. In particular, the megalosauroids/spinosauroids are well-represented with four individuals, and the allosauroids with five. Additionally, I test other large theropods not included in these

clades but still reaching large size, including *Carnotaurus*, *Dilophosaurus*, and the possible early theropod *Herrerasaurus*. I test two main hypotheses in chapter 4.

Hypothesis (1). Large non-tyrannosauroid theropod dinosaur taxa such as *Giganotosaurus* and *Suchomimus* experience higher absolute stresses and strain in their crania and mandibles under simulated feeding loads due to their large skull size and the increased muscle mass present in giant skulls. They were thus able to accommodate high feeding forces due to their large body size.

Hypothesis (2). When muscle force components for skull models are scaled to the same surface area as adult *Tyrannosaurus rex* FMNH PR 2081 to account for body and skull size differences, smaller-bodied theropod dinosaurs such as the abelisaurs experience higher stress and strain relative to the larger-bodied taxa, e.g., megalosauroids and allosauroids due to the evolution of overall more robust skull shape in larger-bodied clades.

1.10. Thesis outline

This thesis is subdivided into three research chapters, plus the introduction and conclusion. Publication details and author contributions are listed at the beginning of the respective chapters.

- Chapter 2 functions as both a Materials and Methods section and as a scientific study. It outlines the process of using CT scanning and white light surface scanning to create 3D models of diapsid skulls. It further delves into the specific protocols involved in converting surface scan data into STL files using Artec Studio 14 Professional, and the tools commonly used in Blender 2.82 and Geomagic Studio 12 to clean up the models and ready them for meshing. It then covers the meshing process in HyperMesh, and the subsequent muscle force application in Abaqus/CAE 6.14-1 before the finite element models are run under static assumptions. Finally, data

comparisons are made between CT scanned models and surface scanned models, and the mesh-weighted arithmetic mean (MWAM) is calculated in R as a method of mitigating von Mises stress differences between types of models.

- Chapter 3 covers the Tyrannosauroidea, as the clade is comprised of multiple genera possessing adequate skull material for FEA. The differences in size and morphology of these genera allow me to elucidate the influence of body size and skull form within a single bipedal dinosaur clade. Additionally, certain individuals within the clade have yet to be tested for their cranial biomechanics, such as *Bistahieversor sealeyi* and *Alioramus altai*. The influence of skull form is considered by comparing stress and strain when muscle forces are equalized across cranial and mandibular models.

- Chapter 4 tests the cranial biomechanics of all remaining theropods that do not fall within the Tyrannosauroidea, including the megalosauroids/spinosauroids, allosauroids, and genera that do not fall into any aforementioned clades. Each theropod is subjected to the same FEA protocols as the tyrannosauroids, with muscle forces derived from the literature.

- Chapter 5 summarizes the findings of the previous chapters and transitions into a conclusionary discussion. The results are placed into a greater context of dinosaur body size evolution and functional morphology, and suggestions of research steps that should be taken next are discussed.

The efficacy of computed tomography scanning versus surface scanning in 3D finite element analysis

Andre J. Rowe analysed the skull material and wrote the manuscript. Emily J. Rayfield supervised the research and commented on the manuscript.

2.1. Abstract

Finite element analysis (FEA) is a commonly used application in biomechanical studies of both extant and fossil taxa to assess stress and strain in solid structures such as bone. FEA can be performed on 3D structures that are generated using various methods, including computed tomography (CT) scans and surface scans. While previous palaeobiological studies have used both CT scanned models and surface scanned models, little research has evaluated to what degree FE results may vary when CT scans and surface scans of the same object are compared. Surface scans do not preserve the internal geometry of 3D structures, which are typically preserved in CT scans. Here, I created 3D models from CT scans and surface scans of the same specimens (crania and mandibles of a Nile crocodile, a green sea turtle, and a monitor lizard) and performed FEA under identical loading parameters. It was found that once surface scanned models are solidified, they output stress and strain distributions and model deformations comparable to their CT scanned counterparts, though differing by notable stress and strain magnitudes in some cases, depending on morphology of the specimen and the degree of reconstruction applied. Despite similarities in overall mechanical behaviour, surface scanned models can differ in exterior shape compared to CT scanned models due to inaccuracies that can occur during scanning and reconstruction, resulting in local differences in stress distribution. Solid-fill surface scanned models generally output lower stresses compared to CT scanned models due to their compact interiors, which must be accounted for in studies that use both types of scans.

2.2. Introduction

Finite element analysis (FEA) is a computational technique that reconstructs stress, strain, and deformation in solid structures. While initially common in engineering, architecture, and orthopaedic sciences, it is now widely used to assess the biomechanics of the human

musculoskeletal system and in recent years it has been a crucial tool in understanding vertebrate biomechanics and evolution (Ross 2005; Rayfield 2007). FEA has been used in studies of 2D (Rayfield 2004, 2005; Pierce et al. 2008; Pierce et al. 2009; Fletcher et al. 2010; Ma et al. 2021) and 3D structures (Moreno et al. 2008; Bell et al. 2009; Oldfield et al. 2011; Cost et al. 2019; Rowe & Snively 2021) to assess patterns and magnitudes of stresses and strain in both extant and extinct organisms, as well as suture morphology in the crania of reptiles (Rayfield 2005; Jones et al. 2017) and mammals (Bright & Gröning 2011; Bright 2012). While studies involving FEA typically pertain to stress and strain occurring in the skull during feeding, studies have focused on the biomechanics of other vertebrate appendages (Arbour & Snively 2009; Lautenschlager 2014; Bishop et al. 2018).

FEA is popular in studies of fossil taxa as it is a non-destructive and non-invasive method to study the structural mechanics of extinct organisms. These studies are sometimes conducted using geometrically accurate 3D models which are generated through various techniques, including photogrammetry (Falkingham 2012), computed tomography (CT) scanning and surface scanning (Rayfield 2007). While CT scanning has seen common use in zoological and palaeobiological studies involving skulls, surface scanning methods have often been used to study fossil vertebrate locomotion via trackway scanning (Bates et al. 2008; Ziegler et al. 2020), studies involving immovable museum specimens (Bates et al. 2009; Cunningham 2014), and studies involving 3D geometric morphometrics (Friess, 2006; Harcourt-Smith et al. 2008; Kuzminsky et al. 2016).

2.3. Computed tomography (CT) scanning

CT scans have an extensive history in the medical field (Power et al. 2016), but in recent decades they have been commonly used in paleontological (Haubitz et al. 1988; Carlson et al. 2003; Racicot 2016) and zoological studies (Copes et al. 2016; Poinapen et al. 2017) as they

allow for a non-invasive visualization of the interior of biological structures and can be used to generate high resolution tomographic data of bone, fossils, and tissues. These data are used to create 3D models which can facilitate biomechanical modelling, geometric morphometric analyses, or phylogenetic analyses.

CT scanning is a powerful tool in biological studies, as the 3D models generated from the scans can capture both internal and external details with precision (Rowe et al. 2016). Image quality in CT scans depends on four basic factors: image contrast, spatial resolution, image noise, and artifacts (Goldman 2007), and can also vary by the size of the specimen being scanned and the type of machine used. While CT scanning offers many advantages, there are disadvantages relative to surface scanning that must be considered, including high costs (Fred 2004), size limitations, and time spent segmenting the data.

2.4. Surface scanning

Surface scanning is an increasingly common digitization technique that has applications similar to CT scanning. Like CT scanning, it is used to generate virtual 3D data that can be valuable in biological studies. Surface scanning is an alternative method that avoids the expenses and large size restrictions of CT scanning, though the resulting 3D models lack the internal anatomy of complex structures such as the endocast of the skull. Since surface scans tend to miss intricate details of smaller specimens, e.g., bone textures and teeth, CT scanning is generally the preferred method when dealing with small specimens in palaeobiological studies. Textures, in a digital context, refers to an image mapped onto a 3D model to provide colouration and other detail. However, not all specimens are amenable to CT scanning, due to their size, weight or accessibility, and surface scanning may offer a viable alternative. This is especially notable in vertebrate palaeontology, as large dinosaur skull material is often difficult to CT scan due to size restrictions (Cunningham et al. 2014). Surface scanning or

photogrammetry is also cheaper than CT scanning, requiring a handheld or mounted scanning device.

Laser scans and white light scans are two types of surface scans used in biological studies. Laser scanners use a one-dimensional type of scan with a line pattern, which may lead to a high error rate for certain objects (Persson et al. 2009). White light scanners utilize a two-dimensional stripe pattern for obtaining three-dimensional data. Generally, white light scanning is accurate and fast in the scanning of plaster models in medical studies (Jeon et al. 2014), though the structures being scanned are relatively simple, e.g., human teeth. Peterson & Krippner (2019) found little difference in the effectiveness of one type of surface scan when comparing the fidelity of 3D printed teeth and osteoderms; both types of models were deemed accurate when compared to the objects being scanned, though the study did not include biomechanical analyses.

Studies have already investigated which 3D scanning type is more reproducible in medical studies; Fahrni et al. (2017) concluded that multi-detector computed tomography (MDCT) led to greater variability in results when compared to three-dimensional surface scanning (3DSS) but noted that more experimentation was necessary to explain their first impression and expand on the results. Kulczyk et al. (2019) examined how cone-beam computed tomography (CBCT) scans compare to optical scans when comparing tooth models in 3D printing and found that high-resolution CBCT is sufficient method to obtain data, but the texture quality was poorer than in optical scan. Soodmand et al. (2018) examined the mean model deviation in CT data compared to reference optical 3D scans and found no significant discrepancies in 3D models of a human femur. Other studies have compared 3D models created via photogrammetry and CT scanning in contexts broader than medical studies. Lautenschlager (2016) noted that while photogrammetry is the most cost efficient and easily reproducible method, it can be limited in its applications due to its inability to capture internal geometries

and complex surfaces. Fahlke & Autenrieth (2016) similarly noted that CT scanning has its main strength in capturing internal features, but surface scanning was otherwise sufficient in 3D model generation. Hamm et al. (2018) concluded that CT scanning was likely the better option for large, complex structures like a *Tyrannosaurus rex* skull, as the data-capture effort of photogrammetry is directly linked to the size and colour of the specimen and to the complexity of its shape. CT scanning is independent of the specimen's shape and complexity, which can be advantageous in both time spent acquiring data and the quality of the models. However, costs may be much higher when CT scanning.

While CT scanning and surface scanning have previously been compared in terms of topography and morphology (Waltenberger et al. 2021) and the efficiency of several different surface scanning methods have been compared in terms of digitization quality (Díez Díaz et al. 2021), little work has evaluated the downstream differences in finite element models created from CT scans versus surface scans. Rahman & Lautenschlager (2016) used the mesh processing software CloudCompare v. 2.6.2 to quantitatively compare 3D models generated via box modelling to corresponding models generated via CT scanning and photogrammetry; it was found that the general shapes of all models were broadly similar but demonstrated variance based on the approach taken and complexity of the specimen examined. Díez Díaz et al. (2021) similarly employed a method of examining model convergence; 3D models were generated from seven different methods and topologically compared using CloudCompare v.2.10-alpha. It was found that accurate 3D models can be obtained with all seven of these different surface digitization methods and techniques, when relying on area and volume measurements.

Generally, little work has evaluated the possible discrepancies in 3D finite element results when comparing surface scanned models and CT scanned models derived from the same material. There is also little work investigating how to reduce possible discrepancies between

results in 3D models generated from different scanning methods. Though the resolution of surface geometry and its influence on FE results has been studied (McCurry et al. 2015), this study is the first to evaluate the use of both CT scans and surface scans in 3D FEA.

2.5. Primary hypotheses and rationale

In this study I investigate the comparable difference in stress and strain output data between finite element models of the same specimen and loading conditions, created either from white light surface scanning or computed tomography methods. I assessed the FE results from 3D models of three reptile skull specimens: a Nile crocodile (*Crocodylus niloticus*) (Figure 2.1), a monitor lizard (*Varanus salvator*) (Figure 2.2), and a green sea turtle (*Chelonia mydas*) (Figure 2.3).

Null hypotheses (1). 3D stress and strain magnitudes and patterns of stress for both the CT scanned models and surface scanned models will be identical when they are analysed with identical boundary conditions and material properties.

Alternative hypotheses (2). 3D stress and strain magnitudes and patterns of stress will vary between CT scanned models and surface scanned models when they are analysed with identical boundary conditions and material properties. I predict that surface scanned models experience lower stress and strain due to possessing dense internal geometries that are reconstructed in model editing software, while CT scanned models possess geometrically accurate interiors containing more hollow space.

Figure 2.1. The *Crocodylus niloticus* skull (BRSUG 28959) used in the study. Left to right: cranium in dorsal view, cranium in ventral view, and mandible in dorsal view. Note both the presence of fibrous tissues in the specimen and the broken left ramus in the mandible. Photos by A. Rowe.

Figure 2.2. The *Varanus salvator* skull (BRSUG 29376/7) used in the study. Left to right: cranium in dorsal view, cranium in ventral view, and the single left ramus in medial view.

Note the partially broken right maxillary and jugal bones in the skulls. The left ramus was duplicated and mirrored in Blender 2.82 to create a full 3D mandible model. Photos by A. Rowe.
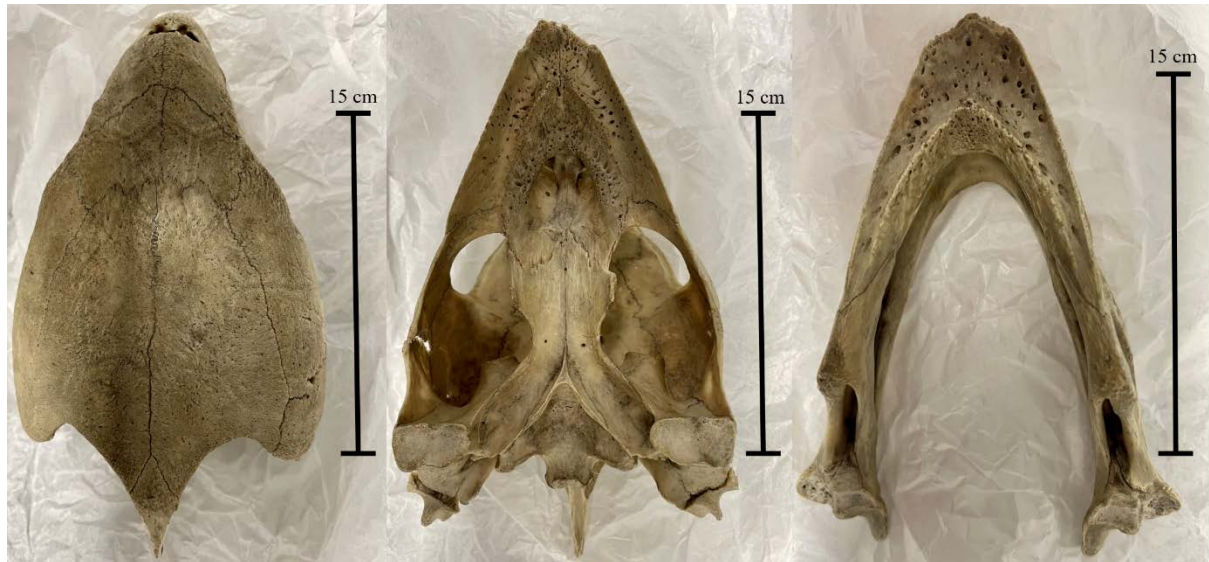
Figure 2.3. The *Chelonia mydas* skull (Ost 160 – Bristol Biological Sciences collection) used in the study. Left to right: cranium in dorsal view, cranium in ventral view, and mandible in dorsal view. Photos by A. Rowe.

These hypotheses relate to the stress and strain of 3D skeletal structures when scanned using two different methods. Within the context of FEA, stress is defined as a force per area (measured in Pascal, equivalent to N/m^2). Strain is the change in dimensions of a body (i.e. ratio between original and deformed condition) due to an external force. The skull models were primarily compared by mean von Mises stress (von Mises, 1913), a value which accurately predicts how close ductile (slightly deformable/non-brittle) materials like bone are to their failure point. Skull models with lower von Mises stress were judged to be stronger under the imposed bite simulations, as lower stresses indicate less susceptibility to breakage or deformation under the imposed load.

2.6. Materials and methods

2.6.1. Scanning procedures

I created 3D models of the crania and mandibles of three phylogenetically disparate taxa using both CT scanning and surface scanning. The reptiles are housed in the University of Bristol Geology collection (BRSUG) or the University of Bristol, School of Biological Sciences teaching collection (Ost/H1b). They were chosen for their morphological diversity and ready availability of muscle data in the literature, including insertions and muscle force components. The Nile crocodile skull was selected for its relatively large size which enabled easier surface scanning, as intricate details including wrinkled textures and teeth are often difficult to capture when scanning small specimens. This specimen possesses fibrous tissues in its cranium and mandible which were captured during CT scanning and surface scanning, a potential issue when surface scanning extant osteological material. Crocodilians are also noted for their akinetic skull properties due to possessing a secondary palette (Ferguson 1981; Bailleul & Holliday 2017), which provides a contrast to monitor lizards which possess a more flexible, kinetic skull lacking a secondary palette (Arnold 1998; Herrel et al. 2007; Handschuh et al. 2019). The green sea turtle was chosen as a means of testing a beaked omnivorous animal (Arthur et al. 2008; Nishizawa et al. 2010) in contrast to sharply toothed carnivores. The Nile crocodile was missing the posterior part of the left mandible and the *Varanus salvator* specimen was missing the entire right mandible and the right maxilla and jugal were displaced from the cranium. This meant that element duplication and minor restoration was required, similar to many fossil specimens.

Each specimen was digitized using a Nikon XT H 225ST μCT scanner housed in the Life Sciences Building, Bristol, UK, and an Artec3D Space Spider surface scanner. CT parameters

were set to 225 kV, 449 mA, 101 W, 1.5 mm copper filter, 0.5 s exposure time, reflection rotating target, 3141 projections, and 4 frames per projection. Manufacturers specifications list the surface scanning 3D point accuracy to 0.05 mm and the 3D resolution at 0.1 mm, but this depends on distance from the specimen to the scanner and specimen size: it is unlikely such resolution was achieved in this study. The surface scanner was connected to a Dell Alienware 13 Core i7-6500U laptop with 16 GB of RAM for processing complex images.

Due to the size of the adult crocodile skull, the cranium and mandible were CT scanned separately, while the turtle and monitor lizard were scanned with both the crania and mandibles held together by foam. All specimens were scanned at 120 µm. The files were imported into Avizo Lite version 9.5 at voxel size 1 and segmented using the Threshold tool. Voxel size 1 was chosen as a default; ideally, it should have been selected as 0.120 to match the scanning resolution. To compensate for this, CT scanned models were scaled down by 8 times to match the magnification scope of their surface scanned counterparts. These models were then exported as STL files, as STL files are simple to work with and supported by the majority of 3D visualization and editing software packages (Sutton et al. 2001).

The same CT scanned individuals were surface scanned using an Artec Space Spider handheld scanner. The scans were made at 7–8 frames per second, with the 'real-time fusion' option enabled. Crania and mandibles were all scanned separately and created as separate 3D object files to avoid large file sizes. Surface scans were imported into Artec Studio 14 Professional where sections of scanned skulls were oriented together, registered, and then merged into a single object. Stray pixels were deleted, as well as frames with maximum error values above 0.3. Once I was satisfied with the alignment of the individual scans, I applied Global Registration to convert all one-frame surfaces to a single coordinate system using information on the mutual position of each surface pair. I then applied a sharp fusion to create a polygonal 3D model, which solidifies the captured and processed frames into an STL file. I

used Sharp Fusion rather than Fast Fusion or Smooth Fusion as it best preserves fine details

of the scans, including small teeth and rugose bone textures. Lastly, where necessary, I used

the small-object filter to clean the model of floating pixels and the fix holes function to fill

any open areas (Figure 2.4). The STL files were then exported from Artec Studio 14

Professional and imported into Blender version 2.82 or Geomagic Studio 12, depending on

the quality of the models.
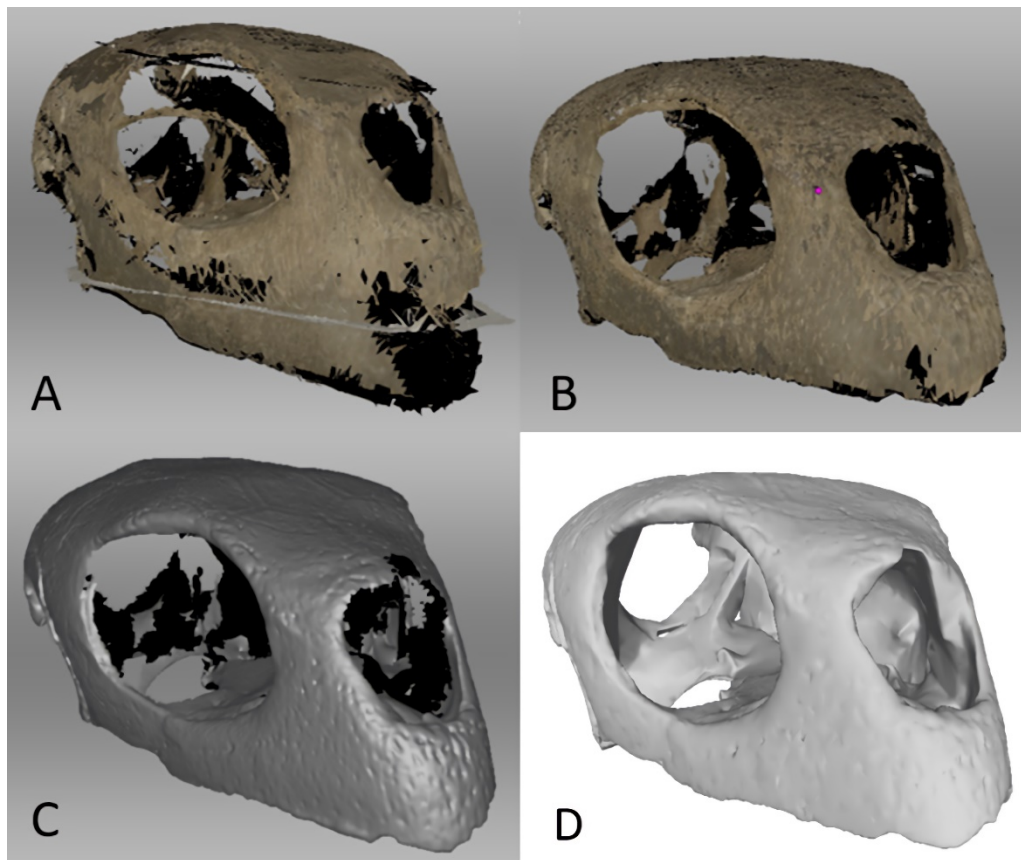
Figure 2.4. Surface scanned *Chelonia* cranium (A) prior to Global Registration in Artec

Studio 14 Professional, (B) after Global Registration and outlier removal in Artec Studio 14

Professional, (C) after Sharp Fusion in Artec Studio 14 Professional, which converts the

scans into an STL file, and (D) the same STL file in MeshLab 2020.06 after surface editing in

Artec Studio 14 Professional and Blender 2.82 to close gaps in the model and better match

the geometry of the CT files.

2.6.2. 3D finite element model editing

Blender 2.82 was used for more precise editing, typically using the Sculpt functions to smooth any unnatural-looking surfaces or creases that tend to appear in surface scanned models. The CT scanned models did not require extensive editing; they were run under Geomagic Studio 12's Mesh Doctor function to remove self-intersections which often resulted after segmentation in Avizo Lite 9.5. Due to surface scanning producing hollow models, it was necessary to import the hollow models into Avizo Lite 9.5 and segment them to achieve results comparable to the CT models. This was done by converting the STL files into TIFF files; the model was imported, I selected 'Scan Surface to Volume,' exported data as type 2D TIFF segmented the interior of the TIFF stack using Avizo's threshold tool and generated a surface which was then exported as an STL. The interior details of surface scanned crania are generally not captured during scanning; this may necessitate splicing bone models from related genera to fill in missing features. However, all 3D models regardless of digitisation techniques are surface-wrapped, hollow models which become solid-meshed when converted into 3D solid FEA models. In this study, surface details were constructed from observations of the CT scanned models using the Sculpt function in Blender 2.82 and the 3D editing tools in Geomagic Studio 12 (Figure 2.4).

For the crocodile mandible, the posterior end of the left hinge was partially broken (Figure 2.1). This was fixed in Blender 2.82 by deleting the broken left ramus at the middle point of the mandible and duplicating the right ramus. The right ramus was then mirrored and reattached at the mandible's anterior to create a complete mandible. The right ramus of the monitor lizard mandible was also missing (Figure 2.2), and an identical procedure utilizing the left half was used to generate a complete mandible. This procedure was used for both the surface scanned models and the CT scanned models to best achieve identical geometries for FE testing. The merging of duplicated geometries in the models resulted in intersecting

triangles, which generally causes meshing procedures to fail when creating finite element meshes. This was fixed by importing models containing self-intersections into MeshLab 2020.06, deleting intersecting triangles, and then using the hole-filling function in Geomagic Studio 12.

The 3D models were then imported into Geomagic Studio 12. Both element and triangle counts were reduced as to shorten analysis times in Abaqus/CAE 6.14-1 (Table 2.1). The mesh wizard tool was then selected, which corrects intersecting triangles, sharp edges, and holes, thus reducing the likelihood of errors when meshing the models. Volume and surface area for each 3D model was recorded (Table 2.2).

Table 2.1. Number of elements and triangles in each model tested.

Specimen name	Specimen number	Cranial elements (CT)	Cranial elements (surface scan)	Mandible elements (CT)	Cranial triangles (CT)	Cranial triangles (surface scan)	Mandible triangles (CT)	Mandible triangles (surface scan)
Nile crocodile (*Crocodylus niloticus*)	BRSUG 28959	1,386,928	1,554,868	2,019,264	167,940	217,306	1,386,928	247,090
Green sea turtle (*Chelonia mydas*)	Ost 160	90,188	246,798	236,498	90,188	246,798	263,498	197,722
Monitor lizard (*Varanus salvator*)	BRSUG 29376/7	159,358	172,470	688,656	159,358	172,470	588,656	135,450

Table 2.2. Volume, surface area, and material properties of each model tested.

Specimen name	Cranial volume (mm³) (CT)	Cranial volume (mm³) (surface scan)	Mandible volume (mm³) (CT)	Cranial surface area (mm²) (CT)	Cranial surface area (mm²) (surface scan)	Mandible surface area (mm²) (CT)	Mandible surface area (mm²) (surface scan)	Mandible volume (mm³) (surface scan)	Young's modulus (GPa)	Poisson's ratio
Nile crocodile (*Crocodylus niloticus*)	1256734	1716394	944250.7	346104.2	229887.7	285409.2	170483.4	1150980	15	0.29
Green sea turtle (*Chelonia mydas*)	153623.1	173715.4	37029.62	77998.11	67361.12	16474.2	14943.83	34135.75	20.49	0.4
Monitor lizard (*Varanus salvator*)	23561.33	24318.68	7452.24	22301.37	16554.88	8863.39	6507.72	10201.48	22.8	0.3

The models were exported from Geomagic Studio 12 and imported into HyperMesh (Altair)
as four-noded tetrahedral elements. Properties were assigned to the various materials,
including Young's modulus, the material's stiffness, and Poisson's ratio, the deformation of
the material in directions perpendicular to the direction of loading. Crocodilian skull bone
properties (Zapata et al. 2010; Porro et al. 2011) and lizard bone properties (Dutel et al. 2021)
were assigned, with extant analogues for alligator bone used in the turtle analyses (Zapata et
al. 2010; Ferreira et al. 2020) (Table 2.2). All materials were treated as isotropic and
homogeneous. As the main purpose of the study was to compare differences in stress and
strain results due to geometry, it was considered acceptable to use these material property
values.

Constraints were assigned at the tips of the two anterior-most tooth edges and at the beak in the case of the turtle skull to simulate feeding loads, while constraints were assigned to the hinges of the articular and quadrate to prevent the model from freely floating. The tooth constraint positions were selected to best illustrate and visually compare von Mises stresses when the contact points are at the farthest anterior position of the skulls. Three constraint points were selected per quadrate and articular hinge for each model. Three degrees of freedom were selected for each analysis at X, Y, and Z. The number of constraint points, typically three per tooth or beak, were kept consistent for each taxon and type of scan (Figure 2.5).

Constraint application.
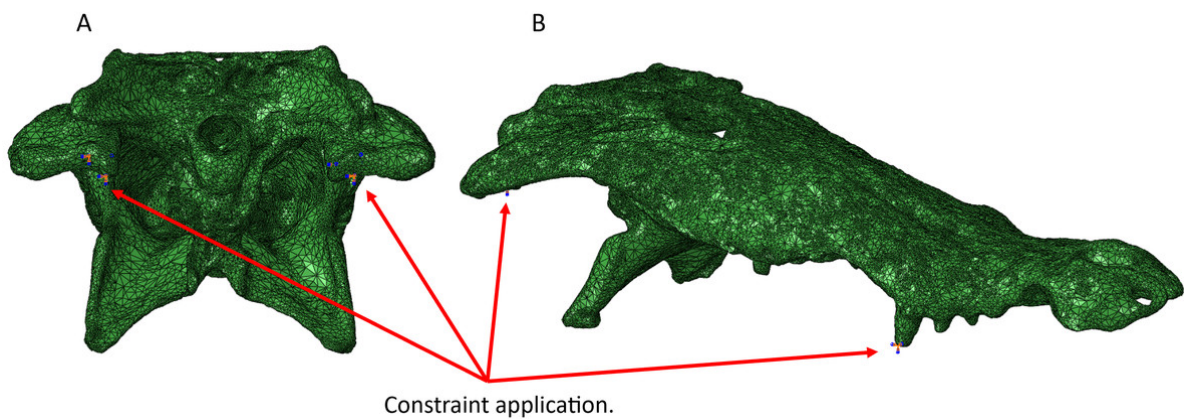
Figure 2.5. Areas of constraint application in the *Crocodylus* CT scanned cranium. Three constraints were applied to each side of the quadrate to prevent the model from floating in space, and an additional constraint was applied to the tooth to simulate contact with a food object. For mandible models, three constraints were applied to the posterior hinge of each articular bone. Identical constraint protocol was followed for each reptile model.

Once satisfied with the constraint selection, these models were imported into Abaqus/CAE

6.14-1 to determine stress and strain in the crania and mandibles of the models. Muscle

locations and the nodes selected to represent muscle attachment and insertion were based on

reconstructions of muscle anatomy from Holliday (2009) for *Varanus* (Figure 2.6) and

Crocodylus (Figure 2.7) and Jones et al. (2012) for *Chelonia*. (Figure 2.8) (Table 2.3). Each

muscle body was assigned a local coordinate system to simulate the direction of pull of the

muscles on the crania and mandibles. A single coordinate system per muscle was created.

Muscle force components applied to the model were calculated by dividing muscle force (N)

by number of nodes selected per muscle (Table A1).
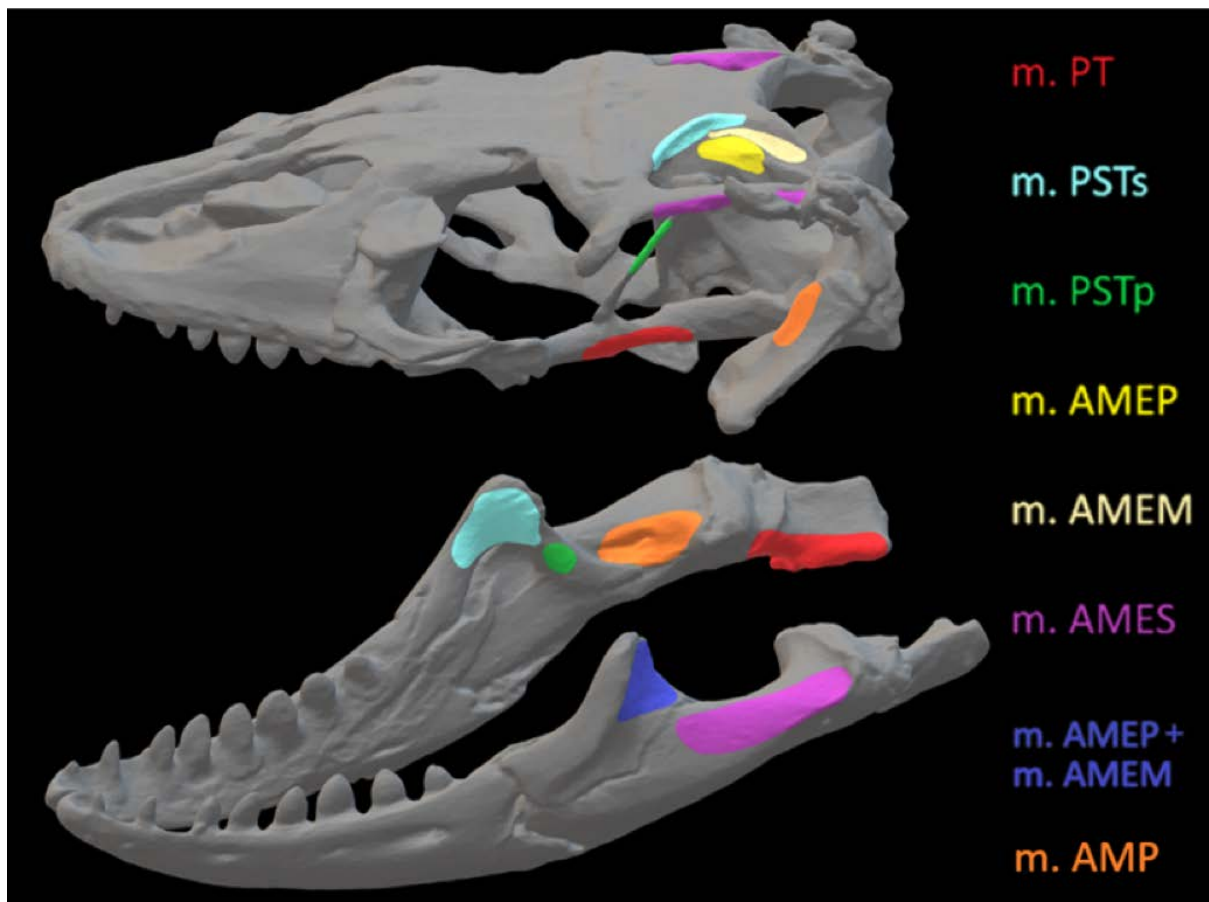
Figure 2.6. Muscle insertions where nodes were mapped for the *Varanus* model in

Abaqus/CAE 6.14-1 based on Holliday (2009). Nodes were mapped as similarly as possible

for both CT scanned and surface scanned models by first applying nodes to CT models and

then using the CT models as references when applying nodes to surface scanned models.

Muscle abbreviations for all models: mPT, M. pterygoideus; mPSTs, M. pseudotemporalis superficialis; mPSTp, M. pseudotemporalis profundus; mAMEP, M. adductor mandibulae externus profundus; mAMEM, M. adductor mandibulae externus medialis; mAMES, M. adductor mandibulae externus superficialis; mPTd, M. pterygoideus dorsalis; mAMP, M. adductor mandibulae posterior; mPRp, M. adductor mandibulae internus Pars pterygoideus; mAP, M. adductor mandibulae externus Pars superficialis lateral head.
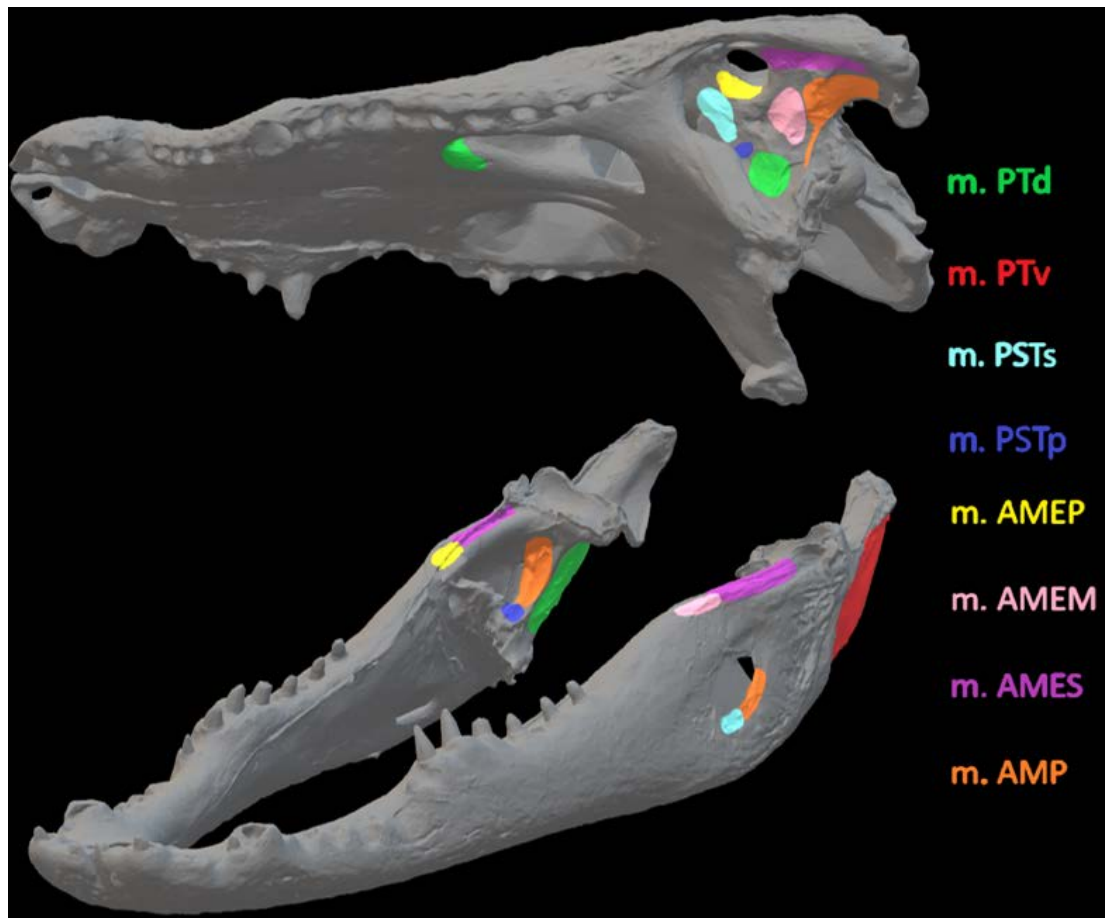
Figure 2.7. Muscle insertions where nodes were mapped for the *Crocodylus* model in Abaqus/CAE 6.14-1 based on Holliday (2009).
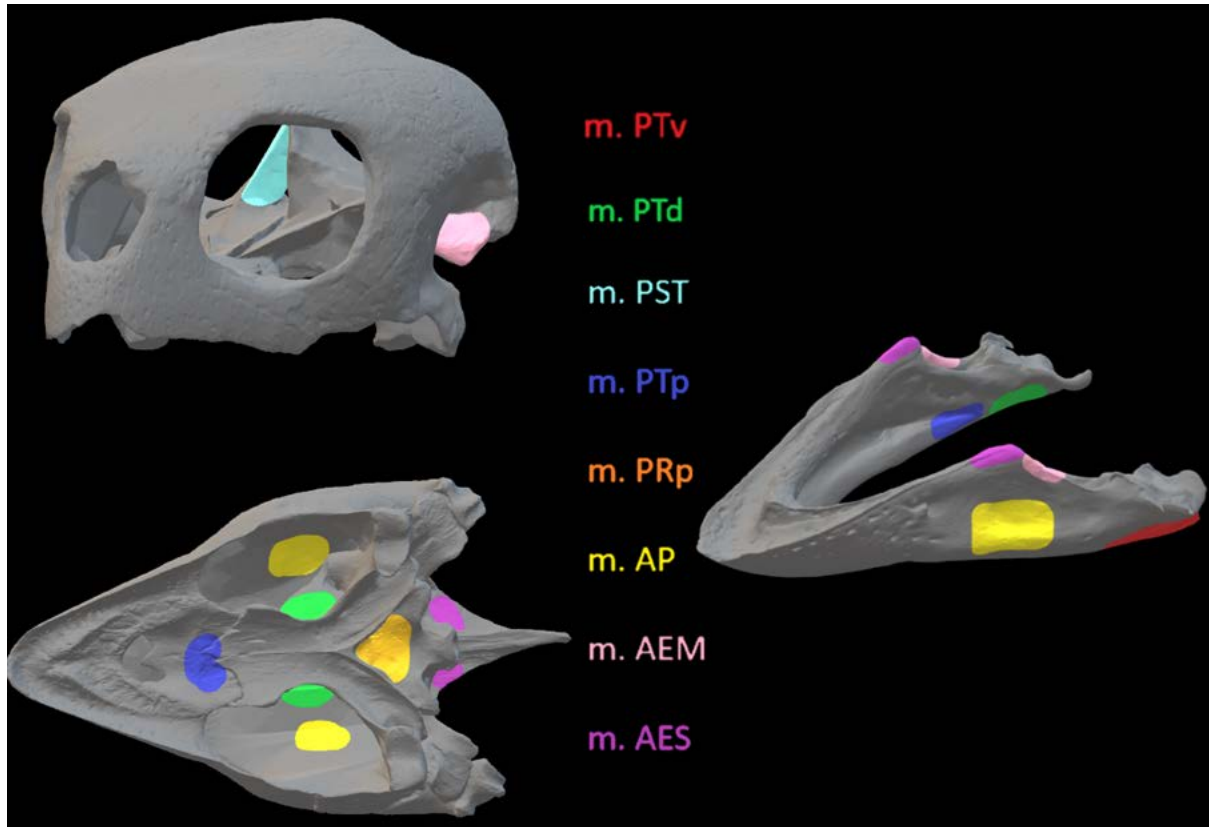
Figure 2.8. Muscle insertions where nodes were mapped for the *Chelonia* model in

Abaqus/CAE 6.14-1 based on Jones et al. (2012).

Table 2.3. Number of nodes across which constraints and muscle forces are applied in each

model.

Crocodylus	Total constraints at quadrate/articular	m. PTd	m. PTv	m. PSTs	m. PSTp	m. AMEP	m. AMEM	m. AMES	m. AMP
CT cranium	6	16	--	27	10	28	14	27	27
CT mandible	6	54	52	32	32	47	38	62	80
Surface scan cranium	6	16	--	23	10	24	14	28	24
Surface scan	6	49	51	30	28	27	41	60	70

mandible								
Varanus	Total constraints at quadrate/articular	m. PT	m. PSTs	m. PSTp	m. AMEP	m. AMEP + m. AMEM	m. AMES	m. AMP
CT cranium	6	32	16	18	18	16	32	30
CT mandible	6	42	32	10	18	16	38	34
Surface scan cranium	6	28	16	20	20	16	32	36
Surface scan mandible	6	40	31	10	26	26	36	38
Chelonia	Total constraints at quadrate/articular	m. PTv	m. PTd	m. PST	m. PTp	m. PRp	m. AP	m. AEM	m. AES
CT cranium	6	--	12	12	6	8	12	12	10
CT mandible	6	20	20	--	16	--	24	16	20
Surface scan cranium	6	--	14	12	6	10	14	12	14
Surface scan mandible	6	20	22	--	16	--	22	16	20

Muscle force values were obtained from previous studies involving taxa that are phylogenetically related to those used in this study, including *Alligator mississippiensis* (Porro et al. 2011; see supplementary information) and *Varanus niloticus* (Dutel et al. 2021). *Platysternon* muscle force values were chosen as a proxy for *Chelonia mydas* due to

41

possessing the highest recorded values of extant turtles which may align more closely with the relatively large *Chelonia* skull (Ferreira et al. 2020; S. Lautenschlager, personal communication 2021). Once all constraints and nodes were applied across CT scanned and surface scanned models, FE analyses were run under linear static assumptions, with unchanging loads and material properties in the software Abaqus (Simulia). Stresses were compared using von Mises stress, which is used to predict failure under ductile fracture, or fracture characterized initially by plastic deformation, commonly occurring in the bone. Stresses were superimposed on the models as contours with a user-specified range of colours to indicate where stresses experienced are least and most substantial, with warmer colours such as red and white signifying high stress, and cooler colours like blue and green representing low stress.

Additionally, I analysed von Mises stresses and deformation occurring at specific points on the models. This was done was plotting ten points at similar locations on each CT scanned model and its corresponding surface scan model. I then selected five nodes per point on each model and calculated the mean von Mises stress value at each point (Table 2.7, 2.8, 2.9). This was done to better understand stresses occurring at specific points on each CT scanned model and its corresponding surface scanned counterpart. A similar method was applied to each point where an unscaled mean displacement was calculated by selecting five nodes. This method revealed the amount of deformation occurring in each model and to what quantitative extent each CT scanned model was deforming when compared to the surface scanned models.

Once I calculated mean von Mises stress values for all models, I also calculated the mesh-weighted athematic mean (MWAM) von Mises stress value for each model using R (R Core Team 2021). This method accounts for element size differences within non-uniform meshes and has been used in previous biomechanical studies in vertebrate palaeobiology (Marcé-

Nogué et al. 2016; Morales-García et al. 2019; Ballell & Ferrón 2021). MWAM values can reduce discrepancies between CT scanned models and surface scanned models.

2.7. Results

In most FE models, mean von Mises stress magnitudes were generally higher in the CT scanned models than the surface scanned models. The CT scanned models which produced von Mises stresses higher than the surface scanned models were the *Crocodylus* cranium and mandible, *Varanus* cranium, and *Chelonia* cranium. The mean von Mises stresses differed overall by 85.76% between both types of models (Figure 2.9), though certain models differed significantly while others were comparable in their results, such as the *Chelonia* mandibles. I also calculated the median von Mises stress values for each model (Figure 2.10). Median von Mises stress values did vary from the mean stress values, in that the *Varanus* and *Chelonia* cranial stresses were slightly higher in the surface scanned models. Mean maximum principal strain values similarly differed overall by 86.04% (Figure 2.11).
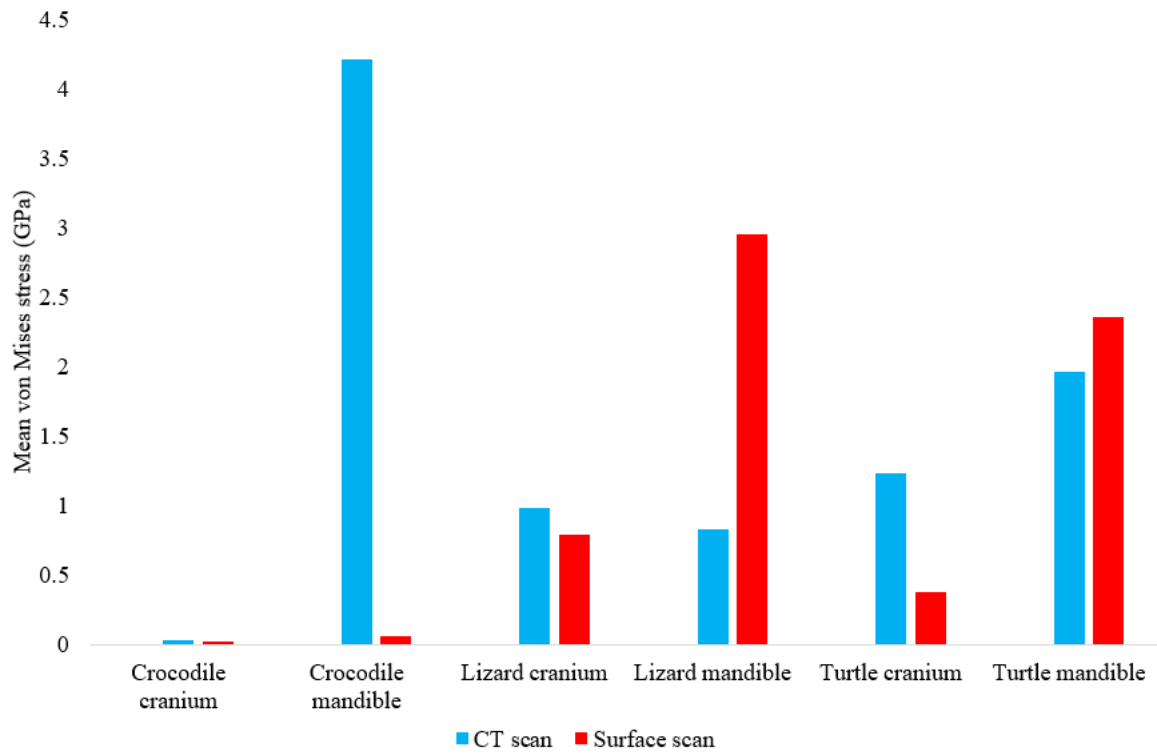
Figure 2.9. Mean unweighted von Mises stress values (GPa) in each FE model. Note the large discrepancies in the models requiring more reconstructive work, i.e., the crocodile and monitor lizard mandibles.
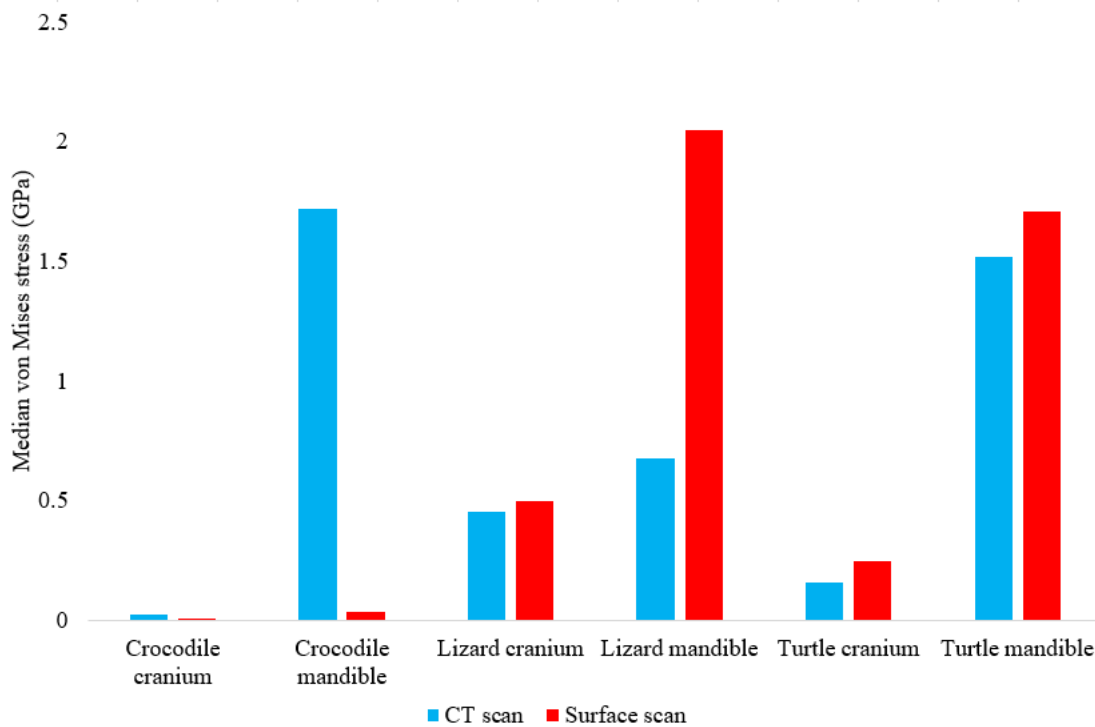
Figure 2.10. Median unweighted von Mises stress values (GPa) in each FE model.

My specific point analysis of the unscaled displacement values yielded consistent results, with models that had undergone extensive reconstructions differing the most in unscaled displacement. While model topography was attempted to be kept the same, small differences resulted from comparing meshes generated from CT and surface scan methods with slightly different geometries which led to differences in von Mises stresses.
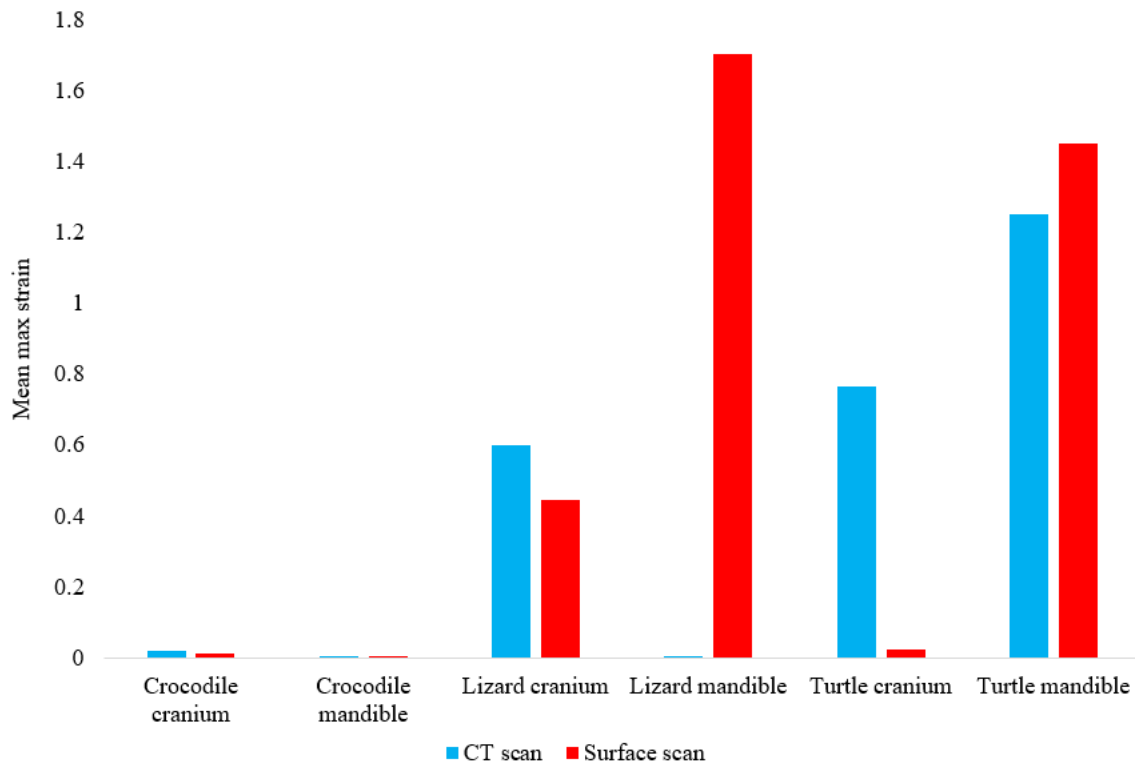
Figure 2.11. Maximum principal strain values (Emax) in each FE model. Y-axis represents the strain percentage.

Calculating the mesh-weighted arithmetic mean (MWAM) values significantly reduced the incongruity between CT scanned and surface scanned model stresses, as they differed overall by an average of 35.55% (Figure 2.12) compared to the unweighted average 85.76% value.
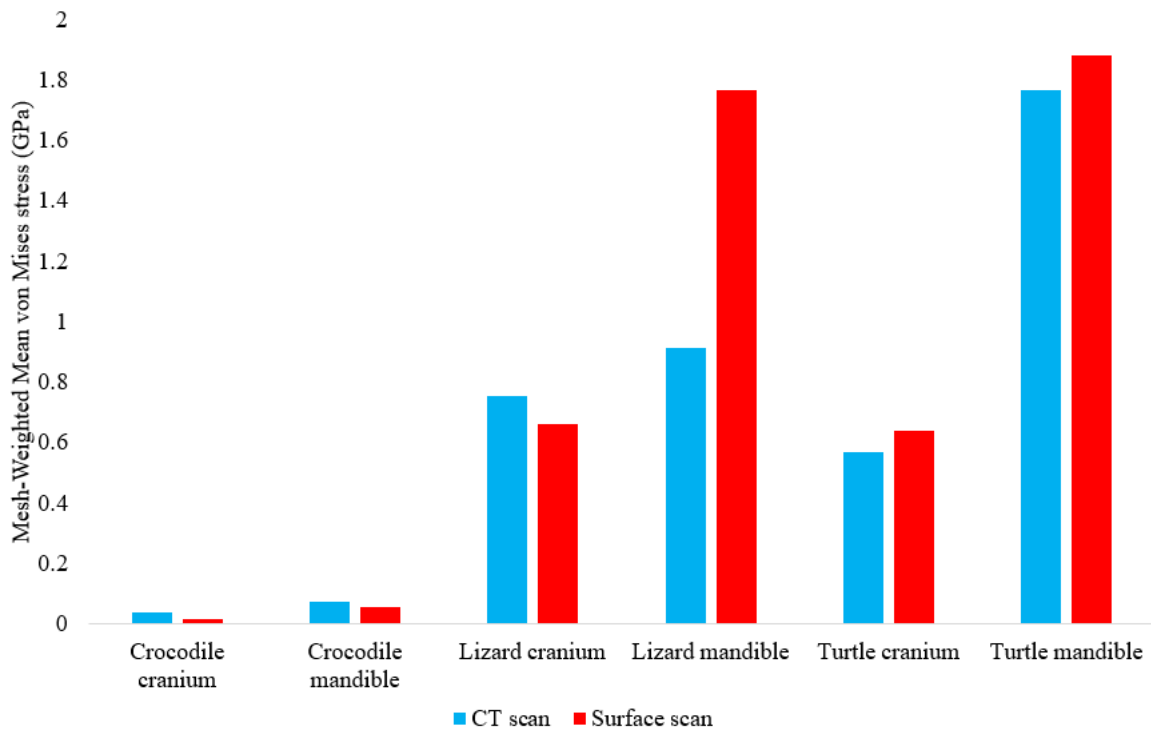
Figure 2.12. Mesh-weighted arithmetic mean (MWAM) von Mises stress values in each FE model. Note the lower discrepancies in von Mises stress values between model types when the MWAM is calculated. This is further elaborated on in the Discussion section.

2.7.1. *Crocodylus* results

The *Crocodylus* crania were two of the more consistent models in terms of surface geometry, von Mises stress results, deformation, and 3D model properties (Table 2.1, 2.2). The number of elements between the two model types differed by 11.42%. Mean unweighted von Mises stress differed by 61.37% and mesh-weighted von Mises stress differed by 82.62%. Maximum principal strain differed by 52.12%. Like many of the models, stress distributions were noted for appearing similar in both versions, despite stress magnitudes being inconsistent (Figure 2.13). Both models were deforming in different ways (Figure 2.14); anterior torsion occurred in each model due to teeth and their constraints only present on the right maxilla, but still resulted in differing behaviours overall. The specific point mean von

Mises stress values overall differed by 75.97% and the mean unscaled displacement values overall differed by 15.27% (Figure 2.15; Table 2.5).

Figure 2.13. von Mises stress results for the *Crocodylus* models, including the CT scanned cranium (A), surface scanned cranium (B), CT scanned mandible (C), and surface scanned mandible (D). All FE model images were scaled to the same maximum stress values for consistency.

Stress, strain and deformation magnitudes in the *Crocodylus* mandible surface scan model deviated significantly from its CT scanned counterpart. I attribute this to the extensive reconstructions which occurred in both models to fix the broken left ramus in the specimen (Figure 2.1). Difficulty in producing an identical model twice, as well the process of creating interior-filled surface scan models, resulted in high variability between models in terms of von Mises stress and topography. Mean unweighted von Mises stress differed by 194.43% and mesh-weighted von Mises stress differed by 23.33%. Max strain differed by 32.6%. The specific point mean von Mises stress values overall differed by 32.55% and the mean unscaled displacement values overall differed by 114.51% (Figure 2.15; Table 2.4, 2.5).

However, like the *Crocodylus* cranium, stress distributions still appear consistent between the models, despite the stark contrast in mean von Mises stress magnitudes and differences in the topography of the models (Figure 2.8, 2.11).
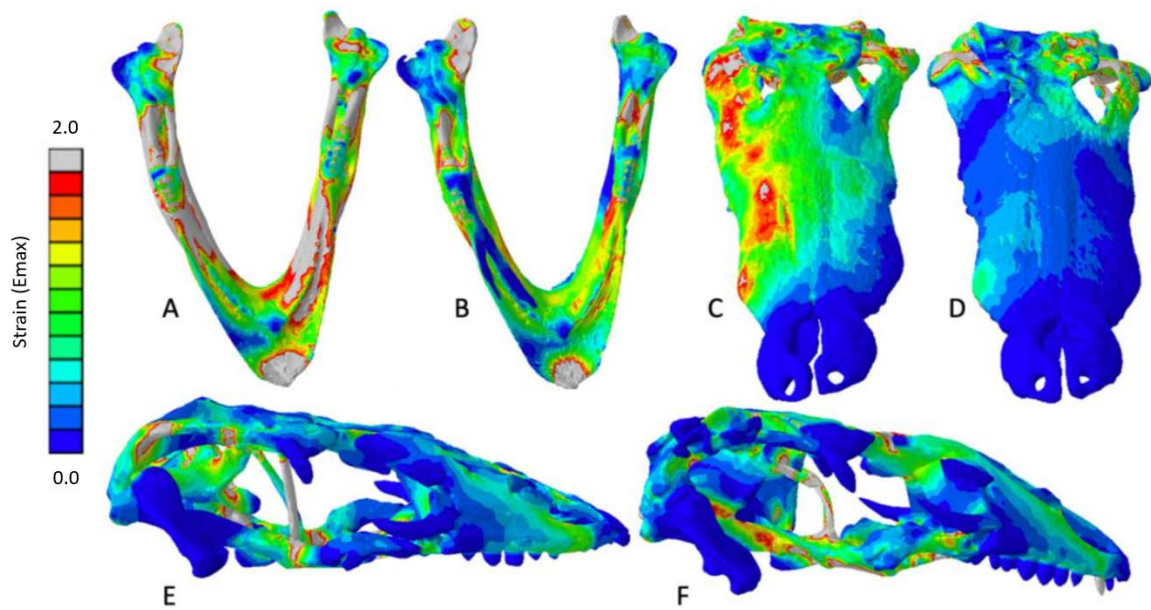
Figure 2.14. Exaggerated strain (Emax) deformation results in a selection of FE models tested, including the CT scanned *Chelonia* mandible (A), surface scanned *Chelonia* mandible (B), CT scanned *Crocodylus* cranium (C), surface scanned *Crocodylus* cranium (D), CT scanned *Varanus* cranium (E), and surface scanned *Varanus* cranium (F). Magnification was at 75%. Models not to scale. von mises stress key indicative of high and low values but not to

scale across all models.

Figure 2.15. Dorsal view of the *Crocodylus* cranium in both CT (A) and surface scan (B) models. The mean von Mises stress of five nodes was recorded at each location, averaged, and documented in Table 2.8. Both FE model images were scaled to the same maximum stress values for consistency. The mean unscaled displacement of five elements to represent deformation was recorded at each point, averaged and documented in Table 2.5 and Figure 2.16.

Table 2.4. Mean von Mises stress values (GPa) at locations 1-10 on *Crocodylus* FE models. These data are plotted on Figure 2.16.

Point	*Crocodylus* cranium CT scan stress	*Crocodylus* cranium surface scan stress	*Crocodylus* mandible CT scan stress	*Crocodylus* mandible surface scan stress	*Crocodylus* cranium model stress difference	*Crocodylus* cranium model stress difference percentage	*Crocodylus* mandible stress difference	*Crocodylus* mandible stress difference percentage
1	0.068	0.093	0.09	0.233	-0.025	31.06%	-0.143	88.54%
2	0.063	0.013	0.095	0.112	0.05	131.58%	-0.017	16.43%
3	0.065	0.016	0.121	0.111	0.049	120.99%	0.01	8.62%
4	0.021	0.003	0.136	0.133	0.018	150%	0.003	2.23%
5	0.048	0.012	0.145	0.137	0.036	120%	0.008	5.67%
6	0.041	0.028	0.158	0.095	0.013	37.68%	0.063	49.80%
7	0.036	0.039	0.033	0.056	-0.003	8%	-0.023	51.69%
8	0.026	0.006	0.053	0.036	0.02	125%	0.017	38.20%
9	0.027	0.031	0.038	0.024	-0.004	13.79%	0.014	45.16%
10	0.062	0.077	0.151	0.183	-0.015	21.58%	-0.032	19.16%
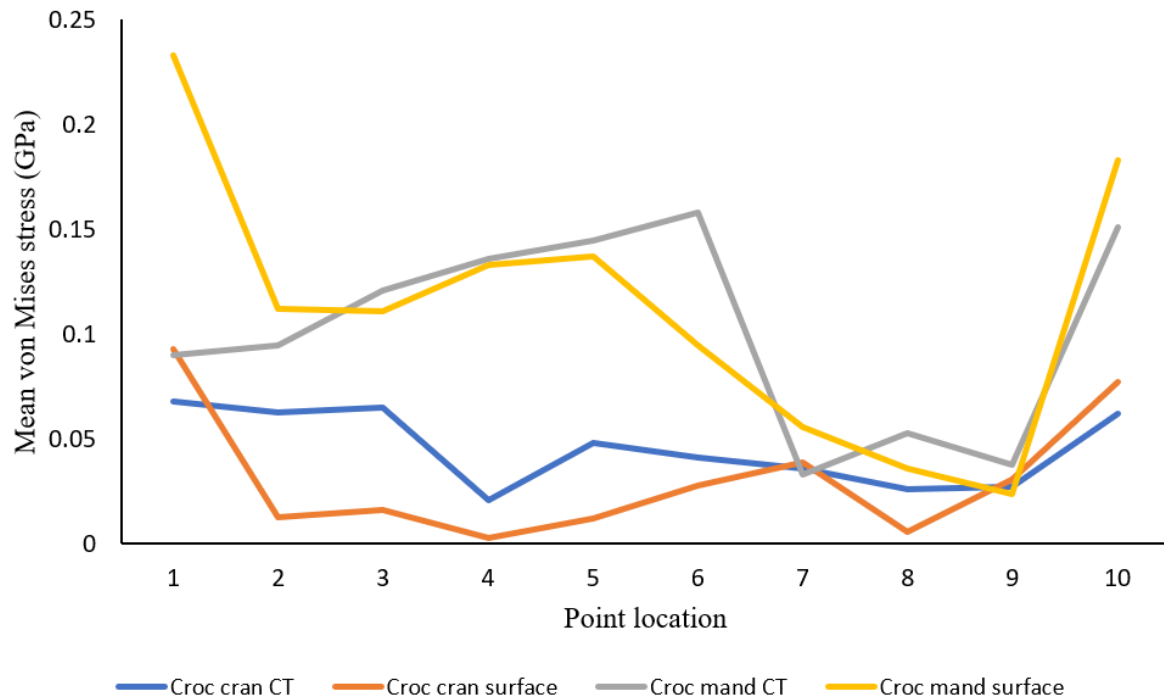
Figure 2.16. Line plot of *Crocodylus* mean von Mises stress for each point.

Figure 2.17. Dorsal view of the *Crocodylus* mandible in both CT (A) and surface scan (B) models. The mean von Mises stress of five elements was recorded at each location, averaged, and documented in Table 2.4 and Figure 2.16. The mean unscaled displacement of five elements to represent deformation was recorded at each point, averaged and documented in Table 2.5 and Figure 2.18. Both FE model images were scaled to the same maximum stress values for consistency. Note the incongruence in FE model topography due to the extensive reconstructions applied to each model of the mandible. This is further elaborated on in the Discussion section.

Table 2.5. Mean unscaled displacement values in cm at locations 1-10 on *Crocodylus* FE models. Mean values were calculated by recording and averaging five unscaled displacement values at each location as indicated on Figures 2.15 and 2.17. These data are plotted on Figure 2.18.

Point	*Crocodylus* cranium CT displacement	*Crocodylus* cranium surface scan displacement	*Crocodylus* mandible CT displacement	*Crocodylus* mandible surface scan displacement	*Crocodylus* cranium model displacement difference	*Crocodylus* cranium model displacement difference percentage	*Crocodylus* mandible displacement difference	*Crocodylus* mandible displacement difference percentage
1	0.00289	0.00248	0.0412	0.0124	0.0004	15.27%	0.0288	107.46%
2	0.00384	0.00244	0.0553	0.0145	0.0014	44.59%	0.0408	116.91%
3	0.0043	0.00329	0.0861	0.0143	0.001	26.61%	0.0718	143.03%
4	0.00525	0.00405	0.0936	0.008	0.0012	25.81%	0.0856	168.61%
5	0.00448	0.00326	0.0509	0.0048	0.0012	31.52%	0.0461	165.53%
6	0.00347	0.00271	0.0214	0.005	0.0008	24.60%	0.0164	124.86%
7	0.00276	0.00245	0.0341	0.0051	0.0003	11.90%	0.029	147.87%
8	0.00495	0.00376	0.0316	0.0099	0.0011	27.32%	0.0217	104.51%
9	0.00384	0.00328	0.0263	0.0195	0.0006	15.73%	0.0068	29.69%
10	0.0029	0.00325	0.0192	0.0109	-0.0004	11.38%	0.0083	55.15%
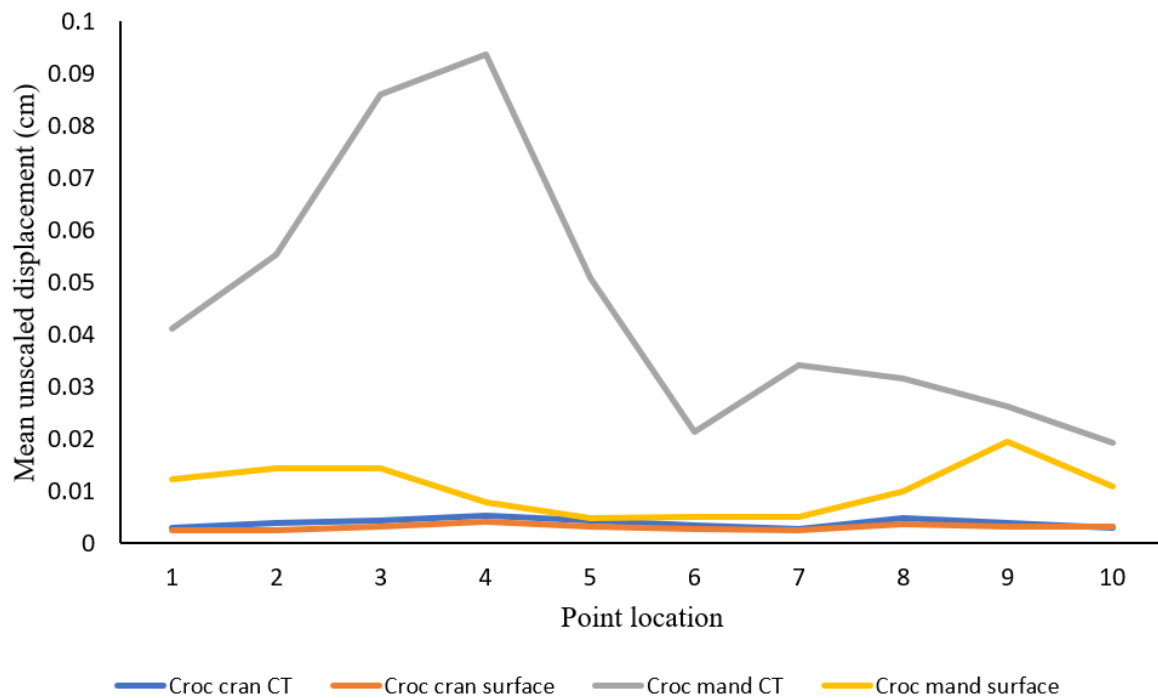
Figure 2.18. Line plot of *Crocodylus* mean unscaled displacement for each point.

2.7.2. *Varanus* results

The *Varanus* crania were two of the most consistent models in their geometry, von Mises stress distributions, and deformation. Mean unweighted von Mises stress differed by 21.14% and mesh-weighted von Mises stress differed by only 3.16%. Mean maximum principal strain differed by 29.5%. As in the other models, stress distributions were noted for their consistency throughout (Figure 2.19), with lower von Mises stress occurring in the surface scanned mandible due to thicker rami as a result of surface scan reconstructions. The CT scanned cranium generally yielded lower von Mises stress throughout, likely as a result of the cranial bones being more geometrically accurate in their robusticity. The specific point mean von Mises stress values overall differed by 83.76% and the mean unscaled displacement values overall differed by 24.52% (Figure 2.21; Table 2.6, 2.7). Deformation was more noticeable in the surface scanned model, especially in the bones of the cranium that were not as dense as the CT scanned model (Figure 2.14).
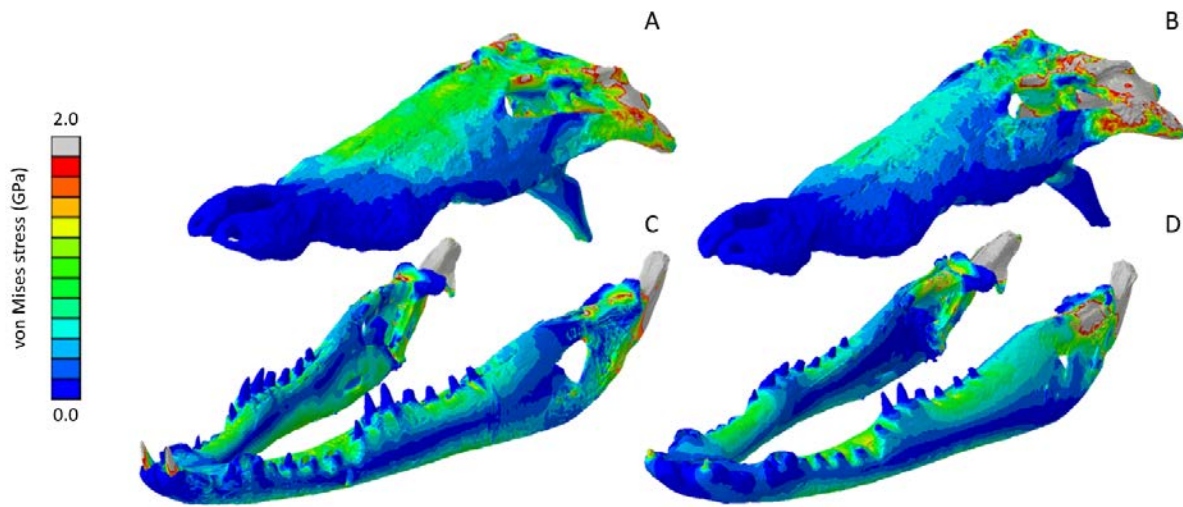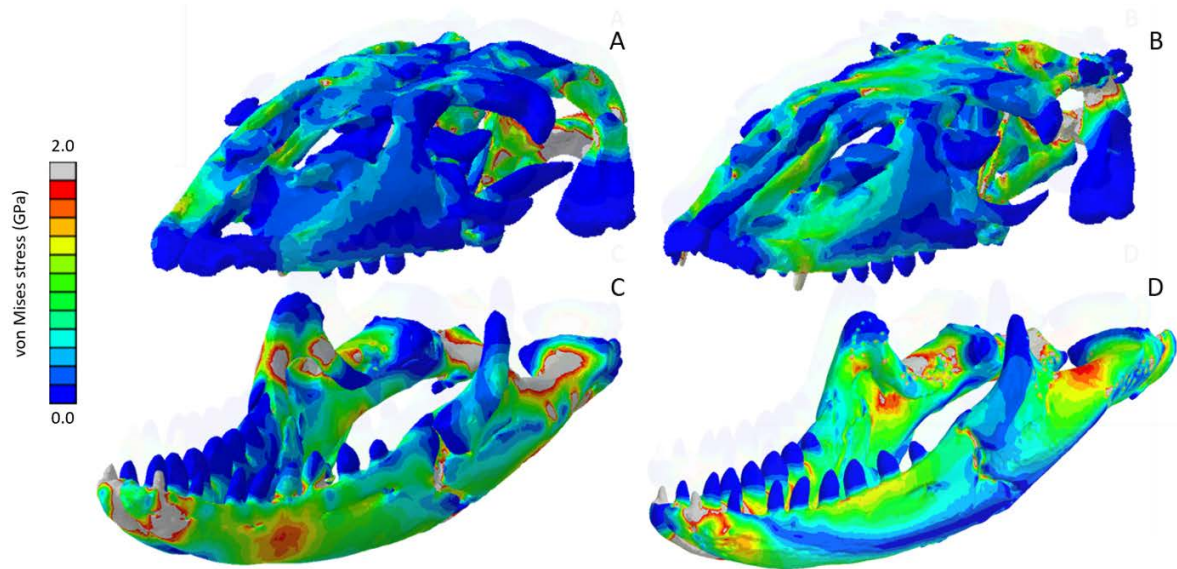
Figure 2.19. von Mises stress results for the *Varanus* models, including the CT scanned cranium (A), surface scanned cranium (B), CT scanned mandible (C), and surface scanned mandible (D). All FE model images were scaled to the same maximum stress values for consistency.

Figure 2.20. Dorsal view of the *Varanus* cranium in both CT (A) and surface scan (B) models. The mean von Mises stress of five elements was recorded at each location, averaged, and documented in Table 2.6. The mean unscaled displacement of five elements to represent deformation was recorded at each point, averaged and documented in Table 2.7. FE model images were scaled to the same maximum stress values for consistency.

The *Varanus* mandible models were two of the most inconsistent in terms of von Mises stress magnitude, deformation, and particularly maximum principal strain. This is likely a result of the relatively extensive reconstructive work applied to both models due to the missing right ramus, comparable to the *Crocodylus* mandible. Mean unweighted von Mises stress differed by 112.55% and mesh-weighted von Mises stress differed by 63.78%. Max strain differed by 199.99%. The specific point mean von Mises stress values overall differed by 99.57% (Figure 2.21) and the mean unscaled displacement values overall differed by 136.95% (Figure 2.19, 2.23; Table 2.6, 2.7). Like the other models, stress distributions were noted for their consistency despite the models having the highest unweighted von Mises stress and maximum strain differences.

Table 2.6. Mean von Mises stress values (GPa) at locations 1-10 on *Varanus* FE models. These data are plotted on Figure 2.21.

Point	*Varanus* cranium CT scan stress	*Varanus* cranium surface scan stress	*Varanus* mandible CT scan stress	*Varanus* mandible surface scan stress	*Varanus* cranium model stress difference	*Varanus* cranium model stress difference percentage	*Varanus* mandible stress difference	*Varanus* mandible stress difference percentage
1	0.006	0.008	0.297	2.471	-0.002	28.57%	-2.174	157.08%

2	0.425	0.927	2.256	4.714	-0.502	74.26%	-2.458	70.53%
3	2.231	2.603	1.829	0.958	-0.372	15.39%	0.871	62.50%
4	0.875	1.166	0.751	1.378	-0.291	28.52%	-0.627	58.90%
5	0.699	0.056	0.038	3.756	0.643	170.33%	-3.718	195.99%
6	0.091	0.605	0.031	8.552	-0.514	147.70%	-8.521	198.56%
7	0.658	0.924	1.433	1.939	-0.266	33.63%	-0.506	30.01%
8	0.523	1.002	2.421	2.612	0.479	62.82%	-0.191	7.59%
9	0.025	1.128	2.885	5.116	-0.903	133.48%	-2.231	55.77%
10	0.012	0.002	0.414	3.604	0.01	142.86%	-3.19	158.79%
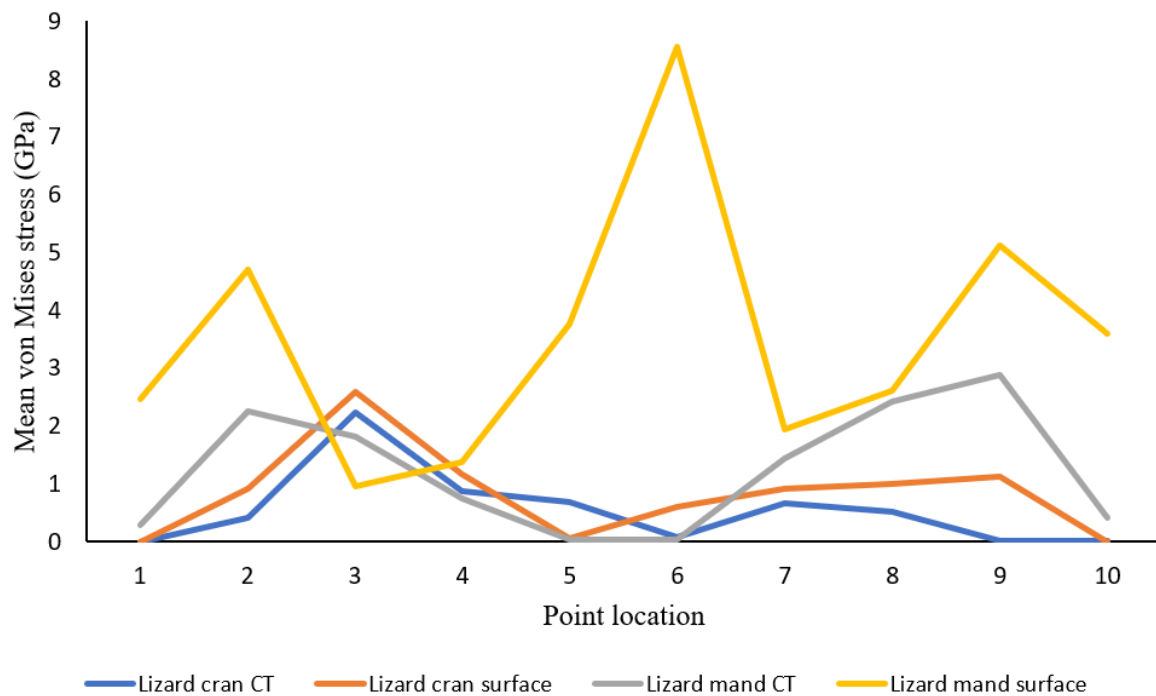
Figure 2.21. Line plot of *Varanus* mean von Mises stress for each point.
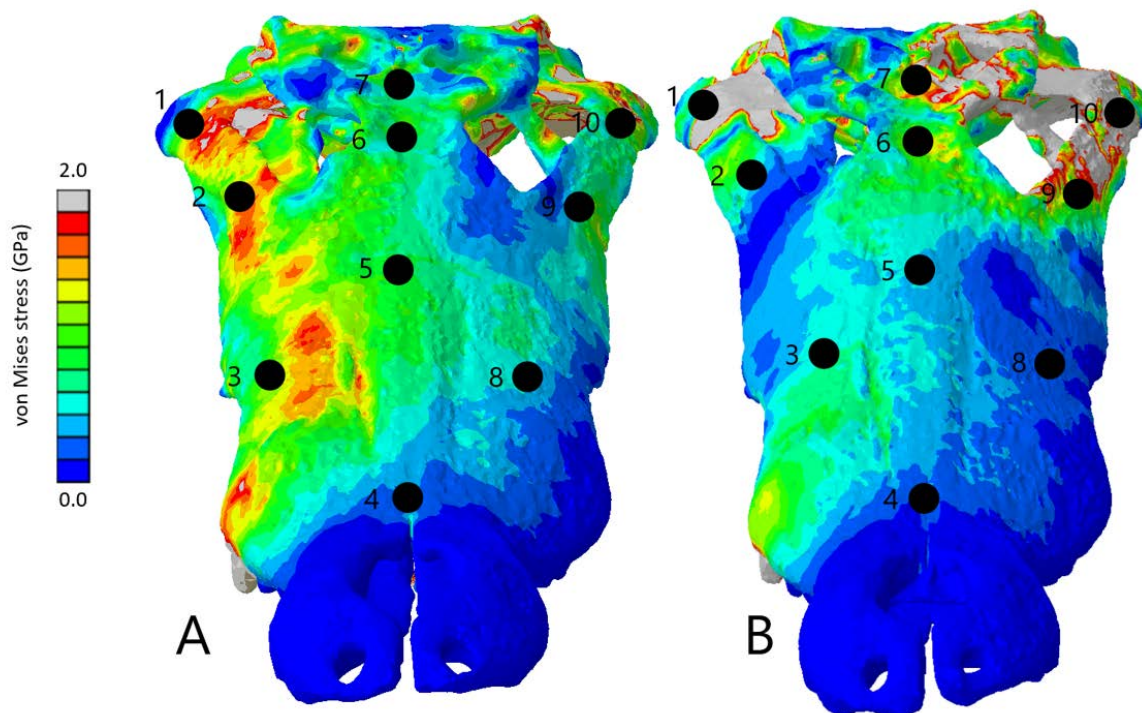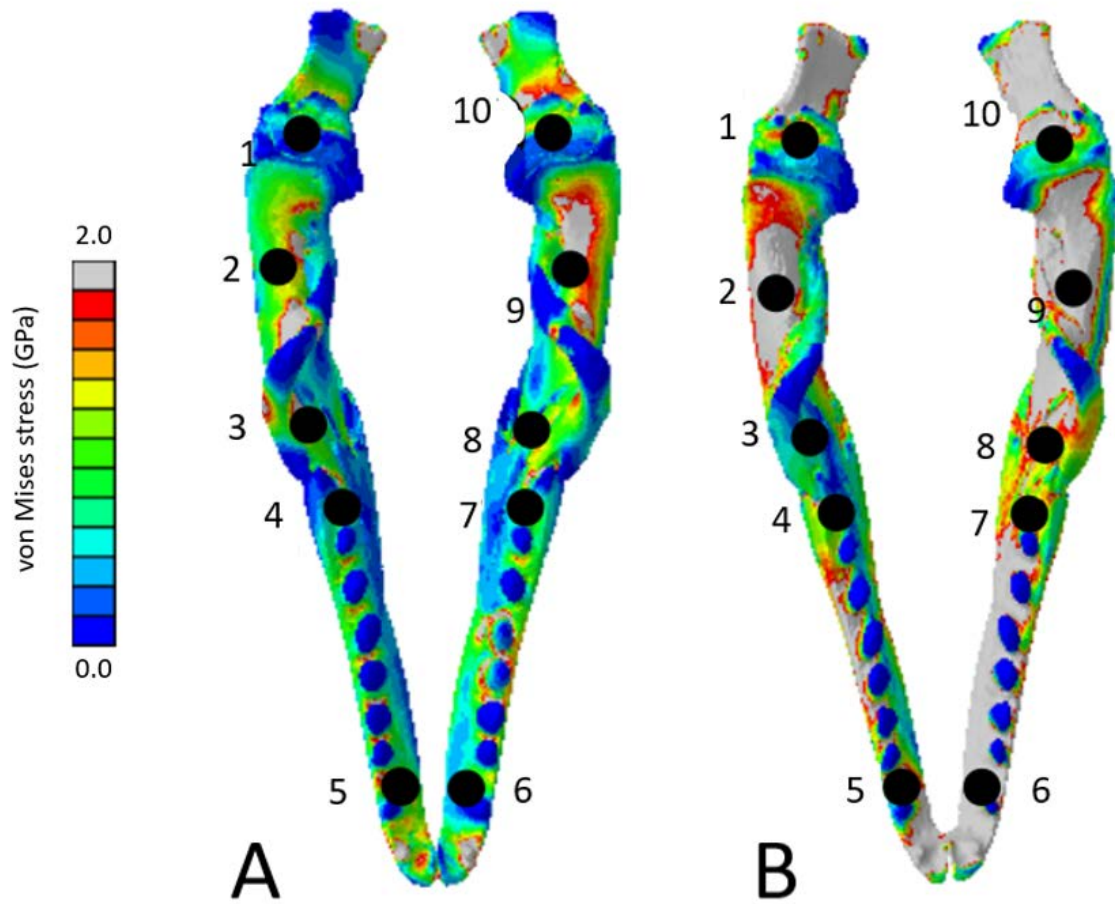
Figure 2.22. Dorsal view of the *Varanus* mandible in both CT (A) and surface scan (B) models. The mean von Mises stress of five elements was recorded at each location, averaged, and documented in Table 2.6. The mean unscaled displacement of five elements to represent deformation was recorded at each point, averaged and documented in Table 2.7. FE model images were scaled to the same maximum stress values for consistency.

Table 2.7. Mean unscaled displacement values in cm at location 1-10 on *Varanus* FE models. Mean values were calculated by taking the average of five unscaled displacement values at each location as indicated on Figures 2.20 and 2.22. These data are plotted on Figure 2.23.

Point	*Varanus* cranium CT displacement	*Varanus* cranium surface scan displacement	*Varanus* mandible CT displacement	*Varanus* mandible surface scan displacement	*Varanus* cranium model displacement difference	*Varanus* cranium model displacement difference percentage	*Varanus* mandible displacement difference	*Varanus* mandible displacement difference percentage
1	0.0115	0.0016	0.0306	0.0373	0.0099	152.22%	-0.0067	19.73%
2	0.0092	0.0099	0.0327	0.0838	-0.0008	7.81%	-0.0511	87.73%
3	0.0131	0.0131	0.0329	0.119	-0.0016	13.01%	-0.0861	113.36%
4	0.0156	0.0156	0.0279	0.141	-0.0012	8%	-0.1131	133.93%
5	0.0144	0.0116	0.0102	0.179	-0.0003	2.62%	-0.1688	178.44%
6	0.0133	0.0118	0.008	0.192	0.0005	4.15%	-0.184	183.96%
7	0.0123	0.0127	0.0205	0.214	-0.0003	2.39%	-0.1935	165.03%
8	0.0124	0.0128	0.0216	0.262	-0.0015	12.45%	-0.2402	169.54%
9	0.0098	0.0105	0.0197	0.186	-0.0007	6.39%	-0.1663	161.69%
10	0.0049	0.0034	0.0133	0.108	0.00149	36.21%	-0.0947	156.14%
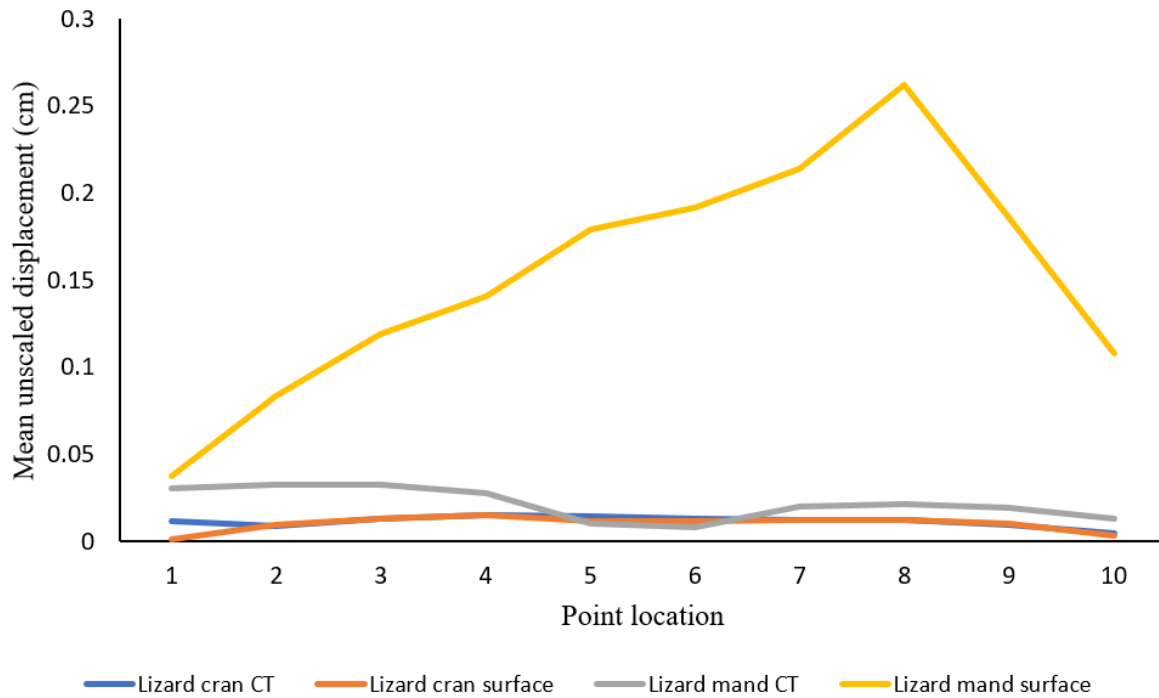
Figure 2.23. Line plot of *Varanus* mean unscaled displacement for each point.

2.7.3. *Chelonia* results

The *Chelonia* crania were relatively consistent in their geometric reconstructions, though the bony interior of the skull was difficult to accurately model in the surface scanned version (Figure 2.24). Mean unweighted von Mises stress differed by 106.73% and mesh-weighted von Mises stress differed by 11.59%. Maximum principal strain differed by 187.25%. The specific point mean von Mises stress values overall differed by 52.34% and the mean unscaled displacement values overall differed by 85.15% (Figure 2.25, 2.26; Table 2.8, 2.9). Stresses in the surface scanned model were more noticeable at the crown of the skull, due to the bony interior being better preserved in the CT scanned model and thus lessening the stresses occurring in bone-laden areas of the model.
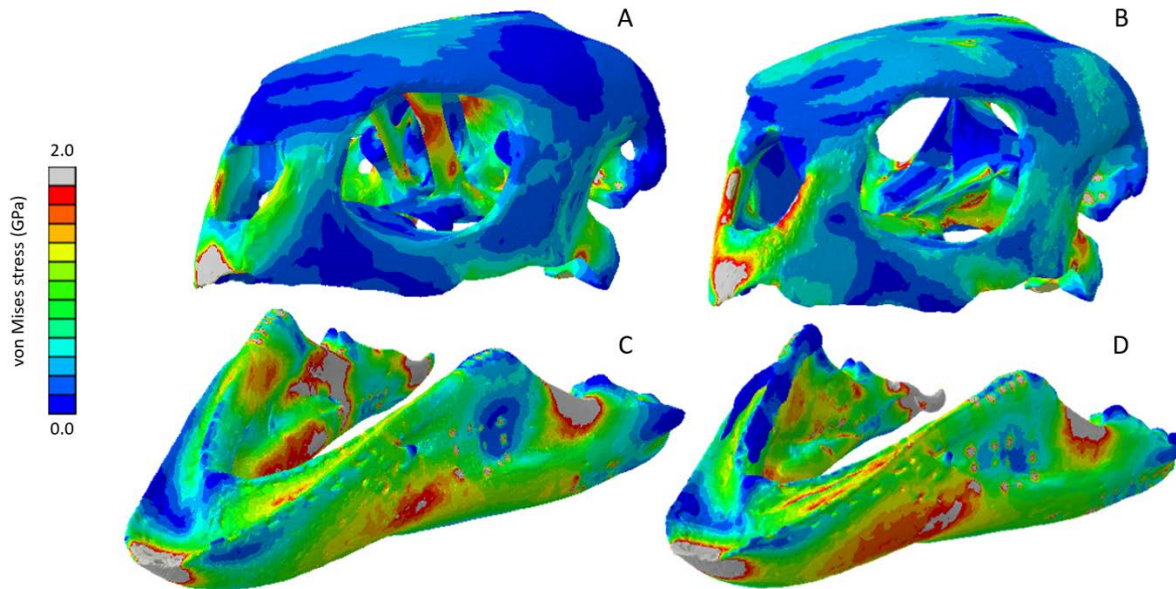
Figure 2.24. von Mises stress results for the *Chelonia* models, including the CT scanned cranium (A), surface scanned cranium (B), CT scanned mandible (C), and surface scanned mandible (D). All FE model images were scaled to the same maximum stress values for consistency.
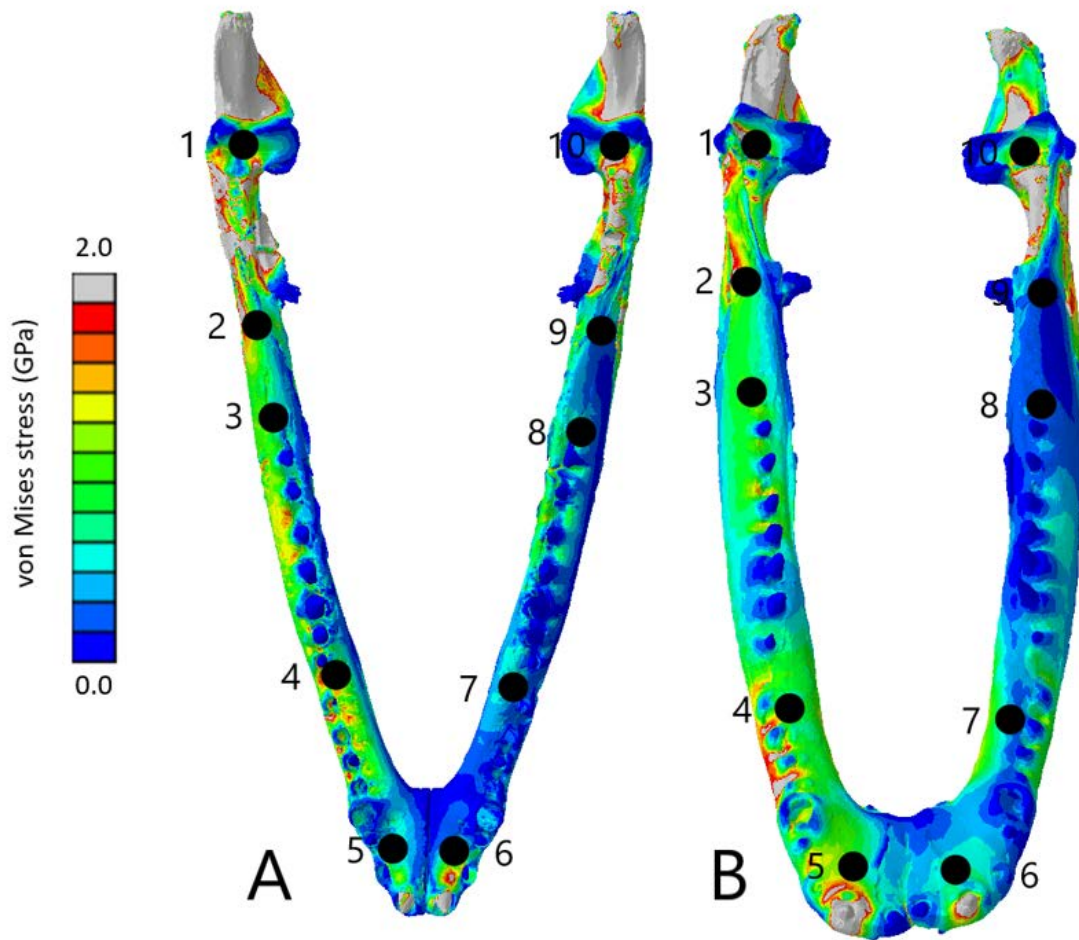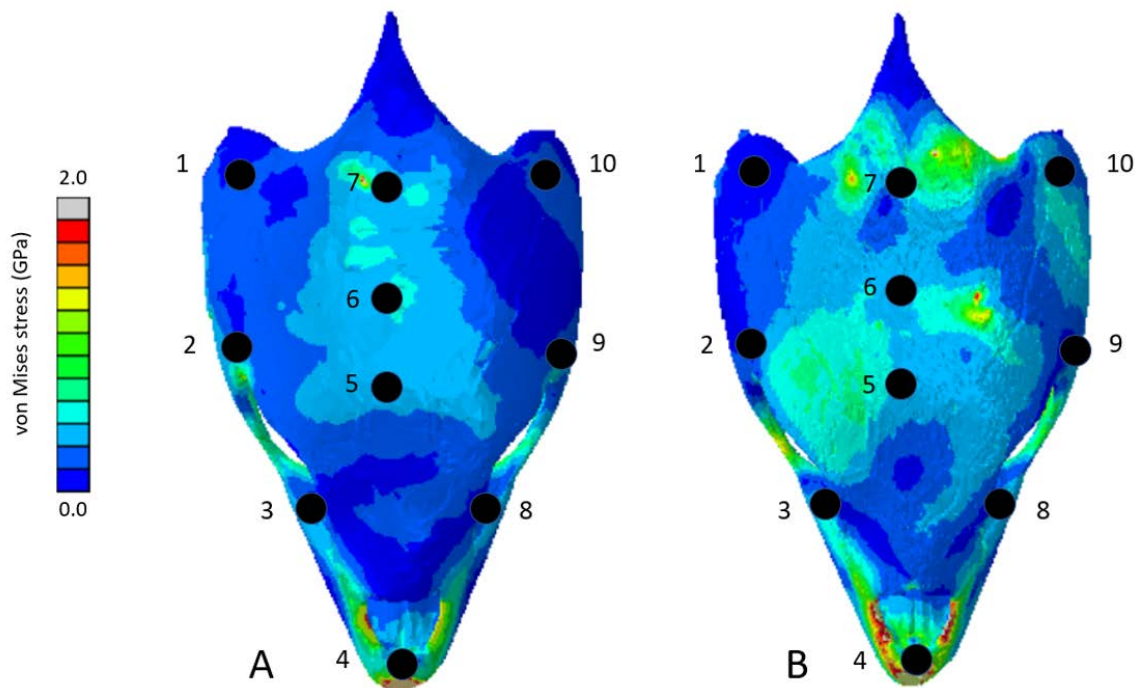
Figure 2.25. Dorsal view of the *Chelonia* cranium in both CT (A) and surface scan (B) models. The mean von Mises stress of five elements was calculated at each point and recorded in Table 2.8. The mean unscaled displacement of five elements to represent deformation was recorded at each point, averaged and documented in Table 2.9. FE model images were scaled to the same maximum stress value for consistency.

Table 2.8. mean von Mises stress values (GPa) at locations 1-10 on *Chelonia* FE models. These data are plotted on Figure 2.26.

Point	*Chelonia* cranium CT scan stress	*Chelonia* cranium surface scan stress	*Chelonia* mandible CT scan stress	*Chelonia* mandible surface scan stress	*Chelonia* cranium model stress difference	*Chelonia* cranium model stress difference percentage	*Chelonia* mandible stress difference	*Chelonia* mandible stress difference percentage
1	0.314	0.138	0.983	1.195	0.176	77.88%	-0.212	19.47%

2	1.693	0.649	7.959	7.795	1.044	89.15%	0.164	2.08%
3	0.818	1.029	3.814	1.156	-0.211	22.85%	2.658	106.96%
4	0.651	0.935	1.539	0.869	-0.284	35.81%	0.67	55.65%
5	0.659	0.669	0.985	1.379	-0.01	1.51%	-0.394	33.33%
6	0.871	0.731	2.403	1.464	0.14	17.48%	0.939	48.56%
7	0.564	1.124	3.191	3.572	0.56	66.35%	-0.381	11.27%
8	0.456	0.802	2.648	2.263	-0.346	55.01%	0.385	16.67%
9	0.419	0.244	2.962	3.921	0.175	52.79%	-0.959	27.87%
10	0.243	0.776	1.224	1.848	-0.533	104.61%	-0.624	104.61%
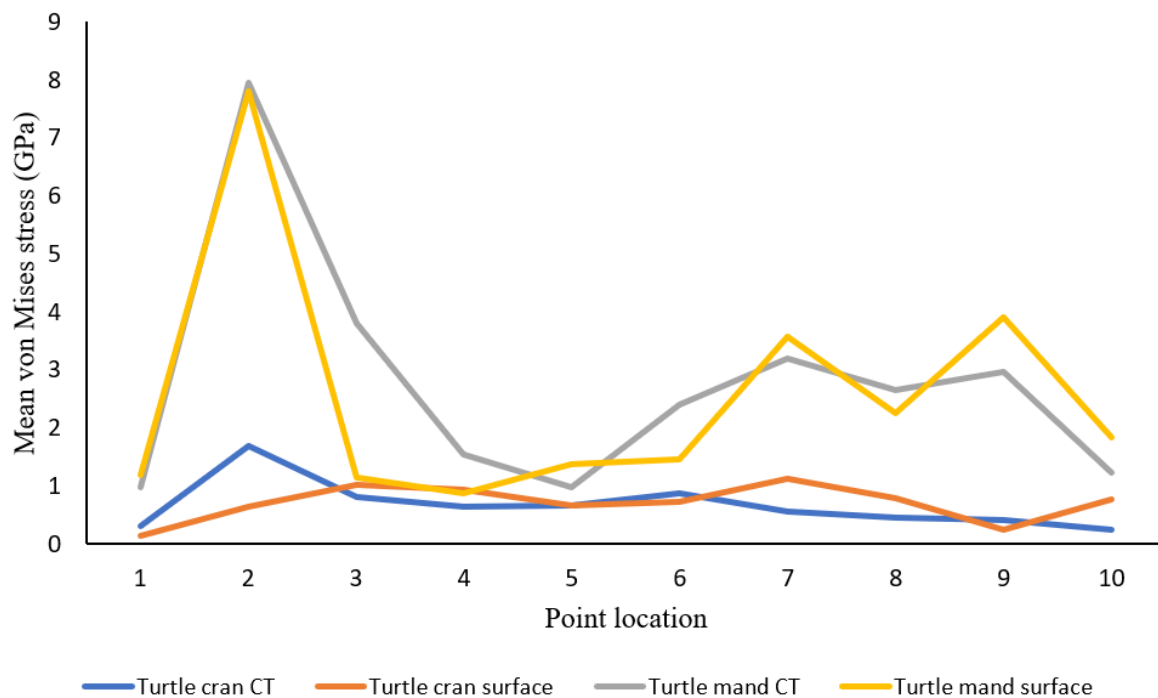
Figure 2.26. Line plot of *Chelonia* mean von Mises stress for each point.

The *Chelonia* mandible models were notable as they differed the least out of all models in terms of stress, strain, and deformity, due to the geometrically simple shape and small size requiring minimal reconstruction in both models (Figure 2.24). Mean unweighted von Mises stress differed by 18.31% and mesh-weighted von Mises stress differed by 6.24%. Max strain differed by 14.79%. The specific point mean von Mises stress values overall differed by

63

38.42% and the mean unscaled displacement values overall differed by 40.77% (Table 2.8, 2.9). The pattern and intensity of deformation was visually identical in both models (Figure 2.14).
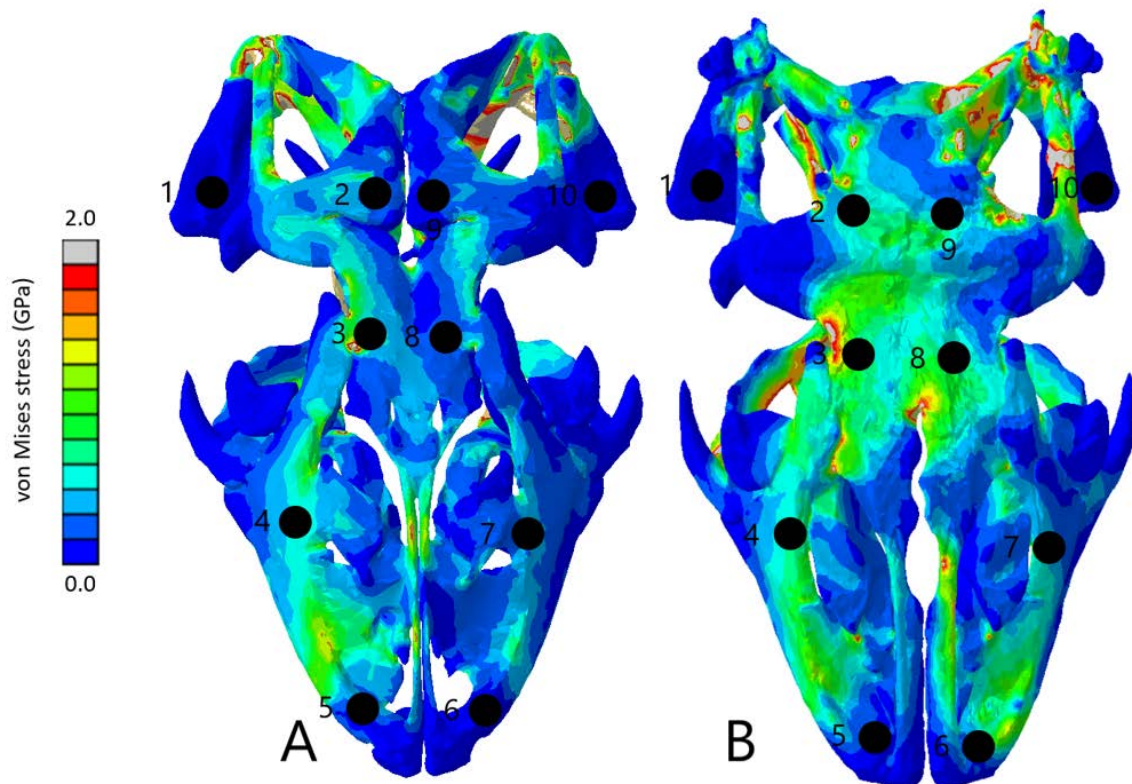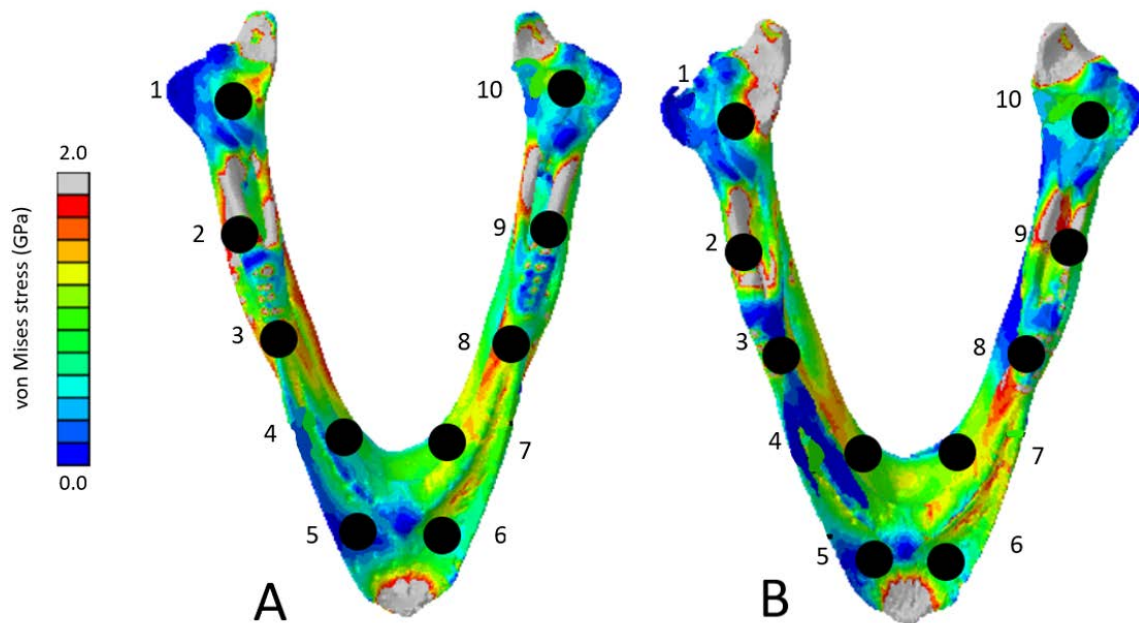

Figure 2.27. Dorsal view of the *Chelonia* mandible in both CT (A) and surface scan (B) models. The mean von Mises stress of five elements was recorded at each location, averaged, and documented in Table 2.8. The mean unscaled displacement of five elements to represent deformation was recorded at each point, averaged and documented in Table 2.9. FE model images were scaled to the same maximum stress value for consistency.

Table 2.9. Mean unscaled displacement values in cm at points 1-10 on *Chelonia* FE models. Mean values were calculated by taking five unscaled displacement values at each location as indicated on Figures 2.25 and 2.27. These data are plotted in Figure 2.28.

Point	*Chelonia* cranium CT displacement	*Chelonia* cranium surface scan displacement	*Chelonia* mandible CT displacement	*Chelonia* mandible surface scan displacement	*Chelonia* cranium model displacement difference	*Chelonia* cranium model displacement difference percentage	*Chelonia* mandible displacement difference	*Chelonia* mandible displacement difference percentage
1	0.0272	0.0747	0.0578	0.0497	-0.0475	93.23%	0.0081	15.07%
2	0.0244	0.0651	0.166	0.0886	-0.0407	90.95%	0.0774	60.80%
3	0.0147	0.039	0.184	0.166	-0.0243	90.50%	0.018	10.29%
4	0.0128	0.0264	0.145	0.102	-0.0136	69.39%	0.043	34.82%
5	0.0214	0.0537	0.117	0.0579	-0.0323	86.02%	0.0591	67.58%
6	0.0237	0.0622	0.135	0.0622	-0.0385	89.64%	0.7728	73.83%
7	0.0268	0.0731	0.154	0.0703	-0.0463	92.69%	0.0837	74.63%
8	0.0123	0.0247	0.174	0.132	-0.0124	67.03%	0.042	27.45%
9	0.0184	0.0449	0.169	0.127	-0.0265	83.73%	0.042	28.38%
10	0.0251	0.0648	0.0635	0.0547	-0.0397	88.32%	0.0088	14.89%
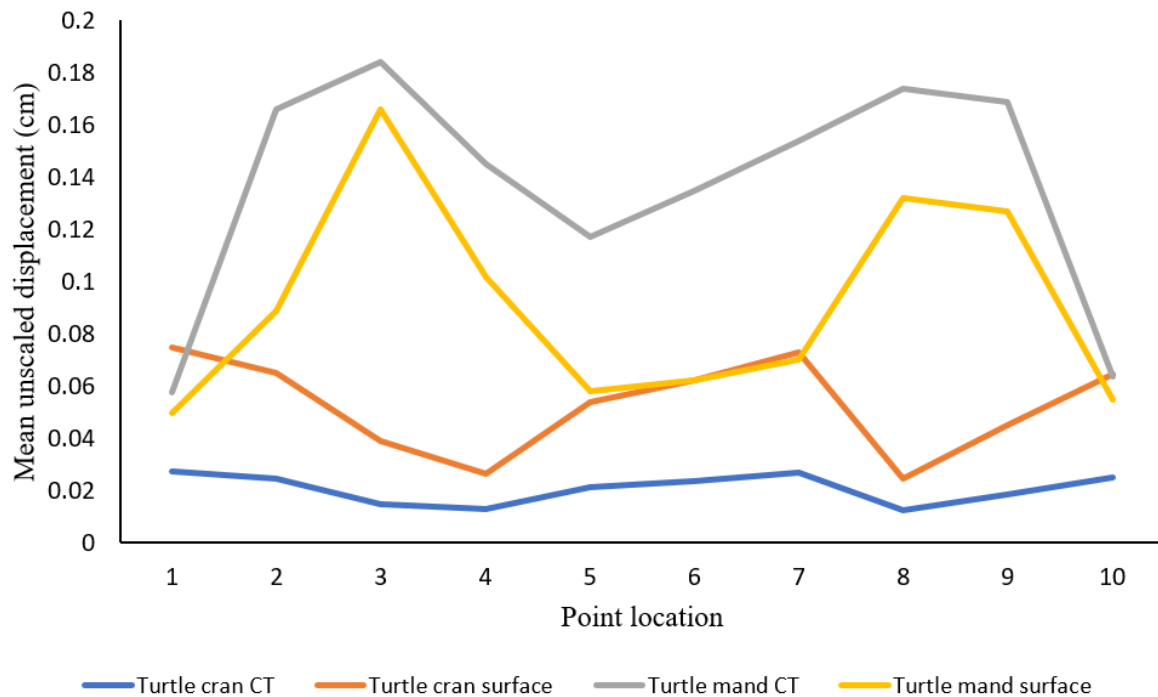
Figure 2.28. Line plot of *Chelonia* mean unscaled displacement for each point.

2.8. Discussion

This study demonstrated that 3D FE results can vary significantly between CT scanned models and surface scanned models, though the distributions of stress/strain occurring in both types of models tends to be similar. I can infer from these results that through use of surface scans, the mechanical attributes (overall stress and strain distribution, deformation patterns) of organisms can be confidently studied. However, the magnitude of stress and strain experienced is more difficult to assess. Calculating the mesh-weighted arithmetic mean (MWAM) to correct for element size can mitigate the differences between von Mises stresses in studies using both types of 3D models, as evidenced in this chapter.

2.8.1. Significance of reconstructions

As demonstrated by the *Crocodylus* and *Varanus* mandible models, surface scanned models which have undergone extensive reconstruction tend to differ most significantly in von Mises stress and strain, as there is a greater likelihood of models deviating from their CT scanned morphology. The *Crocodylus* mandible was missing a portion of its left ramus, and the *Varanus* mandible was missing its right ramus in its entirety, which necessitated the use of model editing software Blender 2.82 and Geomagic Studio 12 to duplicate the existing rami, mirror it, and reattach it to the opposite side of the jaws to complete the mandible. The *Crocodylus* mandible models experienced the greatest discrepancies in von Mises stresses, which I attribute to the extensive editing procedures including duplication and mirroring that can be difficult to precisely reproduce in separate models. The presence of fibrous tissues in the *Crocodylus* crania and mandible also contributed to inconsistencies in surface model generation, leading to further geometric differences between the two models (Figure 2.29).

The *Varanus* rami was similarly duplicated and attached at the anterior symphysis; however, the smaller size and geometric simplicity made the process of producing more identical

models easier than the *Crocodylus* mandible. I attribute the lower von Mises stress occurring in the surface scanned mandible to thicker rami as a result of surface scan reconstructions.

Due to its relatively small size, simple geometry, and completeness, the *Chelonia* mandible required the least extensive reconstruction efforts for both CT and surfaced scanned models. The mandibles also exhibited the smallest discrepancies between model types in terms of von Mises stress and principal strain. I attribute these similarities in FE output to the factors outlined above, which are sharply contrasted by the *Crocodylus* and *Varanus* mandibles. Generally, models which required the least amount of reconstruction yielded stress, strain, and deformation results that did not deviate markedly between CT scanned and surface scanned versions. However, model simplicity is not a strict requirement for stress and strain congruence, as evident in the *Crocodylus* cranium, which were the largest models by surface area and volume and the second largest in terms of element number but still relatively consistent in FE output.

Even in models yielding significant differences in von Mises stress values, the mesh-weighted arithmetic mean (MWAM) was useful in reducing overall stress differences. When this correction is applied only the *Crocodylus* cranium shows an increased in discrepancy in stress values. The MWAM accounts for the different element volumes generated across a model when calculating von Mises stresses. As the geometries of models created via different scanning methods will vary, these calculations are integral to studies assessing biomechanical attributes of different scan types.

Table 2.1 provided the element counts for each type of 3D model. Certain element counts differed substantially between the CT and surface scanned counterparts, particularly in the *Chelonia* cranium and *Varanus* mandible. These differences may have influenced differences in both stress and displacement values. Tseng et al. (2011) found that 300,000 solid elements

produced reaction forces and strain energy comparable to higher resolution models in tests of a CT scanned wolf mandible. McCurry et al. (2015) found size and shape to have a larger overall influence on 3D FEA results than a range of surface resolutions ranging from 20,000-300,000 elements. Thus, comparative studies of this nature should attempt to pair models of more equal element counts, though the size and shapes were generally consistent in most models save for those requiring restorative work.

Figure 2.14 displayed the exaggerated strain deformation in several models, including the *Chelonia* mandibles, *Crocodylus* crania, and *Varanus* crania. The models are sound in their construction, but here I discuss why the results differ – likely due to the different construction techniques required for surface scanned data that is lacking interior geometry, compared to CT scanned data, and how this is exaggerated in more complex skull models compared to mandibles with simpler geometry. The results are different and can be explained, but the models are not unreliable. Geometrically-simple models, e.g., the *Chelonia* mandibles tend to behave in a more similar way, whereas more complex models like the *Crocodylus* crania demonstrate substantially different responses. The *Crocodylus* cranium was the largest and most geometrically-complex specimen used in this chapter; surface scan in-filling likely contributed to differences in both types of models including stress responses as shown in Figure 2.13. Additionally, the *Crocodylus* crania models deviated in their stress responses further when the MWAM was calculated, demonstrating clear differences in model behaviours likely due to model size and complexity.

Figure 2.29. Dorsal view of the Nile crocodile mandible pinpointing areas of infilling during the surface scan reconstructions. Fibrous material remaining on the mandible is the main cause of the surface scanned models being denser than the CT scanned version, as the infilling process connected fibrous tissues together and created a larger model than the CT version. This infilling process may also apply to extinct taxa where matrix may still be attached to the fossil rather than soft tissue.

Finally, stress magnitudes were abnormally high in all models; bone yield strength is typically tested using MegaPascals (MPa), but this chapter used GigaPascals (GPa) due to the high von Mises stress values. This may have been due to user error when scaling model sizes. When CT data was imported into Avizo Lite 9.5, voxel sizes of 1 were chosen for X, Y, and Z rather than 0.120, which resulted in large CT models. These models were then manually scaled down to be equivalent to surface scanned models using the resizing tool in Blender 2.82. As a result, stress magnitudes may have deviated from their actual values. Posthoc it was discovered that although the crocodile muscle forces were in proportion to the Porro et al. (2011) alligator study, the values were too high as they had not been divided by the number of nodes to which the force was applied. As a result, the stress values were erroneously high. However, as the purpose of the study was to compare the behaviour of the

CT derived and surface scan derived models, the conclusions still stand as high values were applied to ach model Stress patterns will remain the same, just the magnitudes will increase in a proportionate manner.

2.9. Future work

This studied used surface scanned models that were solidified post-surface reconstruction using the segmentation tools in Avizo Lite 9.5, as surface scanned models are initially hollow upon creation in Artec Studio 14 Professional. A question remains concerning the validity of hollow surface scanned models and how much they deviate from solidified models in terms of von Mises stress. Studies only requiring the exterior of 3D structures, such as geometric morphometrics, benefit from the time saved in retaining the hollow interior of the models. However, the results of hollow surface scanned models in FE studies and the degree to which their FE output would differ from solid models is not well understood. von Mises stress distributions in hollow models may be similarly worth considering.

This study quantified differences in FE output when comparing different 3D models under identical parameters. One of the difficulties of this study was maintaining identical parameters in both sets of models due to incongruences in model geometry, reconstructions, and muscle nodes. Future work may attempt to compare more geometrically simple models as to limit these inconsistencies between model output. Geometry of the models was kept as consistent as possible; however, variance between models including element count and volume is generally impossible to avoid. Studies of this nature may attempt to mitigate these model variances as much as possible, potentially by testing more geometrically simple models, which limit the likelihood of inconsistencies (although the FE-models presented here reflect the nature of the complex geometry of the skull, which does influence FE-model outputs from CT versus surface scanned models).

As I noted in this chapter, the mesh-weighted arithmetic mean (MWAM) is a powerful method of mitigating von Mises stress differences between CT scanned models and surface scanned models. In all models apart from the *Crocodylus* cranium, the discrepancies in mean von Mises stress were reduced. Future work may attempt to further assess the effectiveness of the MWAM in biomechanical studies involving 3D models, particularly those using different types of scans.

Additionally, Table 2.3 listed the numbers of nodes applied for muscle groups in CT models and surface scanned counterparts. These were generally matching in numbers with some noticeable differences, e.g., 27 and 47 in the mAMEP of the *Crocodylus* mandible. This was another inconsistency in boundary conditions between the model types which arose due to topographical differences in certain models, particularly the *Crocodylus* and *Varanus* mandibles; however, the same force was applied to each model, yet across different number of nodes. This was necessitated as the CT and surface scan models had different geometries. Applying the same force across a different number of nodes may create differences in the area over which force is applied, which could lead to differences in results. The check this, I measured the difference between node application area. On average this was 0.3 mm – a difference in area that would have negligible effect on the stress and strain results for the whole model.

2.10. Conclusion

When their utility in 3D FEA studies is compared to CT scans, white light surface scans are effective in capturing deformation and stress and strain distributions. These aspects relate to overall mechanical behaviour and make surface scan models fine candidates for use in studies concerning questions of relatedness in biomechanical patterns. However, surface scans may

have questionable results when analysing absolute magnitudes of stress and strain in 3D models. As demonstrated in this study, geometrically simple objects requiring minimal editing, such as the *Chelonia* mandible, will not differ much from their CT versions, especially when the MWAM is calculated. Complex objects requiring little editing, such as the *Crocodylus* skull, can also produce comparable stress distributions between surface scan and 3D. Objects which require extensive reconstructions, such as the *Crocodylus* and *Varanus* mandible, will result in incongruent absolute magnitudes, though the MWAM calculation generally still aids in bridging the gap between results. Given some inconsistent behaviours in the *Crocodylus* crania, i.e., deformation response and further deviation when calculating the MWAM, I conclude that large, complex specimens will generally result in more imprecise data output when surface scanning due to the geometric features of a large object that are lost in the reconstruction process. However, preservation of these features will vary depending on the skill of the user, the element count of the models, and the equipment being used to scan the object (Díez Díaz et al. 2021).

Studies utilizing both types of scans should attempt to avoid using specimens requiring extensive reconstructive work if possible, e.g., those missing skeletal elements. When this is not possible, extra care must be taken to ensure that reconstructions are as accurate as possible. MWAM calculations are recommended for all comparative FEA studies attempting to compare stress magnitudes in different model types, though it will not always aid in reducing stress discrepancies as evidenced in the *Crocodylus* crania.

Acknowledgments

Memorial Building and Sue Holwell for loaning me the turtle skull from the University of

Bristol's Life Sciences Building.

Assessing skull function in tyrannosauroid dinosaurs using 3D finite element analysis

3.1. Abstract

Tyrannosauroids are an iconic and well-studied clade of fossil taxa, with *Tyrannosaurus rex* often serving as a model organism for studies of extinct vertebrate musculature, function, and biomechanics. Tyrannosauroids varied greatly in their body size distribution, with certain genera such as *Alioramus* achieving half the body size of *T. rex* at identical growth stages. While the impact of size on locomotory ability has been often studied in theropods, the impact of large body size on feeding performance is largely unknown. This has been due to limitations in 3D scanning methods and software preventing such studies in giant animals. Here I investigated the feeding performance of six tyrannosaur genera of variable body size and skull morphology. I used 3D finite element analysis (FEA) to test whether skull shape becomes more or less resistant to feeding induced forces as taxa body size increases. All cranial and mandibular models were scaled by adult *T. rex* FMNH PR 2081's surface area to better understand the influence of shape on tyrannosauroid skull function. Muscle sensitivity analyses were used to help account for assumptions in my FE results. It was found that *Tyrannosaurus rex* experienced higher absolute stresses compared to its small-bodied relatives as safety factors were not exceeded, and they were able to accommodate these high stresses because their mandibles were so much larger. When surface area values were equalized across genera to account for the effect of size and test efficiency of skull shape, smaller individuals experience notably greater stresses than larger relatives. This is due to the more robust cranial osteology characterized in the allometry of tyrannosauroids. These results may indicate that the wide crania which are characteristic of tyrannosaurids convey a functional advantage that more basal tyrannosauroid taxa lacked, enabling large tyrannosauroids such as *T. rex* to generate and withstand greater bite forces to better prey on large herbivorous dinosaurs that were common in Late Cretaceous North America.

3.2. Introduction

The theropod dinosaur clade Tyrannosauroidea contains some of the largest bipedal predators to have ever existed, including the iconic North American *Tyrannosaurus rex* (Osborn 1905, 1906), *Daspletosaurus torosus* (Russell 1970), and the Chinese *Qianzhousaurus sinensis* (Lü et al. 2014). Tyrannosauroid genera are typically recognized for their broad skulls, small forelimbs, and heterodont dentition (Smith 2005), though basal members of the clade possessed lightly- constructed skulls, slender body plans, and cranial ornamentation in certain taxa (Xu et al. 2004, 2006). The group was first recorded in the Oxfordian stage of Middle Jurassic Asia (160 Ma ago) and gradually spread to North America (Brusatte & Carr 2016) where its heaviest taxon, the 7-tonne *T. rex* (Farlow et al. 1995; Bates et al. 2009; Hutchinson et al. 2011), has been recovered.

The effects of large body size on locomotion and agility have been frequently studied in theropod dinosaurs (Hutchinson & Garcia 2002; Hutchinson 2006; Sellers et al. 2017; Snively et al. 2019). Conversely, the effects of large body size on feeding function have been less clear (Rayfield 2011). The smallest known tyrannosauroid taxa include *Guanlong wucaii*, which attained a body length of 3-3.5 m and a body mass of 125 kg (Holtz 2008), and *Dilong paradoxus,* which reached a minimum length of 1.6 m (Xu et al. 2004). The largest taxon is the 12.3-12.4 m long hypercarnivore *T. rex* (Persons et al. 2020), whose mature growth stages have been documented (Carr 1999, 2020). Overall, the clade is ideal for studies of gigantism and its influence on skull function, given the relatively high number of complete skulls available for study. Additionally, the clade evolved a wide diversity in skull morphologies; *T. rex* in particular is noted for its widely-set, bone-crunching mandibles (Gignac & Erickson 2017) which distinguishes the genus from its slenderer-bodied relatives including *Alioramus altai* (Brusatte et al. 2009). This allows us to test hypotheses of skull shape variation and its possible relationship to feeding biomechanics.

The primary purpose of this study was to compare the cranial and mandibular biomechanical capabilities of several tyrannosauroid genera via 3D modelling and infer how bite capabilities changed with acquisition of large body size in derived tyrannosauroid species. Biomechanics is the study of the mechanical aspects of biological systems, including both locomotion and feeding. In extinct taxa, behaviour and ecology can be inferred by our understanding of biomechanics, and thus we rely on a combination of 3D scanning and experimental methods to better interpret ancient ecosystems and extinct vertebrate evolution. Due to the extremes of non-avian dinosaur anatomy and physiology, including their massive terrestrial body sizes (Therrien & Henderson 2007; Sander et al. 2011; Bates e al. 2016), non-avian dinosaurs are of particular interest in animal biomechanics (Alexander 1989, 1991, 2006; Bishop et al. 2020). Body size is one of the most important quantifiable properties when considering the evolution of extant and extinct metazoans as it is tied to many physiological and fitness characters (Blanckenhorn 2000). Theropod dinosaurs are of particular interest as they are the largest bipeds described by science, with individuals such as *T. rex* attaining the heaviest body masses of any terrestrial bipeds known to science (Therrien & Henderson 2007).

I used finite element analysis (FEA), which is a nondestructive modelling technique that calculates stress and strain experienced by 2D and 3D structures when a force is applied. Stress is the force per unit area, and one possible measurement of how close a structure is to breakage, which is typically expressed in Mega Pascals (MPa). Strain is the unitless measurement of both how much deformation occurs in the structure and another possible measurement of how close it is to breakage. I used maximum principal strain-based metrics here, as it has been suggested that they may better describe and predict the mechanical behaviour of bone than stress-based metrics (Dutel et al. 2021) The FE-method is commonly used in engineering and medical sciences to test for weaknesses in buildings, machines, and human bones, as it can analyze any solid structures.

FEA has seen increasingly common use in studies of vertebrate evolution, usually to study skull function (Ross 2005; Rayfield 2007); however, it is occasionally used to study invertebrate evolution (Hassan et al. 2016; Lemanis & Zlotnikov 2018). Many FEA studies have pertained to 2D models, as they are cheaper and simpler than 3D to construct and analyze, especially in studies examining and comparing many models (Pierce et al. 2008; Rayfield 2011; Morales-García et al. 2019). FEA studies of theropod dinosaur skulls have often been limited to 2D, mainly because of the general large skull size noted in theropod dinosaur clades (Rayfield 2005, 2011; Cuff & Rayfield 2013; Ma et al. 2021). Due to the growing availability of 3D scanning methods and software which can adequately analyze 3D models quickly, FEA studies using 3D models have become more common (Bell et al. 2009; Lautenschlager et al. 2013, 2016; Cost et al. 2019; Rowe & Snively 2021; Barbosa et al. 2023). Typically studies of 3D models include only 2-4 models due to the time taken to scan material, segment bones and generate accurate 3D models, and run the analyses.

Tyrannosauroids are an important clade of theropod dinosaurs due to their relatively complete fossil record, comprised of multiple nearly complete specimens with preserved skull material (Brusatte & Carr 2016; Figure 3.1). Functional analyses concerning the skull generally require complete skulls, particularly those examining feeding biomechanics (Bates & Falkingham 2012). Skull length data was compiled for each specimen to quantify size differences between taxa (Table 3.1). In the study presented here, the crania and mandibles of seven tyrannosauroid specimens were analysed: two mature *T. rex*, a mature *Daspletosaurus torosus,* a mature *Albertosaurus sarcophagus*, a mature *Bistahieversor sealeyi*, young juvenile *Raptorex kriegsteini,* and adolescent *Alioramaus altai*. These individuals were selected due to the completeness of their cranial material, their phylogenetic differences including cranial morphologies and body sizes, and availability. Differences in morphologies allows us to better understand changes in feeding stresses the animals experienced as they

gradually attained larger body sizes and how they were able to cope with higher feeding stresses at their largest body sizes.

Due to the massive size of some tyrannosauroid skull material, particularly derived tyrannosaurids, it is challenging to create 3D model data of various taxa. Large size is a limiting factor in studies of skull function in giant animals; the CT scanning of taxa including adult *T. rex* requires costly and difficult-to-use equipment (Reims et al. 2016). It is in recent years that the more widely available usage of surface scanning has made the acquisition of 3D fossil data more achievable for large specimens and museums mounts (Cunningham et al. 2014; Díez Díaz et al. 2021). Thus, it is now possible for us to accurately investigate a giant-bodied dinosaur clade entirely using 3D FEA. This had been a limiting factor of studies of large theropod skull function. Surface scan methods can capture shape but cannot resolve internal anatomy, so have traditionally not been used for structural analysis of large fossil skulls. However, in Chapter 2, I tested the relative performance of surface scanned versus CT scanned skulls of the same specimen (Chapter 2; Rowe & Rayfield 2022). This allowed us to understand that while solid surface scanned models were stronger than their CT counterparts, the patterns of stress and strain were almost identical. Thus, I can compare the relative performance of CT and surface scanned skulls in the same dataset. The study presented in this chapter is one of the first analyze skull mechanics in a wide array of theropod dinosaur individuals within a single clade. Each specimen was either surface scanned using a handheld surface scanner or generated via computed tomography scanning, resulting in geometrically accurate 3D skull models representing the morphological diversity of Tyrannosauroidea.

Table 3.1. Specimen numbers, skull lengths, body masses, and replica status for each tyrannosauroid specimen included in this study in descending order of skull length.

Specimen name	Specimen number	Skull length (mm)	Body mass estimate (kg)	Original or replica
Tyrannosaurus rex	FMNH PR 2081	1,275 (Gignac & Erickson 2017)	7,377 (Campione et al. 2014)	Original
Tyrannosaurus rex	MOR 555	1,200 (Padian 2022)	6,216 (Campione et al. 2014)	Original
Bistahieversor sealeyi	NMMNH P-27469	1,070 (Carr & Williamson 2010)	3,300 (Molina-Pérez & Larramendi 2019)	Original
Daspletosaurus torosus	FMNH PR308	1,050 (Carr 1999)	2,700 (Christiansen & Farina 2004)	Replica
Albertosaurus sarcophagus	TMP 1981.010.0001	880 (Currie 2003)	1,685 (Christiansen & Farina 2004)	Replica
Alioramus altai	IGM 100/1844	700 (Lü et al. 2014)	369 (Brusatte et al. 2009)	Original
Raptorex kriegsteini	LH PV18	300 (Sereno et al. 2009)	65 (Sereno et al. 2009)	Replica

3.2.1. Specimens

In this study, seven individual tyrannosauroid skull specimens representing six genera were tested using 3D finite element analysis. As indicated in Table 3.1., the taxa vary greatly in skull length and overall estimated body masses, as well as skull shape. Additionally, specimens vary in their ontogenetic stage.

We include two mature specimens of *Tyrannosaurus rex*. MOR 555 and FMNH PR 2081 are both mature specimens, though MOR 555 is considered to be a younger adult of roughly ~23–27 years old at death, while FMNH PR 2081 is roughly 28 (Carr 2020). FMNH PR 2081 is often noted as one of the most complete and senescent *T. rex* specimens (Brochu 2003) and it is the largest specimen in this study, with a length of 12.3-12.4 m (Holtz 2011) and an estimated mass of 7 tonnes (Campione et al. 2014).

Albertosaurus is a genus of large-bodied tyrannosaurid from Middle Maastrichtian of northwestern North America approximately 71 Ma. The type species, *A. sarcophagus*, is included in this study (Osborn 1905). While it is one of the larger tyrannosaurid genera described in the literature, reaching lengths of 8-9 m (Russell 1970) and body mass estimates of approximately 1.7 tons (Christiansen & Farina 2004), it is still notably smaller than other Late Cretaceous tyrannosaurids such as the 4.5-5 tonne *Tarbosaurus* (Molina-Pérez & Larramendi 2019) and 6 tonne *Tyrannosaurus*. We also include *Daspletosaurus torosus* as another large-bodied tyrannosaurid from Campanian to Maastrichtian (77-75 Ma) North America. It is one of the larger tyrannosaurids like *Albertosaurus*, attaining lengths of 9 m (Russell 1970) and body masses of 2-3 tonnes (Campione et al. 2014).

Bistahieversor sealeyi is a basal eutyrannosaurian from the Campanian (75.5-74.5) Ma of New Mexico, USA, from the Kirtland and Fruitland Formations (Carr & Williamson 2010). It is one of the largest tyrannosauroid genera, estimated to have attained lengths of 9 m and 3.3

tonnes (Molina-Pérez & Larramendi 2019). It is also noted for its brain and sinus system which was nearly identical to tyrannosaurids like *Tyrannosaurus* (McKeown et al. 2020).

Alioramus is another subadult tyrannosaurid which is noted for its relatively slender body and smaller mass estimates (Brusatte et al. 2009; Lü et al. 2014). It is represented by two species, *A. remotus* (Kurzanov 1976) and *A. altai* (Brusatte et al. 2009); *A. remotus* does not have a complete skull and we therefore used *A. altai* in our analyses. It was been suggested that Alioramin genera maintained their slender bodies into maturity and hunted smaller, more agile prey to avoid competition with larger tyrannosaurids (Foster et al. 2022).

Raptorex kriegsteini is recognized from a single individual recovered from Mongolia. It was originally considered to originate from the Barremian–Aptian of Lower Cretaceous China (~125.8–124.1 Ma) (Sereno et al. 2009); later work placed it as Late Cretaceous and likely originating from the Nemegt of Mongolia (Fowler et al. 2011). It is characterized by its relatively large skull, strong hindlimbs, and two-fingered forearms which are noted in tyrannosaurids, in contrast to basal tyrannosauroids (Sereno et al. 2009). The specimen has been estimated to be roughly 5-6 years of age based on lines of arrested growth (LAGs) (Fowler et al. 2011). Due to its age and proximity to the large Mongolian tyrannosaurid genus, *Tarbosaurus* (Maleev 1955), it may represent a juvenile form; however, this has been disputed in phylogenetic analyses of tyrannosaurids and it may instead represent a valid genus (Brusatte & Carr 2016; Carr 2023).

Two hypotheses were tested with results from simulated stress and strain in 3D cranial and mandible models of a variety of tyrannosauroid specimens at various body sizes and skeletal morphologies.

Hypothesis (1). Larger tyrannosaurid taxa such as *Tyrannosaurus rex* and *Daspletosaurus torosus* experience higher absolute stresses and strain in their skull and mandible under

simulated feeding loads due to their large size and increased muscle mass. Despite this, they were able to accommodate high feeding forces due to morphological differences in the skull between large and small taxa enabling large taxa to adequately absorb high stresses with minimal chance of breakage. This was one of the conclusions noted in Rowe & Snively 2021, though the total specimen pool was smaller, and it pertained only to the mandibles at different growth stages. A similar phenomenon is observed in giant pliosaurs (Foffa et al. 2014), wherein the large adults experience higher stresses than small individuals.

Hypothesis (2). When muscle force values for cranial and mandibular models are equalized to account for size and test for cranium and mandible shape to accommodate feeding loads, the smaller-bodied tyrannosaur specimens (*Raptorex kriegsteini, Alioramus altai,* and *Albertosaurus sarcophagus*) experience higher stress and strain relative to the larger-bodied taxa (*Tyrannosaurus* rex, *Daspletosaurus torosus*, and *Bistahieversor sealeyi*) due to the more robust cranial osteology in larger taxa**.**
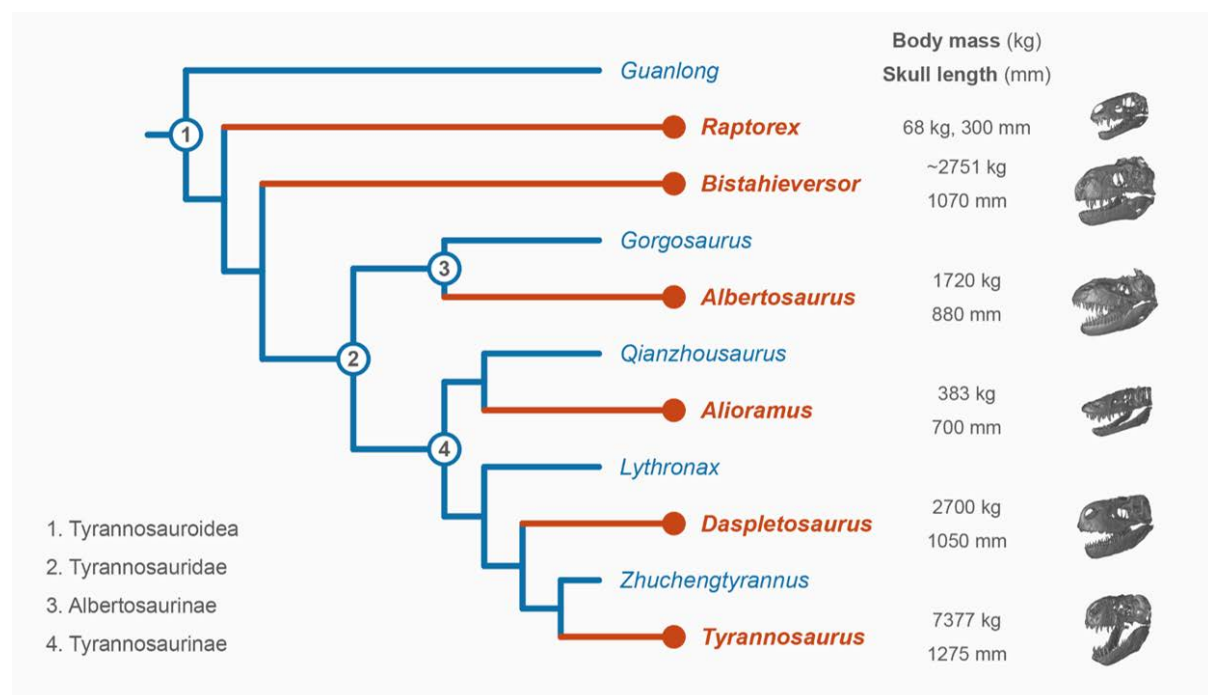
Figure 3.1. Skull models of the six genera tested plotted on a cladogram with mass and body length estimates. Cladogram based on Brusatte & Carr 2016.

3.3. Materials and methods

3.3.1. Surface scanning

In this study, three models were constructed from surface scan datasets. I included a replica of the large North American tyrannosaurid *Dapsletosaurus torosus* (FMNH PR308) which is housed in the Field Museum geology collections. Due to the size and mass of the skull, the individual was surface scanned using an Artec Space Spider white light surface scanner. The crania and mandibles were scanned as separate files, because large file sizes typically result in significant slowdown in Artec Studio Professional 14 during scanning.

In Artec Studio Professional 14, the scans were aligned to best resemble the entire skull. Stray pixels and other outliers were deleted, as well as frames with max error values above 0.3. I then applied global registration to convert all one-frame surfaces to a single coordinate system using information on the mutual position of each surface pair. The Sharp Fusion tool was used to create a polygonal 3D model, which solidifies the captured and processed frames into an STL file. I used Sharp Fusion rather than Fast or Smooth Fusion as it best preserves fine details of scans, including teeth and rugose textures. Lastly, I used the small-object filter to clean the model of floating pixels and the fix holes function to fill any gaps.

The *Daspletosaurus*'s cranial model had a filled antorbital fenestra, promaxillary fenestra, and nares. These elements were hollowed out in the final STL model using the 3D eraser tool in Artec Studio Professional, to be as anatomically accurate as possible (Figure 3.2).
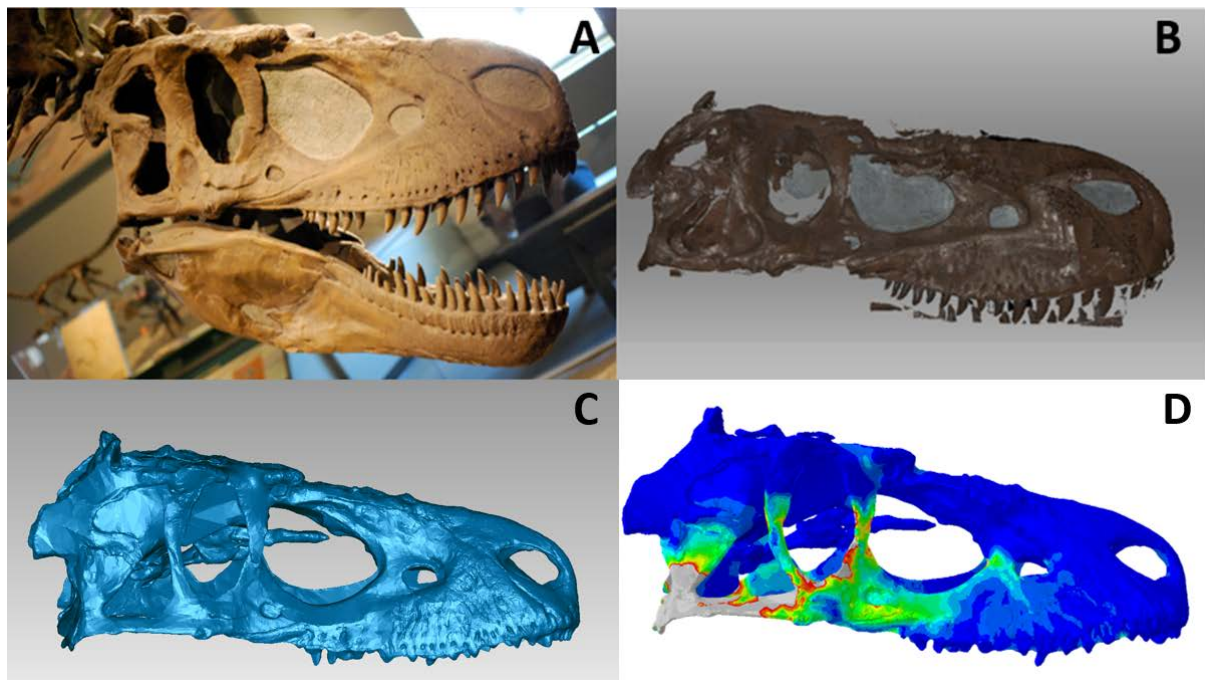
Figure 3.2. 3D finite element analysis workflow demonstrated using the *Daspletosaurus torosus* (FMNH PR308) skull. (A) FMNH PR308 skull replica mounted at the Field Museum, Chicago, IL, USA. (B) Aligned surface scans of FMNH PR308 in Artec Studio Professional 14 prior to Sharp Fusion, which converts scans into the STL file type. (C) STL file in Geomagic Studio 12. Internal anatomy was reconstructed based on Russel 1970 and photographs of the specimen. (D) Finite element model in Abaqus/CAE 6.14-1.

The *Albertosaurus sarcophagus* skull was surface scanned at the Las Vegas Natural History Museum (LVNHM) and downloaded from Sketchfab. It is a replica of a disarticulated specimen at the Royal Tyrell Museum of Palaeontology which only contains the left jugal and maxilla in their original articulation (D. Henderson, personal communication 2022). The STL file of the skull model was originally comprised of both the cranium and mandible as a single model. The downloaded file was uploaded into Blender 2.82, where the mandible was deleted and the file was saved as only a cranium. A similar protocol was then followed to create a file containing only the mandible model.

3.3.2. Computed tomography scanning

Four of the seven tyrannosauroid skull specimens analysed in this study were CT scanned at various institutions in the United States. These include a senescent *Tyrannosaurus rex* (FMNH PR 2081), the *Bistahieversor sealeyi* holotype (NMMNH P-27469), *Aliormaus altai* (IGM 100/1844), and a replica of the juvenile *Raptorex kriegsteini* (LH PV18). The *Tyrannosaurus rex* (popularly known as "Sue") was CT scanned at Rocketdyne Division, Boeing North America, Inc., of Chatsworth, CA using a Minatron 205 scanner (Brochu 2003). The Minatron 205 scanner, built by Scientific Measurement Systems, Inc. generated 748 2 mm thick coronal slices. These were manipulated with VoxBlast 2.2 (VayTek, Inc., Fairfield, IA) to make three-dimensional models and to generate synthetic resliced stacks in the sagittal and horizontal planes. Slice thickness was 2mm for the full-skull sagittal and horizontal sets, and 0.5mm for the horizontal stack through the braincase.

The *Bistahieversor* 3D model was generated from CT scanning at the Microtron Facility at Los Alamos National Laboratory, using a Bremsstrahlung source (Scanditronix M22 medical therapy source, Microtron) with 10MeV x-rays with a 0.25mm lead filter (McKeown et al. 2020). The *Alioramus altai* (IGM 100/1844) skull bones (Brusatte et al. 2009) were CT scanned in a GE phoenix v|tome|x CT scanner at the American Museum of Natural History Microscopy and Imaging Facility. 13 elements were scanned with the following general settings: voltage between 140 and 210 kV, amperage between 125 and 175 μA, and a slice thickness ranging from 0.09 to 0.14 mm (Gold et al. 2013). Because of the *Alioramus* skull disarticulation, I assembled the bones into a complete skull using Artec Studio Professional 14. This was done by individually opening the STL files in Artec Studio, aligning the bones based on imagery from Brusatte et al. 2009, and exporting the combined meshes as a single file.

Because of taphonomic deformation that is commonly seen in vertebrate fossils and the influence deformation can have on data (Kammerer et al. 2020; Demuth et al. 2022), the 3D

model of *Bistahieversor* was retrodeformed using mesh editing software. This was achieved by importing the deformed model into Artec Studio Professional 14 and deleting the more severely deformed half of the cranium. The less deformed half of the cranium was then duplicated, mirrored, and reattached to the original along the midline. The now-complete skull was uploaded into MeshLab 2020.06 to check for and delete self-intersections which are common in procedures where 3D models are merged (Figure 3.3). This step was vital as self-intersecting triangles make meshing impossible. The model was then imported into Blender 2.82 and the 'Sculpt' module was selected. The midline of the model was then smoothened to better resemble how the skull would appear when the skull was undeformed. Lastly, the model was uploaded into Geomagic Studio 12 and the Mesh Doctor tool was selected, which corrects the model for spikes, holes, self-intersections, and other potential sources of error when meshing a 3D model.
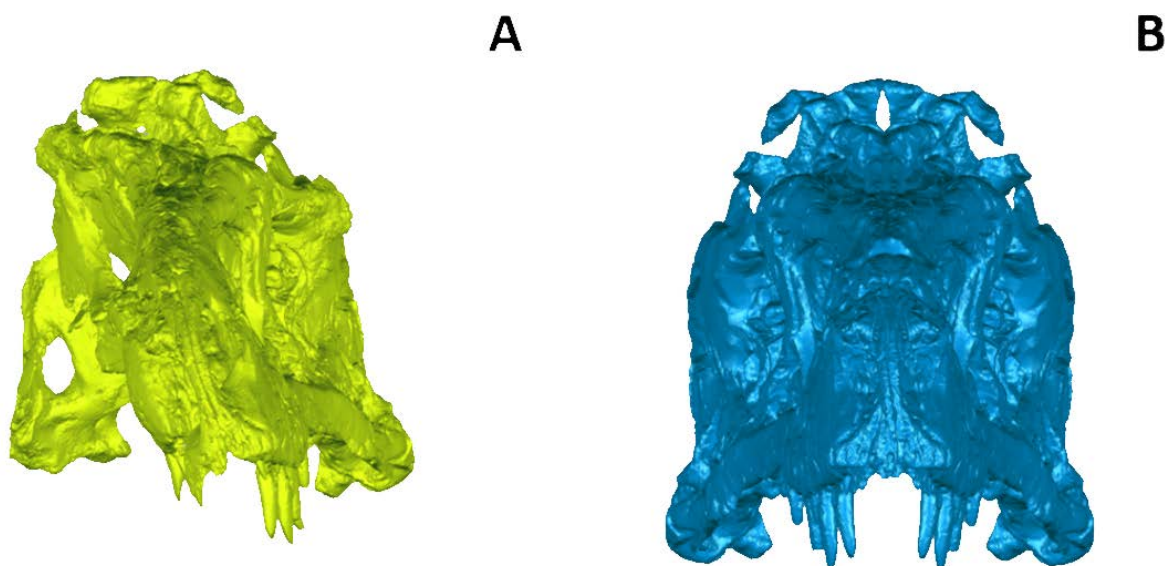
Figure 3.3. *Bistahieversor sealeyi* 3D cranial models used in this study. (A) Deformed *Bistahieversor* cranium in anterior view, and (B) *Bistahieversor* cranium after digital retrodeformation in Artec Studio Professional 14, MeshLab 2020.06, and Geomagic Studio 12. Both models are visualized in Geomagic Studio 12.

3.3.3. 3D model meshing and finite element analysis

Models were decimated to be at an ideal triangle count which avoids long analysis times and freezing issues when meshing the models in HyperMesh while maintaining small details in the models (Table 2). The models were then imported into Geomagic Studio 12 and the Mesh Doctor tool was selected to clear the models of self-intersections, spikes, and highly creased edges. These geometric issues may cause errors when meshing in HyperMesh, and thus, it was critical to remove as many potential sources of error as possible. Once the models were error-free and watertight, they were imported into HyperMesh (Altair) as four-noded tetrahedral elements.

Table 3.2. Quantitative properties for each 3D mesh. All properties were calculated in MeshLab 2020.06.

Specimen name/number	Cranial triangle count	Mandibular triangle count	Cranial element counts	Mandibular element counts	Cranial volume (mm^3)	Mandibular volume (mm^3)
Tyrannosaurus rex/FMNH PR 2081	1,284,114	860,746	1,926,171	1,291,119	642,017	430,375
Tyrannosaurus rex/MOR 555	1,270,954	711,910	1,906,431	1,067,865	635,435	355,957
Bistahieversor sealeyi/NMMNH P-27469	923,682	529,002	1,385,523	793,503	461,821	264,485
Daspletosaurus torosus/FMNH	386,920	467,596	580,380	956,394	193,440	318,802

PR308						
Albertosaurus sarcophagus /TMP 1981.010.0001	651,876	317,422	977,814	476,133	325,886	158,705
Alioramus altai/ IGM 100/1844	465,994	38,102	698,991	57,153	23,296	19,045
Raptorex kriegsteini/LH PV18	289,478	204,770	434,217	307,155	144,711	102,385

The HyperMesh output format was selected for Abaqus/CAE 6.14-1, as meshed models were saved as CAE files which are used for FEA in Abaqus. In the volume tetra sub-panel, element size was set to 10, and in the Tetramesh parameters sub-panel, I selected for optimized mesh quality and for the mesh speed to be gradual. I then highlighted the entire model and selected the mesh tool. Once meshing was successful, I applied the appropriate material properties to the meshed models. The bone properties were assigned based on crocodilian skull bone: Young's modulus of 15,000 MPa and Poisson's ratio of 0.29 (Zapata et al. 2010; Porro et al. 2011; Ballell et al. 2019). This is because of the close evolutionary relationship between crocodilians and dinosaurs, and the lack of soft tissue preservation in fossils requiring use of extant phylogenetic bracketing (Witmer 1995). Dentine properties were not applied to the teeth, as they do not affect general stress plot comparisons in 3D von Mises stress results (Herbst et al. 2021).

Constraints were selected for under the Load Collectors tab and then applied at the quadrate in cranial models, and at the hinges of the articular in the mandibles to prevent the models from freely floating during FEA. Three constraints were selected for each hinge of the quadrate or articular, for a total of six constraints per model. The models were constrained from rigid body motion in all directions by selecting a single degree of freedom for X, Y, and Z. I applied feeding loads by selecting the Load Collectors tab, selecting card image 'history,' and checking 'CLoad' and 'Load Case.' In the Forces sub-panel, five nodes were selected for each premaxillary tooth at both sides of the cranium or mandible, totalling 10 nodes for each analysis. This was to simulate feeding in the animals; in these cases, it simulates the anterior-most teeth making contact with prey items. Lastly, I selected for a 'static' procedure and exported the file as a CAE file.

Once the CAE file was imported into Abaqus (Simulia), I applied muscle forces to the models to accurately assess the effects of muscle loading on the skull during a feeding simulation. Locations of muscle insertions were derived from Holliday (2009), Gignac & Erickson (2017), and Rowe & Snively (2021) (Figure 3.4). Muscle forces for FMNH PR 2081 were derived from Rowe & Snively (2021), which were derived from Gignac and Erickson (2017). Muscle forces for other tyrannosauroids were scaled from FMNH PR 2081 using the subtemporal fenestra method outlined in Sakamoto (2006). This was done by measuring the surface area of the adductor chamber using ImageJ and multiplying the surface area by the isometric muscle tension of 31.5 N/cm^2. This method has proved to be a reliable proxy across amniote clades; additionally, most biomechanical modelling of the amniote skull reliably falls within a predictive distribution with no theropod dinosaur taxa as outliers (Sakamoto 2021). In a second dataset, muscle forces were scaled to FMNH PR 2081, as it's the largest specimen, to maintain a consistent ratio of muscle force: skull surface area which accounted for skull size differences between taxa using the method outlined in Dumont et al.

(2009) (Table 3.3). All tyrannosauroid muscle force components are listed in Table A2 and

A3.
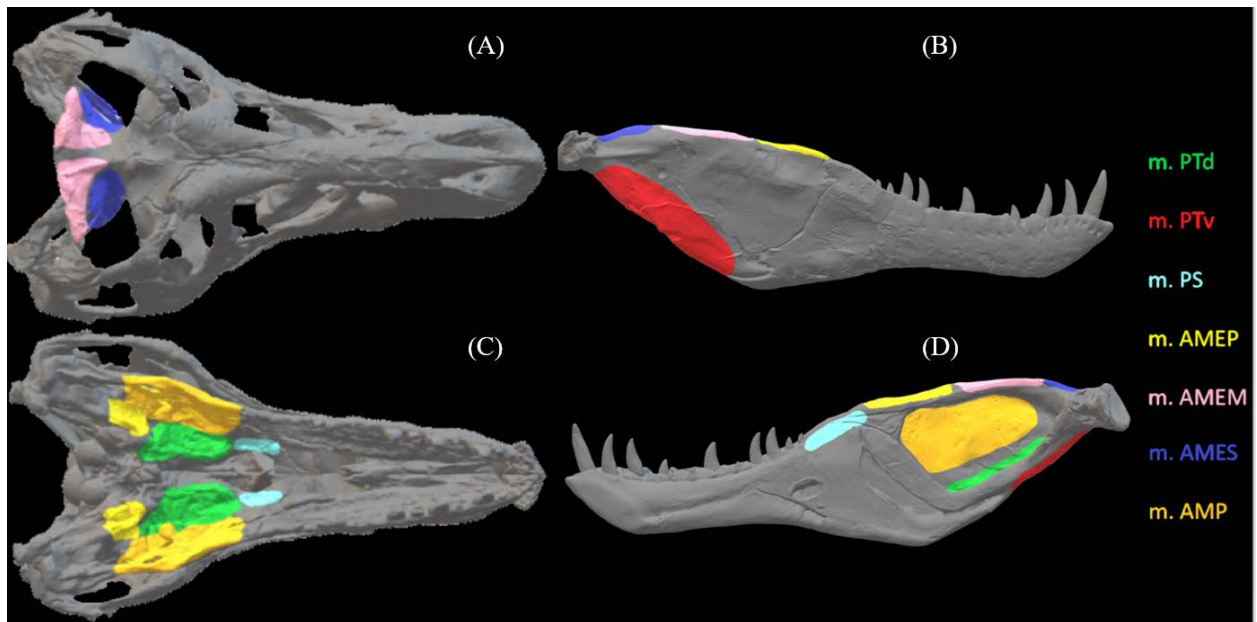
Figure 3.4. *Tyrannosaurus rex* (MOR 555) surface scanned skull model illustrating node

placement to simulate muscle attachment sites. (A) Cranium in dorsal view, (B) mandible in

lateral view, (C) cranium in ventral view, and (D) mandible in medial view. Muscle

abbreviations: m. PTd, M. pterygoideus dorsalis; m. PTv, M. pterygoideus ventralis; m. PS,

M. pseudotemporalis complex; m. AMEP, M. adductor mandibulae externus profundus; m.

AMEM, Musculus adductor mandibulae externus medialis; m. AMES, M. adductor

mandibulae externus superficialis; m. AMP, M. adductor mandibulae posterior.

Table 3.3. Surface area values for each specimen used in this study. Surface area values were

computed in both MeshLab 2020.06 and Avizo Lite 9.5 to check for consistency. * Indicates

surface scanned model.

Specimen name	Specimen number	Cranial model surface area (mm^2)	Mandible model surface area (mm^2)

Tyrannosaurus rex	FMNH PR 2081	4604695	1924344
*Tyrannosaurus rex**	MOR 555	4600059	1921720
Bistahieversor sealeyi	NMMNH P-27469	1777871	885024
*Daspletosaurus torosus**	FMNH PR308	1526939	803412
*Albertosaurus sarcophagus**	TMP 1981.010.0001	1382871	677021
Alioramus altai	IGM 100/1844	457843	160486
Raptorex kriegsteini	LH PV18	904346	49811

Muscle insertions were applied by selecting nodes along the insertion area. The muscle force components were divided by the number of nodes selected for that muscle, and the resultant forces were applied at X, Y, Z. When muscle insertions and forces were all accounted for, I selected the Create Job tool in Abaqus/CAE 6.14-1 and submitted the request. Once the analysis was finished, I exported von Mises stresses, max strain, and element volume spreadsheets for each model. Because the models were a mix of CT scans and surface scans and I was comparing their biomechanical output, I calculated the mesh-weighted arithmetic mean (MWAM) in R (R Core Team 2021). This method accounts for element size differences within non-uniform meshes and has been used in previous biomechanical studies of vertebrate palaeobiology (Marcé-Nogué et al. 2016; Morales-García et al. 2019; Ballell & Ferrón 2021). It can reduce discrepancies in von Mises stress between 3D models derived from CT scans and surface scans. The code requires no additional R packages to function and is as follows:

Stressfile<-read.table("model_smises.txt",header = T)

Stressfile

Volumefile<-read.table("model_evol.txt",header=T)

Volumefile

Stress<-Stressfile$SMises

Stress<-as.numeric(Stress)

length(Stress)

Volume<-Volumefile$Evol

Volume<-as.numeric(Volume)

length(Volume)

StressVolume<-numeric(length = length(Stress))

for (i in 1:length(Stress)) {StressVolume[i]<-Stress[i]*Volume[i]}

MWAM<-SumArea<-mean(StressVolume)/mean(Volume)

I scaled muscle forces in each tyrannosauroid model by measuring surface area values of each model in Avizo Lite 9.5 and MeshLab 2020.06. I then scaled each cranium model relative to FMNH PR 2081's cranium, and each mandible model relative to FMNH PR 2081's mandible by adjusting muscle force components based on surface area values accordingly in each Abaqus database file. I then reran each FE analysis using the same assumptions and calculated the MWAM.

I applied muscle sensitivity analyses after calculating my results from the actual sized and muscle force scaled models. While previous studies have shown good predictive power of the subtemporal fenestrae and skull width in determining bite forces (Sakamoto 2022), this step was important due to the number of assumptions necessary when studying the musculature of

extinct taxa, including muscle placement and size (Bates & Falkingham 2018). This was done by using Python scripts to generate muscle force components 10% higher and lower than the initial values for each individual muscle group and reran multiple analyses (Morales-García et al. 2019). I selected Macro Manager in Abaqus/CAE 6.14-1 and selected Work under the directory where the other files were stored. The macro would then begin recording my actions. I applied the 10% increases and decreases across the muscle force components of the *Raptorex*, *Albertosaurus,* and largest *Tyrannosaurus* crania and mandibles, submitted the job request, and then stopped recording the macro. In Notepad, the resultant Python script was opened and edited to remove the first line which defined the name of the script and any blank spaces before the start of other lines. The file was saved and copied across all other tyrannosauroid folders containing CAE files.

3.4. Results

I calculated the mesh-weighted von Mises stress results for tyrannosauroid crania and mandibles separately, due to the complexities of analysing an entire 3D skull model (Figure 3.5). Maximum principal strain results were also exported for each specimen to better understand deformation occurring in the models and to elucidate any possible links between von Mises stress and strain during each feeding scenario. Muscle force values were scaled to the senescent *Tyrannosaurus rex* FMNH PR 2081 for each tyrannosauroid to better compare stresses and strain when size is eliminated and only shape is considered in the analyses.
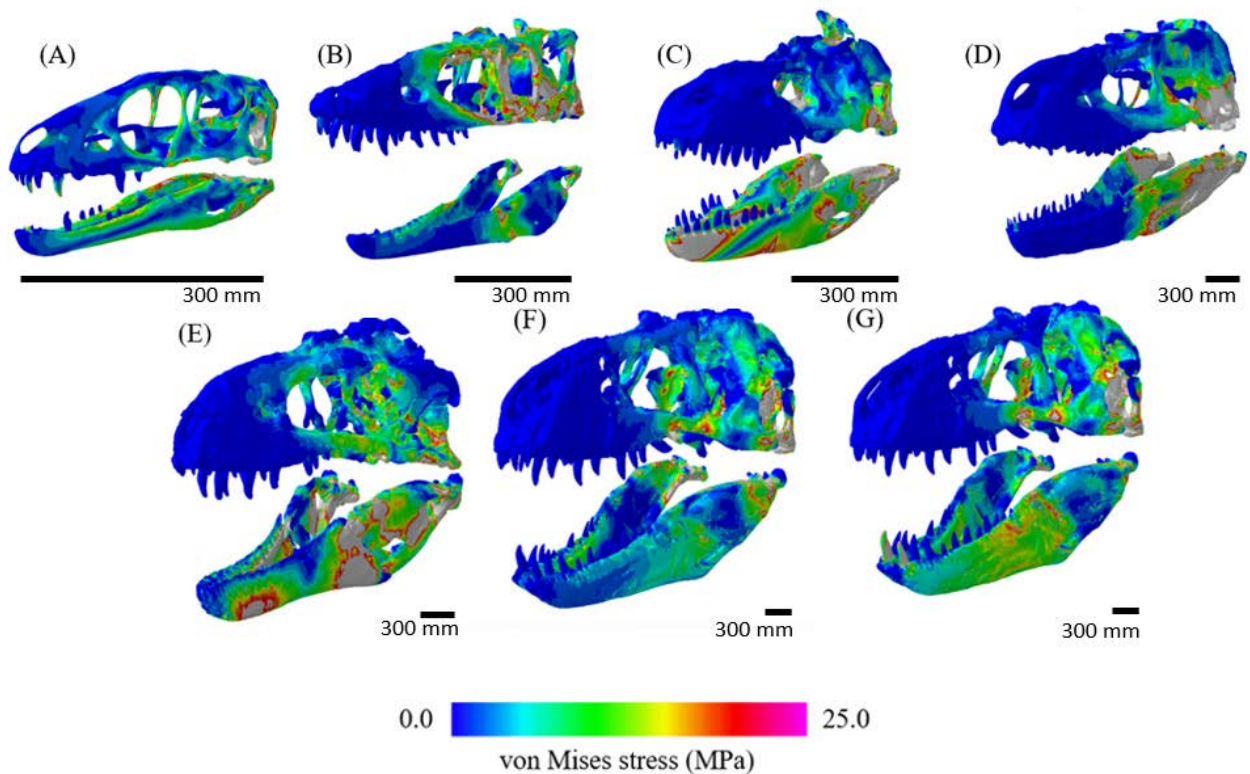
Figure 3.5. von Mises stress, a measurement of how close a structure is to breaking, for each tyrannosauroid 3D skull model tested at actual size (models not shown to scale – see scale bar). Warmer colours such as red and white indicate areas of high stress, i.e., where the skull is closest to breaking, while cooler colours indicate low stress. (A) *Raptorex kriegsteini*, (B) *Alioramus altai*, (C) *Albertosaurus sarcophagus*, (D) *Daspletosaurus torosus*, (E) *Bistahieversor sealeyi*, (F) *Tyrannosaurus rex* (MOR 555), and (G) the largest *Tyrannosaurus rex* (FMNH PR 2081).

3.4.1. Actual size von Mises stress

When the MWAM was calculated, the overall highest von Mises stresses were experienced by the middle-sized tyrannosauroids, *Daspletosaurus torosus* and *Bistahieversor sealeyi*, particularly at the mandible (Figure 3.6, 3.7). Similarly high bending stresses were calculated for the two adult *Tyrannosaurus rex* specimens, the largest individuals in the dataset. The lowest bending stresses were observed in the three smallest tyrannosauroids, *Albertosaurus*

sarcophagus, *Alioramus altai* and *Raptorex kriegsteini*. Cranial bending stresses were particularly low in *Albertosaurus sarcophagus*, which may be attributed to the compactness of the reconstructed skull model used (more in Discussion).
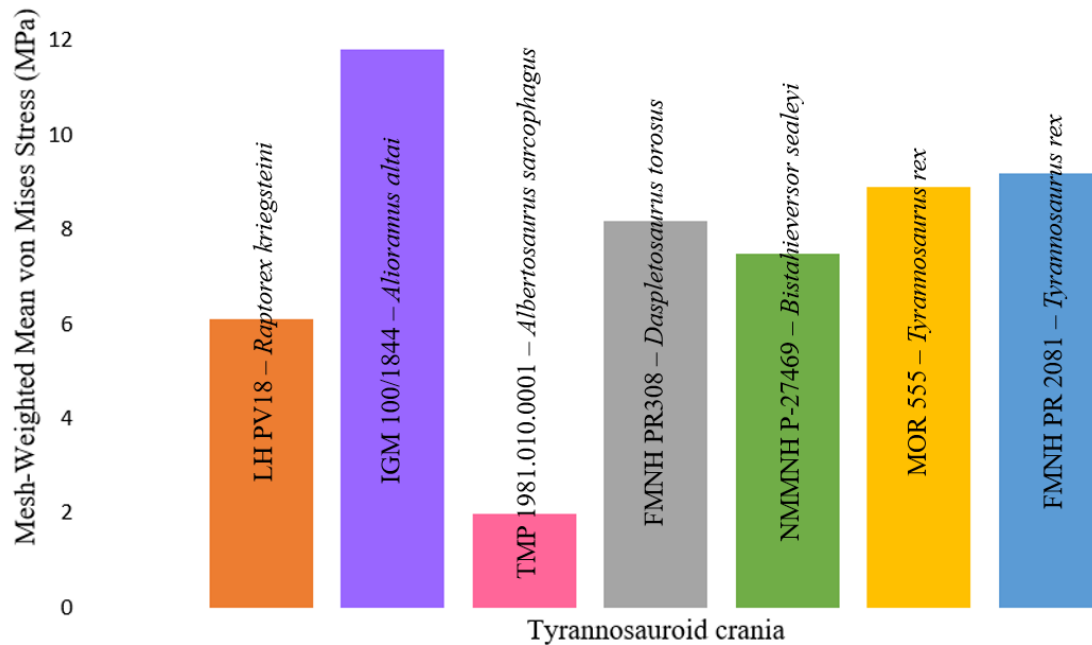
Figure 3.6. Mesh-weighted von Mises stress results for each tyrannosauroid crania.
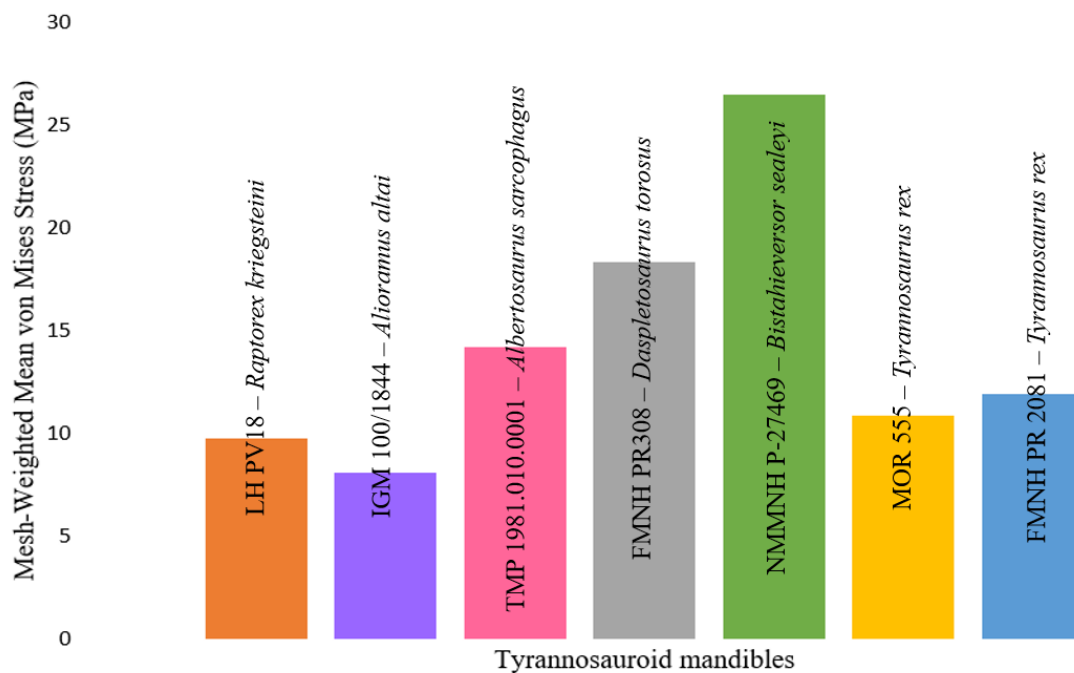
Figure 3.7. Mesh-weighted von Mises stress results for each tyrannosauroid mandible.

3.4.2. Actual size maximum principal strain

In addition to exporting von Mises stress results from Abaqus/CAE 6.14-1, I exported and calculated the mean maximum principal strain values for each mesh (Figure 3.8, 3.9). These values were exported separately from the von Mises stress results and elemental volume data. Strain values were comparatively high in the smallest three tyrannosaurid crania. The larger tyrannosauroid mandibles experienced higher strain with the exception of the *Tyrannosaurus* mandibles. In general, the actual size strain results were lowest in the *Tyrannosaurus* skulls.
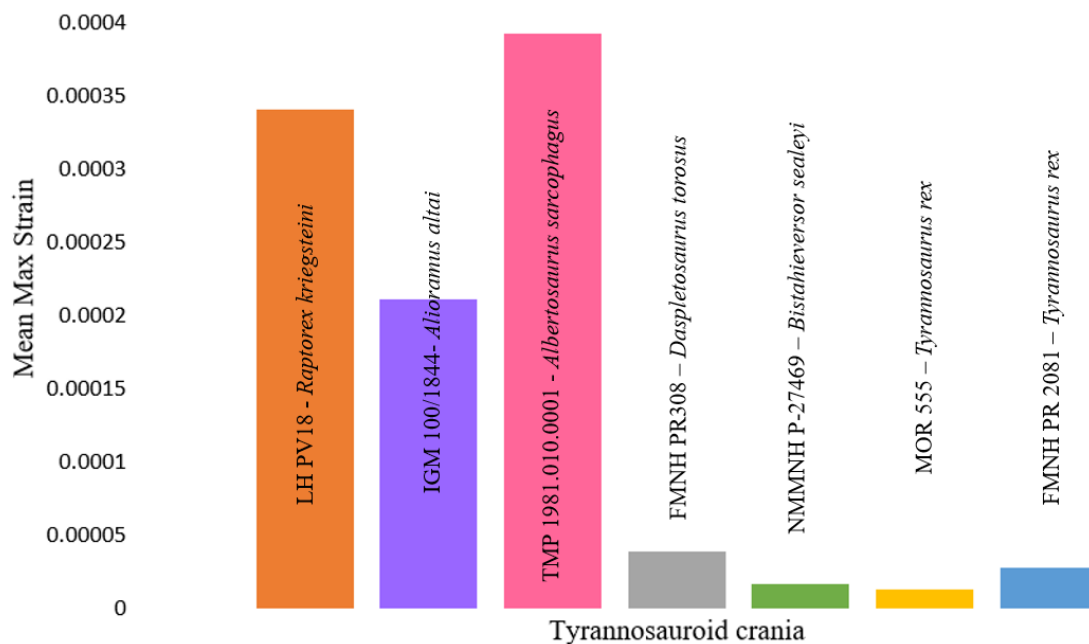
Figure 3.8. Mean maximum principal strain results for tyrannosauroid crania.
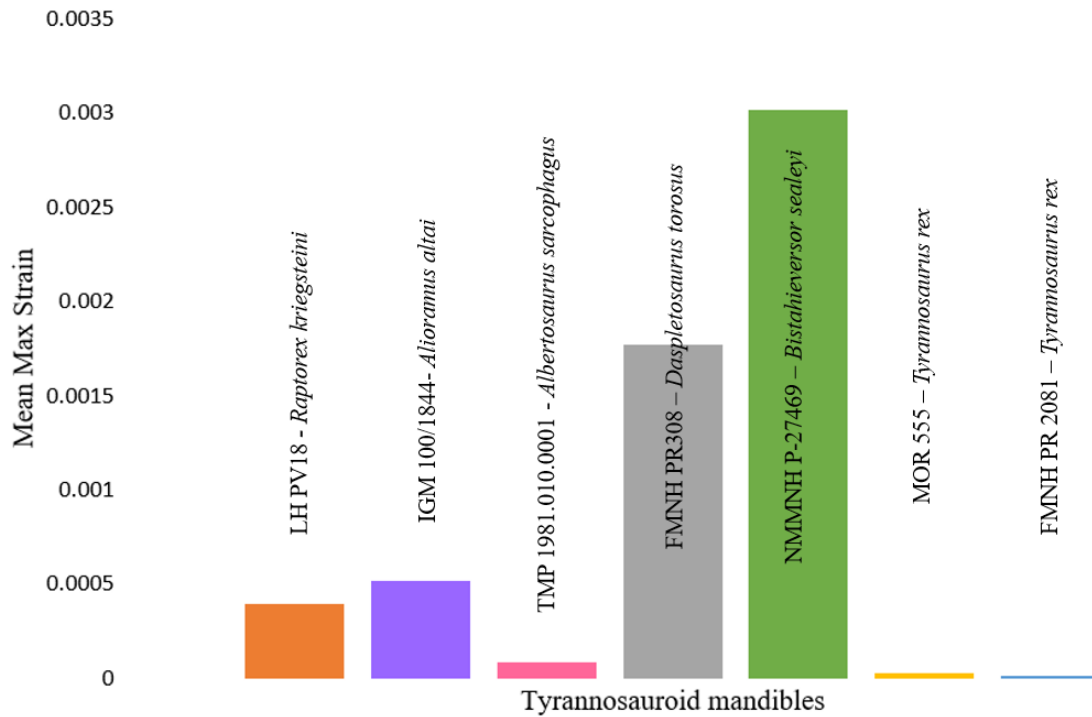
Figure 3.9. Mean maximum principal strain results for each tyrannosauroid mandible.

3.4.3. Surface area equalized von Mises stress

When muscle force component values were scaled to FMNH PR 2081, the largest individual in the dataset, to normalise size and account for only shape, smaller tyrannosauroid specimens generally experienced much higher von Mises stresses relative to their larger relatives (Figure 3.10, 3.11, 3.12). *Alioramus* was an exception in terms of cranial stresses; it experienced noticeably higher stresses than the smaller *Raptorex*, though this may be due to anatomical reconstructions from piecing together CT scanned skull bones (see Discussion).
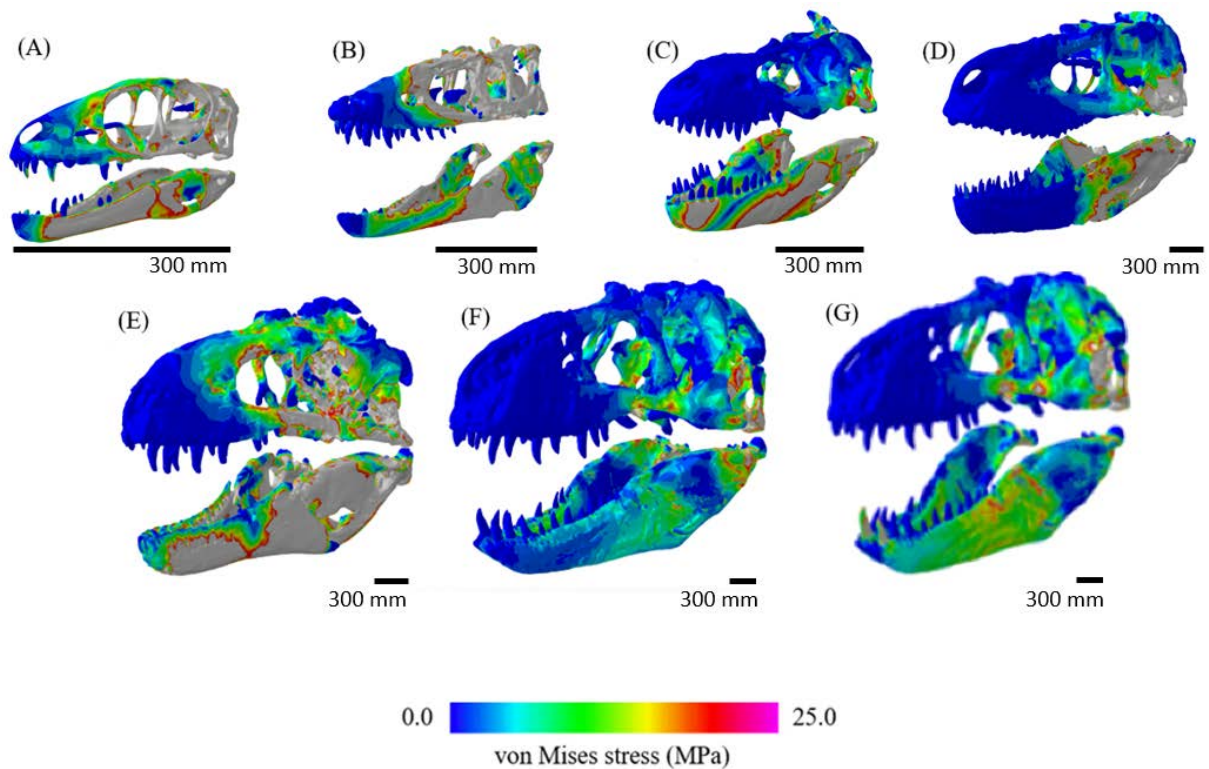
Figure 3.10. von Mises stress for each tyrannosauroid 3D skull model when surface area values were scaled to FMNH PR 2081 (models not shown to scale – see scale bars). Note the high bending stresses in the smaller tyrannosauroid models relative to the larger individuals as indicated by areas of red and grey, particularly in *Raptorex* and *Alioramus*, while the *T. rex* crania appears more stress resistant. (A) *Raptorex kriegsteini*, (B) *Alioramus altai*, (C) *Albertosaurus sarcophagus*, (D) *Daspletosaurus torosus*, (E) *Bistahieversor sealeyi*, (F) *Tyrannosaurus rex* (MOR 555), and (G) *Tyrannosaurus rex* (FMNH PR 2081).
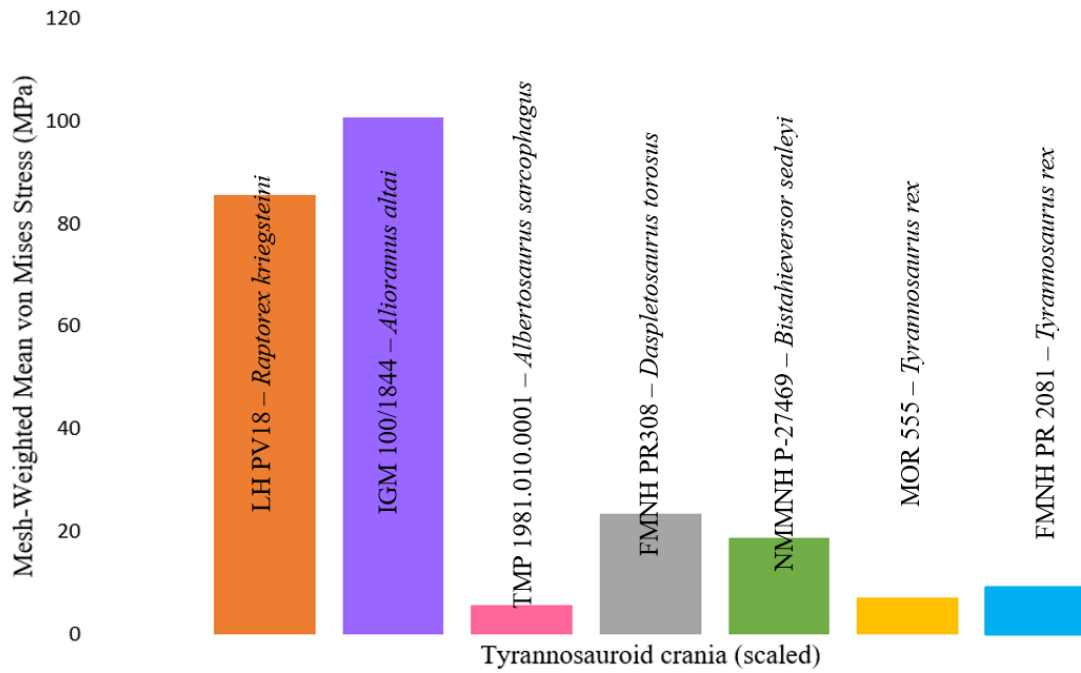
Figure 3.11. Surface area scaled mesh-weighted von Mises stress results for the tyrannosauroid crania. Note the general trend toward higher stresses in smaller taxa.
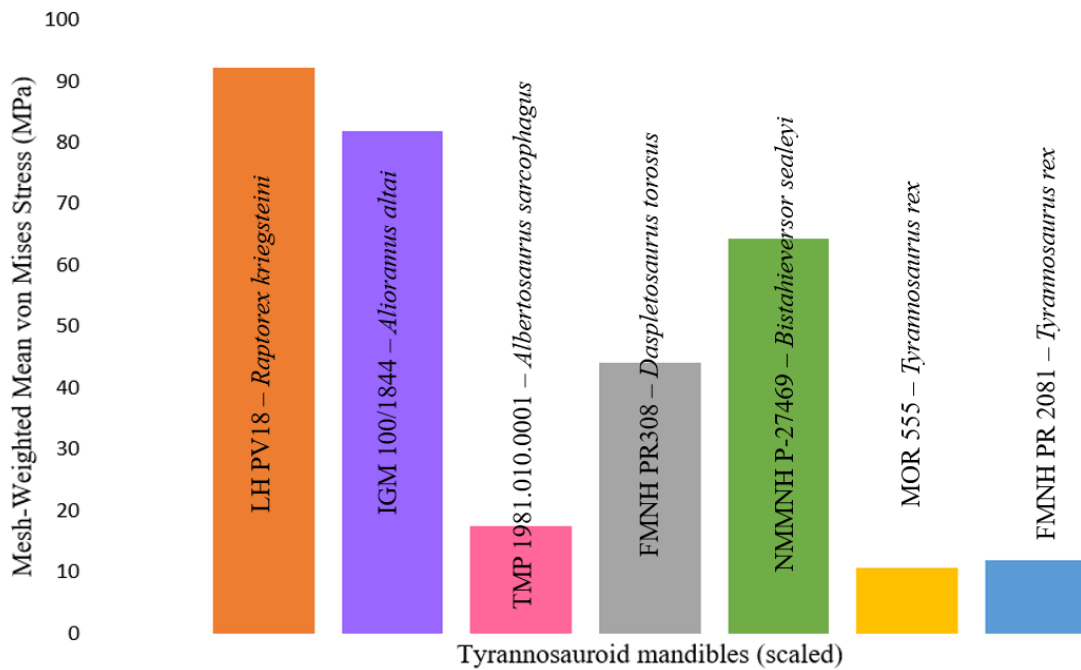
Figure 3.12. Surface area scaled mesh-weighted von Mises stress results for the tyrannosauroid mandibles. As is the case for the crania, there is a general trend toward higher stresses in small individuals.

In the surface area scaled stress results, higher cranial stresses are demonstrated in smaller taxa, though the medium-sized tyrannosauroids still experience higher stresses than both *Tyrannosaurus* specimens. This trend appears in the surface area scaled mandible results as well; the higher stresses in the medium-sized tyrannosauroid mandibles when compared to *Tyrannosaurus* may be attributed to their narrower jaws (see Discussion).

3.4.4. Surface area equalized maximum principal strain

In addition, I exported and calculated the mean maximum principal strain for each specimen when scaled to FMNH PR 2081 (Figure 3.13, 3.14). The cranium of *Alioramus* was notably high in strain output, likely due to the extensive reconstructive work. Strain in the mandibles were highest in the medium-sized tyrannosauroids, *Daspletosaurus* and *Bistahieversor*.
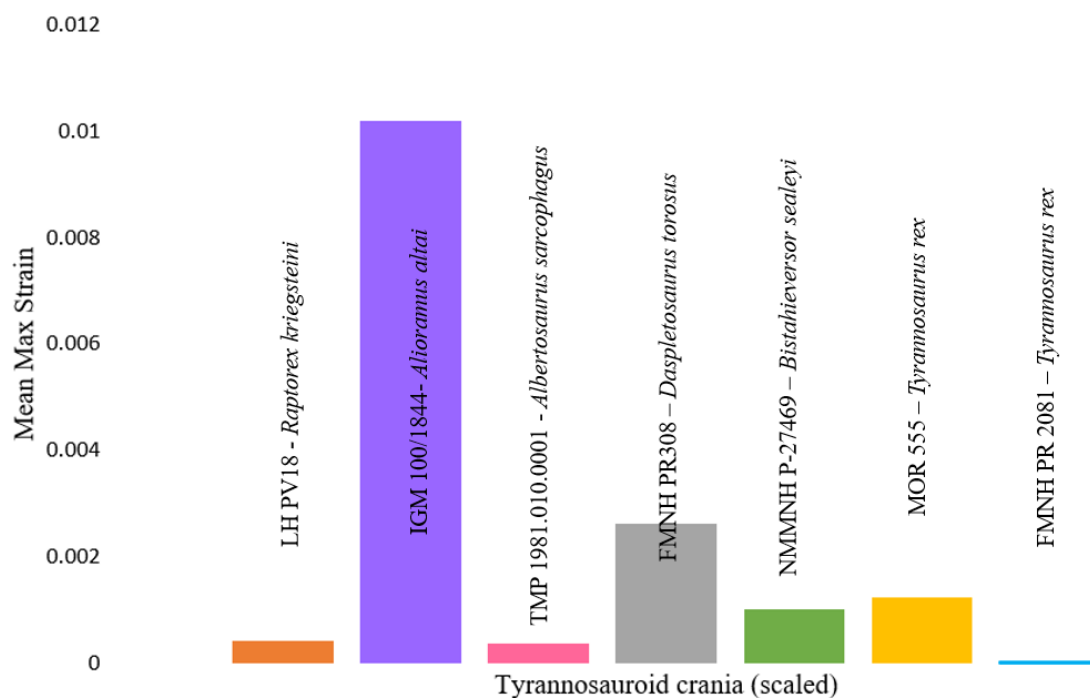
Figure 3.13. Surface area scaled mean maximum principal strain results for the tyrannosauroid crania. *Alioramus* experienced much higher strain than the other individuals, likely due to the extensive reconstructions applied (see Discussion).
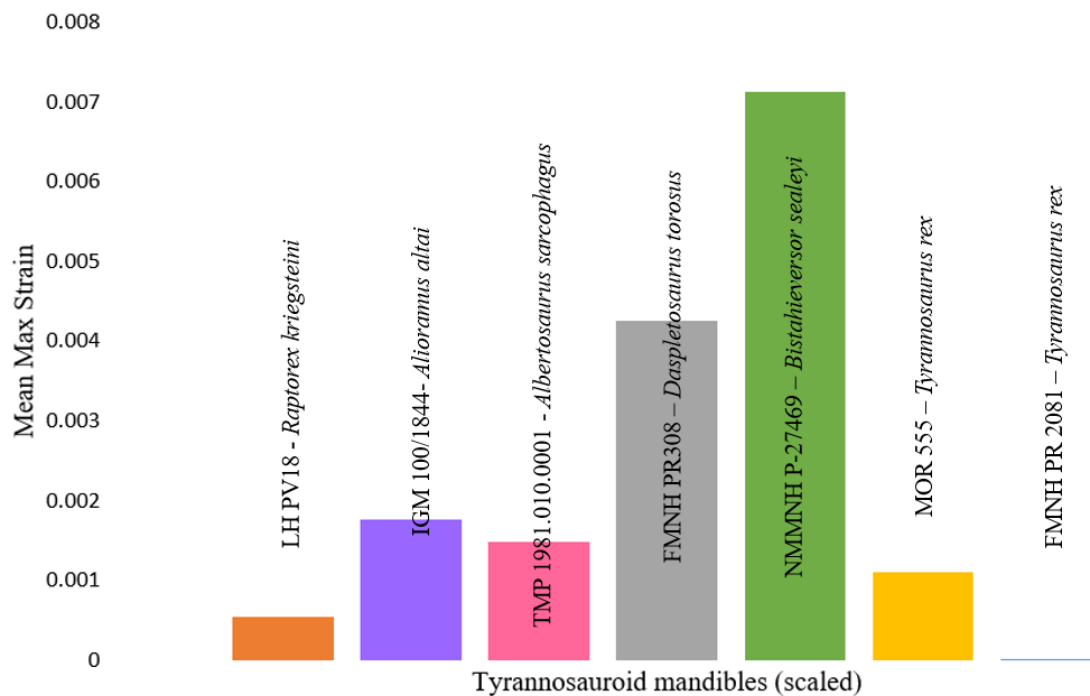
Figure 3.14. Surface area scaled mean maximum principal strain results for the tyrannosauroid mandibles.

3.4.5. Muscle sensitivity results

Muscle sensitivity testing was used to validate the von Mises stress results. Ten randomizations were applied to the *Albertosaurus sarcophagus* cranium muscle force components at X, Y, and Z for each muscle group. The other two tyrannosaurid muscle force components were changed to be 10% higher and 10% lower. The mean von Mises stress was calculated for each group of sensitivity tests (Table 3.4, 3.5). Specimens were chosen to represent the range of body sizes and morphologies in the specimen pool.

Table 3.4. Muscle sensitivity results for three different tyrannosaurid crania tested.

Tyrannosaurid crania	Baseline von Mises stress mean	von Mises stress mean 10% higher	von Mises stress mean 10% lower	Percentage von Mises stress mean difference (10% higher)	Percentage von Mises stress mean difference (10% lower)
Raptorex kriegsteini	7.111209	7.729046	7.748312	8.3265%	8.57501%
Albertosaurus sarcophagus	1.988823	1.905102	2.183277	4.30008%	9.32164%
Tyrannosaurus rex (FMNH PR 2081)	9.201477	9.790244	9.110124	6.20025%	0.997761%

Table 3.5. Muscle sensitivity results for three different tyrannosaurid mandibles tested.

Tyrannosaurid mandibles	Baseline von Mises stress mean	von Mises stress mean 10% higher	von Mises stress mean 10% lower	Percentage von Mises stress mean difference (10% higher)	Percentage von Mises stress mean difference (10% lower)
Raptorex kriegsteini	9.720271	9.920344	9.901121	2.03734%	1.8434%

Albertosaurus sarcophagus	14.21646	17.31926	17.92455	19.678%	23.0739%
Tyrannosaurus rex (FMNH PR 2081)	11.9148	12.3112	13.2155	3.27252%	10.3516%

3.5. Discussion

This study was the first to generate and analyse a large 3D dataset of a single clade of theropod dinosaurs. This was made possible because of the availability of CT data and advances in surface scanning methods. My actual size results indicate higher von Mises stresses generally occurring in larger tyrannosaurids, particularly in the middle-sized specimens such as *Daspletosaurus* and *Bistahieversor* (Figure 3.5, 3.6). This may be due to the notably wide mandible of *T. rex* acting as a buffer against the high stresses of a bone-crunching bite (Gignac and Erickson 2017; Rowe & Snively 2021), which the middle-sized tyrannosaurids were likely incapable of inflicting, or due to the higher stresses and strain which tend to occur in 3D models which have undergone a high degree of reconstruction/retrodeformation (Chapter 2; Rowe & Rayfield 2022).

Tyrannosaurid feeding mechanics have been previously characterized by their rigid, akinetic skull (Cost et a. 2019), upturned dentary, and reinforced post-dentary region (Ma et al. 2021), which all contributed to the stress-resistant skull noted in *Tyrannosaurus*. Additionally, the presence of fused, robust, arch-like nasal bones aided in transmitting all force from the bite directly to the prey item as well as aiding in compression and shear resistance (Rayfield 2004; Snively et al. 2006). These anatomical features are generally reflected in my results, with both *Tyrannosaurus* specimens demonstrating higher stresses and lower principle strain,

as they must accommodate more stress per unit area when feeding due to the high forces required to bite through and consume bone (Gignac & Erickson 2017).

3.5.1. Significance of large body size

My results indicate an advantage in terms of stress resistance during feeding in larger tyrannosauroids, most notably in *Tyrannosaurus*. This was demonstrated in the scaled results, where all small tyrannosauroids experienced much higher bending stresses, particularly at the mandible. *Tyrannosaurus* is noted for its robust jaws which it gradually attains through ontogeny (Carr 1999, 2020); the wide shape likely provides a functional advantage to the taxon which enables it to accommodate high stresses and effectively prey on the large herbivorous dinosaurs in its ecosystem (Chin et al. 1998; De Palma et al. 2013). Slenderer tyrannosauroids such as *Qianzhousaurus sinensis* have previously been hypothesized to use their slenderer, more gracile bodies to better pursue smaller prey which would not have required such a rigid bite to subdue (Foster et al. 2022). Given the close relationship between *Qianzhousaurus* and *Alioramus*, my results generally support these hypotheses, as the *Alioramus* skull was one of the most highly stressed during feeding in the study. Thus, I predict it would not have been capable of withstanding the stresses of a powerful bite and would have instead preyed on small dinosaurs and mammals in its ecosystem.

–The conclusions I can derive from the middle-sized tyrannosauroids are less clear. Given their relatively high stresses at actual size, it is unlikely that *Daspletosaurus* and *Bistahieversor* could withstand the resultant forces associated with *Tyrannosaurus*'s specialised bone-cracking feeding biomechanics. There are three possible explanations for this: (1) the herbivorous dinosaurs that co-existed with the middle-sized tyrannosauroids did not reach the same large sizes as those that lived alongside *Tyrannosaurus*; (2) middle-sized tyrannosauroids relied more on scavenging than *Tyrannosaurus*; (3) reconstructive work on

the *Daspletosaurus* and *Bistahieversor* models caused higher stresses and strain in their results. Scavenging behaviour is difficult to assess in fossil taxa and has been a subject of debate specifically concerning *Tyrannosaurus*(Ruxton & Houston 2003; Holtz Jr. 2008), though the subject has rarely focused on other theropod dinosaur taxa. While it is most probable that all tyrannosauroids were opportunists that spent most of their time searching for food like modern taxa (Herbers 1981), a difficult question to assess is the ratio of food that is actively hunted versus scavenged, or how it varies between taxa. Middle-sized tyrannosauroids may have been reliant on different strategies when compared to *Tyrannosaurus* and further work is needed to establish this possible difference, though body size estimates can be compared (Table 3.6).

Table 3.6. Body length and mass estimates for various herbivorous dinosaurs which were likely food sources for the tyrannosauroid genera included in this chapter. *Refers to Mongolian genera which were too large as adults to be adequate prey for *Alioramus* and *Rapotex*; juveniles were more likely to be prey, but juvenile body estimates are unavailable.

Herbivorous dinosaur genus	Potential tyrannosauroid predator	Body length estimate (m)	Body mass estimate (kg)
Edmonstosaurus	*Tyrannosaurus*	12 (Wosik & Evans 2022)	5,080 (Wosik & Evans 2022)
Triceratops	*Tyrannosaurus*	8-9 (Seebacher 2001)	4,964 (Seebacher 2001)
Ankylosaurus	*Tyrannosaurus*	8 (Arbour &	4,336.34 –

		Mallon 2017)	7,212.12 (Arbour & Mallon 2017)
Pentaceratops	*Bistahieversor*	5.5 (Paul 2016)	2,494.76 (Paul 2016)
Corythosaurus	*Daspletosaurus/Albertosaurus*	8 (Paul 2016)	2,540.12 (Paul 2016)
Lambeosaurus	*Daspletosaurus/Albertosaurus*	7-7.7 (Paul 2016)	2,267.96 – 2,993.71 (Paul 2016)
Styracosaurus	*Daspletosaurus/Albertosaurus*	5-5.5 (Paul 2010)	2,449.4 (Paul 2010)
Saurolophus*	*Alioramus/Raptorex*	13 (Paul 2010)	9,979.03 (Paul 2010)
Saichania*	*Alioramus/Raptorex*	5-7 (Seebacher 2001)	1360.78 – 1995.81 (Seebacher 2001)

3.5.2. Ontogenetic patterns in relation to feeding mechanics

Tyrannosauroid ontogeny has been well documented (Carr 1999, 2020) and previous work

has assessed the feeding performance of juvenile tyrannosaurine tyrannosaurids when

compared to a senescent individual (Rowe & Snively 2021). Rowe & Snively (2021)

primarily quantified von Mises stresses in the mandible of *Raptorex*, a juvenile

Tyrannosaurus (BMRP 2002.4.1), and a mature *Tyrannosaurus* (FMNH PR 2081) using CT

scanned 3D models. It was found that, when tested at true size, older, larger individuals

experience higher overall feeding-induced stresses due to the widely-set jaws associated with

mature tyrannosaurids. When individuals were scaled to equivalent size, smaller, immature

individuals experienced higher overall bending stresses.

Similar trends were noted in this study, where larger tyrannosauroid skulls comprising

different genera yielded comparatively higher von Mises stresses, particularly at the cranium

(Figure 3.6). constructed skulls and experience lower stresses than smaller taxa at actual size.

Large tyrannosauroids possessed strongly constructed skulls but also experience higher

stresses than smaller taxa at actual size and are thus accommodating more force per unit area.

This may represent a trade-off where the expanded tyrannosauroid posterior skull and

increased adductor muscle mass generates high bite forces, which results in the need to

accommodate greater stresses in the skull during feeding. The trend applies to ontogenetic

stages in *Tyrannosaurus* as observed in Rowe & Snively (2021), as well as across

phylogenetically disparate tyrannosauroid genera of different skull sizes as evidenced in this

chapter. Ma et al. (2021) similarly noted a trend in jaw strengthening ontogenetically in

tyrannosaurids using 2D models of *Tarbosaurus* and *Tyrannosaurus* and attributed bone

functional adaptation to the overall mandible strengthening observed in mature individuals.

3.5.3. 3D scanning methodology and its influence on 3D finite element data

The tyrannosauroid skulls used in this study were scanned using two different methods: white

light surface scanning and CT scanning. Additionally, the *Alioramus* skull was disarticulated,

which required some extra reconstructive work; it was pieced together in Artec Studio

Professional 14 and Blender 2.82 by importing the individual bones and aligning them. The

Albertosaurus was an articulated replica based on a disarticulated individual (Currie 2003); thus, the 3D model I used may be more compacted than the real skull. The *Daspletosaurus* was a replica which was surface scanned and required editing to create the interior anatomy, as the replica is in a closed-mouth position. Additionally, as indicated in Figure 4, *Bistahieversor* was a CT scanned specimen which I retrodeformed using 3D editing software, chiefly Blender 2.82 and Geomagic Studio 12.

Because of differences in results that arise in FE studies using both CT scans and surface scans (Chapter 2; Rowe & Rayfield, 2022), this necessitated the use of the mesh-weighted arithmetic mean (MWAM). This method alleviates potential von Mises stress differences by incorporating element volume into the calculation of stress. However, even when the MWAM is calculated for 3D FEA data, extensive mesh reconstructions such as duplicating and mirroring a mandible ramus to replace a broken half are often a factor generating von Mises stress outliers, which were the steps taken when I retrodeformed *Bistahieversor*'s mandible. 3D FEA of the skull requires all bones to be present, and hence, some reconstructions will be necessary, particularly when analysing fossil taxa which are often broken, incomplete, or deformed due to geologic processes.

The *Daspletosaurus* (surface scan-derived), *Bistahieversor* (CT-derived), and *Alioramus* (CT-derived) specimens included in this study were often the outliers when compared to the other tyrannosauroids*; Daspletosaurus* and *Bistahieversor* often experienced higher stresses than the larger *T. rex* specimens. Notably, the *Alioramus* experienced higher cranial stresses and particularly maximum principal strain (Figure 3.13) than the smaller *Raptorex* specimen; this trend did not occur in the mandibles, which may be due to the anatomical simplicity of the mandibles requiring less intensive reconstruction efforts. The high stresses in *Daspletosaurus* and *Bistahieversor* are also likely due to extensive reconstructive modelling;

however, there is still a general trend towards higher stress in larger tyrannosauroids at their true size, despite the effects of 3D editing.

Additionally, there is the possibility of casts having an influence on my results when compared to original material. Both *Tyrannosaurus* specimens, *Bistahieversor*, and *Alioramus* were composed of original material; *Daspletosaurus*, *Albertosaurus*, and *Raptorex* were replicas (Table 3.1). Most notably, the *Albertosaurus* replica is an articulated skull based on disarticulated material. Stress and strain output in the *Albertosaurus* were low compared to the other specimens; it may be that any unnatural compactness in the replica resulted in comparatively low FE values.

3.6. Future work

3.6.1. Other 3D tyrannosauroids

One of the previous limitations of comparative 3D FEA studies was the general inability for many researchers to scan large fossils and the time required to create suitable 3D models. Wider availability of surface scanning methods in recent years has made it possible for researchers to scan datasets of large taxa that are not easily amenable to CT scanning (e.g. Coombs et al. 2022); thus, large taxa including non-avian dinosaurs may be more widely included in 3D FEA studies. Surface scanning methods including white light scanning and photogrammetry produce high-quality 3D models of fossils when subjected to visual perception metrics (Díez Díaz 2021); however, researchers must be wary of the missing interior anatomy of surface scanned models (Chapter 2; Rowe & Rayfield 2022).

As noted in this study, Tyrannosauroidea is an important clade of theropod dinosaurs because of their strong diversity in both morphology and body size, with many members of the group attaining the largest sizes of any bipeds in Earth's history (Brusatte et al. 2010). Additionally, they possess one of the most relatively well-understood fossil records of all non-avian

dinosaurs (Holtz Jr. 2004), making large scale FE studies possible. Thus, many individuals in the group are amenable to CT and surface scanning than the total number included in this study, including smaller basal members *Guanlong wucaii* (Xu et al. 2006) and *Dilong paradoxus* (Xu et al. 2004). Large, derived specimens ideal for 3D FEA include *Teratophoneus curriei* (Carr et al. 2011), *Lythronax argestes* (Loewen et al. 2013), and *Gorgosaurus libratus* (Lambe 1914), though certain individuals including *Lythronax* require some degree of reconstruction which may influence FE results. Most of the replica specimens included in this dataset did not provide noticeable outliers in terms of skull stresses; the exception, *Albertosaurus sarcophagus*, was a more compacted replica, unlike the *Dapletosaurus* and *Raptorex*. Museum replicas generally work well in FE studies, assuming a high degree of similarity to the original fossil in cases where the original is not available (Cunningham et al. 2014).

3.6.2. Large body size and function in mammals

Cope's rule is often referenced when referring to trends of large body size acquisition in fossil taxa (Cope 1885; Hone & Benton 2005). While Cope's rule is not observed in all fossil lineages (Moen 2006; Butler & Goswami 2008; Waller & Svensson 2017), it has been documented in both non-avian dinosaurs (Benson et al. 2014, 2018) and Cenozoic mammals (Alroy 1998; Raia et al. 2012). This study is among the first to investigate the possible influence of large body size on skull function in a non-avian dinosaur lineage. Cenozoic mammals are another vertebrate lineage which could prove ideal in studies of large body size and feeding function; their diverse fossil record and availability of specimens makes the group amenable to 3D scanning and FEA. Despite their availability, the group has seen limited biomechanical testing in large individuals, instead opting to focus on smaller taxa (Cox et al. 2011, 2015; Morales-García et al. 2019) or using livestock as a means of better understanding the mechanics of FEA (Bright & Gröning 2011; Bright 2012; Zhu et al. 2019).

Additionally, a 3D FEA study of large mammal linages could address hypotheses of muscle force components and their influence on mammal feeding biomechanics. Larger tyrannosauroids generally experienced higher bending stresses relative to smaller individuals at actual size; it is unknown if this occurs in large carnivorous mammals. Similar hypotheses about skull shape could be tested by scaling, as was done in this study. Cave bears and their extant relatives would be ideal candidates, given their appropriate sample sizes and ontogenetic cranial data (Fuchs et al. 2015).

3.7. Conclusion

The main conclusions of this study are (1) that tyrannosauroid dinosaurs generally experienced higher stresses in their skulls during feeding as body size increased and (2) the widely-set jaws of large tyrannosaurids enabled those taxa to better accommodate high degrees of von Mises stress during feeding. Thus, the data supports both my hypotheses concerning tyrannosauroid body size and its relationship to feeding biomechanics. While large body size seems to confer a functional advantage in tyrannosaurids, particularly *T. rex*, smaller individuals including *Alioramus* may have utilized their differing size in an ecological niche distinct from *T. rex* and other giant theropods. The ability to effectively absorb high feeding stresses may have contributed to the evolutionary success of large tyrannosaurids and aided their dominance over the medium-sized theropods that preceded them. While feeding biomechanics in other theropod lineages have not yet been thoroughly studied using 3D models, this is the main topic of Chapter 4.

Acknowledgements

CHAPTER 4

Skull function in theropod dinosaurs: Implications for body size and macroevolution

4.1. Abstract

Theropoda is one of the most extensively studied dinosaur clades, containing carnivorous taxa such as *Tyrannosaurus rex* and *Giganotosaurus carolinii*. The clade is notable as it contains the largest terrestrial bipeds ever described. Large body size evolved in several independent lineages of theropods at different points in the Early Cretaceous. While the impact of large body size on theropod dinosaur locomotion has been assessed in previous studies, its effects on feeding function remains largely unknown, due to previous limitations in 3D scanning methods. As feeding and locomotor abilities are linked to evolutionary success in fossilized and extant organisms, understanding skull function in dinosaurs is critical in assessing their paleobiology. In chapter 3 I discovered that while the skulls of tyrannosauroid dinosaurs experienced greater absolute stress with increased size, the skull became relatively stronger in larger taxa. Tyrannosauroids are one of several theropod dinosaur clades to evolve large body size, with others including the megalosauroids and allosauroids. In this chapter I test the hypothesis that the trend of increasing absolute stress with increasing strength can be observed across different lineages of theropod dinosaurs that trend toward large body size. I used CT scanning and surface scanning to create accurate 3D models of 21 theropod dinosaur skulls across several clades including the Megalosauroidea, Allosauroidea, and Abelisauroidea. 3D finite element analysis was used to study stress and strain occurrences in the skull during simulated feeding loads. Loads were applied from estimated muscle masses and skulls were scaled to the surface area of adult *T. rex* FMNH PR 2081 to account for size and assess stress and strain while examining only skull shape. I found that large non-tyrannosauroid theropods generally do not experience higher stresses at larger sizes as seen in tyrannosauroids. When muscle force components were scaled, smaller theropods experienced higher stresses, particularly abelisauroids and *Herrerasaurus*. These results indicate that tyrannosauroid skulls were more adept at absorbing high stresses

associated with strong bite forces and gigantic body sizes, and the general trend of skull strengthening with large body size is most notable in tyrannosauroids and mostly absent in basal theropod dinosaurs.

4.2. Introduction

Theropod dinosaurs are some of the most charismatic fossil organisms, due to their relatively well-understood fossil record, ancestral carnivory, and acquisition of large body size occurring in several lineages. The first individuals may have appeared in the Carnian Late Triassic 231 Ma (Martínez et al. 2011), though the herrerasaurids' status as true theropod dinosaurs is debated (Novas, 1995; Nesbitt et al. 2009; Langer et al. 2010). The first unambiguous theropod dinosaurs, the coelophysids, appeared in the Carnian stage of the Late Triassic (228 Ma) (Cope 1887).

Theropod dinosaurs evolved large body size several times throughout the Mesozoic and are the largest bipeds known to have ever lived. The crested theropod *Dilophosaurus wetherilli* was the largest terrestrial animal that appeared in the Sinemurian stage of Jurassic North America (193 Ma) (Marsh & Rowe 2020), attaining a body mass of at least 325 kg (Christiansen & Fariña 2004). Despite its relatively large size compared to extant carnivores, it did not reach the size of massive Cretaceous theropod dinosaurs such as the 8,000 kg *Spinosaurus* (Dal Sasso et al. 2005) or the 5,600 kg *Acrocanthosaurus* (Therrien and Henderson 2007). The possibly semi-aquatic *Spinosaurus* (Ibrahim et al. 2014; Ibrahim et al. 2020; Hone & Holtz 2021) may have been the largest biped in Earth's history in terms of length, with some estimates reaching 14 metres (Sereno et al. 2022). However, the largest mass estimates are usually assigned to *Tyrannosaurus*, with certain individuals reaching estimated masses of 6,000 – 9,500 kg (Hutchinson et al. 2011; Persons et al. 2019). The

tyrannosauroids are notable as they began at large body size and became larger, despite their narrow stratigraphic range (Hone et al. 2005).

Body size is an important topic in evolutionary studies, as it is among the most significant traits of an organism (Bell 2014). Large body size may confer several advantages to animal taxa, including increased predation opportunities (Hone & Benton 2005), better tolerance to environmental extremes (Peters 1986), and reduced mortality in individuals (Brown & Sibly 2006). However, it does come with possible negative attributes, including a greater mortality during mass extinction events (Ripple et al. 2017), heat retention (Zamora-Camacho et al. 2014), and greater caloric needs to sustain a large body, though many large herbivores tend to feed on low calorie foods unlike carnivores (Case 1979; Burness et al. 2001).

The trend towards large body size over geologic time is usually referred to as Cope's rule. While Cope's rule does not apply to all fossil lineages such as Mesozoic birds (Butler & Goswami 2008), there is evidence for its occurrence in certain non-avian dinosaur clades (Hone & Benton 2005; Benson et al. 2014;), most Cenozoic mammal clades (Alroy 1998; Raia et al. 2011), and in pterosaurs (Benson et al. 2014). Notably, there is little evidence for the rule in herbivorous theropods (Zanno & Makovicky 2013), while Ornithischian and sauropod dinosaurs demonstrate a directional trend of increasing body mass (Hunt & Carrano 2010). In the case of theropod dinosaurs, small genera were always present, possibly due to an ecological niche for small predators that persisted through the Mesozoic (Hone et al. 2005). The larger body sizes seen in some ceratosaurs, and non-coelurosaurian tetanurans (allosauroids and megalosauroids) represent three separate evolutionary shifts to a shared large body size regime in those clades (Benson et al. 2018). Tyrannosauroids similarly attained larger bodies over time (Hone et al. 2005), though basal tyrannosauroids were relatively small animals with *Guanlong* reaching an estimated 125 kg in body mass (Xu et al. 2006; Paul 2016).

Previous biomechanical studies of theropod dinosaurs have generally pertained to locomotion (Alexander 1991; Hutchinson & Garcia 2002; Hutchinson 2006) with some work on feeding function. Macroevolution studies of skull function in giant dinosaurs have mostly been limited to 2D models (Rayfield 2005, 2011) or studies of the lower jaw (Ma et al. 2022), as 3D skulls are complex structures, and creating digital models require computed tomography (CT), surface scanning, or photogrammetry to generate a geometrically accurate 3D file. Additionally, CT scanning is costly, and may require museum specimens to be dismounted and shipped, potentially damaging specimens. It is in recent years that white light surface scanning has become more commonplace in palaeontology and zoology, making 3D scans more accessible to researchers regardless of specimen size or location (Cunningham et al. 2014; Chapter 2; Rowe & Rayfield 2022). This has enabled larger scale comparative studies utilizing 3D data, particularly finite element analysis (FEA), to study the skulls of extinct vertebrates (Ross 2005; Rayfield 2007; Lautenschlager 2013; Lautenschlager et al. 2016, Cost et al. 2019; Rowe & Snively 2021, Jamison-Todd et al. 2022).

Two main hypotheses were examined in this chapter, utilizing the methodology outlined in chapter 2 and building on previous hypotheses in chapter 3 concerning tyrannosauroid feeding mechanics and body size evolution.

Hypothesis (1). Large non-tyrannosauroid theropod dinosaur taxa such as *Giganotosaurus* and *Suchomimus* experience higher absolute stresses and strain in their crania and mandibles under simulated feeding loads due to their large skull size and the increased muscle mass present in giant skulls. They were thus able to accommodate high feeding forces due to their large body size.

Hypothesis (2). When muscle force components for skull models are scaled to the same surface area as adult *Tyrannosaurus rex* FMNH PR 2081 to account for body and skull size

differences, smaller-bodied theropod dinosaurs such as the abelisaurs experience higher stress and strain relative to the larger-bodied taxa, e.g., megalosauroids and allosauroids due to the evolution of overall more robust skull shape in larger-bodied clades.

4.3. Materials and methods

First, I compiled skull lengths from the literature and comparisons of 3D models to better understand possible relationships between size and skull stresses (Table 4.1). As in previous chapters, my data pool is a mixture of 3D models originated from computed tomography (CT) scanning and white light surface scanning (Chapter 2, 3; Rowe & Rayfield 2022; Table 4.2). This is due to the large size of certain theropod dinosaur skulls which may cause difficulty in CT scanning, necessitating the use of surface scanning. Many of the models used in this chapter were generated from surface data of full skeletal mounts; hence, CT scanning the skulls would have been nearly impossible.

As in chapter 3, theropod dinosaur skull models were generated from a mixture of fossil and cast scans as indicated in Table 4.2. Additionally, certain casts were composites due to missing material in various theropod dinosaur taxa. This included the *Suchomimus* skull, which was missing its quadratojugal, quadrate, squamosal, occipital, and surangular. These bones were reconstructed based on the skull of the related Brazilian spinosaurid *Irritator* (Sues et al. 2002). The *Torvosaurus*' nasals, postorbitals, squamosal were absent and filled in based on related megalosauroid taxa.

The *Baryonyx* skull was CT scanned at the Natural History Museum, London, using a Nikon Metrology HMX ST 225. As the skull is disarticulated, each piece was individually scanned. The *Allosaurus* and *Carnotaurus* models were generated from CT data based on the original skull material; the *Spinosaurus* and *Giganotosaurus* models were CT scanned from casts. Other theropod dinosaurs were surface scanned due to the portability of surface scanning

allowing me to acquire data from specimens that would normally be impossible to CT scan. The *Suchomimus*, *Torvosaurus*, *Acrocanthosaurus*, *Ceratosaurus*, and *Herrerasaurus* were surface scanned at the Dinosaur Discovery Museum, Kenosha, Wisconsin, USA. The museum casts include the entire skeletons for each theropod, and thus a ladder and cherry-picker were needed to reach the skulls.

The *Monolophosaurus* skull was scanned at the Milwaukee Public Museum, Wisconsin, USA. Like the Kenosha casts, the skull was attached to the skeleton, though a ladder was not required due to the relatively small size of the mount. The *Dilophosaurus* was scanned at the Science Museum of Minnesota, Saint Paul, Minnesota, USA. The cast consisted of the right half of the skull with a detached mandible. The *Majungasaurus* replica was scanned at the Field Museum, Chicago, IL, USA. It was composed of only the skull with a separate mandible like the *Dilophosaurus*, which made surface scanning easier as the mandible did not obscure parts of the cranium. The *Neovenator* was a surface scanned model based on a sculpture at Dinosaur Isle Museum, Isle of Man, UK, as the holotype is incomplete and filled using information on *Allosaurus* (M. Munt, personal communication 2021).

4.3.1. Model editing

Surface scanned models were created in Artec Studio 14 Professional using the same procedures outlined in chapters 2, 3, and Rowe & Rayfield (2022). The scans were captured at 7–8 frames per second, with the 'real-time fusion' option enabled. Crania and mandibles were all scanned separately whenever possible and created as separate 3D object files to avoid large file sizes. Surface scans were oriented together, registered, and then merged into a single object. Stray pixels and frames with maximum error values above 0.3 were deleted, as well as cervical vertebrae (typically C1 and C2) that were captured in certain specimens, including *Monolophosaurus, Suchomimus, Acrocanthosaurus, Ceratosaurus,* and

Herrerasaurus. I applied Global Registration to convert all one-frame surfaces to a single coordinate system using information on the mutual position of each surface pair. I then selected sharp fusion to create a polygonal 3D model, which solidifies the captured and processed frames into an STL file. I used Sharp Fusion as it best preserves fine details of the scans, including small teeth and rugose bone textures which are common in abelisauroids. Lastly, I used the small-object filter to clean the model of floating pixels and the fix holes function to fill any open areas.

A procedure similar to the one applied to the *Bistahieversor sealeyi* skull in chapter 3 was applied here to the *Dilophosaurus* model. The cast was a resin model of a skull filled with matrix, comprising approximately half of the cranium and a single mandibular ramus. Thus, this half of the skull was digitised and imported into Blender 2.82, where it was then duplicated, mirrored, and reattached to fill the missing half. The resulting file was then imported into MeshLab 2020.06 where the intersecting triangles were selected and then deleted, as self-intersections make meshing impossible. Finally, the model was imported into Geomagic Studio 12 where the model's holes were filled, and the Mesh Doctor tool corrected for spikes and other potential sources of meshing error. As was done with the *Alioramus altai* digitised skull in chapter 3, the disarticulated *Baryonyx* skull bones were imported piece-by-piece into Artec Studio 14 Professional and aligned based on illustrations from Charig & Milner 1997. These files were then exported with the bone models merged, until the entire mandible was reconstructed virtually. The procedure I followed for the *Dilophosaurus* model was then applied to fix self-intersections and ready the model for meshing in HyperMesh.

Once all models were finalized in Geomagic Studio 12, the model surface areas (Table 4.2), numbers of triangles, elements, and the volume were calculated and recorded for each model (Table 4.3). All values were kept as closely together as possible in order to avoid potentially influencing the results by having unusually high or low values for any model.

Table 4.1. Skull lengths for each taxon. Lengths were referenced from the literature wherever possible. *Suchomimus* was compared to *Spinosaurus* using Blender 2.82's measuring tools to best estimate an approximate length, and a similar technique was used for *Neovenator* by comparing it to *Allosaurus*, due to their close evolutionary relationships.

Specimen name	Specimen number	Skull length (cm)	Literature reference
Spinosaurus aegyptiacus	FSAC-KK 11888	175	Dal Sasso et al. 2005
Giganotosaurus carolinii	MUCPv-Ch1	163.4	Canale et al. 2022
Suchomimus tenerensis	MNN GDF501	145	N/A. Estimated from FSAC-KK 11888 comparison.
Acrocanthosaurus atokensis	NCSM 14345	129	Currie & Carpenter 2000
Torvosaurus gurneyi	BYUVP 2002-2014, 2016-2018, 4882-4884, 4860, 4890, 4998, 5110, 5286, 9120-9122, 9249	115	Hendrickx & Mateus 2014

Baryonyx walkeri	NHMUK VP R9951	93	Charig & Milner 1997
Monolophosaurus jiangi	IVPP 84019	80	Brusatte et al. 2010
Allosaurus jimmadseni	MOR 693	72	Henderson & Nicholls 2015
Neovenator salerii	MIWG.6348	72	N/A. Estimated from MOR 693 comparison.
Majungasaurus crenatissimus	FMNH PR 2100	65	Sampson & Witmer 2007
Carnotaurus sastrei	MACN-Pv-CH 894	59.6	Bonaparte et al. 1990
Dilophosaurus wetherilli	UCMP 77270	59	Welles 1984
Herrerasaurus ischigualastensis	PVSJ 407	56	Sereno & Novas 1992
Ceratosaurus nasicornis	BYUVP 12893	55	Gilmore 1920

Table 4.2. All specimens tested, their specimen numbers, and the 3D model surface areas

(mm^2). Multiple specimen numbers denote a composite specimen. Surface area values were

calculated in both MeshLab 2020.06 and Avizo Lite 9.5 for consistency and found to be the same in mm^2. *Surface scanned models. **Composite cast.

Specimen name	Specimen number	Cranial model surface area (mm^2)	Mandible model surface area (mm^2)	Scan of cast?
Spinosaurus aegyptiacus	FSAC-KK 11888	2257382	1575902	Yes
Giganotosaurus carolinii	MUCPv-Ch1	1880562	N/A	Yes
*Suchomimus tenerensis**	MNN GDF501	828898	677021	Yes**
*Acrocanthosaurus atokensis**	NCSM 14345	1545905	1169611	Yes
*Torvosaurus gurneyi**	BYUVP 2002-2014, 2016-2018, 4882-4884, 4860, 4890, 4998, 5110, 5286, 9120-9122, 9249	1815301	869156	Yes**
Baryonyx walkeri	NHMUK VP R9951	N/A	369971	No
*Monolophosaurus jiangi**	IVPP 84019	551013	249787	Yes
Allosaurus	MOR 693	788710	306512	No

jimmadseni				
*Neovenator salerii***	MIWG.6348	567398	245641	No
*Majungasaurus crenatissimus**	FMNH PR 2100	706964	258754	Yes
Carnotaurus sastrei	MACN-Pv-CH 894	949904	306760	No
*Dilophosaurus wetherilli**	UCMP 77270	608045	184758	Yes
*Herrerasaurus ischigualastensis**	PVSJ 407	94382	51683	Yes
*Ceratosaurus nasicornis**	BYUVP 12893	360584	182932	Yes

Table 4.3. 3D model triangles, elements, and volume measurements (mm^3). All values were calculated in MeshLab 2020.06.

Specimen	Cranial triangle count	Mandibular triangle count	Cranial element count	Mandibular element count	Cranial volume (mm³)	Mandibular volume (mm³)
Spinosaurus aegyptiacus	366500	229448	549750	344172	183222	114716
Giganotosaurus carolinii	97,534	N/A	146301	N/A	48741	N/A
Suchomimus tenerensis	499980	400008	749970	600012	249988	200000

Acrocanthosaurus atokensis	400014	350026	600021	525039	200001	175015
Torvosaurus gurneyi	499,234	400,066	748,851	600,099	249,613	200,031
Baryonyx walkeri	N/A	304,666	N/A	456,999	N/A	152,333
Monolophosaurus jiangi	369,856	309,978	554,784	464,967	184,912	154,991
Allosaurus jimmadseni	155,102	114,838	232,613	172,257	77,493	57,411
Neovenator salerii	599,992	499,990	899,988	749,985	299,974	249,997
Majungasaurus crenatissimus	498,980	399,982	748,470	599,793	249,472	199,898
Carnotaurus sastrei	497,700	398,508	746,550	597,762	248,756	199,249
Dilophosaurus wetherilli	349,972	299,972	524,958	449,958	174,974	149,984
Herrerasaurus ischigualastensis	350,006	315,016	525,009	472,524	174,985	157,506
Ceratosaurus nasicornis	398,798	314,918	598,197	472,377	199,391	157,459

4.3.2. Finite element analyses

As in previous chapters, all models were meshed using HyperMesh software. Element size was set to 10, and in the Tetramesh parameters sub-panel, I selected for optimized mesh quality and for the mesh speed to be gradual. Once the model was meshed successfully, I applied the appropriate material properties to the meshed models. The bone properties were assigned based on crocodilian skull bone: Young's modulus of 15,000 MPa and Poisson's ratio of 0.29 (Zapata et al. 2010; Porro et al. 2011; Ballell et al. 2019) for each theropod dinosaur given the close evolutionary relationship between crocodilians and dinosaurs. As in chapters 2 (Rowe & Rayfield 2022) and 3, dentine properties were not applied to the teeth, as they generally have little influence on stress plot comparisons in 3D FE results (Herbst et al. 2021).

Six total constraints were applied to the hinges of the quadrate of the cranium and the articular of the mandible to prevent models from freely floating in space during hypothetical feeding scenarios. Loads were applied to the two premaxillary teeth on each side of the cranium and mandible to simulate contact with prey during a bite. Once the mesh was imported into Abaqus (Simulia), I applied muscle forces to the models to accurately assess the effects of muscle loading on the skull during a feeding simulation. Locations of muscle insertions were derived from Holliday 2009, Gignac & Erickson 2017, and Rowe & Snively 2021. Muscle forces for all theropods were scaled from FMNH PR 2081 using the subtemporal fenestra method outlined in Sakamoto (2006) (Table A4). This was done by measuring the surface area of the adductor chamber using ImageJ and multiplying the surface area by the isometric muscle tension of 31.5 N/cm^2 (Figure 4.1). This method has been demonstrated for its reliability in Sakamoto 2022.

The ratio between muscle force and skull surface area was recorded for the adult *T. rex* FMNH PR 2081, the largest dinosaur in my dataset (Chapter 3). All other models were then scaled to the same muscle force: surface area ratio to normalise size effect and test how the skull shape accommodates stress and strain as outlined in Dumont et al. (2008) (Table A5). I then reran all analyses and generated new heatmaps for crania and mandibles. This method is to test for the biomechanical influence of only skull shape rather than both body size and skull shape, due to the high morphological variability in the theropod skull models.

70 cm
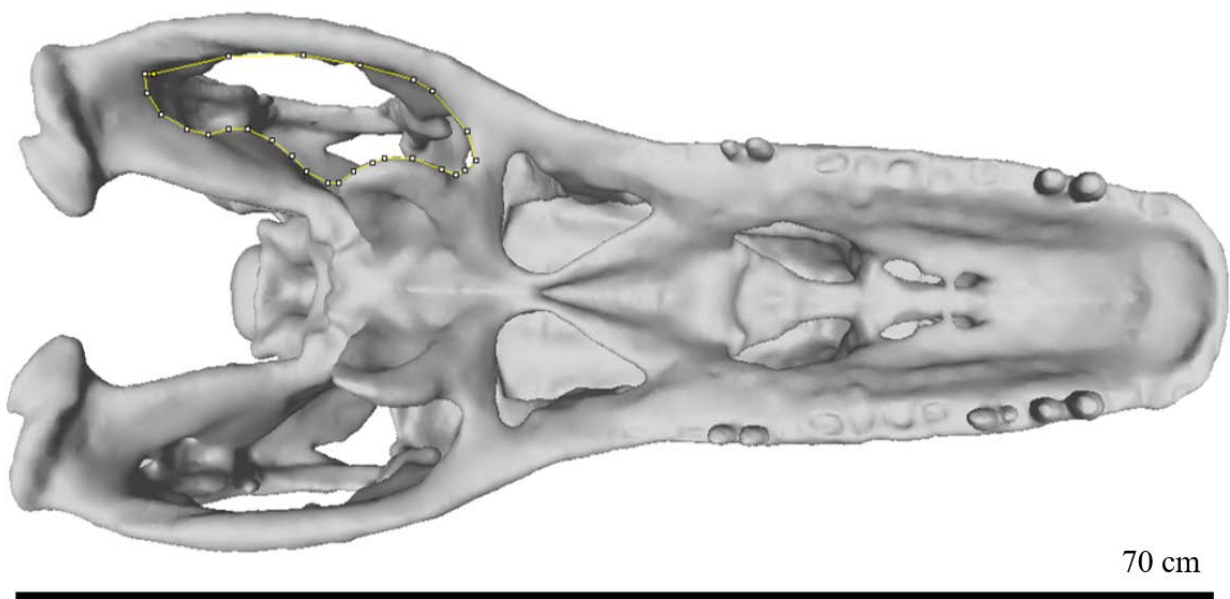
Figure 4.1. *Allosaurus jimmadseni* (MOR 693) cranium in ventral view, with one adductor chamber measured in ImageJ (Fiji). Adductor chamber measurements were multiplied by isometric muscle tension 31.5 N/cm^2 to calculate muscle force components applied in Abaqus/CAE 6.14-1.

As in Chapters 2, 3, and Rowe & Rayfield 2022, mesh-weighted arithmetic mean (MWAM) values were calculated using R (2021) for each theropod specimen as to reduce possible discrepancies between CT-derived models and surface scan-derived models (Marcé-Nogué et al. 2016; Morales-García et al. 2019; Ballell & Ferrón 2021). Crania and mandibles were analysed separately and figured at different limits of maximum stress values to better

demonstrate the patterns of stresses in both types of models, as mandibles are generally more fragile than crania.

4.4. Results

I generated von Mises stress and maximum principal strain data for each theropod dinosaur model as outlined in the methods. As demonstrated by the *Crocodyus* and *Varanus* mandibles in chapter 2 and several tyrannosauroid skulls in chapter 3, models with a high degree of editing applied prior to meshing tend to output relatively high von Mises stress and maximum principal strain relative to un-modified models. This was one of the considerations applied to certain models in the study, particularly the *Baryonyx* mandible.

4.4.1. Actual size data

3D finite element heatmaps were generated for each cranial model, with von Mises stress limits ranging from 0 – 25 MegaPascals in the display figures (Figure 4.2). Heatmap results for the mandibles were set to display limits ranging from 0 – 40 MegaPascals as at 0 – 25 MegaPascals the patterns of stresses were less clear (Figure 4.3). Note the missing *Baryonyx* material in Figure 4.2 and the missing *Giganotosaurus* material in Figure 4.3. This was due to an inadequate amount of cranial material in the *Baryonyx* specimen (Charig & Milner 1986) for FEA and the lack of a mandible in the *Giganotosaurus* replica.
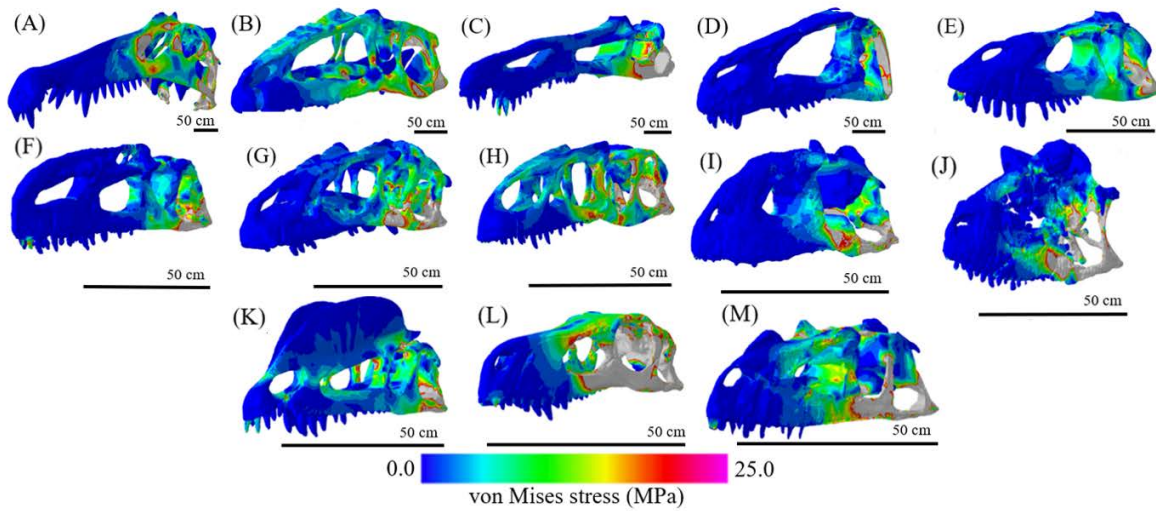
Figure 4.2. Finite element heatmaps for all non-tyrannosauroid theropod cranial models at actual size after simulated adductor contraction and biting at the two front teeth. Areas of high stress are indicated by hotter colours, and low stress is indicated by cooler colours. (A) *Spinosaurus aegyptiacus*, (B) *Giganotosaurus carolinii* , (C) *Suchomimus tenerensis*, (D) *Acrocanthosaurus atokensis*, (E) *Torvosaurus gurneyi*, (F) *Monolophosaurus jiangi*, (G) *Allosaurus jimmadseni*, (H) *Neovenator salerii*, (I) *Majungasaurus crenatissimus*, (J) *Carnotaurus sastrei*, (K) *Dilophosaurus wetherilli*, (L) *Herrerasaurus ischigualastensis Dilophosaurus wetherilli*, (M) *Ceratosaurus nasicornis*. Note the low stress occurrences in the cranial ornamentation of *Monolophosaurus* (F) and *Dilophosaurus* (K). Also note the very high stresses occurring in the basal ambiguous theropod *Herrerasaurus* (L).
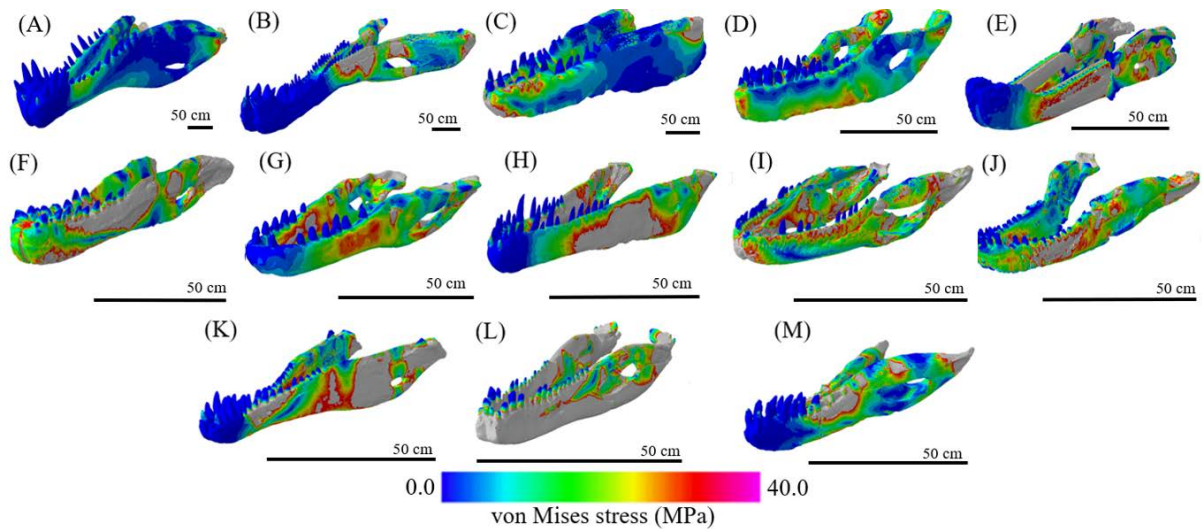
Figure 4.3. Finite element heatmaps for all non-tyrannosauroid theropod mandible models at actual size after simulated adductor contraction and biting at the two front teeth. (A) *Spinosaurus aegyptiacus*, (B) *Suchomimus tenerensis*, (C) *Acrocanthosaurus atokensis*, (D) *Torvosaurus gurneyi*, (E) *Baryonyx walkeri*, (F) *Monolophosaurus jiangi*, (G) *Allosaurus jimmadseni*, (H) *Neovenator salerii*, (I) *Majungasaurus crenatissimus*, (J) *Carnotaurus sastrei*, (K) *Dilophosaurus wetherilli*, (L) *Herrerasaurus ischigualastensis*, (M) *Ceratosaurus nasicornis*.

Mesh-weighted von Mises stress data was compiled and compared for all crania (Figure 4.4) and plotted against skull lengths to better visualise the effects of large skulls on feeding-induced stresses (Figure 4.5). I also calculated and compiled mean von Mises stress results across each mandible (Figure 4.6) and plotted against skull length (Figure 4.7). I then calculated P-values for each dataset to better access the possible relationships between skull length and von Mises stress during feeding scenarios.
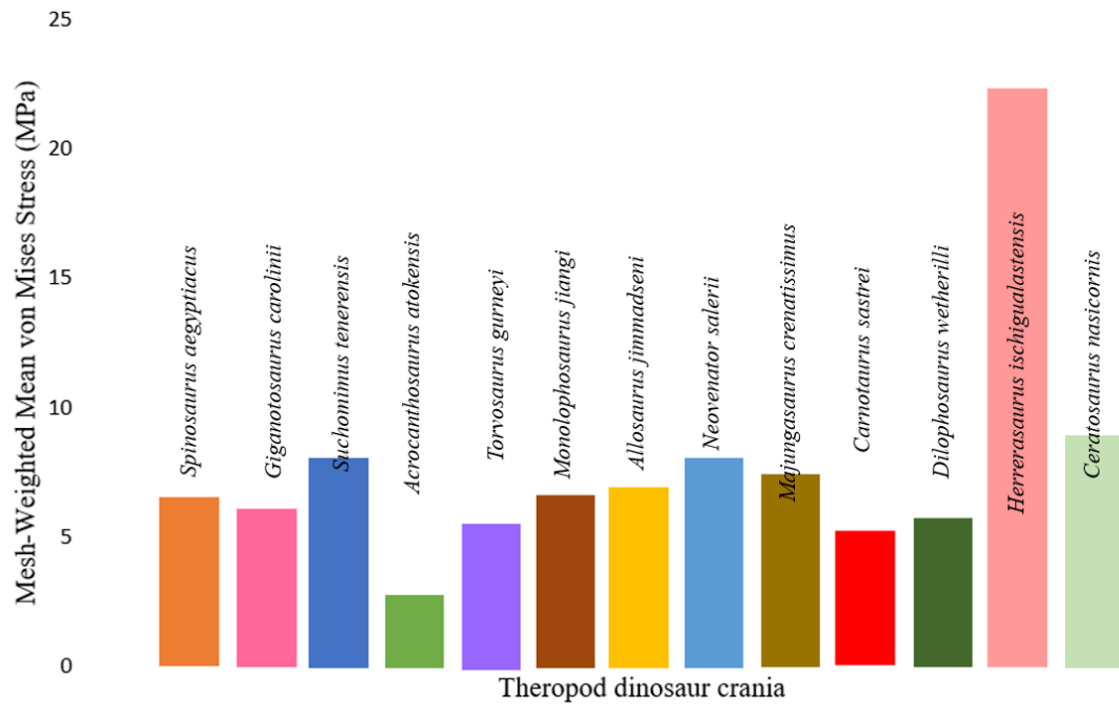
Figure 4.4. Calculated mesh-weighted mean von Mises stress results for each theropod dinosaur cranium at actual size.
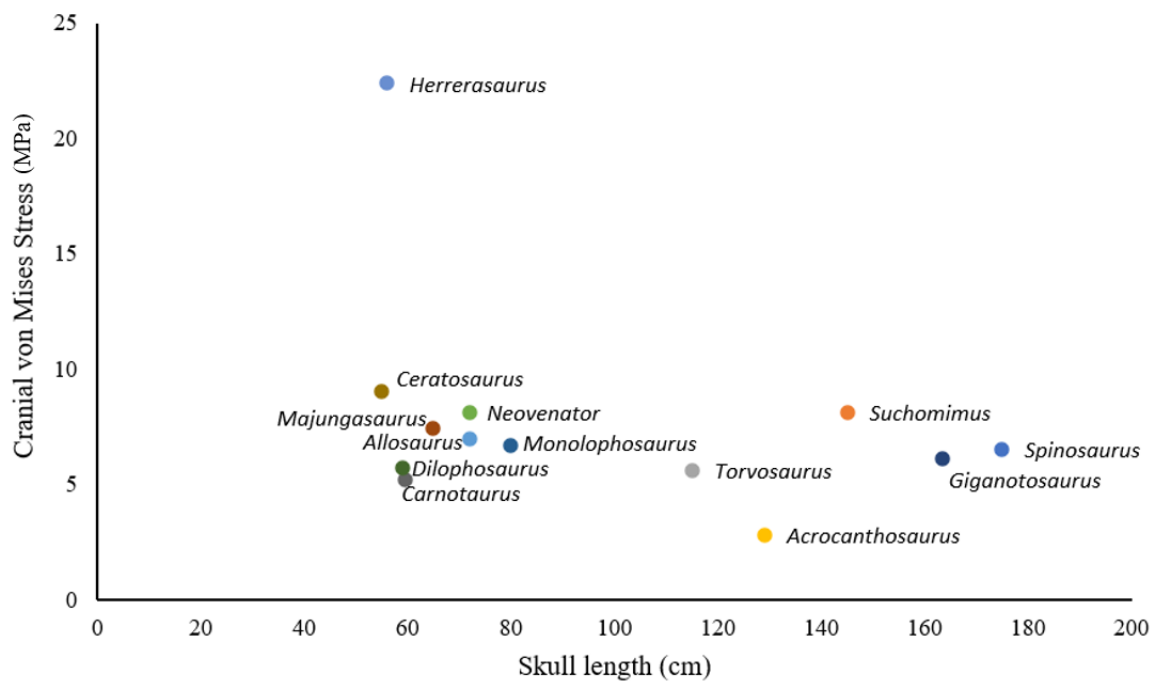
Figure 4.5. Skull lengths plotted against mesh-weighted mean cranial von Mises stresses for each theropod dinosaur at actual size. Skull lengths in cm.

Calculating a linear regression with skull lengths (x) and cranial von Mises stresses (y) yielded a P-value of 0.2621, indicating a weak relationship between the two. von Mises stresses are generally fairly consistent with each taxa, with *Herrerasaurus* displaying the highest cranial stresses.
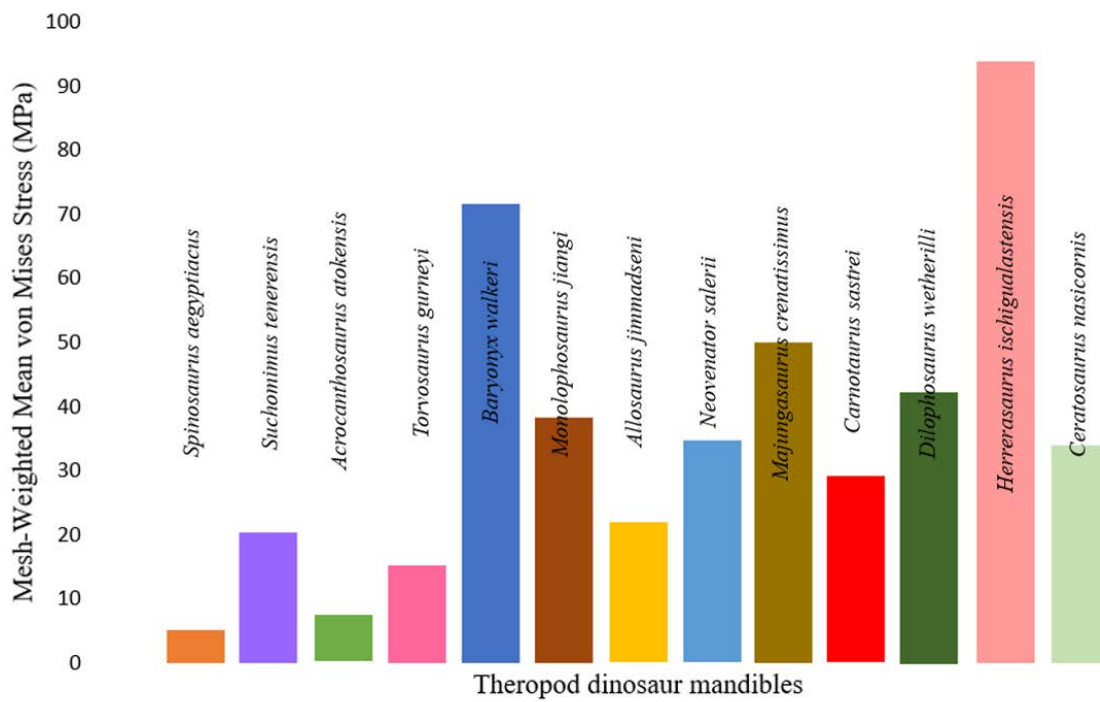
Figure 4.6. Calculated mesh-weighted mean von Mises stress results for each theropod dinosaur mandible at actual size.
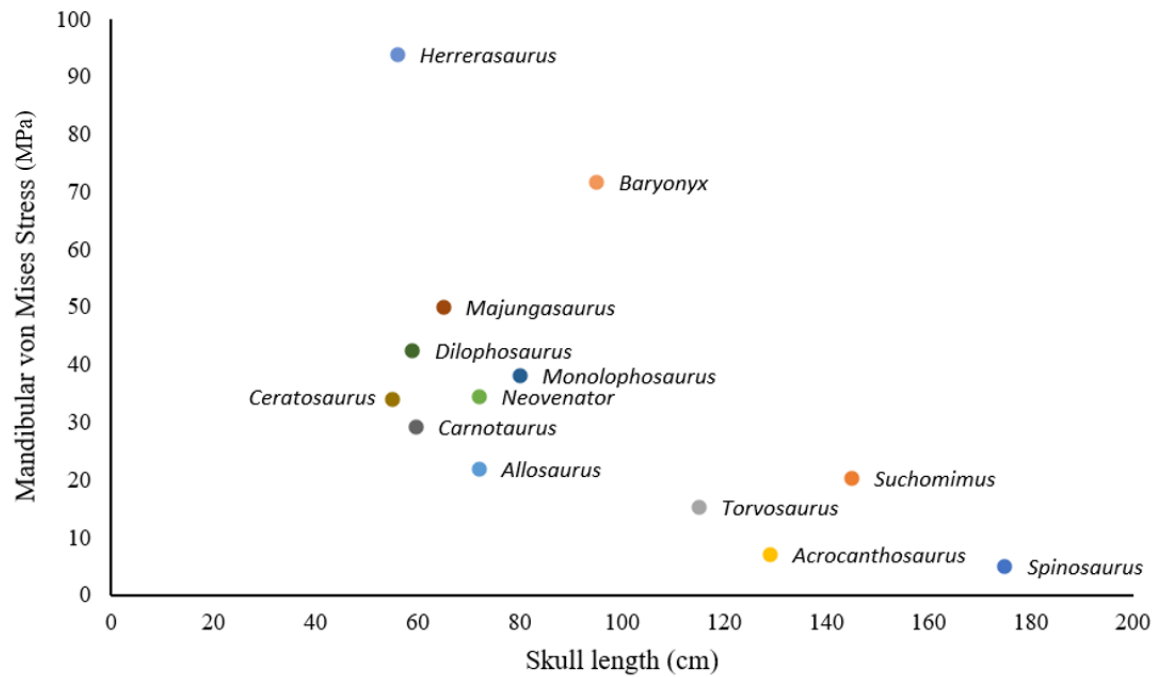
Figure 4.7. Skull lengths plotted against mesh-weighted mean mandibular von Mises stresses for each theropod dinosaur at actual size. Skull lengths in cm.

Calculating a linear regression with skull lengths (x) and mandibular von Mises stresses (y) yielded a P-value of 0.03268, indicating a moderate statistically significant relationship between skull length and mandible stress. *Herrerasaurus* demonstrated the highest stress values as it did when examining the cranium. *Baryonyx* similarly exhibited high stresses, though this may partly due to the reconstruction of the mandible from merged CT-scanned bones.

Mean max principal strain was calculated as for the crania (Figure 4.8) and mandibles (Figure 4.9) as well. Note that strain is unitless.
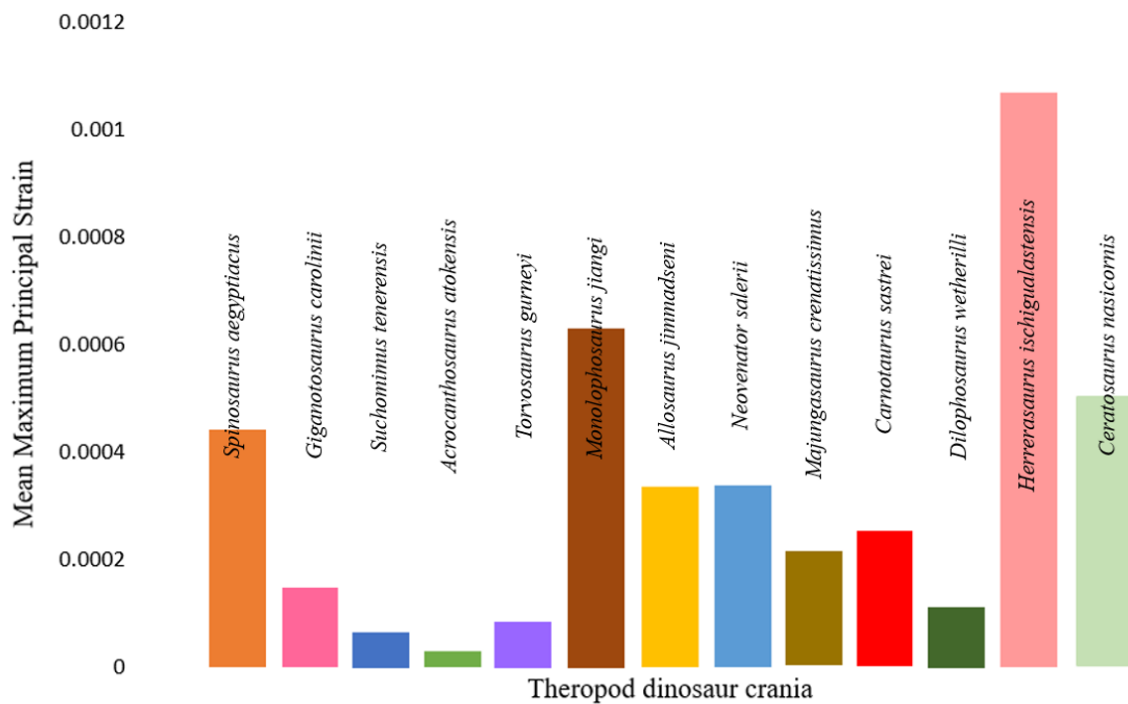
Figure 4.8. Calculated mean maximum principal strain results for each theropod dinosaur cranium at actual size.

As in the von Mises stress data, *Herrerasaurus* experiences the highest cranial strain, with *Monolophosaurus*, *Ceratosaurus*, and *Spinosaurus* also experiencing higher strains. Generally, there is no trend in the data in terms of skull size, though some of the larger theropod do experience low strain, including *Suchomimus*, *Acrocanthosaurus*, and *Giganotosaurus.*
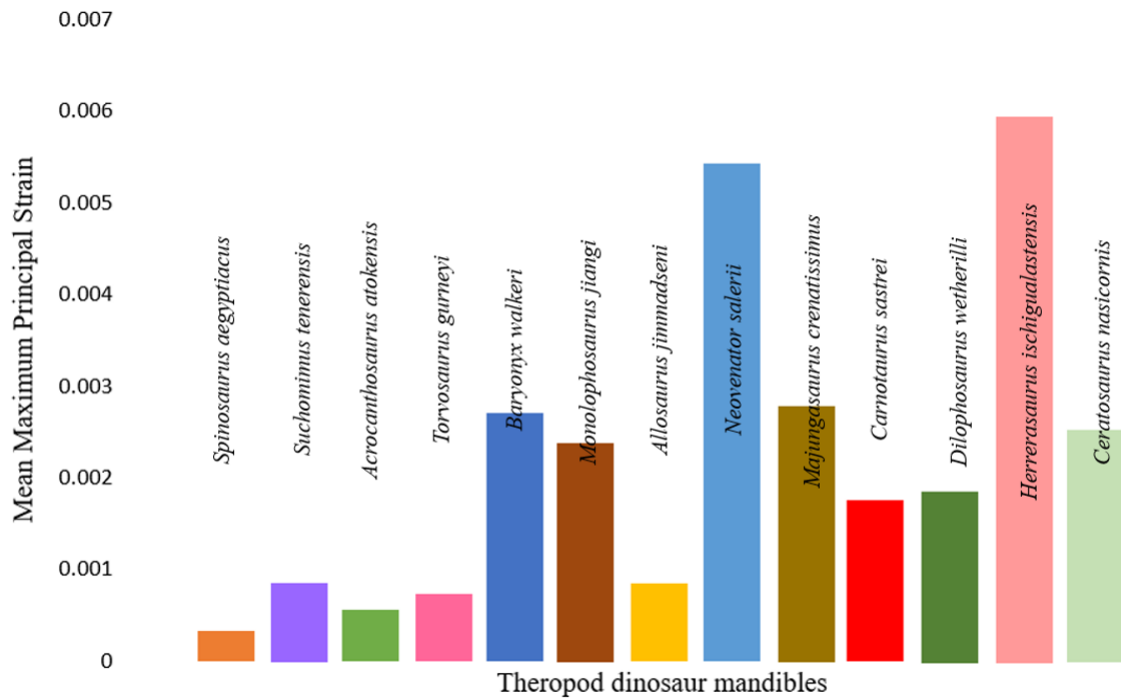
Figure 4.9. Calculated mean maximum principal strain results for each theropod dinosaur mandible at actual size.

As in previous plots, *Herrerasaurus* experiences the highest values, with certain medium-sized theropods also exhibiting high mandibular strain including *Neovenator, Baryonyx*, and *Majungasaurus*. *Baryonyx*'s high strain may be partly attributed to its reconstruction; however, it is the most diminutive megalosauroid mandible of the dataset which may also contribute to its relatively high strain.

4.4.2. Scaled data

FEA heatmaps were compiled for all crania (Figure 4.10) and mandibles (Figure 4.11) which were scaled to the same muscle force: surface area ratio.
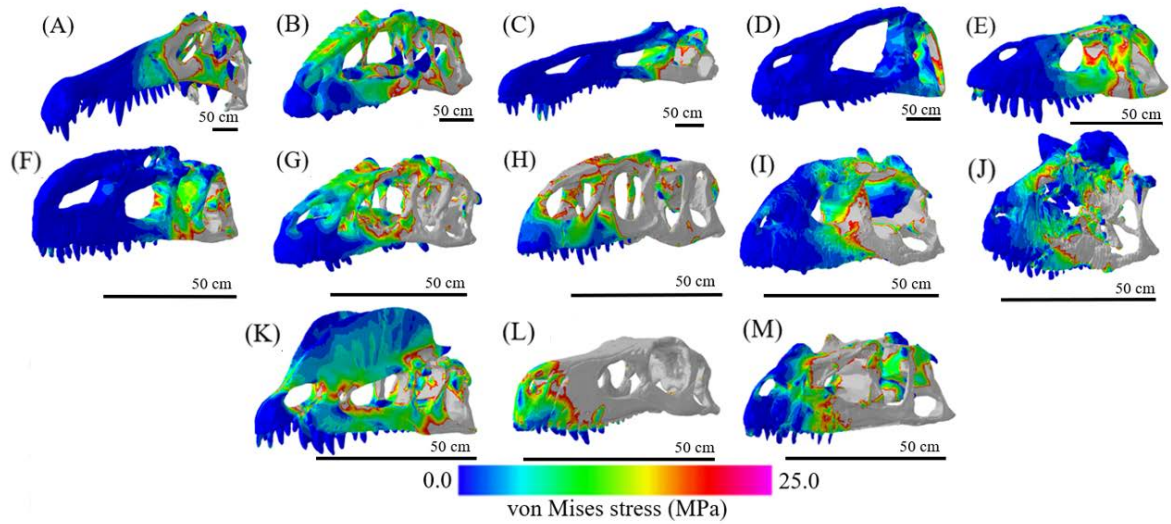
Figure 4.10. Finite element heatmaps for all non-tyrannosauroid theropod cranial models when muscle forces were scaled to the force:surface area ratio of adult *T. rex* FMNH PR 2081. (A) *Spinosaurus aegyptiacus*, (B) *Giganotosaurus carolinii* , (C) *Suchomimus tenerensis*, (D) *Acrocanthosaurus atokensis*, (E) *Torvosaurus gurneyi*, (F) *Monolophosaurus jiangi*, (G) *Allosaurus jimmadseni*, (H) *Neovenator salerii*, (I) *Majungasaurus crenatissimus*, (J) *Carnotaurus sastrei*, (K) *Dilophosaurus wetherilli*, (L) *Herrerasaurus ischigualastensis Dilophosaurus wetherilli*, (M) *Ceratosaurus nasicornis*.
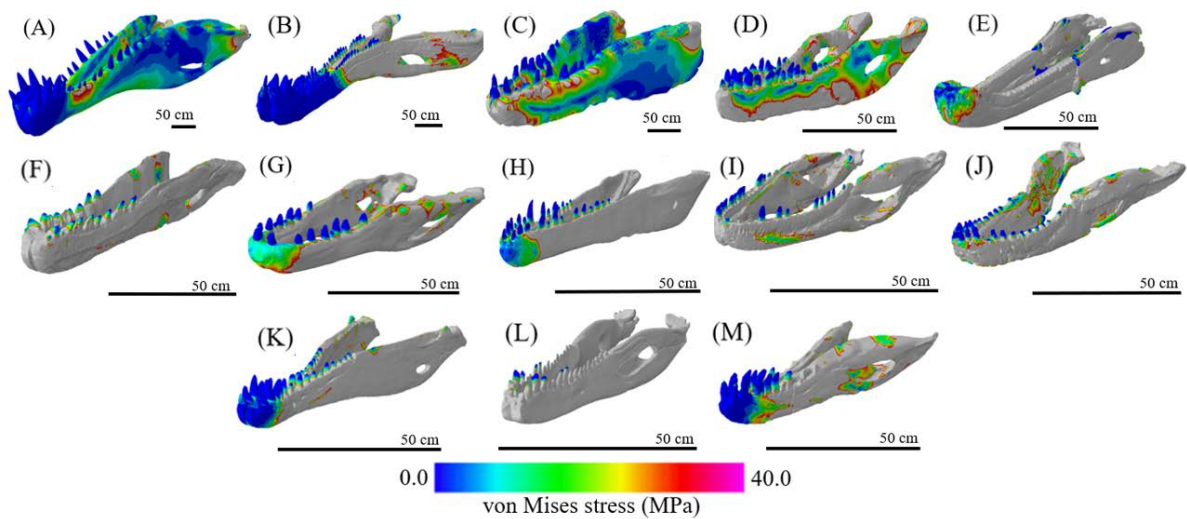
Figure 4.11. Finite element heatmaps for all non-tyrannosauroid theropod mandible models when muscle forces were scaled to the force:surface area ratio of adult *T. rex* FMNH PR 2081. (A) *Spinosaurus aegyptiacus*, (B) *Suchomimus tenerensis*, (C) *Acrocanthosaurus atokensis*, (D) *Torvosaurus gurneyi*, (E) *Baryonyx walkeri*, (F) *Monolophosaurus jiangi*, (G) *Allosaurus jimmadseni*, (H) *Neovenator salerii*, (I) *Majungasaurus crenatissimus*, (J) *Carnotaurus sastrei*, (K) *Dilophosaurus wetherilli*, (L) *Herrerasaurus ischigualastensis*, (M) *Ceratosaurus nasicornis*.

Mesh-weighted mean von Mises stresses were then compared across all muscle force-equalised crania (Figure 4.12) and plotted against skull lengths (Figure 4.13) to better assess how theropod skull shapes respond to feeding loads. I then compiled muscle force-equalised data for the mandibles (Figure 4.14, 4.15). Maximum principal strain values were then calculated for each mandible (Figure 4.16, 4.17).
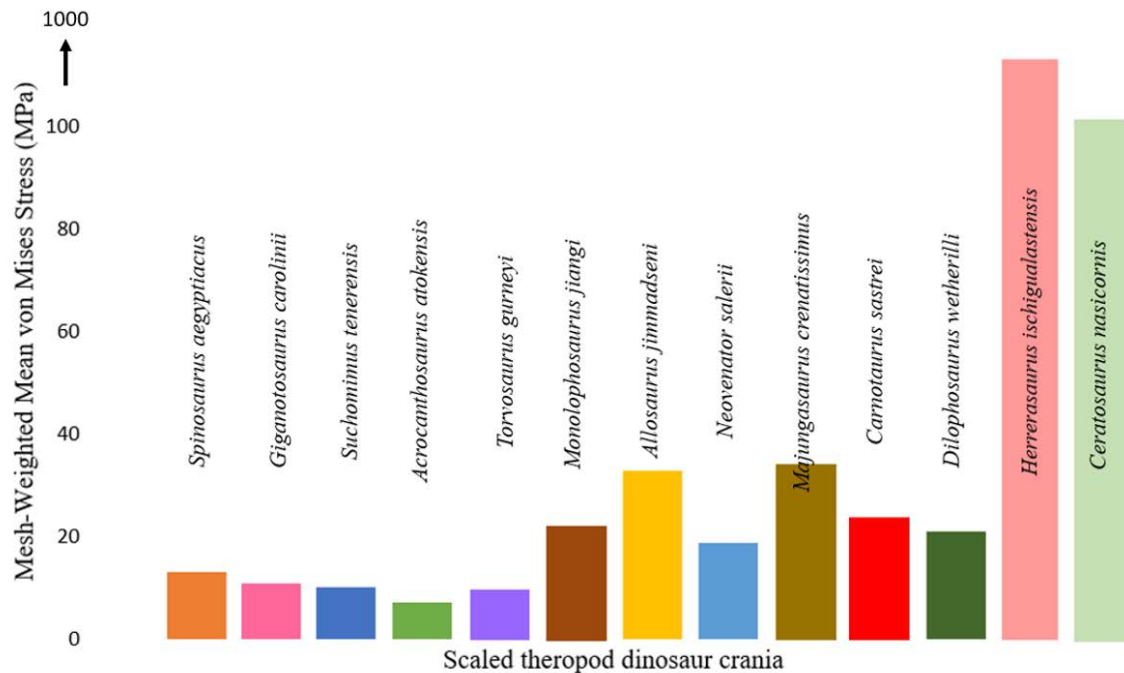
Figure 4.12. Calculated mesh-weighted mean von Mises stress results for each theropod dinosaur cranium when muscle forces were scaled to the force:surface area ratio of adult *T. rex* FMNH PR 2081 as a means of testing how skull shape responds to loading.
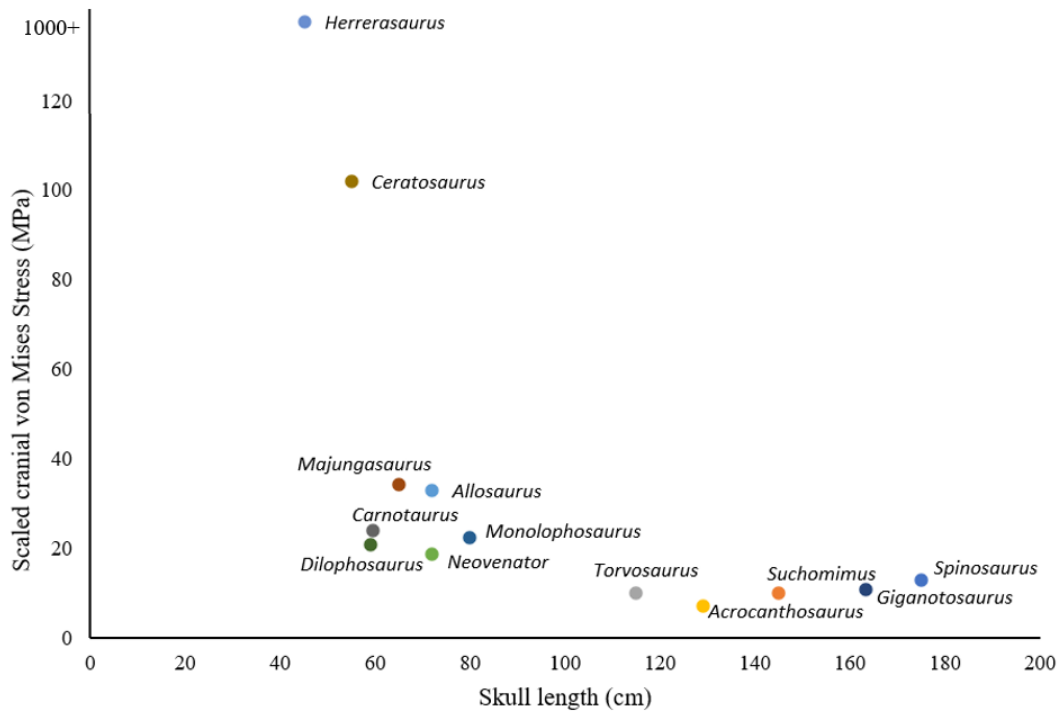
Figure 4.13. Calculated mesh-weighted mean von Mises stress results for each theropod dinosaur cranium when muscle forces were scaled to the force:surface area ratio of adult *T. rex* FMNH PR 2081 as a means of testing how skull shape responds to loading. As in the actual size models, note the trends towards lower stresses with acquisition of larger crania. Skull lengths in cm.

Calculating a linear regression with skull lengths (x) and cranial von Mises stresses (y) for the scaled muscle force dataset yielded a P-value of 0.2976, indicating a weak relationship. The two shortest skulls, *Ceratosaurus* and *Herrerasaurus*, exhibit the highest cranial stresses, while the lowest are attributed to the large megalosauroids and allosauroids, particularly *Acrocanthosaurus*.
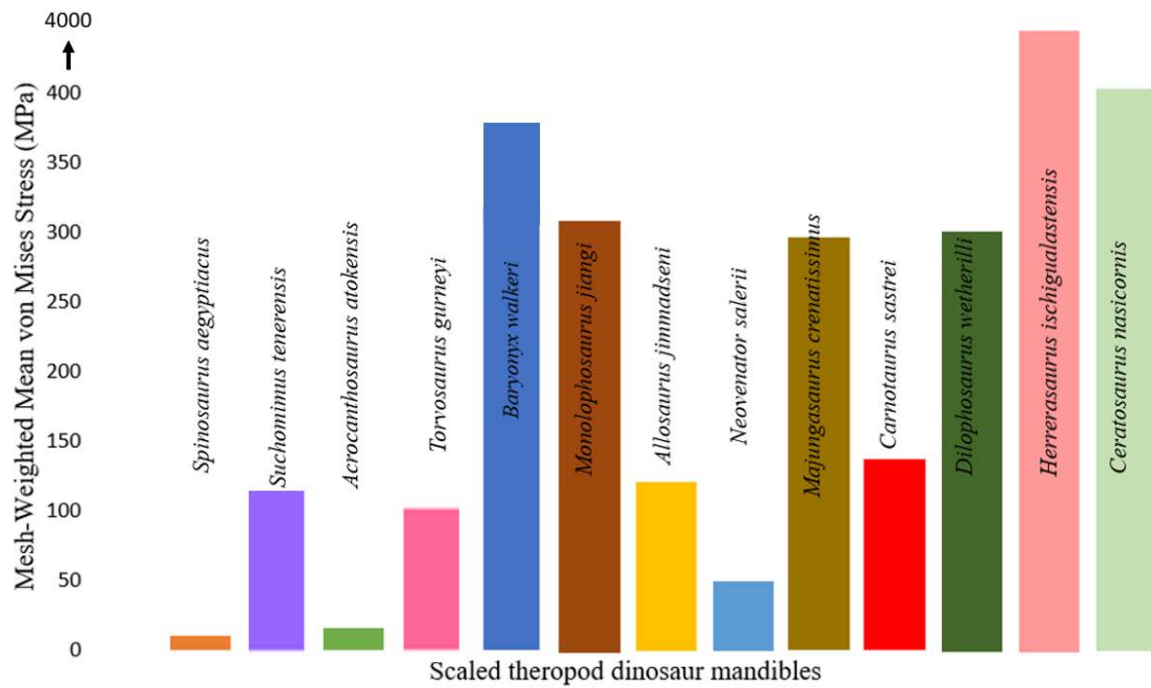
Figure 4.14. Calculated mesh-weighted mean von Mises stress results for each theropod dinosaur mandible when muscle forces were scaled to the force:surface area ratio of adult *T. rex* FMNH PR 2081 as a means of testing how skull shape responds to loading.
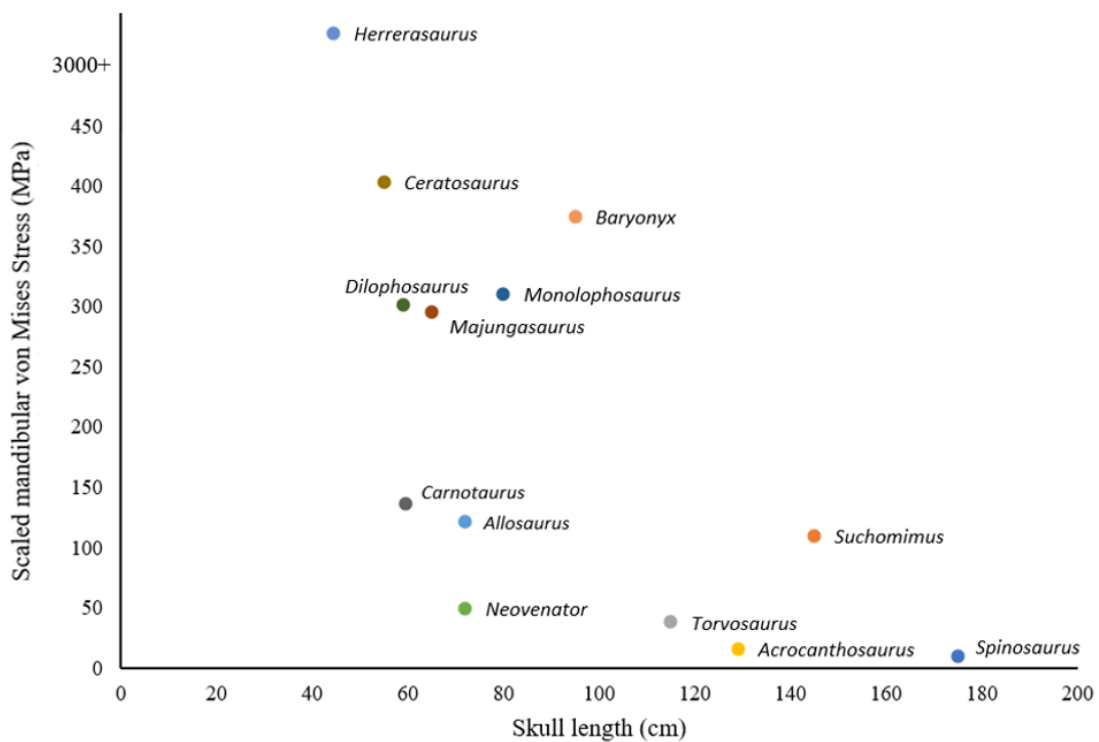
Figure 4.15. Calculated mesh-weighted mean von Mises stress results for each theropod

dinosaur mandible when muscle forces were scaled to the force:surface area ratio of adult *T. rex* FMNH PR 2081 as a means of testing how skull shape responds to loading. As in the actual size models, note the trends towards lower stresses with acquisition of larger mandibles. Skull lengths in cm.

Calculating a linear regression with skull lengths (x) and mandibular von Mises stresses (y) for the scaled muscle force dataset yielded a P-value of 0.2583, indicating a weak relationship. As in previous analyses, *Herrerasaurus*, *Ceratosaurus*, and *Baryonyx* exhibit the highest stress values, while the large megalosauroid and allosauroids are generally the most stress resistant, especially *Spinosaurus* and *Acrocanthosaurus*.
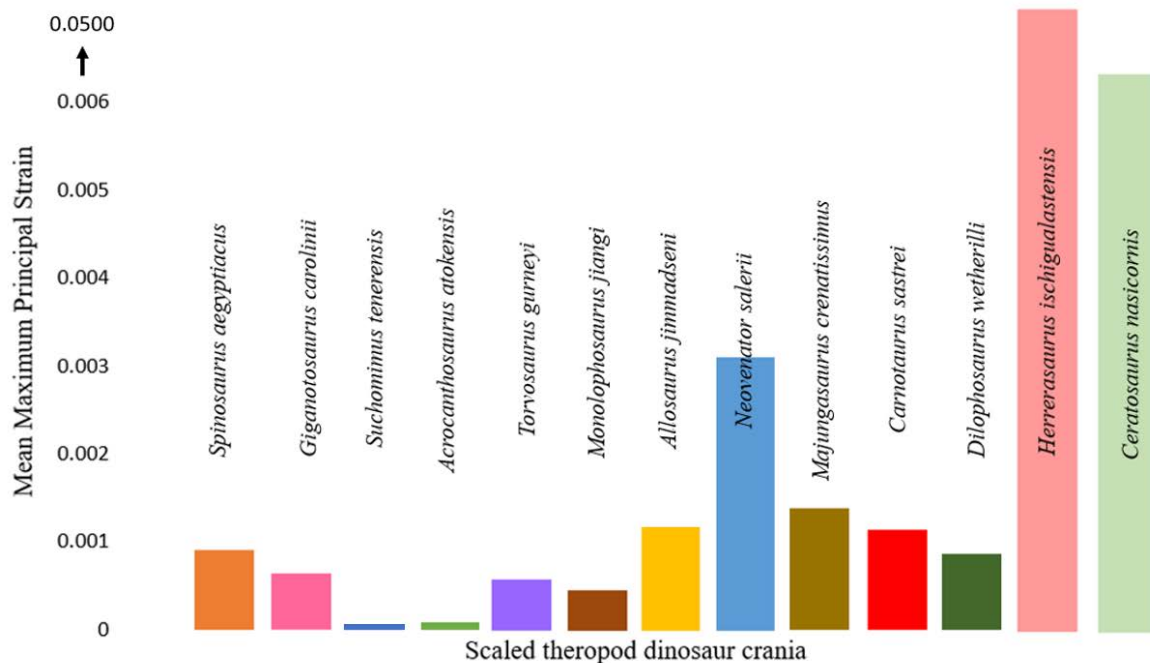
Figure 4.16. Calculated mean maximum principal strain results for each theropod dinosaur cranium when muscle forces were scaled to the force:surface area ratio of adult *T. rex* FMNH PR 2081 as a means of testing how skull shape responds to loading.

Cranial strain results for the muscle force scaled dataset revealed the highest strain in *Herrerasaurus*, *Ceratosaurus*, and *Neovenator*. Lowest strains were present in *Acrocanthosaurus* and *Suchomimus*.
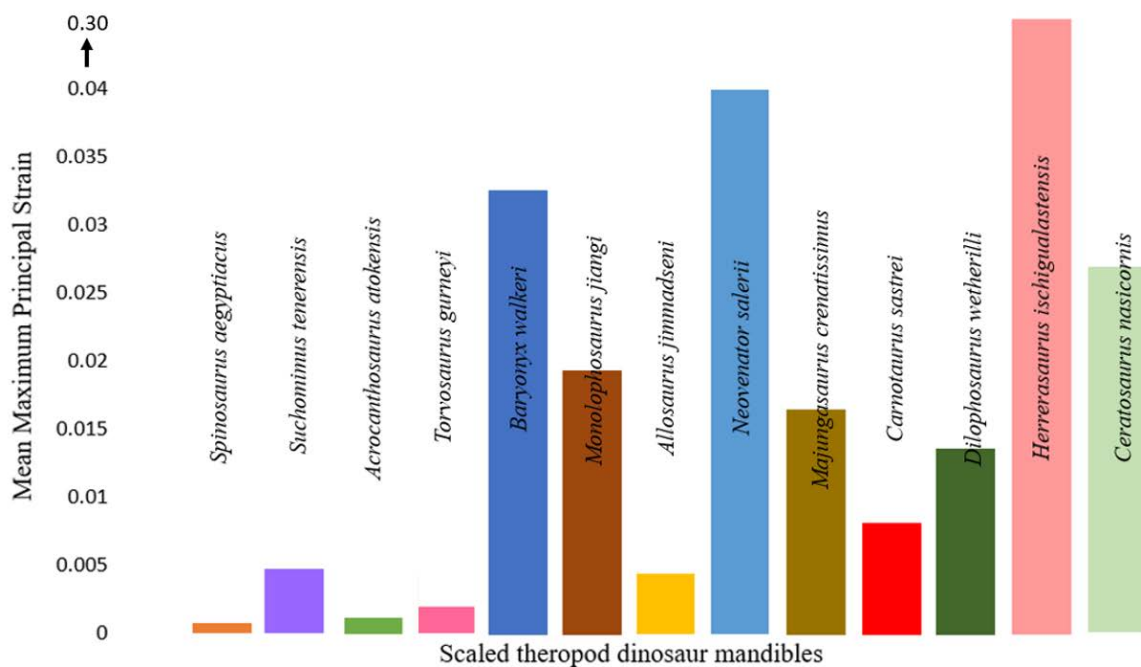
Figure 4.17. Calculated mean maximum principal strain results for each theropod dinosaur mandible when muscle forces were scaled to the force:surface area ratio of adult *T. rex* FMNH PR 2081 as a means of testing how skull shape responds to loading.

Strain results for the muscle force scaled mandibles yielded the highest strains in *Herrerasaurus*, *Neovenator*, and *Baryonyx*. The lowest values were present in *Spinosaurus* and *Acrocanthosaurus*.

4.5. Discussion

This is the largest data set of 3D theropod dinosaur skull models ever analysed; thus, I have examined biomechanical trends in giant theropods with amounts of 3D data not previously possible. I discuss several major points from this study, concerning large body size, macroevolution, and skull form in the Theropoda, with comments on the tyrannosauroid specimens analysed in chapter 3.

4.5.1. Significance for large body size evolution

Non-avian theropod dinosaurs are a classic example of Cope's rule, the general trend towards large body size (Benson et al. 2018) This study contains 3D models of some of the largest taxa in the clade, such as *Giganotosaurus* and *Spinosaurus*. At actual size, it was demonstrated previously that tyrannosauroids generally experience higher biting stresses at larger body sizes but are able to effectively absorb high stresses during feeding (Rowe & Snively 2021; Chapter 3). This is likely due to the widely-set quadrates and mandibles in mature tyrannosauroids enabling the bone-crunching bite (Bates & Falkingham 2012; Gignac & Erickson 2017). Additionally, tyrannosaurids are have been noted for their fused nasal bones (Snively et al. 2006) and *Tyrannosaurus rex* in particular for its stiff, akinetic skull capable of roughly 60,000 N bite forces (Cost et al. 2019). These traits allow large tyrannosaurids to efficiently transfer forces from their teeth to the prey items, which distinguishes the clade from other large theropod dinosaurs like those analysed here.

Other giant theropod lineages analysed in this chapter include the megalosauroids or spinosauroids, and allosauroids. While large theropod taxa in these lineages attain heights, lengths, and body masses comparable to *Tyrannosaurus*, they do not have the aforementioned traits that are characteristic of mature *T. rex* such as fused nasal bones. Likewise, there is not a trend in this study of the largest individuals experiencing the highest feeding stresses, as the overall smaller abelisauroids and *Herrerasaurus* demonstrated the highest von Mises stresses

at true size. Non-tyrannosauroid theropod dinosaurs generally experience lower skull stresses with larger mandible size, unlike the clearer trends seen in chapter 3.

Generally, medium-sized taxa including the smaller allosauroids and abelisauroids congregate in one area, while large-sized allosauroid and megalosauroid taxa congregate in another (Figure 4.5, 4.7). Abelisauroids and smaller allosauroids may have occupied similar ecological niches. Medium-sized theropod clades were generally outcompeted by juvenile forms of larger dinosaurs, hence the success of tyrannosauroid and megalosauroids when compared to abelisauroids (Schroeder et al. 2021). Thus, feeding function may have influenced the direction of body mass evolution in certain theropod clades, given the success of large-bodied carnivorous taxa and their clustering towards the similar mechanical stress output.

There is a moderately significant trend toward lower stresses in the mandibles of larger non-tyrannosauroid theropods (Figure 4.7), which is opposite the trend seen in the tyrannosauroids. This may be in part due to the different feeding strategies used by large theropod lineages. As the tyrannosauroid bite was optimised for a stiff, crushing bite (Cost et al. 2019), allosauroid skulls were better equipped for slashing motions when feeding, aided by a wider gape when opening their mouths, particularly in mature *Allosaurus* (Rayfield et al. 2001; Lautenschlager 2015). Thus, the skulls of smaller, non-tyrannosauroid theropods may not have required such a stress-resistant skull when procuring food, as their feeding strategies were so different. Rayfield et al. (2001) noted that *Allosaurus* can accommodate higher stresses than demonstrated when used in a slashing motion; however, other similarly-sized theropods have not yet been as extensively analysed. Theropods of comparable skull lengths and body sizes, i.e., *Neovenator* and *Monolophosaurus* may be able to similarly absorb stresses as in *Allosaurus*, though more extensive work should be done concerning the biomechanics of understudied taxa.

Certain megalosauroid taxa such as *Spinosaurus* are commonly hypothesized to have been piscivorous (Hone & Holtz 2021); shoreline feeding likely would not have required a strong bite, though megalosauroids did not exclusively prey on marine animals, as they consumed iguanodontids and pterosaurs (Charig & Milner 1986; Buffetaut et al. 2004). However, it is unknown if these instances were scavenging or predation. It has been previously demonstrated that spinosaur skulls mechanically outperform those of crocodilians in terms of torsion resistance; however, this is due to their massive size (Cuff & Rayfield 2013). Thus, large body size appears to convey a functional advantage in certain lineages regardless of skull shape, as larger size generally indicates more muscle mass and higher bite forces, enabling an increased range of prey procurement. This is noticeable in Figures 4.10-17, as taxa possessing slender and short skulls tend to perform poorly when muscle forces were scaled to adult *T. rex* (FMNH PR 2081). Ma et al. (2021) similarly noted a trend of general jaw strengthening in all carnivorous theropod lineages. This was facilitated via curved bone effect (Milne 2016), bone functional adaptation, and the dorsoventral expansion of the post-dentary region. . The vertebrate mandible is generally better adapted for feeding function, whereas the cranium in subject to multiple constraints (Bell et al. 2009); thus, my cranial and mandibular results do not demonstrate identical trends. This may be due to the theropod cranium serving in more roles than the mandible (Witmer 2001; Ma et al. 2021) which may more constraints on cranial morphology and result in differing biomechanical trends.

4.5.2. Skull shape significance

Theropod dinosaurs possessing relatively short skulls tend to perform poorly when muscle forces were equalized to test for the effects of shape, particularly *Herrerasaurus* and abelisauroids such as *Ceratosaurus*, all basal saurischians with slender skulls. Additionally, the *Suchomimus* mandible performs relatively poorly despite the overall large body size and skull length. This is likely due to the narrower jaws; thus, in cross section the force per unit

area is greater. This is not unlike one of the conclusions from Cuff & Rayfield (2013), where size-scaled spinosaurs were outperformed by crocodilians in terms of torsion resistance during feeding. In my study, the greatest stress resistant theropods were the giant megalosauroids and allosauroids, including *Spinosaurus*, *Acrocanthosaurus*, and *Giganotosaurus*, i.e., the largest dinosaurs in the dataset, particularly at the cranium. Generally, cranial models experienced lower stresses than their mandibular counterparts at both actual size (Figure 4.5, 4.7) and when surface area values were equalised (Figure 4.13, 4.15); however, mandibles are geometrically-simpler structures and more susceptible to breakage than crania.

Cranial ornamentation appears to play little role in absorbing feeding stresses in taxa possessing prominent head crests and horns, including *Dilophosaurus*, *Monolophosaurus*, *Ceratosaurus*, and *Carnotaurus*. This is noticeable in both the FE heatmaps (Figure 4.2, 4.10) and the mean von Mises stress data (Figure 4.4), as the stress values are highly comparable to similarly sized theropods, such as *Allosaurus* and *Majungasaurus*. Thus, cranial features such as crests and horns may function species recognition tools or a different purpose. Xing et al. (2015) examined crest deformation in a CT-based FE model of the Chinese neotheropod *Sinosaurus* and found the crest was not suitable for sustaining high external shearing loads. However, the authors note that the crest may have served some unknown structural or mechanical purpose and the effects of shearing on soft tissues should be investigated using fluid-solid interaction approaches.

Dilophosaurus, another neotheropod distinguished for its head crest like that in *Sinosaurus*, is generally considered to have a relatively weak bite and may have been aided by its relatively large body size (Welles 1984). *Carnotaurus* and other abelisauroids are also considered to have relatively weak bite forces (Mazzetta et al. 2009; Sakamoto 2022); their feeding biomechanics were likely unaided by the presence of skull ornamentation. Snively et al.

(2011) examined the bony struts in *Majungasaurus* and compared them to extant giraffes as a means of testing intraspecific combat hypotheses. It was found that during simulated head-strike loads, *Majungasaurus* was susceptible to higher stresses than the giraffe and the intraorbital strut of *Majungasaurus* transmits compressive stress from the skull roof to the basicranium. The stress and strain of *Majungasaurus* in this chapter does not differ noticeably from other similarly-sized theropods and the bony struts do not display any hotter colours in the FE heatmaps indicating stress absorption (Figure 4.2, 4.10).

Brusatte et al. (2012) found that phylogenetic relationships were a key determinant of theropod dinosaur skull shape rather than biting function, but that the correlation could be weaker at lower taxonomic levels, which were examined in this chapter. Similarly, Lautenschlager (2022) found that elliptical and keyhole-shaped orbits are beneficial for skull function in large theropods as a means of dissipating feeding stresses; hence, skull form and large body size all appear to be linked to feeding function at lower taxonomic levels in carnivorous theropods.

Baryonyx was an outlier due to its relatively small size for a megalosauroid (Figure 4.7), as well as its skull disarticulation resulting in high stress and strain in its 3D model (Chapter 2; Rowe & Rayfield 2022). This was noted as a possible factor in *Alioramus*'s stress and strain output in chapter 3. *Herrerasaurus* was the most notable outlier in both actual size (Figure 4.5, 4.7) and muscle force scaled analyses (Figure 4.13, 4.15); small, basal, ambiguous theropods may not have possessed adequate size and skull morphology for feeding on larger herbivores, which were uncommon but not absent in the Late Triassic (Sulej & Niedźwiedzki 2019). Conversely, the presence of large sauropod dinosaurs (Gallina et al. 2014) and armoured ornithischian dinosaurs (Brown et al. 2020) in the Early Cretaceous may have necessitated large body size evolution and a stress-resistant skull in allosauroids and megalosauroids

4.6. Future work

As this study concerned large body size trends and their biomechanical effects in theropod dinosaurs, a future study may examine influence of miniaturization on feeding mechanics in theropods. Paravian theropods have seen little research into their skull biomechanics, with tyrannosauroids receiving much attention in coelurosaur function due to their relatively complete fossil record and large size. A study comparing skull mechanics between coelurosaurs and birds may reveal the influence of small body size on feeding mechanics and their implications for coelurosaur evolution.

Additionally, it is worth analysing the differing morphologies of the theropod dinosaur crania and mandibles to quantify shape variation in the clade. Previous work has investigated morphological variation in theropod dinosaur skulls (Brusatte et al. 2012; Foth & Rauhut 2013; Schaeffer et al. 2020); however, these studies used 2D morphometric analysis rather than 3D due to the difficulties in acquiring 3D data. As this is currently the largest data pool of 3D theropod dinosaur data in existence, the models are ideal candidates for a comprehensive 3D morphometrics study on theropod skull shape evolution like those carried out in Lautenschlager (2022). The models could be also refined to include air spaces and other intricate details that are not possible in 2D studies for future biomechanical analyses. Finally, this study examined feeding stresses in theropods when identical loads were applied to the teeth. In each model, loads were applied only to the front two teeth on each side of the skull. Future work may examine feeding stresses when loads are applied to the midline and back of the tooth row, and how these results may vary between theropod clades, similar to what was done in Ma et al. (2021). Additionally, other mechanical stresses may be studied using 3D models, including torsion, as was done in Cuff & Rayfield (2013).

4.7. Conclusion

Feeding function appears to be benefitted by the acquisition of large body size in theropod dinosaurs, while especially beneficial in giant megalosauroids and allosauroids such as *Spinosaurus* and *Acrocanthosaurus*. Large body size is generally linked to increased predation opportunities in ecological contexts (Cohen et al. 1993; Hone & Benton 2005) as well as a preference for large prey to efficiently fulfil caloric needs of large predators (Carbone et al. 2007). The small, basal ambiguous theropod *Herrerasaurus* performs relatively poorly compared to derived taxa. Skull shape may also play a significant role in feeding biomechanics, generally concerning skull width as demonstrated by tyrannosauroids; however, cranial ornamentation seems to have little effect on absorbing biting stresses as demonstrated by *Dilophosaurus* and other taxa. Additionally, the gigantic spinosaurs maintain a crocodile-like rostrum but are still able to absorb high feeding stresses when muscle forces are scaled to *T. rex*, likely due to their sheer size alone. While the evolution of large body size in theropod dinosaurs may not have been directly influenced by the ability to better handle high feeding stresses, it is likely a beneficial trait that aided in the success of several lineages, including the tyrannosauroids and megalosauroids.

Acknowledgments

CHAPTER 5

Conclusions

5.1. Hypotheses from chapter 2

Chapter 2 focused on how computed tomography (CT) scanned models compare in their 3D finite element results when compared to white light surface scanned models. All analyses assumed equal parameters including muscle forces and loads applied to the teeth. Three extant diapsid skulls were used in this chapter: a Nile crocodile, a monitor lizard, and a green sea turtle. The main purposes of this chapter were to set up the main materials and methods of the thesis and to elucidate how well CT and surface scanned models can be compared in large FEA studies, as the theropod dinosaur models I examined in later chapters were generated from both types of scanning procedures. Two hypotheses were tested in chapter 2.

Null hypothesis (1). 3D stress and strain magnitudes and patterns of stress for both the CT scanned models and surface scanned models will be identical when they are analysed with identical boundary conditions and material properties.

Alternative hypothesis (2). 3D stress and strain magnitudes and patterns of stress will vary between CT scanned models and surface scanned models when they are analysed with identical boundary conditions and material properties. I predict that surface scanned models experience lower stress and strain due to possessing dense internal geometries that are reconstructed in model editing software, while CT scanned models possess geometrically accurate interiors containing more hollow space.

My main expectation for this chapter was that surface scanned 3D models would output overall lower von Mises stress and strain, due to the in-filling that occurs in the surface scanning process. CT scanning preserves the internal geometry of structures, which includes empty spaces that may otherwise be filled in during surface scanning and in-filling. Therefore, surface scanned models would require higher loads to reach their failure point.

5.1.1. Chapter 2 results

Several major conclusions were found in chapter 2. Firstly, calculating the mesh-weighted arithmetic mean (MWAM) was shown to reduce the discrepancies in von Mises stresses between CT and surface scans by incorporating the element volume in the results. Element volume is downloaded from Abaqus/CAE 6.14-1 in the same manner as von Mises stress, maximum principal strain, and other types of data. The MWAM reduced stress discrepancies between all models except for the Nile crocodile skull, possibly due to the complexities of the models.

Another conclusion was that extensive model editing leads to unnaturally high stresses and strain in 3D structures. This was demonstrated by the Nile crocodile and monitor lizard mandibles, as both mandibles were missing a ramus, partially in the Nile crocodile. This required 3D editing procedures to be applied, namely duplicating the existing mandibular ramus, mirroring it, and reattaching it to complete the mandible. The highest stresses and strains in the analyses were all experienced by the Nile crocodile and monitor lizard mandibles, likely due to the editing procedures applied. Similar results occur in later chapters with the *Alioramus* and *Baryonyx* 3D models.

Similarly, geometrically-simple 3D model tend to output nearly identical results when comparing CT and surface scan derived data, even without calculating the MWAM. This was most evident in my green sea turtle mandible results, as the stress values were the closest in each dataset. The MWAM still aided in reducing discrepancies in these results, even when the range between model stresses and strains was minimal.

5.2. Hypotheses from chapter 3

Chapter 3 concerned the evolution of large body size and feeding biomechanics in tyrannosauroid dinosaurs. The clade is one of the most well-understood in the Theropoda, due to its relatively well-resolved fossil record containing several nearly complete individuals

(Brusatte & Carr 2016), enabling comparative studies into their functional morphology. Two hypotheses were formulated and tested in this chapter, which largely related to the hypotheses from Rowe & Snively 2021.

Hypothesis (1). Larger tyrannosaurid taxa such as *Tyrannosaurus rex* and *Daspletosaurus torosus* experience higher absolute stresses due to their large size and increased muscle mass. Despite this, they were able to accommodate high forces because the mandible was so much larger and could adequately absorb high stresses with minimal chance of breakage. This was one of the conclusions noted in Rowe & Snively 2021, though the total specimen pool was smaller, and it pertained only to the mandibles.

Hypothesis (2). When surface area values for cranial and mandibular models are equalized, the smaller-bodied tyrannosaur specimens (*Raptorex kriegsteini*, *Alioramus altai*, and *Albertosaurus sarcophagus*) experience higher stress relative to the larger-bodied taxa (*Tyrannosaurus rex, Daspletosaurus torosus*, and *Bistahieversor sealeyi*) due to the more robust cranial osteology characterized in the allometry of tyrannosaurs.

My main expectations for this chapter were that the largest tyrannosauroids would experience the highest von Mises stresses, and that this trend would be linear with regard to body size. Additionally, when surface area values were equalized, I expected a linear trend of smaller tyrannosauroids experiencing the highest stresses with gradual decreases occurring in larger individuals. These expectations were mostly derived from the results of Rowe & Snively 2021. Calculating the mesh-weighted arithmetic mean (MWAM) would aid in decreasing possible discrepancies in von Mises stress results between CT scanned models and surface scanned.

5.2.1. Chapter 3 results

At actual size, large tyrannosauroids generally experience higher stresses than smaller taxa, though it was not a linear trend. The middle-sized tyrannosauroids, *Daspletosaurus torosus*, and *Bistahieversor sealeyi*, experienced higher absolute stresses than *Tyrannosaurus rex*. Additionally, *Alioramus altai*, the second smallest individual in the dataset, experienced the highest stresses at the cranium, though the mandible stresses were the lowest of all.

When surface area values were scaled to adult *Tyrannosaurus rex* FMNH PR 2081, the stress results were more linear as expected, with skull stresses decreasing as individual body sizes increased. The *Alioramus altai* cranium and *Albertosaurus sarcophagus* skull were the only outliers, with the *Alioramus* cranium experiencing higher stresses than the smaller *Raptorex kriegsteini* cranium, and both the *Albertosaurus* cranium and mandible experiencing the lowest stresses of the dataset. The MWAM was applied to every calculation for both actual size and surface area scaled model analyses.

5.2.2. Chapter 3 discussion

My tyrannosauroid skull data generally supported my expectations for the chapter. At increasing body size, large tyrannosauroids skulls would have experienced relatively high stresses during feeding, due to their widely-set mandibles and the muscle attachments necessary for delivering a powerful bite. Large tyrannosauroids possessed strongly constructed skulls but also experience higher stresses than smaller taxa at actual size and are thus accommodating more force per unit area. This may represent a trade-off where the expanded tyrannosauroid posterior skull and increased adductor muscle mass generates high bite forces, which results in the need to accommodate greater stresses in the skull during feeding.

Tyrannosaurus rex in particular has been noted for its rigid, akinetic skull (Cost et al. 2019), fused nasals (Snively et al. 2006), and muscle architecture (Bates & Falkingham 2018). These

mechanical factors enable the animal to transmit nearly all feeding forces directly to prey while adequately absorbing stresses in the skull during feeding with minimal risk of failure. This may have been a requirement for the hypercarnivorous diet of the animal, given its shared habitat with *Triceratops* (Nabavizadeh 2023) and *Edmontosaurus* (Wosik & Evans 2022). Large tyrannosaurids in general are noted for their heterodonty (Reichel 2010), general jaw strengthening possibly through ontogeny due to bone functional adaptation (Ma et al. 2021; Rowe & Snively 2021), and a keyhole-shaped orbit (Lautenschlager 2022). The higher outliers of the actual size results, *Daspletosaurus* and *Bistahieversor*, may have experienced higher stresses than *Tyrannosaurus* for two main reasons. The first explanation is that the high degree of reconstruction applied to the *Daspletosaurus* and *Bistahieversor* 3D models caused higher-than-normal von Mises stresses during the feeding simulations. This was one of the main conclusions from chapter 2 and Rowe & Rayfield 2022, where it was found that 3D models requiring significant reconstructive work, including the *Crocodylus* and *Varanus* mandibles, will output high stress and strain relative to the less-edited models. Both middle-sized tyrannosauroids were subjected to duplication, mirroring, and attachment procedures to produce complete 3D models free of deformation, which may have influenced the final FE results.

The other explanation concerns the ecology of middle-sized tyrannosauroids when compared to *T. rex*. While *T. rex* is often noted for its bone-crunching bite which could subdue large herbivorous dinosaurs (Gignac & Erickson 2017), the functional morphology and ecology of middle-sized tyrannosaurids is lesser known. Hence, scavenging behaviour remains a possibility, as middle-sized tyrannosauroid taxa may have lacked the biomechanical efficiency of the larger *T. rex*. Additionally, the herbivorous dinosaurs they may have fed on, including the ceratopsian *Pentaceratops sternbergii*, did not approach the size of those taxa

fed on by *T. rex* (Lucas et al. 2006); thus, a highly stress-resistant bite may not have been as necessary as the one delivered by *T. rex.*

Finally, *Alioramus* exhibited unusually high stresses and strain in most plots, which is likely due to the high degrees of reconstruction. This was one of the major findings of chapter 2 and Rowe & Rayfield (2022) where the *Crocodylus* and *Varanus* mandibles exhibited unusually high stresses which may be due to extensive reconstructions. The middle-sized tyrannosauroids may have been similarly affected by reconstructions and may require further study to assess the degree that 3D recontructions influence FE data.

5.3. Hypotheses from chapter 4

Chapter 4 mainly pertained to the large, non-tyrannosauroid theropod dinosaur clades and their functional morphology using 3D models and FEA. Previous work has assessed the skull mechanics of various large theropod dinosaurs in a comparative context; however, these studies used 2D models rather than 3D models, and did not address questions of large body size acquisition in relation to biomechanics (Rayfield 2011). Given the availability of surface scanning techniques and software, I was able to create accurate 3D models of a phylogenetically disparate range of theropod dinosaur skulls for FE testing. My hypotheses for this chapter draw upon the conclusions from chapter 3 and Rowe & Snively 2021.

Hypothesis (1). Large-bodied non-tyrannosauroid theropod dinosaur taxa including *Giganotosaurus* and *Suchomimus* experience higher absolute stresses and strain in their crania and mandibles under simulated feeding loads due to their large skull size and the increased muscle mass present in giant skulls. They were thus able to accommodate high feeding forces due to their large body size.

Hypothesis (2). When muscle force components for skull models are scaled to the same surface area as adult *Tyrannosaurus rex* FMNH PR 2081 to account for body and skull size

159

differences, smaller-bodied theropod dinosaurs such as the abelisaurs experience higher stress and strain relative to the larger-bodied taxa, e.g., megalosauroids and allosauroids due to the evolution of overall larger skulls in larger-bodied clades.

My main expectations for this chapter were similar to my anticipated results from chapter 3. At actual size, I assumed that larger theropod dinosaur taxa would experience higher von Mises skull stresses than the smaller taxa, namely the abelisauroids. Additionally, it was presumed that when surface area values were scaled to the senescent *T. rex* FMNH PR 2081, smaller taxa would experience higher stresses with a gradual shift to lower stresses in larger individuals.

5.3.1. Chapter 4 results

My non-tyrannosauroid theropod skull data did not exhibit trends comparable to the tyrannosauroids at actual size. The largest animals in the dataset, including the *Spinosaurus aegyptiacus, Giganotosaurus carolinii,* and *Acrocanthosaurus atokensis* experienced the lowest feeding stresses, while the smaller tetanuran theropods and abelisauroids generally clustered when skull lengths were plotted against skull stresses. *Herrerasaurus ischigualastensis* was included despite its ambiguous status as a true theropod dinosaur; it experienced the highest stress and strain of the dataset by a wide margin.

Surface area scaled results for the theropods displayed a trend of decreasing stresses with the acquisition of large body size, similar to the tyrannosauroids. Smaller theropods such as *Ceratosaurus* and *Majungasaurus* exhibited the highest overall skull stresses, while the largest theropods, *Giganotosaurus, Acrocanthosaurus,* and *Spinosaurus* exhibited the lowest FE values. Like in the actual size analyses, *Herrerasaurus* was an outlier in terms of stress and strain, generating values notably greater than every other individual. Abelisauroids and smaller tetanuran theropods experienced clustering when skull lengths and stresses were

plotted against each other, particularly in the cranium, while the mandible results showed more variability.

5.3.2. Chapter 4 discussion

Given my results in this chapter, my first hypothesis was generally not supported by my data. Larger theropod taxa experienced lower skull stresses, which was not anticipated given the results of the tyrannosauroid study. This may be due to several reasons, chiefly concerning the biomechanical and physiological feeding capabilities allowed by the skulls of giant tyrannosauroids which were lacked by non-tyrannosauroid theropods. As *Tyrannosaurus rex* was characterised by its osteophagy during feeding, it required a large, widely-set skull capable of withstanding high stresses from its large adductor muscles when biting into large prey. Despite their body size, other large non-tyrannosauroid theropods likely did not exhibit bone-pulverizing strategies when feeding, owing to their relatively slender skull morphologies relative to *T. rex* (Figure 5.1).

Figure 5.1. Comparison of a mature *Tyrannosaurus rex* skull and a mature *Torvosaurus gurneyi* skull to illustrate differences in skull morphology between the genera, particularly

regarding mandible width. Left to right: senescent *Tyrannosaurus rex* (FMNH PR 2081) (Field Museum of Natural History, IL, Chicago, USA); adult *Torvosaurus gurneyi* (BYUVP; various specimen numbers) (Dinosaur Discovery Museum, WI, Kenosha, USA). Photos by A. Rowe.

My linear regression tests found generally relationships between skull lengths and von Mises stresses in the non-theropod 3D models, with the exception of the actual size mandibles, which demonstrated a moderately significant relationship via P-value of 0.03268. This may be due to the skulls of various theropod lineages being equipped for different types of biting mechanics. As the tyrannosauroid bite was optimised for a stiff, crushing bite (Cost et al. 2019), allosauroid skulls were better equipped for delivering slashing motions when feeding, aided by a wider gape when opening its mouth (Rayfield et al. 2001; Lautenschlager 2015). Thus, the skulls of smaller, non-tyrannosauroid theropods may not have required such a stress-resistant skull when procuring food, as their feeding strategies differed from *Tyrannosaurus*. Similarly, certain megalosauroid taxa such as *Spinosaurus* are commonly hypothesized to have been piscivorous (Hone & Holtz 2021); shoreline feeding likely would not have required a strong bite, though megalosauroids did not exclusively prey on marine animals (Charig & Milner 1986; Buffetaut et al. 2004). Theropod clades in general are optimised for stress-resistance regardless of size or feeding strategy; this was demonstrated by the appearance of keyhole-shaped orbits throughout the group (Lautenschlager 2022). Additionally, Ma et al. (2021) observed a general trend of jaw strengthening in all theropod lineages regardless of diet and occurring in ontogenetic series of tyrannosaurids.

Another observation was made when analysing skull mechanics in theropod dinosaurs possessing cranial ornamentation, such as crests and horns. The skull stresses of these dinosaurs were not noticeably influenced by the presence of such ornamentation, supporting hypotheses that these structures existed for purposes of species recognition or other non-

mechanically related function, such as in *Dilophosaurus wetherilli* (Marsh & Rowe 2020).

The same may hold true for the horns of *Carnotaurus sastrei* (Cerroni et al. 2020). Snively et al. (2011) noted that *Majungasaurus*'s bony struts were not as well equipped for stress absorption as extant giraffes, and Xing et al. (2015) found that *Sinosauurs* was not able to adequately deal with shearing stresses acting on its head crest. In general, cranial ornamentation seems to play little role in absorbing feeding stresses in theropod dinosaurs, though future work may use fluid-solid techniques to better assess soft tissues and their potential role.

5.4. Conclusion

This thesis examined the feeding biomechanics of large theropod dinosaurs in relation to body and skull size. This was achieved via a combination of 3D imaging techniques and the finite element method to better understand if biomechanical trends, e.g., stress and strain patterns exist by examining skull stresses during hypothetical feeding scenarios when identical loads are applied to the teeth of large carnivorous dinosaurs. I also investigated different types of 3D models in FEA, and the influence of calculating the mesh-weighted arithmetic mean (MWAM) when comparing stress data from different model types, as my computational dinosaur skull models are derived from different scanning methods.

The major conclusions from my analyses of the tyrannosauroid skulls were that stresses generally increased with the acquisition of large size, as the animals were capable of absorbing high stresses when crushing herbivorous dinosaur skeletons. This is due to their widely-set skulls, which are absent in the non-tyrannosauroid theropods. These results were supportive of my hypotheses concerning the clade, as increasing skull stresses with large body size is noted in the ontogeny of tyrannosaurids (Rowe & Snively 2021). Other theropod lineages generally do not experience higher stresses with large body size, likely as they

would not be able to adequately absorb the high stresses that were tolerated by *T. rex*. This result did not support my first hypothesis of chapter 4, as other theropod dinosaurs do not experience the same skull stress trends as those in tyrannosauroids. These results seem to indicate that the evolution of large body size in different theropod dinosaur lineages may have occurred to suit a variety of feeding and hunting behaviours; tyrannosauroids were crushing down on large prey as risk of breakage was minimal, while abelisauroids and other theropod clades pursued smaller prey, as their lower bite forces and less-stress resistant skulls did not enable feeding on the giant dinosaurs of the Late Cretaceous.

5.5. Wider context

Previous work examining large body size in theropod dinosaurs and its influence on biomechanics have pertained mostly to locomotion rather than feeding (Alexander 1991, 2006), due to limited availability in 3D scanning equipment and software. The major conclusions from locomotory studies of large theropods have revealed that body size exerts an influence on the degree of postural crouch, as well as the relationship between speed and kinematic parameters (Bishop et al. 2018). Giant theropods such as *T. rex* were likely uncapable of achieving fast speeds, as it would require unrealistically large mass of extensor muscle (Hutchinson & Garcia 2002), though they could pivot their bodies with relative ease (Snively et al. 2019). Given the conclusions from this thesis concerning the skull stresses of large tyrannosauroids and their relative durability compared to other theropod lineages, I may infer that large tyrannosauroids relied primarily on ambush predation to subdue herbivorous dinosaurs, as evidence for predation behaviour in tyrannosaurids exists (Happ 2008; DePalma et al. 2013) and the animals were not likely capable of chasing prey over long distances.

Previous work has demonstrated that allosauroids, including *Allosaurus*, used a slashing bite to rip flesh off prey and the animal possessed a relatively weak bite relative to other large

theropod taxa (Rayfield et al. 2001). This was seemingly reaffirmed by my results, as the non-tyrannosauroid theropods experiences relatively lower skull stresses, as they could not likely absorb high stresses without a significant risk of breakage in contrast to large tyrannosauroids. An explanation for this phenomenon may be linked to the ecology of carnivorous dinosaurs; tyrannosauroids were more inclined to predation and bone-consuming behaviours (Gignac & Erickson 2017), while other large theropod taxa relied more on scavenging and consumed fewer bones. Additionally, large tyrannosaurids such as *T. rex* co-existed with some of the largest herbivores of the Cretaceous, possibly necessitating large body size acquisition as a means of feeding efficiently (chapter 3).

Megalosauroids are less clear in their body size function and skull stresses, as their feeding behaviours and ecology may have differed notably from other theropod taxa, given their possibly semi-aquatic habitats (Ibrahim et al. 2020; Hone & Holtz 2021). One possible advantage of large body size in the clade is to deter potential predators and competitors (Preisser & Orrock 2012), as their long rostrum was not as equipped for agonistic encounters as the mandible of a typical large tyrannosauroid. Large body size has been demonstrated to be relevant in the feeding biomechanics of spinosaurs, as it enabled the animals to experience less torsion when feeding by virtue of large size alone (Cuff & Rayfield 2013). A combination of these attributes may have contributed to the evolution of large sizes and overall less-powerful skulls in the clade, though many taxa are still poorly understood and require more specimens, particularly *Spinosaurus*.

5.6. Future work

Several major courses of study can be pursued based on the conclusion from this thesis. Perhaps the most immediate concerns the accuracy of the FE theropod skull models I used. CT-derived models were generally the most geometrically accurate of all models, due to CT

imaging capturing internal details of the dinosaur skulls. One of the main caveats of surface scanning is the inability to capture interior details of objects, as well as miniscule textures which may influence FE results. Thus, model editing in software including Blender 2.82 and Avizo Lite 9.5 could incorporate air spaces and other anatomical details that may be absent in the surface scanned models.

Skull sutures may be of interest in dinosaur FE models as they modulate how stresses and strain and transmitted between bones; previous work has evaluated sutures in carnivorous dinosaurs using FEA (Rayfield 2005). As suture studies in FEA have been limited, the 3D models used in this thesis may prove valuable for future work quantifying and evaluating their function in different dinosaur taxa.

Additionally, muscle force components could be refined for accuracy in non-tyrannosauroid dinosaur taxa. Muscle force values for this thesis were derived from Gignac & Erickson 2017, Cost et al. 2019, and Rowe & Snively 2021; all studies chiefly concerned *Tyrannosaurus rex*, with scaling applied to calculate values for the smaller tyrannosaurid *Raptorex kriegsteini* in the case of Rowe & Snively 2021. Similar methodology was used to calculate muscle forces for other tyrannosauroids (chapter 3) and theropod dinosaurs (chapter 4). However, in many non-tyrannosauroid theropod taxa, skull morphologies deviate noticeably from the widely-set skull present in large tyrannosauroids. Thus, an in-depth muscle study using large-bodied megalosauroids and allosauroids could yield more accurate data to represent each lineage, which could then be scaled to smaller-bodied taxa.

Finally, the relationship between body size and feeding biomechanics can still be investigated in other non-avian dinosaur clades. Sauropod dinosaurs such as *Apatosaurus* and *Diplodocus* are noted as the largest terrestrial animals in the fossil record; FEA and muscle reconstruction studies have focused on members of the clade (Button et al. 2014; Button et al. 2016;

Lautenschlager et al. 2016). However, sauropod feeding studies have not yet addressed questions of feeding biomechanics in relation to body size trends as this thesis did concerning theropod dinosaurs. This may prove more difficult to assess in sauropods, given the overall smaller sample size of complete skulls compared to theropods.

This appendix contains the Supplementary Material of Chapter 2, 3, and ,
including supplementary tables.

Table A1. Muscle force values used in chapter 2 and Rowe & Rayfield 2022. *Crocodylus* values are from Porro et al. 2011, *Varanus* values are from Dutel et al. 2021, and *Chelonia* values are from Ferreira et al. 2020.

Crocodylus	mames	mamem	mamep	mamp	mpsts	mpstp	mptd	mptv
	13.3	13.3	10.36	125.59	11.61	11.61	291.17	124.03
Varanus	mames	mamem	mamep	mamp	mpt	mpsts	mpstp	
	84.9	116.04	88.76	3.84	193.9	24.43	22.42	
Chelonia	mptd	mptv	maem	maes	map	mprp	mptp	mpst
	10	0	252	167	45	15	40	20

Table A2. Muscle forces used in actual size tyrannosauroid 3D models in chapter 3.

FMNH RP 2081	mames	mamem	mamep	mamp	mps	mptd	mptv
Left mandible/cranium half							
x	12963.79	4871.557	12212.41	10211.07	10152.18	2640.76	40916.35
y	-603.857	-127.531	481.8402	696.2445	3030.572	374.4074	14928.05
z	4145.241	1284.736	2530.278	2578.988	3139.306	2735.851	-15531.1
Right mandible/cranium half							
x	-12963.8	-4871.56	-12212.4	-10211.1	-10152.2	-2640.76	-40916.3
y	-603.857	-127.531	481.8402	696.2445	3030.572	374.4074	14928.05
z	4145.241	1284.736	2530.278	2578.988	3139.306	2735.851	-15531.1
MOR 555	mames	mamem	mamep	mamp	mps	mptd	mptv
Left mandible ramus/cranium half							
x	13359.32	5020.188	12585.01	10522.61	10461.92	2721.321	42164.71
y	-622.281	-131.422	496.541	717.487	3123.035	385.83	15383.51
z	4271.712	1323.933	2607.476	2657.673	3234.83	2819.212	-16002
Right mandible ramus/cranium half							
x	-13359.3	-5020.19	-12585	-10522.6	-10461.9	-2721.32	-42164.7
y	-622.281	-131.422	496.541	717.487	3123.035	385.83	15383.51
z	4271.712	1323.933	2607.476	2657.673	3234.83	2819.212	-16002
NMMNH P-27469	mames	mamem	mamep	mamp	mps	mptd	mptv
Left mandible ramus/cranium half							
x	11319.99	4253.844	10663.88	8916.31	8864.89	2305.912	35728.16
y	-527.288	-111.361	420.743	607.961	2646.296	326.933	13035.16
z	3619.621	1121.831	2209.436	2251.97	2741.238	2388.943	-13561.7
Right mandible ramus/cranium half							
x	-11320	-4253.84	-10663.9	-8916.31	-8864.89	-2305.91	-35728.2
y	-527.288	-111.361	420.743	607.961	2646.296	326.933	13035.16

	mames	mamem	mamep	mamp	mps	mptd	mptv
z	3619.621	1121.831	2209.436	2251.97	2741.238	2388.943	-13561.7
FMNH PR308	mames	mamem	mamep	mamp	mps	mptd	mptv
Left mandible ramus/cranium half							
x	12560.84	4720.138	11832.82	9893.685	9836.626	2558.679	39644.57
y	-585.088	-123.567	466.864	285.4603	2936.378	362.769	14464.05
z	4016.397	1244.803	2451.629	2498.827	3041.728	2650.814	-15048.4
Right mandible ramus/cranium half							
x	-12560.8	-4720.14	-11832.8	-9893.69	-9836.63	-2558.68	-39644.6
y	-585.088	-123.567	466.864	674.604	2936.378	362.769	14464.05
z	4016.397	1244.803	2451.629	2498.827	3041.728	2650.814	-15048.4
TMP 1981.010.0001	mames	mamem	mamep	mamp	mps	mptd	mptv
Left mandible ramus/cranium half							
x	9982.12	3751.1	9403.56	7862.52	7817.18	2033.385	31505.6
y	-464.97	-98.199	371.017	536.108	2333.54	288.294	11494.6
z	3191.836	989.247	1948.314	1985.82	2417.265	2106.605	-11958.9
Right mandible ramus/cranium half							
x	-9982.12	-3751.1	-9403.56	-7862.52	-7817.18	-2033.39	-31505.6
y	-464.97	-98.199	371.017	536.108	2333.54	288.294	11494.6
z	3191.836	989.247	1948.314	1985.82	2417.265	2106.605	-11958.9
IGM 100/1844	mames	mamem	mamep	mamp	mps	mptd	mptv
Left mandible ramus/cranium half							
x	5315.158	1997.338	5007.09	4186.539	4162.394	1082.712	16775.7
y	-247.581	-52.2877	197.5545	440.854	1242.534	153.507	6120.502
z	1699.549	526.7418	1037.414	1057.385	1287.115	1121.699	-6367.75
Right mandible ramus/cranium half							
x	-5315.16	-1997.34	-5007.09	-4186.54	-4162.39	-1082.71	-16775.7
y	-247.581	-52.2877	197.5545	440.854	1242.534	153.507	6120.502
z	1699.549	526.7418	1037.414	1057.385	1287.115	1121.699	-6367.75
LH PV18	mames	mamem	mamep	mamp	mps	mptd	mptv
Left mandible ramus/cranium half							
x	-0.208572	0.040019616	-0.091877513	-0.070300493	-0.18226041	-0.160395833	-1.3800389
y	0.987615723	0.256309788	1.108385598	0.516281507	1.31793108	0.195079551	2.5516119
z	0.023800652	-0.002534276	0.075321932	0.041798346	-0.33682559	0.041498436	0.8398233
Right mandible ramus/cranium half							
x	0.183804075	0.041661446	0.090333353	0.070300493	0.198109141	0.164616776	-1.3714672
y	0.870336356	0.266825062	1.089757269	0.516281507	1.432533783	0.200213224	2.5357634
z	0.020974325	-0.002638246	-0.074056017	0.041798346	-0.366114772	0.0425905	0.8346070

Table A3. Muscle forces used in scaled tyrannosauroid 3D models in chapter 3.

FMNH PR 2081	mames	mamem	mamep	mamp	mps	mptd	mptv

Left mandible/cranium half							
x	12963.79	4871.557	12212.41	10211.07	10152.18	2640.76	40916.35
y	-603.857	-127.531	481.8402	696.2445	3030.572	374.4074	14928.05
z	4145.241	1284.736	2530.278	2578.988	3139.306	2735.851	-15531.1
Right mandible/cranium half							
x	-12963.8	-4871.56	-12212.4	-10211.1	-10152.2	-2640.76	-40916.3
y	-603.857	-127.531	481.8402	696.2445	3030.572	374.4074	14928.05
z	4145.241	1284.736	2530.278	2578.988	3139.306	2735.851	-15531.1
MOR 555	mames	mamem	mamep	mamp	mps	mptd	mptv
Left mandible ramus/cranium half							
x	13359.32	5020.188	12585.01	10522.61	10461.92	2721.321	42164.71
y	-622.281	-131.422	496.541	717.487	3123.035	385.83	15383.51
z	4271.712	1323.933	2607.476	2657.673	3234.83	2819.212	-16002
Right mandible ramus/cranium half							
x	-13359.3	-5020.19	-12585	-10522.6	-10461.9	-2721.32	-42164.7
y	-622.281	-131.422	496.541	717.487	3123.035	385.83	15383.51
z	4271.712	1323.933	2607.476	2657.673	3234.83	2819.212	-16002
NMMNH P-27469	mames	mamem	mamep	mamp	mps	mptd	mptv
Left mandible ramus/cranium half							
x	29205.57	10974.92	27512.81	23004.08	22871.42	5949.253	92178.65
y	-1360.4	-287.311	1085.517	1568.539	6827.444	843.4871	33630.71
z	9338.622	2894.324	5700.345	5810.083	7072.394	6163.473	-34989.3
Right mandible ramus/cranium half							
x	-29205.6	-10974.9	-27512.8	-23004.1	-22871.4	-5949.25	-92178.7
y	-1360.4	-287.311	1085.517	1568.539	6827.444	843.4871	33630.71
z	9338.622	2894.324	5700.345	5810.083	7072.394	6163.473	-34989.3
FMNH PR308	mames	mamem	mamep	mamp	mps	mptd	mptv
Left mandible ramus/cranium half							
x	37933.75	14254.82	35735.12	29878.93	29706.61	7727.211	119726.6
y	-1766.97	-373.172	1409.929	862.09	8867.862	1095.562	43681.43
z	12129.52	3759.305	7403.92	7546.458	9186.019	8005.458	-45446.1
Right mandible ramus/cranium half							
x	-37933.7	-14254.8	-35735.1	-29878.9	-29706.6	-7727.21	-119727
y	-1766.97	-373.172	1409.929	2037.304	8867.862	1095.562	43681.43
z	12129.52	3759.305	7403.92	7546.458	9186.019	8005.458	-45446.1
TMP 1981.010.0001	mames	mamem	mamep	mamp	mps	mptd	mptv
Left mandible ramus/cranium half							
x	33240.46	12491.16	31313.85	26182.19	26031.21	6771.172	104913.6
y	-1548.35	-327.003	1235.487	1785.24	7770.688	960.019	38277.02
z	10628.81	3294.193	6487.886	6612.781	8049.492	7014.995	-39823.3
Right mandible ramus/cranium half							
x	-33240.5	-12491.2	-31313.9	-26182.2	-26031.2	-6771.17	-104914
y	-1548.35	-327.003	1235.487	1785.24	7770.688	960.019	38277.02

z	10628.81	3294.193	6487.886	6612.781	8049.492	7014.995	-39823.3
IGM 100/1844	mames	mamem	mamep	mamp	mps	mptd	mptv
Left mandible ramus/cranium half							
x	9586.267	3602.343	9030.644	7550.722	7507.174	1952.748	30256.18
y	-446.53	-94.3046	356.3036	795.1117	2240.999	276.8609	11038.76
z	3065.258	950.0165	1871.05	1907.07	2321.405	2023.064	-11484.7
Right mandible ramus/cranium half							
x	-9586.27	-3602.34	-9030.64	-7550.72	-7507.17	-1952.75	-30256.2
y	-446.53	-94.3046	356.3036	795.1117	2240.999	276.8609	11038.76
z	3065.258	950.0165	1871.05	1907.07	2321.405	2023.064	-11484.7
LH PV18	mames	mamem	mamep	mamp	mps	mptd	mptv
Left mandible ramus/cranium half							
x	-8.05714	1.545958	-3.54923	-2.71571	-7.04072	-6.19609	-53.3109
y	38.1516	9.901247	42.81694	19.94395	50.91168	7.535923	98.56877
z	0.919419	-0.0979	2.909686	1.61467	-13.0116	1.603085	32.44238
Right mandible ramus/cranium half							
x	7.100351	1.609382	3.489577	2.715708	7.652956	6.359146	-52.9798
y	33.62109	10.30745	42.09732	19.94395	55.33878	7.734237	97.95654
z	0.810238	-0.10192	-2.86078	1.61467	-14.143	1.645271	32.24087

Table A4. Muscle forces used in actual size non-tyrannosauroid theropod dinosaur 3D models in chapter 4.

Spinosaurus	mames	mamem	mamep	mamp	mps	mptd	mptv
Left mandible ramus/cranium half							
x	9216.519	3463.401	8682.333	7259.486	7217.624	1877.43	29089.21
y	-429.308	-90.6674	342.561	494.99	2154.564	266.1826	10613
z	2947.031	913.3745	1798.884	1833.513	2231.867	1945.034	-11041.7
Right mandible ramus/cranium half							
x	-9216.52	-3463.4	-8682.33	-7259.49	-7217.62	-1877.43	-29089.2
y	-429.308	-90.6674	342.561	494.99	2154.564	266.1826	10613
z	2947.031	913.3745	1798.884	1833.513	2231.867	1945.034	-11041.7
Giganotosaurus	mames	mamem	mamep	mamp	mps	mptd	mptv
Left mandible ramus/cranium half							
x	17812.13	6693.477	16779.75	14029.91	13949	3628.38	56218.71
y	-829.694	-175.227	662.0441	956.6331	4163.977	514.4329	20511.01
z	5695.524	1765.216	3476.579	3543.504	4313.377	3759.034	-21339.6
Right mandible ramus/cranium half							
x	-17812.1	-6693.48	-16779.7	-14029.9	-13949	-3628.38	-56218.7
y	-829.694	-175.227	662.0441	956.6331	4163.977	514.4329	20511.01
z	5695.524	1765.216	3476.579	3543.504	4313.377	3759.034	-21339.6
Suchomimus	mames	mamem	mamep	mamp	mps	mptd	mptv
Left mandible ramus/cranium half							

x	7154.616	2688.575	6739.937	5635.407	5602.91	1457.415	22581.42
y	-333.264	-70.3835	265.9239	384.2517	1672.549	206.6327	8238.675
z	2287.726	709.036	1396.441	1423.323	1732.558	1509.895	-8571.49
Right mandible ramus/cranium half							
x	-7154.62	-2688.58	-6739.94	-5635.41	-5602.91	-1457.41	-22581.4
y	-333.264	-70.3835	265.9239	384.2517	1672.549	206.6327	8238.675
z	2287.726	709.036	1396.441	1423.323	1732.558	1509.895	-8571.49
Acrocanthosaurus	mames	mamem	mamep	mamp	mps	mptd	mptv
Left mandible ramus/cranium half							
x	16438.45	6177.27	15485.68	12947.91	12873.25	3348.556	51883.08
y	-765.707	-161.713	610.9867	882.8568	3842.848	474.7594	18929.18
z	5256.28	1629.081	3208.462	3270.227	3980.725	3469.134	-19693.9
Right mandible ramus/cranium half							
x	-16438.4	-6177.27	-15485.7	-12947.9	-12873.2	-3348.56	-51883.1
y	-765.707	-161.713	610.9867	882.8568	3842.848	474.7594	18929.18
z	5256.28	1629.081	3208.462	3270.227	3980.725	3469.134	-19693.9
Torvosaurus	mames	mamem	mamep	mamp	mps	mptd	mptv
Left mandible ramus/cranium half							
x	13553.7	5093.237	12768.14	10675.72	10614.15	2760.926	42778.25
y	-631.335	-133.334	503.7662	727.9265	3168.476	391.4451	15607.35
z	4333.869	1343.198	2645.417	2696.343	3282.158	2860.344	-16237.8
Right mandible ramus/cranium half							
x	-13553.7	-5093.24	-12768.1	-10675.7	-10614.2	-2760.93	-42778.2
y	-631.335	-133.334	503.7662	727.9265	3168.476	391.4451	15607.35
z	4333.869	1343.198	2645.417	2696.343	3282.158	2860.344	-16237.8
Baryonyx	mames	mamem	mamep	mamp	mps	mptd	mptv
Left mandible ramus/cranium half							
x	4991.06	1875.55	4701.78	3931.26	3908.59	1016.693	15752.8
y	-232.485	-49.0995	185.5085	268.054	1166.77	144.147	5747.3
z	1595.918	494.6235	974.157	992.91	1208.633	1053.303	-5979.47
Right mandible ramus/cranium half							
x	-4991.06	-1875.55	-4701.78	-3931.26	-3908.59	-1016.69	-15752.8
y	-232.485	-49.0995	185.5085	268.054	1166.77	144.147	5747.3
z	1595.918	494.6235	974.157	992.91	1208.633	1053.303	-5979.47
Monolophosaurus	mames	mamem	mamep	mamp	mps	mptd	mptv
Left mandible ramus/cranium half							
x	7967.38	2993.997	7505.594	6275.589	6239.401	1622.977	25146.67
y	-371.123	-78.379	296.1328	427.9027	1862.55	230.1062	9174.589
z	2547.612	789.5825	1555.076	1585.012	1929.377	1681.419	-9545.21
Right mandible ramus/cranium half							
x	-7967.38	-2994	-7505.59	-6275.59	-6239.4	-1622.98	-25146.7
y	-371.123	-78.379	296.1328	427.9027	1862.55	230.1062	9174.589
z	2547.612	789.5825	1555.076	1585.012	1929.377	1681.419	-9545.21

Allosaurus	mames	mamem	mamep	mamp	mps	mptd	mptv
Left mandible ramus/cranium half							
x	6227.378	2340.136	5866.441	4905.058	4876.773	1268.534	19654.87
y	-290.073	-61.2618	231.4601	334.4527	1455.786	179.8531	7170.943
z	1991.237	617.1449	1215.462	1238.86	1508.019	1314.212	-7460.62
Right mandible ramus/cranium half							
x	-6227.38	-2340.14	-5866.44	-4905.06	-4876.77	-1268.53	-19654.9
y	-290.073	-61.2618	231.4601	334.4527	1455.786	179.8531	7170.943
z	1991.237	617.1449	1215.462	1238.86	1508.019	1314.212	-7460.62
Neovenator	mames	mamem	mamep	mamp	mps	mptd	mptv
Left mandible ramus/cranium half							
x	6364.746	2391.756	5995.848	5013.258	4984.349	1296.516	20088.43
y	-296.472	-62.6131	236.5659	341.8303	1487.899	183.8205	7329.126
z	2035.161	630.7584	1242.274	1266.188	1541.284	1343.202	-7625.2
Right mandible ramus/cranium half							
x	-6364.75	-2391.76	-5995.85	-5013.26	-4984.35	-1296.52	-20088.4
y	-296.472	-62.6131	236.5659	341.8303	1487.899	183.8205	7329.126
z	2035.161	630.7584	1242.274	1266.188	1541.284	1343.202	-7625.2
Majungasaurus	mames	mamem	mamep	mamp	mps	mptd	mptv
Left mandible ramus/cranium half							
x	5586.324	2099.239	5262.543	4400.126	4374.752	1137.949	17631.57
y	-260.213	-54.9554	207.6334	300.0237	1305.926	161.3388	6432.758
z	1786.257	553.6153	1090.341	1111.33	1352.781	1178.926	-6692.62
Right mandible ramus/cranium half							
x	-5586.32	-2099.24	-5262.54	-4400.13	-4374.75	-1137.95	-17631.6
y	-260.213	-54.9554	207.6334	300.0237	1305.926	161.3388	6432.758
z	1786.257	553.6153	1090.341	1111.33	1352.781	1178.926	-6692.62
Carnotaurus	mames	mamem	mamep	mamp	mps	mptd	mptv
Left mandible ramus/cranium half							
x	8379.486	3148.859	7893.814	6600.189	6562.128	1706.924	26447.36
y	-390.319	-82.4331	311.4501	450.0356	1958.889	242.0083	9649.137
z	2679.385	830.4229	1635.511	1666.996	2029.172	1768.389	-10038.9
Right mandible ramus/cranium half							
x	-8379.49	-3148.86	-7893.81	-6600.19	-6562.13	-1706.92	-26447.4
y	-390.319	-82.4331	311.4501	450.0356	1958.889	242.0083	9649.137
z	2679.385	830.4229	1635.511	1666.996	2029.172	1768.389	-10038.9
Dilophosaurus	mames	mamem	mamep	mamp	mps	mptd	mptv
Left mandible ramus/cranium half							
x	8608.434	3234.894	8109.492	6780.522	6741.421	1753.561	27169.97
y	-400.983	-84.6854	319.9596	462.3317	2012.411	248.6205	9912.774
z	2752.593	853.1121	1680.197	1712.542	2084.614	1816.705	-10313.2
Right mandible ramus/cranium half							
x	-8608.43	-3234.89	-8109.49	-6780.52	-6741.42	-1753.56	-27170

y	-400.983	-84.6854	319.9596	462.3317	2012.411	248.6205	9912.774
z	2752.593	853.1121	1680.197	1712.542	2084.614	1816.705	-10313.2
Herrerasaurus	mames	mamem	mamep	mamp	mps	mptd	mptv
Left mandible ramus/cranium half							
x	5586.324	2099.239	5262.543	4400.126	4374.752	1137.949	17631.57
y	-260.213	-54.9554	207.6334	300.0237	1305.926	161.3388	6432.758
z	1786.257	553.6153	1090.341	1111.33	1352.781	1178.926	-6692.62
Right mandible ramus/cranium half							
x	-5586.32	-2099.24	-5262.54	-4400.13	-4374.75	-1137.95	-17631.6
y	-260.213	-54.9554	207.6334	300.0237	1305.926	161.3388	6432.758
z	1786.257	553.6153	1090.341	1111.33	1352.781	1178.926	-6692.62
Ceratosaurus	mames	mamem	mamep	mamp	mps	mptd	mptv
Left mandible ramus/cranium half							
x	5082.639	1909.964	4788.051	4003.393	3980.307	1035.347	16041.84
y	-236.751	-50.0004	188.9123	272.9724	1188.179	146.7919	5852.755
z	1625.201	503.6992	992.0314	1011.129	1230.809	1072.629	-6089.19
Right mandible ramus/cranium half							
x	-5082.64	-1909.96	-4788.05	-4003.39	-3980.31	-1035.35	-16041.8
y	-236.751	-50.0004	188.9123	272.9724	1188.179	146.7919	5852.755
z	1625.201	503.6992	992.0314	1011.129	1230.809	1072.629	-6089.19

Table A5. Muscle forces used in scaled non-tyrannosauroid theropod dinosaur 3D models in chapter 4.

Spinosaurus	mames	mamem	mamep	mamp	mps	mptd	mptv
Left mandible ramus/cranium half							
x	23778.62	8935.574	22400.42	18729.47	18621.47	4843.769	75050.15
y	-1107.61	-233.922	883.8074	1277.074	5558.775	686.7512	27381.53
z	7603.34	2356.506	4641.12	4730.464	5758.218	5018.188	-28487.6
Right mandible ramus/cranium half							
x	-23778.6	-8935.57	-22400.4	-18729.5	-18621.5	-4843.77	-75050.2
y	-1107.61	-233.922	883.8074	1277.074	5558.775	686.7512	27381.53
z	7603.34	2356.506	4641.12	4730.464	5758.218	5018.188	-28487.6
Giganotosaurus	mames	mamem	mamep	mamp	mps	mptd	mptv
Left mandible ramus/cranium half							
x	37761.72	14190.17	35573.06	29743.41	29571.89	7692.165	119183.7
y	-1758.95	-371.481	1403.533	2028.062	8827.632	1090.598	43483.33
z	12074.51	3742.258	7370.347	7512.23	9144.358	7969.151	-45239.9
Right mandible ramus/cranium half							
x	-37761.7	-14190.2	-35573.1	-29743.4	-29571.9	-7692.16	-119184
y	-1758.95	-371.481	1403.533	2028.062	8827.632	1090.598	43483.33
z	12074.51	3742.258	7370.347	7512.23	9144.358	7969.151	-45239.9
Suchomimus	mames	mamem	mamep	mamp	mps	mptd	mptv

Left mandible ramus/cranium half							
x	19389.01	7286.039	18265.23	15271.95	15183.89	3949.594	61195.65
y	-903.146	-190.739	720.6537	1041.322	4532.607	559.9747	22326.81
z	6199.739	1921.488	3784.354	3857.205	4695.232	4091.814	-23228.7
Right mandible ramus/cranium half							
x	-19389	-7286.04	-18265.2	-15272	-15183.9	-3949.59	-61195.7
y	-903.146	-190.739	720.6537	1041.322	4532.607	559.9747	22326.81
z	6199.739	1921.488	3784.354	3857.205	4695.232	4091.814	-23228.7
Acrocanthosaurus	mames	mamem	mamep	mamp	mps	mptd	mptv
Left mandible ramus/cranium half							
x	32498.81	12212.46	30615.19	25598.02	25450.41	6620.095	102572.8
y	-1513.8	-319.707	1207.921	1745.408	7597.31	938.5993	37422.99
z	10391.67	3220.693	6343.129	6465.238	7869.894	6858.478	-38934.7
Right mandible ramus/cranium half							
x	-32498.8	-12212.5	-30615.2	-25598	-25450.4	-6620.1	-102573
y	-1513.8	-319.707	1207.921	1745.408	7597.31	938.5993	37422.99
z	10391.67	3220.693	6343.129	6465.238	7869.894	6858.478	-38934.7
Torvosaurus	mames	mamem	mamep	mamp	mps	mptd	mptv
Left mandible ramus/cranium half							
x	29953.69	11256.05	28217.58	23593.33	23457.28	6101.647	94539.92
y	-1395.25	-294.669	1113.323	1608.717	7002.333	865.0936	34492.24
z	9577.851	2968.467	5846.372	5958.917	7253.569	6321.361	-35885.6
Right mandible ramus/cranium half							
x	-29953.7	-11256.1	-28217.6	-23593.3	-23457.3	-6101.65	-94539.9
y	-1395.25	-294.669	1113.323	1608.717	7002.333	865.0936	34492.24
z	9577.851	2968.467	5846.372	5958.917	7253.569	6321.361	-35885.6
Baryonyx	mames	mamem	mamep	mamp	mps	mptd	mptv
Left mandible ramus/cranium half							
x	12078.37	4538.831	11378.31	9513.649	9458.788	2460.396	38121.78
y	-562.614	-118.821	448.9306	648.6907	2823.583	348.8357	13908.47
z	3862.122	1196.989	2357.46	2402.842	2924.891	2548.992	-14470.3
Right mandible ramus/cranium half							
x	-12078.4	-4538.83	-11378.3	-9513.65	-9458.79	-2460.4	-38121.8
y	-562.614	-118.821	448.9306	648.6907	2823.583	348.8357	13908.47
z	3862.122	1196.989	2357.46	2402.842	2924.891	2548.992	-14470.3
Monolophosaurus	mames	mamem	mamep	mamp	mps	mptd	mptv
Left mandible ramus/cranium half							
x	18643.67	7005.954	17563.09	14684.88	14600.2	3797.766	58843.21
y	-868.427	-183.407	692.9508	1001.292	4358.368	538.4486	21468.54
z	5961.413	1847.623	3638.879	3708.929	4514.741	3934.52	-22335.8
Right mandible ramus/cranium half							
x	-18643.7	-7005.95	-17563.1	-14684.9	-14600.2	-3797.77	-58843.2
y	-868.427	-183.407	692.9508	1001.292	4358.368	538.4486	21468.54

	z	5961.413	1847.623	3638.879	3708.929	4514.741	3934.52	-22335.8
Allosaurus	mames	mamem	mamep	mamp	mps	mptd	mptv
Left mandible ramus/cranium half								
x	15070.25	5663.129	14196.79	11870.24	11801.79	3069.852	47564.78
y	-701.977	-148.253	560.1336	809.3755	3523.003	435.2446	17353.68
z	4818.794	1493.491	2941.418	2998.042	3649.405	3180.394	-18054.7
Right mandible ramus/cranium half								
x	-15070.3	-5663.13	-14196.8	-11870.2	-11801.8	-3069.85	-47564.8
y	-701.977	-148.253	560.1336	809.3755	3523.003	435.2446	17353.68
z	4818.794	1493.491	2941.418	2998.042	3649.405	3180.394	-18054.7
Neovenator	mames	mamem	mamep	mamp	mps	mptd	mptv
Left mandible ramus/cranium half								
x	15402.69	5788.051	14509.95	12132.08	12062.12	3137.569	48614.01
y	-717.462	-151.524	572.4894	827.2294	3600.716	444.8456	17736.48
z	4925.091	1526.435	3006.302	3064.175	3729.906	3250.549	-18453
Right mandible ramus/cranium half								
x	-15402.7	-5788.05	-14510	-12132.1	-12062.1	-3137.57	-48614
y	-717.462	-151.524	572.4894	827.2294	3600.716	444.8456	17736.48
z	4925.091	1526.435	3006.302	3064.175	3729.906	3250.549	-18453
Majungasaurus	mames	mamem	mamep	mamp	mps	mptd	mptv
Left mandible ramus/cranium half								
x	11340.24	4261.456	10682.96	8932.256	8880.747	2310.037	35792.1
y	-528.232	-111.559	421.4957	609.0482	2651.03	327.5179	13058.5
z	3626.101	1123.839	2213.392	2256.001	2746.146	2393.219	-13586
Right mandible ramus/cranium half								
x	-11340.2	-4261.46	-10683	-8932.26	-8880.75	-2310.04	-35792.1
y	-528.232	-111.559	421.4957	609.0482	2651.03	327.5179	13058.5
z	3626.101	1123.839	2213.392	2256.001	2746.146	2393.219	-13586
Carnotaurus	mames	mamem	mamep	mamp	mps	mptd	mptv
Left mandible ramus/cranium half								
x	17010.36	6392.184	16024.44	13398.38	13321.12	3465.056	53688.14
y	-792.347	-167.339	632.2436	913.5723	3976.545	491.2768	19587.75
z	5439.152	1685.759	3320.088	3384.001	4119.219	3589.829	-20379
Right mandible ramus/cranium half								
x	-17010.4	-6392.18	-16024.4	-13398.4	-13321.1	-3465.06	-53688.1
y	-792.347	-167.339	632.2436	913.5723	3976.545	491.2768	19587.75
z	5439.152	1685.759	3320.088	3384.001	4119.219	3589.829	-20379
Dilophosaurus	mames	mamem	mamep	mamp	mps	mptd	mptv
Left mandible ramus/cranium half								
x	19024.64	7149.115	17921.98	14984.95	14898.54	3875.371	60045.63
y	-886.173	-187.155	707.1107	1021.753	4447.428	549.4513	21907.23
z	6083.229	1885.378	3713.236	3784.718	4606.997	4014.919	-22792.2
Right mandible ramus/cranium half								

x	-19024.6	-7149.11	-17922	-14985	-14898.5	-3875.37	-60045.6
y	-886.173	-187.155	707.1107	1021.753	4447.428	549.4513	21907.23
z	6083.229	1885.378	3713.236	3784.718	4606.997	4014.919	-22792.2
Herrerasaurus	mames	mamem	mamep	mamp	mps	mptd	mptv
Left mandible ramus/cranium half							
x	14245.13	5353.061	13419.48	11220.32	11155.62	2901.771	44960.51
y	-663.542	-140.136	529.4651	765.0605	3330.111	411.4141	16403.53
z	4554.955	1411.719	2780.369	2833.893	3449.592	3006.261	-17066.2
Right mandible ramus/cranium half							
x	-14245.1	-5353.06	-13419.5	-11220.3	-11155.6	-2901.77	-44960.5
y	-663.542	-140.136	529.4651	765.0605	3330.111	411.4141	16403.53
z	4554.955	1411.719	2780.369	2833.893	3449.592	3006.261	-17066.2
Ceratosaurus	mames	mamem	mamep	mamp	mps	mptd	mptv
Left mandible ramus/cranium half							
x	10606.45	3985.712	9991.705	8354.281	8306.105	2160.563	33476.12
y	-494.052	-104.341	394.2222	569.6389	2479.491	306.3253	12213.53
z	3391.469	1051.119	2070.171	2110.023	2568.453	2238.363	-12706.9
Right mandible ramus/cranium half							
x	-10606.5	-3985.71	-9991.71	-8354.28	-8306.11	-2160.56	-33476.1
y	-494.052	-104.341	394.2222	569.6389	2479.491	306.3253	12213.53
z	3391.469	1051.119	2070.171	2110.023	2568.453	2238.363	-12706.9

REFERENCES

Alexander, R. M. 1989. Dynamics of dinosaurs and other extinct giants. Columbia University Press.

Alexander, R. M. 1991. How dinosaurs ran. Scientific American 264, 130–136.

Alexander, R. M. 2006. Dinosaur biomechanics. Proceedings of the Royal Society B: Biological Sciences 273, 1849–1855.

Allen, V. R., Kilbourne, B. M., Hutchinson, J. R. 2021. The evolution of pelvic limb muscle moment arms in bird-line archosaurs. Science Advances 7, eabe2778.

Alroy, J. 1998. Cope's rule and the dynamics of body mass evolution in North American fossil mammals. Science 280, 731–734.

Amirouche, F. 2007. Fundamentals of Multibody Dynamics: Theory and Applications. Springer Science & Business Media.

Angielczyk, K. D., Burroughs, R. W., Feldman, C. R. 2015. Do turtles follow the rules? Latitudinal gradients in species richness, body size, and geographic range area of the world's turtles. Journal of Experimental Zoology Part B: Molecular and Developmental Evolution. 324 (3): 270–294.

Arbour, V. M. & Snively, E. 2009. Finite element analyses of ankylosaurid dinosaur tail club impacts. The Anatomical Record 292, 1412–1426.

Arbour, V. M. & Mallon, J. C. 2017. Unusual cranial and postcranial anatomy in the archetypal ankylosaur *Ankylosaurus magniventris*. FACETS. 2: 764-794.

Arden, T. M. S., Klein, C. G., Zouhri, S., Longrich, N. R. 2019. Aquatic adaptation in the skull of carnivorous dinosaurs (Theropoda: Spinosauridae) and the evolution of aquatic habits in spinosaurids. Cretaceous Research 93, 275–284.

Arnold, E. N. 1998. Cranial Kinesis in Lizards; pp. 323–357 in Hecht, M. K., Macintyre, R. J., Clegg, M. T. (eds.), Evolutionary Biology, Evolutionary Biology Springer US, Boston, MA.

Arthur, K. E., Boyle, M. C., Limpus, C. J. 2008. Ontogenetic changes in diet and habitat use in green sea turtle (*Chelonia mydas*) life history. Marine Ecology Progress Series 362:303–311. DOI: 10.3354/meps07440.

Bailleul, A. M. & Holliday, C. M. 2017. Joint histology in *Alligator mississippiensis* challenges the identification of synovial joints in fossil archosaurs and inferences of cranial kinesis. Proceedings of the Royal Society B: Biological Sciences 284:20170038.

Bakker, R. T. 1986. Dinosaur Heresies. William Morrow, New York.

Ballell, A., Moon, B. C., Porro, L. B., Benton, M. J., Rayfield, E. J. 2019. Convergence and functional evolution of longirostry in crocodylomorphs. Palaeontology 62, 867–887.

Ballell, A., & Ferrón, H. G. 2021. Biomechanical insights into the dentition of megatooth sharks (Lamniformes: Otodontidae). Scientific Reports 11:1232.

Barbosa, G. G., Langer, M. C., Martins, N. O, Montefeltro, F. C. 2023. Assessing the palaeobiology of *Vespersaurus paranaensis* (Theropoda, Noasauridae), Cretaceous, Bauru Basin – Brazil, using Finite Element Analysis. Cretaceous Research 150, 105594.

Bates, K. T., Manning, P. L., Vila, B., Hodgetts, D. 2008. Three-dimensional modelling and analysis of dinosaur trackways. Palaeontology 51:999–1010.

Bates, K. T., Manning, P. L., Hodgetts, D., Sellers, W. I. 2009. Estimating mass properties of dinosaurs using laser imaging and 3D computer modelling. PLoS One 4, e4532.

Bates, K. T. & Falkingham, P. L. 2012. Estimating maximum bite performance in *Tyrannosaurus rex* using multi-body dynamics. Biology Letters 8, 660–664.

Bates, K. T., Benson, R. B. J., Falkingham, P. L. 2012. A computational analysis of locomotor anatomy and body mass evolution in Allosauroidea (Dinosauria: Theropoda). Paleobiology. 38 (3): 486–507.

Bates, K. T., Mannion, P. D., Falkingham, P. L., Brusatte, S. L., Hutchinson, J. R., Otero, A., Sellers, W. I., Sullivan, C., Stevens, K. A., Allen, V. 2016. Temporal and phylogenetic evolution of the sauropod dinosaur body plan. Royal Society Open Science 3, 150636.

Bates, K. T. & Falkingham, P. L. 2018. The importance of muscle architecture in biomechanical reconstructions of extinct animals: a case study using *Tyrannosaurus rex.* Journal of Anatomy 233, 625–635.

Bathe, K. J. 2006. Finite Element Procedures. Cambridge, MA: Klaus-Jürgen Bathe. ISBN 978-0979004902.

Bell, M. 2014. Patterns in palaeontology: Trends of body-size evolution in the fossil record - a growing field. Palaeontology Online. 2014; 4:1–9.

Bell, P. R., Snively, E., Shychoski, L. 2009. A comparison of the jaw mechanics in hadrosaurid and ceratopsid dinosaurs using finite element analysis. The Anatomical Record 292, 1338–1351.

Benson, R. B. J., Carrano, M. T., Brusatte, S. L. 2009. A new clade of archaic large-bodied predatory dinosaurs (Theropoda: Allosauroidea) that survived to the latest Mesozoic. Naturwissenschaften 97, 71.

Benson, R. B. J., Campione, N. E., Carrano, M. T., Mannion, P. D., Sullivan, C., Upchurch, P., Evans, D. C. 2014. Rates of dinosaur body mass evolution indicate 170 million years of sustained ecological innovation on the avian stem lineage. PLOS Biology 12, e1001853.

Benson, R. B. J., Frigot, R. A., Goswami, A., Andres, B., Butler, R. J. 2014. Competition and constraint drove Cope's rule in the evolution of giant flying reptiles. Nature Communications 5, 3567.

Benson, R. B. J., Hunt, G., Carrano, M. T., Campione, N. 2018. Cope's rule and the adaptive landscape of dinosaur body size evolution. Palaeontology 61, 13–48.

Bishop, P. J., Graham, D. F., Lamas, L. P., Hutchinson, J. R., Rubenson, J., Hancock, J. A., Wilson, R. S., Hocknull, S. A., Barrett, R. S., Lloyd, D. G., Clemente, C. J. 2018. The influence of speed and size on avian terrestrial locomotor biomechanics: Predicting locomotion in extinct theropod dinosaurs. PLOS ONE 13, e0192172.

Bishop, P. J., Hocknull, S. A., Clemente, C. J., Hutchinson, J. R., Barrett, R. S., Lloyd, D. G. 2018. Cancellous bone and theropod dinosaur locomotion. Part II—a new approach to inferring posture and locomotor biomechanics in extinct tetrapod vertebrates. PeerJ 6:e5779.

Bishop, P. J., Falisse, A., De Groote, F., Hutchinson, J. R. 2021. Predictive simulations of running gait reveal a critical dynamic role for the tail in bipedal dinosaur locomotion. Science Advances 7, eabi7348.

Bittencourt, J. & Kellner, W. A. 2004. The phylogenetic position of Staurikosaurus pricei from the Triassic of Brazil. Journal of Vertebrate Paleontology. 24 (3, supplement): 39A.

Blanckenhorn, W. U. 2000. The evolution of body size: what keeps organisms small? Quarterly Review of Biology 75, 385–407.

Bonaparte, J. F., Novas, F. E., Coria, R. A. 1990. *Carnotaurus sastrei*, the horned, lightly built carnosaur from the Middle Cretaceous of Patagonia. Contributions in Science. 416: 1–41.

Breithaupt, B. H., Matthews, N. A., Noble, T. A. 2004. An integrated approach to three-dimensional data collection at dinosaur tracksites in the Rocky Mountain West. Ichnos 11, 11–26.

Bright, J. A. & Gröning, F. 2011. Strain accommodation in the zygomatic arch of the pig: A validation study using digital speckle pattern interferometry and finite element analysis. Journal of Morphology 272:1388–1398.

Bright, J. A. 2012. The importance of craniofacial sutures in biomechanical finite element models of the domestic pig. PLOS ONE 7:e31769.

Britt, B. B. 1991. Theropods of Dry Mesa Quarry (Morrison Formation, Late Jurassic), Colorado, with emphasis on the osteology of *Torvosaurus tanneri*. Brigham Young University Geological Studies. 37:1–72.

Brochu, C. A. 2003. Osteology of Tyrannosaurus rex: Insights from a nearly complete skeleton and high-resolution computed tomographic analysis of the skull. Journal of Vertebrate Paleontology 22, 1–138.

Brown, C. M., Greenwood, D. R., Kalyniuk, J. E., Braman, D. R., Henderson, D. M., Greenwood, C. L., Basinger, J. F. 2020 Dietary palaeoecology of an Early Cretaceous armoured dinosaur (Ornithischia; Nodosauridae) based on floral analysis of stomach contents. Royal Society Open Science 7: 200305.

Brown, J. H. & Maurer, B.A. 1986. Body size, ecological dominance and Cope's rule. Nature 324, 248–250.

Brown, J. H. & Sibly, R. M. 2006. Life-history evolution under a production constraint. Proceedings of the National Academy of Sciences 103(47):17595–17599.

Brusatte, S. L., Carr, T. D., Erickson, G. M., Bever, G. S., Norell, M. A. 2009. A long-snouted, multihorned tyrannosaurid from the Late Cretaceous of Mongolia. Proceedings of the National Academy of Sciences of the United States of America, 106(41), 17261–17266.

Brusatte, S. L., Benson, R. B. J., Currie, P. J., Xijin, Z. 2010. The skull of *Monolophosaurus jiangi* (Dinosauria: Theropoda) and its implications for early theropod phylogeny and evolution. Zoological Journal of the Linnean Society 158, 573–607.

Brusatte, S. L., Norell, M. A., Carr, T. D., Erickson, G. M., Hutchinson, J. R., Balanoff, A. M., Bever, G. S., Choiniere, J. N., Makovicky, P. J., Xu, X. 2010. Tyrannosaur paleobiology: New research on ancient exemplar organisms. Science 329, 1481–1485.

Brusatte, S.L., Sakamoto, M., Montanari, S., Harcourt Smith, W. E. H. 2012. The evolution of cranial form and function in theropod dinosaurs: insights from geometric morphometrics. Journal of Evolutionary Biology 25: 365-377.

Brusatte, S. L., Lloyd, G. T., Wang, S. C., Norell, M. A. 2014. Gradual assembly of avian body plan culminated in rapid rates of evolution across the dinosaur-bird transition. Current Biology 24, 2386–2392.

Brusatte, S. L. & Carr, T. D. 2016. The phylogeny and evolutionary history of tyrannosauroid dinosaurs. Scientific Reports 6, 20252.

Buffetaut, E., Martill, D., Escuillié, F. 2004. Pterosaurs as part of a spinosaur diet. Nature 430, 33–33.

Burness, G. P., Diamond, J., Flannery, T. 2001. Dinosaurs, dragons, and dwarfs: The evolution of maximal body size. Proceedings of the National Academy of Sciences 98, 14518–14523.

Butler, R. J. & Goswami, A. 2008. Body size evolution in Mesozoic birds: little evidence for Cope's rule. Journal of Evolutionary Biology 21, 1673–1682.

Button, D. J., Rayfield, E. J., Barrett, P. M. 2014. Cranial biomechanics underpins high sauropod diversity in resource-poor environments. Proceedings of the Royal Society B: Biological Sciences 281, 20142114.

Button, D. J., Barrett, P. M., Rayfield, E. J. 2016. Comparative cranial myology and biomechanics of *Plateosaurus* and *Camarasaurus* and evolution of the sauropod feeding apparatus. Palaeontology 59, 887–913.

Bybee, P. J., Lee, A. H., Lamm, E. 2006. Sizing the Jurassic theropod dinosaur *Allosaurus*: Assessing growth strategy and evolution of ontogenetic scaling of limbs. Journal of Morphology. 267 (3): 347–359.

Campione, N. E., Evans, D. C., Brown, C. M., Carrano, M. T. 2014. Body mass estimation in non-avian bipeds using a theoretical conversion to quadruped stylopodial proportions. Methods in Ecology and Evolution, 5(9), 913-923.

Canale, J. I., Apesteguía, S., Gallina, P. A., Mitchell, J., Smith, N. D., Cullen, T. M., Shinya, A., Haluza, A., Gianechini, F. A., Makovicky, P. J. 2022. New giant carnivorous dinosaur reveals convergent evolutionary trends in theropod arm reduction. Current Biology. 32 (14): 3195–3202.

Carbone, C., Teacher, A., Rowcliffe, J. 2007. The costs of carnivory. PLoS Biology 5, 363–368.

Carlson, W. D., Rowe, T., Ketcham, R. A., Colbert, M. W. 2003. Applications of high-resolution X-ray computed tomography in petrology, meteoritics and palaeontology. Geological Society, London, Special Publications 215, 7–22.

Carr, T. D. 1999. Craniofacial ontogeny in Tyrannosauridae (Dinosauria, Coelurosauria). Journal of Vertebrate Paleontology 19, 497–520.

Carr, T. D. 2020. A high-resolution growth series of *Tyrannosaurus rex* obtained from multiple lines of evidence. PeerJ 8, e9192.

Carr, T. D. 2023. A reappraisal of tyrannosauroid fossils from the Iren Dabasu Formation (Coniacian–Campanian), Inner Mongolia, People's Republic of China. Journal of Vertebrate Paleontology 42, e2199817.

Carr, T. D. & Williamson, T.E . 2010. *Bistahieversor sealeyi*, gen. et sp. nov., a new tyrannosauroid from New Mexico and the origin of deep snouts in Tyrannosauroidea. Journal of Vertebrate Paleontology 30, 1–16.

Carr, T. D., Williamson, T. E., Britt, B. B., Stadtman, K. 2011. Evidence for high taxonomic and morphologic tyrannosauroid diversity in the Late Cretaceous (Late Campanian) of the American Southwest and a new short-skulled tyrannosaurid from the Kaiparowits formation of Utah. Naturwissenschaften 98, 241–246.

Carr, T. D., Varricchio, D. J., Sedlmayr, J. C., Roberts, E. M., Moore, J. R. 2017. A new tyrannosaur with evidence for anagenesis and crocodile-like facial sensory system. Scientific Reports 7.

Carrano, M. T., Loewen, M. A., Sertic, J. J. W. 2011. New materials of *Masiakasaurus knopfleri* Sampson, Carrano, and Forster, 2001, and implications for the morphology of the Noasauridae (Theropoda: Ceratosauria). Smithsonian Contributions to Paleobiology. 95 (95): 53pp.

Carrano, M. T., Benson, R. B. J., Sampson, S. D. 2012. The phylogeny of Tetanurae (Dinosauria: Theropoda). Journal of Systematic Palaeontology. 10 (2): 211–300.

Case, T. J. 1979. Optimal body size and an animal's diet. Acta Biotheor 28, 54–69.

Cerroni, M. A., Canale, J. I., Novas, F. E. 2020. The skull of *Carnotaurus sastrei* Bonaparte 1985 revisited: insights from craniofacial bones, palate and lower jaw. Historical Biology: 1–42.

Charig, A. J. & Milner, A. C. 1986. *Baryonyx*, a remarkable new theropod dinosaur. Nature 324, 359–361.

Charig, A. J. & Milner, A. C. 1997. *Baryonyx walkeri*, a fish-eating dinosaur from the Wealden of Surrey. Bulletin of the Natural History Museum of London. 53: 11–70.

Chin, K., Tokaryk, T. T., Erickson, G. M., Calk, L. C. 1998. A king-sized theropod coprolite. Nature 393, 680–682.

Christiansen, P. & Fariña, R. A. 2004. Mass prediction in theropod dinosaurs. Historical Biology 16, 85–92.

Chure, D. J & Loewen, M. A. 2020. Cranial anatomy of *Allosaurus jimmadseni*, a new species from the lower part of the Morrison Formation (Upper Jurassic) of Western North America. PeerJ 8:e7803.

Cohen, J. E., Pimm, S. L., Yodzis, P., Saldaña, J. 1993. Body sizes of animal predators and animal prey in food webs. Journal of Animal Ecology 62, 67–78.

Coombs, E. J., Felice, R. N., Clavel, J., Park, T., Bennion, R. F., Churchill, M., Geisler, J. H., Beatty, B., Goswami, A. 2022. The tempo of cetacean cranial evolution. Current Biology 32, 2233-2247.e4.

Cope, E. D. 1885. On the evolution of the Vertebrata, progressive and retrogressive. American Naturalist. 19 (2): 140–148.

Cope, E. D. 1887. The dinosaurian genus Coelurus. The American Naturalist. xxi 5: 367-369.

Cope, E. D. 1896. The primary factors of organic evolution. Open Court Publishing Company, Chicago. 547 p.

Copes, L. E., Lucas, L. M., Thostenson, J. O., Hoekstra, H. E., Boyer, D. M. 2016. A collection of non-human primate computed tomography scans housed in MorphoSource, a repository for 3D data. Scientific Data 3:160001.

Coria, R. A. & Salgado, L. 1995. A new giant carnivorous dinosaur from the Cretaceous of Patagonia. Nature 377, 224–226.

Cost, I. N., Middleton, K. M., Sellers, K. C., Echols, M. S., Witmer, L. M., Davis, J. L., Holliday, C. M. 2020. Palatal biomechanics and its significance for cranial kinesis in *Tyrannosaurus rex*. The Anatomical Record 303: 999-1017.

Cox, P. G., Fagan, M. J., Rayfield, E. J., Jeffery, N. 2011. Finite element modelling of squirrel, guinea pig and rat skulls: using geometric morphometrics to assess sensitivity. Journal of Anatomy 219, 696–709.

Cox, P. G., Rinderknecht, A., Blanco, R. E. 2015. Predicting bite force and cranial biomechanics in the largest fossil rodent using finite element analysis. Journal of Anatomy 226, 215–223.

Cuff, A. R. & Rayfield, E. J. 2013. Feeding mechanics in spinosaurid theropods and extant crocodilians. PLOS ONE 8, e65295.

Cullen, T. M., Canale, J. I., Apesteguía, S., Smith, N. D., Hu, D., Makovicky, P. J. 2020. Osteohistological analyses reveal diverse strategies of theropod dinosaur body-size evolution. Proceedings of the Royal Society B: Biological Sciences 287, 20202258.

Cunningham, J. A., Rahman, I. A., Lautenschlager, S., Rayfield, E. J., Donoghue, P. C. J. 2014. A virtual world of paleontology. Trends in Ecology & Evolution 29:347–357.

Currie, P. J. & Carpenter, K. 2000. A new specimen of *Acrocanthosaurus atoke*nsis (Theropoda, Dinosauria) from the Lower Cretaceous Antlers Formation (Lower Cretaceous, Aptian) of Oklahoma, USA. Geodiversitas 22 (2), pp. 207-246 : 210-233.

Currie, P. J. 2003. Allometric growth in tyrannosaurids (Dinosauria: Theropoda) from the Upper Cretaceous of North America and Asia. Canadian Journal of Earth Sciences 40, 651.

Dal Sasso, C., Maganuco, S., Buffetaut, E., Mendez, M. A. 2005. New information on the skull of the enigmatic theropod *Spinosaurus*, with remarks on its size and affinities. Journal of Vertebrate Paleontology 25, 888–896.

Damuth, J. 1993. Cope's rule, the island rule and the scaling of mammalian population density. Nature 365, 748–750.

Dececchi, T. A. & Larsson, H. C. E. 2013. Body and limb size disassociation at the origin of birds: Uncoupling allometric constraints across a macroevolutionary transition. Evolution 67: 2741-2752.

Demuth, O. E., Benito, J., Tschopp, E., Lautenschlager, S., Mallison, H., Heeb, N., Field, D. J. 2022. Topology-based three-dimensional reconstruction of delicate skeletal fossil remains and the quantification of their taphonomic deformation. Frontiers in Ecology and Evolution 10.

DePalma, R. A., Burnham, D. A., Martin, L. D., Rothschild, B. M., Larson, P. L. 2013. Physical evidence of predatory behavior in *Tyrannosaurus rex*. Proceedings of the National Academy of Sciences 110, 12560–12564.

Díez Díaz, V., Mallison, H., Asbach, P., Schwarz, D., Blanco, A. 2021. Comparing surface digitization techniques in palaeontology using visual perceptual metrics and distance computations between 3D meshes. Palaeontology 64:179–202.

Dumont, E. R., Grosse, I. R., Slater, G. J. 2009. Requirements for comparing the performance of finite element models of biological structures. Journal of Theoretical Biology 256, 96–103.

Dutel, H., Gröning, F., Sharp, A. C., Watson, P. J., Herrel, A., Ross, C. F., Jones, M. E. H., Evans, S. E., Fagan, M. J. 2021. Comparative cranial biomechanics in two lizard species: impact of variation in cranial design. Journal of Experimental Biology 224.

Eddy, D. R. & Clarke, J. A. 2011. New information on the cranial anatomy of *Acrocanthosaurus atokensis* and its implications for the phylogeny of Allosauroidea (Dinosauria: Theropoda). PLOS ONE 6, e17932.

Erickson, G. M., Makovicky, P. J., Currie, P. J., Norell, M. A., Yerby, S. A., Brochu, C. A. 2004. Gigantism and comparative life-history parameters of tyrannosaurid dinosaurs. Nature 430, 772–775.

Fabbri, M., Navalón, G., Benson, R. B. J., Pol, D., O'Connor, J., Bhullar, B.-A. S., Erickson, G. M., Norell, M. A., Orkney, A., Lamanna, M. C., Zouhri, S., Becker, J., Emke, A., Dal Sasso, C., Bindellini, G., Maganuco, S., Auditore, M., Ibrahim, N. 2022. Subaqueous foraging among carnivorous dinosaurs. Nature 603, 852–857.

Fahlke, J., & Autenrieth, M. 2016. Photogrammetry vs. micro-CT scanning for 3D surface generation of a typical vertebrate fossil – a case study. Journal of Paleontological Techniques. 14. 1-18.

Fahrni, S., Campana, L., Dominguez, A., Uldin, T., Dedouit, F., Delémont, O., Grabherr, S. 2017. CT-scan vs. 3D surface scanning of a skull: First considerations regarding reproducibility issues. Forensic Sciences Research 2:93–99.

Falkingham, P. 2012. Acquisition of high resolution three-dimensional models using free, open-source, photogrammetric software. Palaeontologia Electronica 15:1T:15p.

Farlow, J. O., Smith, M. B., Robinson, J. M. 1995. Body mass, bone "strength indicator," and cursorial potential of *Tyrannosaurus rex*. Journal of Vertebrate Paleontology 15, 713–725.

Ferguson, M. W. J. 1981. The structure and development of the palate in *Alligator mississippiensis*. Archives of Oral Biology 26:427–443.

Ferreira, G. S, Lautenschlager, S., Evers, S. W., Pfaff, C., Kriwet, J., Raselli, I., Werneburg, I. 2020. Feeding biomechanics suggests progressive correlation of skull architecture and neck evolution in turtles. Scientific Reports 10:5505.

Fiorillo, A. R. & Gangloff, R. A. 2000. Theropod teeth from the Prince Creek Formation (Cretaceous) of northern Alaska, with speculations on Arctic dinosaur paleoecology. Journal of Vertebrate Paleontology. 20 (4): 675.

Fletcher, T. M., Janis, C. M., Rayfield, E. J. 2010. Finite element analysis of ungulate jaws: Can mode of digestive physiology be determined? Palaeontologia Electronica Vol. 13, Issue 3; 21A:15p.

Foffa, D., Cuff, A. R., Sassoon, J., Rayfield, E. J., Mavrogordato, M. N., Benton, M. J. 2014. Functional anatomy and feeding biomechanics of a giant upper Jurassic pliosaur (Reptilia: Sauropterygia) from Weymouth Bay, Dorset, UK. Journal of Anatomy 225, 209–219.

Foster, W., Brusatte, S. L., Carr, T. D., Williamson, T. E., Yi, L., Lü, J. 2022. The cranial anatomy of the long-snouted tyrannosaurid dinosaur Qianzhousaurus sinensis from the Upper Cretaceous of China. Journal of Vertebrate Paleontology 41, e1999251.

Foth, C. & Rauhut, O. W. M. 2013. Macroevolutionary and morphofunctional patterns in theropod skulls: A morphometric approach. Acta Palaeontologica Polonica 58(1), 1-16.

Fowler, D. W., Woodward, H. N., Freedman, E. A., Larson, P. L., Horner, J. R. 2011. Reanalysis of "*Raptorex kriegsteini*": A juvenile tyrannosaurid dinosaur from Mongolia. PLoS ONE 6, e21376.

Fred, H. L. 2004. Drawbacks and limitations of computed tomography. Texas Heart Institute Journal 31:345–348.

Friess, M. 2006. The study of craniofacial growth patterns using 3D laser scanning and geometric morphometrics. Three-Dimensional Image Capture and Applications VII 6056:184–188.

Fuchs, M., Geiger, M., Stange, M., Sánchez-Villagra, M. R. 2015. Growth trajectories in the cave bear and its extant relatives: an examination of ontogenetic patterns in phylogeny. BMC Evolutionary Biology 15, 239.

Gallina, P. A., Apesteguía, S., Haluza, A., Canale, J. I. 2014. A diplodocid sauropod survivor from the Early Cretaceous of South America. PLOS ONE 9, e97128.

Galton, P. M. & Jensen, J. A. 1979. A new large theropod dinosaur from the Upper Jurassic of Colorado. Brigham Young University Geology Studies 26(1):1–12.

Gignac, P. M. & Erickson, G. M. 2017. The biomechanics behind extreme osteophagy in *Tyrannosaurus rex*. Scientific Reports 7, 2012.

Gilmore, C.W. 1920. Osteology of the carnivorous Dinosauria in the United States National Museum, with special reference to the genera *Antrodemus* (*Allosaurus*) and *Ceratosaurus*. Bulletin of the United States National Museum. 110 (110): 1–154.

Glut, D. F. 1982. The New Dinosaur Dictionary. Secaucus, NJ: Citadel Press. pp. 226–228.

Gold, M. E., Brusatte, S. L, Norell, M. A. 2013. The cranial pneumatic sinuses of the tyrannosaurid *Alioramus* (Dinosauria: Theropoda) and the evolution of cranial pneumaticity in theropod dinosaurs. American Museum Novitates 3790, 1–46.

Goldman, L. W. 2007. Principles of CT: Radiation dose and image quality. Journal of Nuclear Medicine Technology 35:213–225.

Hamm, C. A., Mallison, H., Hampe, O., Schwarz, D., Mews, J., Blobel, J., Issever, A. S., Asbach, P. 2018. Efficiency, workflow and image quality of clinical computed tomography scanning compared to photogrammetry on the example of a *Tyrannosaurus rex* skull from the Maastrichtian of Montana, U.S.A. Journal of Paleontological Techniques 21: 1-13.

Handschuh, S., Natchev, N., Kummer, S., Beisser, C. J., Lemell, P., Herrel, A., Vergilov, V. 2019. Cranial kinesis in the miniaturised lizard *Ablepharus kitaibelii* (Squamata: Scincidae). Journal of Experimental Biology 222.

Happ, J. 2008. An analysis of predator-prey behavior in a head-to-head encounter between *Tyrannosaurus rex* and *Triceratops*. In Larson, P.; Carpenter, K. (eds.). *Tyrannosaurus rex, the Tyrant King (Life of the Past)*. Bloomington: Indiana University Press. pp. 355–368.

Harcourt-Smith, W. E. H., Tallman, M., Frost, S. R., Wiley, D. F., Rohlf, F. J., Delson, E. 2008. Analysis of selected hominoid joint surfaces using laser scanning and geometric morphometrics: A preliminary report. In: Sargis, E. J. & Dagosto, M., Eds., Mammalian Evolutionary Morphology, Springer, Dordrecht, 373-383.

Hassan, M. A., Westermann, G. E. G., Hewitt, R. A., Dokainish, M. A. 2002. Finite-element analysis of simulated ammonoid septa (extinct Cephalopoda): septal and sutural complexities do not reduce strength. Paleobiology 28, 113–126.

Haubitz, B., Prokop, M., Döhring, W., Ostrom, J. H., Wellnhofer, P. 1988. Computed tomography of Archaeopteryx. Paleobiology 14:206–213.

Heim, N. A., Knope, M. L., Schaal, E. K., Wang, S. C., Payne, J. L. 2015. Cope's rule in the evolution of marine animals. Science 347, 867–870.

Henderson, D. M. & Nicholls, R. 2015. Balance and strength—estimating the maximum prey-lifting potential of the large predatory dinosaur *Carcharodontosaurus saharicus*. The Anatomical Record 298: 1367-1375.

Hendrickx, C. & Mateus, O. 2014. *Torvosaurus gurneyi* n. sp., the largest terrestrial predator from Europe, and a proposed terminology of the maxilla anatomy in nonavian theropods. PLoS One 9, e88905.

Hendrickx, C., Hartman, S. A., Mateus, O. 2015. An overview of non-avian theropod discoveries and classification. PalArch's Journal of Vertebrate Palaeontology, 12(1): 1-73.

Herbers, J. M. 1981. Time resources and laziness in animals. Oecologia 49, 252–262.

Herbst, E. C., Lautenschlager, S., Bastiaans, D., Miedema, F., Scheyer, T. M. 2021. Modeling tooth enamel in FEA comparisons of skulls: Comparing common simplifications with biologically realistic models. iScience 24, 103182.

Herrel, A., Schaerlaeken, V., Meyers, J. J., Metzger, K. A., Ross, C. F. 2007. The evolution of cranial design and performance in squamates: Consequences of skull-bone reduction on feeding behavior. Integrative and Comparative Biology 47:107–117.

Holliday, R. 2005. Ageing and the extinction of large animals. Biogerontology 6, 151–156.

Holliday, C. M. 2009. New insights into dinosaur jaw muscle anatomy. The Anatomical Record 292:1246–1265.

Holtz, T. R. Jr. 1998. A new phylogeny of the carnivorous dinosaurs. Gaia (Lisboa) 15: 5-61.

Holtz, T. R., Jr. 2004. Tyrannosauroidea. In Weishampel, D. B.; Dodson, P.; Osmólska, H. (eds.). The Dinosauria (Second ed.). Berkeley: University of California Press. pp. 111–136. ISBN 978-0-520-24209-8.

Holtz, T. R., Jr. 2008. Chapter 20: A critical re-appraisal of the obligate scavenging hypothesis for *Tyrannosaurus rex* and other tyrant dinosaurs. In Larson, P.; Carpenter, K. (eds.). *Tyrannosaurus rex*: The Tyrant King. Book Publishers. pp. 371–394. ISBN 978-0-253-35087-9.

Holtz, T. R. Jr. 2012. Dinosaurs: The Most Complete, Up-to-Date Encyclopedia for Dinosaur Lovers of All Ages. Random House, New York.

Hone, D. W. E. & Benton, M. J. 2005. The evolution of large size: how does Cope's Rule work? Trends in Ecology & Evolution 20, 4–6.

Hone, D. W. E., Keesey, T. M., Pisani, D., Purvis, A. 2005. Macroevolutionary trends in the Dinosauria: Cope's rule. Journal of Evolutionary Biology 18, 587–595.

Hone, D. W. E. & Holtz, R, Jr. 2021. Evaluating the ecology of *Spinosaurus*: Shoreline generalist or aquatic pursuit specialist? Palaeontologia Electronica 24, 1–28.

Horner, J. R., Weishampel, D. B., Forster, C. A. 2004. Hadrosauridae. In Weishampel, D. B., Dodson, P., Osmólska H. (eds.). The Dinosauria (2nd ed.). Berkeley: University of California Press. pp. 438–463.

Hurum, J.H. & Sabath, K. 2003. Giant theropod dinosaurs from Asia and North America: skulls of *Tarbosaurus bataar* and *Tyrannosaurus rex* compared. Acta Palaeontologica Polonica, 48.

Hutchinson, J. R. 2006. The evolution of locomotion in archosaurs. Comptes Rendus Palevol, Cent ans après Marey : Aspects de la morphologie fontionnelle aujourd'hui 5, 519–530.

Hutchinson, J. R. & Garcia, M. 2002. *Tyrannosaurus* was not a fast runner. Nature 415, 1018–1021.

Hutchinson, J. R. & Allen, V. 2009. The evolutionary continuum of limb function from early theropods to birds. Naturwissenschaften 96, 423–448.

Ibrahim, N., Sereno, P. C., Dal Sasso, C., Maganuco, S., Fabbri, M., Martill, D. M., Zouhri, S., Myhrvold, N., Iurino, D. A. 2014. Semiaquatic adaptations in a giant predatory dinosaur. Science 345, 1613–1616.

Ibrahim, N., Maganuco, S., Dal Sasso, C., Fabbri, M., Auditore, M., Bindellini, G., Martill, D. M., Zouhri, S., Mattarelli, D. A., Unwin, D. M., Wiemann, J., Bonadonna, D., Amane, A., Jakubczak, J., Joger, U., Lauder, G. V., Pierce, S. E. 2020. Tail-propelled aquatic locomotion in a theropod dinosaur. Nature 581, 67–70.

Irmis, R. B., Nesbitt, S. J., Padian, K., Smith, N. D., Turner, A. H., Woody, D., Downs, A. 2007. A Late Triassic dinosauromorph assemblage from New Mexico and the rise of dinosaurs. Science. 317 (5836): 358–361.

Jamison-Todd, S., Moon, B. C., Rowe, A. J., Williams, M., Benton, M. J. 2022. Dietary niche partitioning in Early Jurassic ichthyosaurs from Strawberry Bank. Journal of Anatomy 1– 15.

Jeon, J.-H., Kim, H.-Y., Kim, J.-H., Kim, W.-C. 2014. Accuracy of 3D white light scanning of abutment teeth impressions: evaluation of trueness and precision. The Journal of Advanced Prosthodontics 6:468–473.

Jones, M. E. H., Werneburg, I., Curtis, N., Penrose, R., O'Higgins, P., Fagan, M. J., Evans, S. E. 2012. The head and neck anatomy of sea turtles (Cryptodira: Chelonioidea) and skull shape in Testudines. PLOS ONE 7:e47852.

Jones, M. E. H., Gröning, F., Dutel, H, Sharp, A., Fagan, M. J., Evans, S. E. 2017. The biomechanical role of the chondrocranium and sutures in a lizard cranium. Journal of The Royal Society Interface 14:20170637.

Kammerer, C. F., Deutsch, M., Lungmus, J. K., Angielczyk, K. D. 2020. Effects of taphonomic deformation on geometric morphometric analysis of fossils: a study using the dicynodont *Diictodon feliceps* (Therapsida, Anomodontia). PeerJ 8, e9925.

Kulczyk, T., Rychlik, M., Lorkiewicz-Muszyńska, D., Abreu-Głowacka, M., Czajka-Jakubowska, A., Przystańska, A. 2019. Computed tomography versus optical scanning: A comparison of different methods of 3D data acquisition for tooth replication. BioMed Research International 2019:e4985121.

Kuzminsky, S. C., Tung, T. A., Hubbe, M., Villaseñor-Marchal, A. 2016. The application of 3D geometric morphometrics and laser surface scanning to investigate the standardization of cranial vault modification in the Andes. Journal of Archaeological Science: Reports 10:507–513.

Lakin, R. J., Barrett, P. M., Stevenson, C., Thomas, R. J., Wills, M. A. 2020. First evidence for a latitudinal body mass effect in extant Crocodylia and the relationships of their reproductive characters. Biological Journal of the Linnean Society. 129 (4): 875–887.

Lambe, L. M. 1914. On a new genus and species of carnivorous dinosaur from the Belly River Formation of Alberta, with a description of *Stephanosaurus marginatus* from the same horizon. Ottawa Naturalist. 28: 13–20.

Langer, M. C. & Benton, M. J. 2006. Early dinosaurs: a phylogenetic study. Journal of Systematic Palaeontology. 4 (4): 309–358.

Langer, M. C., Ezcurra, M. D., Bittencourt, J. S., Novas, F. E. 2010. The origin and early evolution of dinosaurs. Biological Reviews 85, 55–110.

Larson, P. 2008. One Hundred Years of *Tyrannosaurus rex*: The Skeletons. In Larson; Carpenter (eds.). *Tyrannosaurus rex*: The Tyrant King. Indiana University Press.

Lautenschlager, S. 2013. Cranial myology and bite force performance of *Erlikosaurus andrewsi*: a novel approach for digital muscle reconstructions. Journal of Anatomy 222, 260–272.

Lautenschlager, S. 2014. Morphological and functional diversity in therizinosaur claws and the implications for theropod claw evolution. Proceedings of the Royal Society B: Biological Sciences 281:20140497.

Lautenschlager, S. 2015. Estimating cranial musculoskeletal constraints in theropod dinosaurs. Royal Society Open Science 2, 150495.

Lautenschlager, S. 2016. Reconstructing the past: methods and techniques for the digital restoration of fossils. Royal Society Open Science 3:160342.

Lautenschlager, S. 2022. Functional and ecomorphological evolution of orbit shape in Mesozoic archosaurs is driven by body size and diet. Communications Biology 5, 1–11.

Lautenschlager, S., Witmer, L. M., Altangerel, P., Rayfield, E. J. 2013. Edentulism, beaks, and biomechanical innovations in the evolution of theropod dinosaurs. Proceedings of the National Academy of Sciences 110, 20657–20662.

Lautenschlager, S., Brassey, C. A., Button, D. J., Barrett, P. M. 2016. Decoupled form and function in disparate herbivorous dinosaur clades. Scientific Reports 6, 1–10.

Lemanis, R. & Zlotnikov, I. 2018. Finite element analysis as a method to study molluscan shell mechanics. Advanced Engineering Materials 20, 1700939.

Lindstedt, S. L. & Calder, W. A. 1981. Body size, physiological time, and longevity of homeothermic animals. The Quarterly Review of Biology 56, 1–16.

Loewen, M. A., Irmis, R. B., Sertich, J. J. W., Currie, P. J., Sampson, S. D. 2013. Tyrant dinosaur evolution tracks the rise and fall of Late Cretaceous oceans. PLOS ONE 8, e79420.

Longrich, N. R., Pereda-Suberbiola, X., Jalil, N., Khaldoune, F., Jourani, E. 2017. An abelisaurid from the latest Cretaceous (late Maastrichtian) of Morocco, North Africa. Cretaceous Research. 76: 40–52.

Lü, J., Yi, L., Brusatte, S. L., Yang, L., Li, H., Chen, L. 2014. A new clade of Asian Late Cretaceous long-snouted tyrannosaurids. Nature Communications 5, 3788.

Lucas, S. G., Sullivan, R. M., Hunt, A. P. 2006. Re-evaluation of *Pentaceratops* and *Chasmosaurus* (Ornithischia, Ceratopsidae) in the Upper Cretaceous of the Western Interior: New Mexico Museum of Natural History and Science, Bulletin 35.

Ma, W., Pittman, M., Butler, R. J., Lautenschlager, S. 2021. Macroevolutionary trends in theropod dinosaur feeding mechanics. Current Biology ISSN 0960-9822.

Maleev, E. A. 1955. Translated by F. J. Alcock. New carnivorous dinosaurs from the Upper Cretaceous of Mongolia. Doklady Akademii Nauk SSSR. 104 (5): 779–783.

Manning, P. L., Margetts, L., Johnson, M. R., Withers, P. J., Sellers, W. I., Falkingham, P. L., Mummery, P. M., Barrett, P. M., Raymont, D. R. 2009. Biomechanics of dromaeosaurid dinosaur claws: Application of x-ray microtomography, nanoindentation, and finite element analysis. The Anatomical Record 292, 1397–1405.

Mantell, G. 1827. Illustrations of the geology of Sussex: a general view of the geological relations of the southeastern part of England, with figures and descriptions of the fossils of Tilgate Forest. London: Fellow of the Royal College of Surgeons. p. 92.

Marcé-Nogué, J., Esteban-Trivigno, S. de, Escrig, C., Gil, L. 2016. Accounting for differences in element size and homogeneity when comparing finite element models: Armadillos as a case study. Palaeontologia Electronica 19:1–22.

Marsh, O. C. 1877. Notice of new dinosaurian reptiles from the Jurassic formation. American Journal of Science and Arts. 14 (84): 514–516.

Marsh, O. C. 1884. On the united metatarsal bones of *Ceratosaurus*. American Journal of Science. s3-28 (164): 161–162.

Marsh, A. D. & Timothy R. 2020. A comprehensive anatomical and phylogenetic evaluation of *Dilophosaurus wetherilli* (Dinosauria, Theropoda) with descriptions of new specimens from the Kayenta Formation of northern Arizona. Journal of Paleontology 94: 1-103.

Martinez, R. N., Sereno, P. C., Alcober, O. A., Colombi, C. E., Renne, P. R., Montañez, I. P., Currie, B. S. 2011. A basal dinosaur from the dawn of the dinosaur era in Southwestern Pangaea. Science 331, 206–210.

Mazzetta, G. V., Cisilino, A. P., Blanco, R. E., Calvo, N. 2009. Cranial mechanics and functional interpretation of the horned carnivorous dinosaur *Carnotaurus sastrei*. Journal of Vertebrate Paleontology 29, 822–830.

McCurry, M. R., Evans, A. R., McHenry, C. R. 2015. The sensitivity of biological finite element models to the resolution of surface geometry: a case study of crocodilian crania. PeerJ 3:e988.

McKeown, M., Brusatte, S. L., Williamson, T. E., Schwab, J. A., Carr, T. D., Butler, I. B., Muir, A., Schroeder, K., Espy, M. A., Hunter, J. F., Losko, A. S., Nelson, R. O., Gautier, D. C., Vogel, S. C. 2020. Neurosensory and sinus evolution as tyrannosauroid dinosaurs developed giant size: Insight from the endocranial anatomy of *Bistahieversor sealeyi*. The Anatomical Record 303, 1043–1059.

Milne, N. 2016. Curved bones: An adaptation to habitual loading. Journal of Theoretical Biology 407, 18–24.

Moen, D. S. 2006. Cope's rule in cryptodiran turtles: do the body sizes of extant species reflect a trend of phyletic size increase? Journal of Evolutionary Biology 19, 1210–1221.

Molina- Pérez, R. & Larramendi, A. 2019. Dinosaurs: Facts and figures: the theropods and other dinosauriformes. Princeton University Press. pp. 44.

Morales-García, N. M., Burgess, T. D., Hill, J. J., Gill, P. G., Rayfield, E. J. 2019. The use of extruded finite-element models as a novel alternative to tomography-based models: a case study using early mammal jaws. Journal of the Royal Society, Interface 16:20190674.

Moreno, K., Wroe, S., Clausen, P., McHenry, C., D'Amore, D. C., Rayfield, E. J., Cunningham, E. 2008. Cranial performance in the Komodo dragon (*Varanus komodoensis*) as revealed by high-resolution 3-D finite element analysis. Journal of Anatomy 212, 736–746.

Nabavizadeh, A. 2023. How *Triceratops* got its face: An update on the functional evolution of the ceratopsian head. The Anatomical Record 306, 1951–1968.

Nesbitt, S. J., Smith, N. D., Irmis, R. B., Turner, A. H., Downs, A., Norell, M. A. 2009. A complete skeleton of a Late Triassic saurischian and the early evolution of dinosaurs. Science 326, 1530–1533.

Nishizawa, H., Asahara, M., Kamezaki, N., Arai, N. 2010. Differences in the skull morphology between juvenile and adult green turtles: Implications for the ontogenetic diet shift. Current Herpetology 29:97–101.

Novas, F. E. 2010. Dinosaur monophyly. Journal of Vertebrate Paleontology 16:4, 723-741.

Oldfield, C. C., McHenry, C. R., Clausen, P. D., Chamoli, U., Parr, W. C. H., Stynder, D. D., Wroe, S. 2012. Finite element analysis of ursid cranial mechanics and the prediction of feeding behaviour in the extinct giant *Agriotherium africanum*. Journal of Zoology 286:171–171.

Osborn, H. F. 1905. *Tyrannosaurus* and other cretaceous carnivorous dinosaurs. Bulletin of the American Museum of Natural History, 21, 259–265.

Osborn, H. F. 1906. *Tyrannosaurus*, Upper Cretaceous carnivorous dinosaur (second communication). Bulletin of the American Museum of Natural History, 22, 281–296.

Padian, K. 2022. Why tyrannosaurid forelimbs were so short: An integrative hypothesis. Acta Palaeontologica Polonica 67 (1): 63–76.

Paul, G. S. 1988. Predatory Dinosaurs of the World. Simon & Schuster, New York.

Paul, G. S. 2010. The Princeton Field Guide to Dinosaurs (First ed.). Princeton: Princeton University Press. pp. 67–162.

Paul, G. S. 2016. The Princeton Field Guide to Dinosaurs (Second ed.). Princeton University Press. p. 105.

Persons IV, W. S., Currie, P. J., Erickson, G. M. 2020. An older and exceptionally large adult specimen of Tyrannosaurus rex. The Anatomical Record 303, 656–672.

Persson, A. S. K., Odén, A., Andersson, M., Sandborgh-Englund, G. 2009. Digitization of simulated clinical dental impressions: virtual three-dimensional analysis of exactness. Dental Materials 25:929–936.

Peters, R. H. 1986. The Ecological Implications of Body Size. Cambridge University Press. Cambridge, UK.

Peterson, J. E., & Krippner, M. L. 2017. Comparisons of fidelity in the digitization and 3D printing of vertebrate fossils. Joint 52nd Northeastern Annual Section and 51st North-Central Annual GSA Section Meeting – 2017. 290684.

Pierce, S. E., Angielczyk, K. D., Rayfield, E. J. 2008. Patterns of morphospace occupation and mechanical performance in extant crocodilian skulls: A combined geometric morphometric and finite element modeling approach. Journal of Morphology 269:840–864.

Pierce, S. E., Angielczyk, K. D., Rayfield, E. J. 2009. Shape and mechanics in thalattosuchian (Crocodylomorpha) skulls: implications for feeding behaviour and niche partitioning. Journal of Anatomy 215, 555–576.

Pincheira-Donoso, D., Hodgson, D. J., Tregenza, T. 2008. The evolution of body size under environmental gradients in ectotherms: why should Bergmann's rule apply to lizards? BMC Evolutionary Biology. 8 (68): 68.

Poinapen, D., Konopka, J. K., Umoh, J. U., Norley, C. J. D., McNeil, J. N., Holdsworth, D. W. 2017. Micro-CT imaging of live insects using carbon dioxide gas-induced hypoxia as anesthetic with minimal impact on certain subsequent life history traits. BMC Zoology 2:9.

Polly, P. D., Stayton, C. T., Dumont, E. R., Pierce, S. E., Rayfield, E. J., Angielczyk, K. D. 2016. Combining geometric morphometrics and finite element analysis with evolutionary modeling: towards a synthesis. Journal of Vertebrate Paleontology 36, e1111225.

Porro, L. B., Holliday, C. M., Anapol, F., Ontiveros, L. C., Ontiveros, L. T., Ross, C. F. 2011. Free body analysis, beam mechanics, and finite element modeling of the mandible of *Alligator mississippiensis*. Journal of Morphology 272, 910–937.

Power, S. P., Moloney, F., Twomey, M., James, K., O'Connor, O. J., Maher, M. M. 2016. Computed tomography and patient risk: Facts, perceptions and uncertainties. World Journal of Radiology 8:902–915.

Preisser, E. L. & Orrock, J. L. 2012. The allometry of fear: interspecific relationships between body size and response to predation risk. Ecosphere 3(9): 77.

R Core Team. 2021. R: A language and environment for statistical computing. R Foundation for Statistical Computing, Vienna, Austria.

Racicot, R. 2016. Fossil secrets revealed: X-ray CT scanning and applications in paleontology. The Paleontological Society Papers 22:21–38.

Rahman, I. & Lautenschlager, S. 2016. Applications of three-dimensional box modeling to paleontological functional analysis. The Paleontological Society Papers, 22, 119-132.

Raia, P., Carotenuto, F., Passaro, F., Fulgione, D., Fortelius, M., Kalisz, A. E. S., McPeek, E. M. A. 2012. Ecological specialization in fossil mammals explains Cope's rule. The American Naturalist 179, 328–337.

Rauhut, O. W. M. 2003. The interrelationships and evolution of basal theropod dinosaurs. Special Papers in Palaeontology. 69: 1–213.

Rauhut, O. W. M., Milner, A. C., Moore-Fay, S. 2010. Cranial osteology and phylogenetic position of the theropod dinosaur *Proceratosaurus bradleyi* (Woodward, 1910) from the Middle Jurassic of England. Zoological Journal of the Linnean Society. 158 (1): 155–195.

Rauhut, O. W. M.; Carrano, M. T. 2016. The theropod dinosaur *Elaphrosaurus bambergi*, from the Late Jurassic of Tendaguru, Tanzania. Zoological Journal of the Linnean Society. 178 (3): 546–610.

Rayfield, E. J. 2004. Cranial mechanics and feeding in *Tyrannosaurus rex*. Proceedings of the Royal Society B: Biological Sciences 271:1451–1459.

Rayfield, E. J. 2005. Aspects of comparative cranial mechanics in the theropod dinosaurs *Coelophysis, Allosaurus* and *Tyrannosaurus*. Zoological Journal of the Linnean Society 144:309–316.

Rayfield, E. J. 2005. Using finite-element analysis to investigate suture morphology: A case study using large carnivorous dinosaurs. The Anatomical Record Part A: Discoveries in Molecular, Cellular, and Evolutionary Biology 283A:349–365.

Rayfield, E. J. 2007. Finite element analysis and understanding the biomechanics and evolution of living and fossil organisms. Annual Review of Earth and Planetary Sciences 35:541–576.

Rayfield, E. J. 2011. Structural performance of tetanuran theropod skulls, with emphasis on the Megalosauridae, Spinosauridae and Carcharodontosauridae. In P. M. Barrett & A. R. Milner (Eds.), Studies on fossil Tetrapods (Vol. 86, pp. 241–253). London: Special Papers in Palaeontology.

Rayfield, E. J., Norman, D. B., Horner, C. C., Horner, J. R., Smith, P. M., Thomason, J. J., Upchurch, P. 2001. Cranial design and function in a large theropod dinosaur. Nature 409, 1033.

Reichel, M. 2010. The heterodonty of *Albertosaurus sarcophagus* and *Tyrannosaurus rex*: biomechanical implications inferred through 3-D models. Canadian Journal of Earth Sciences. 47, 1253–1261.

Reims, N., Schulp, A., Bohnel, M., Larson, P. 2016. An XXL-CT-scan of an XXL *Tyrannosaurus rex* skull. 19th World Conference on Non-Destructive Testing 1-9.

Ripple, W. J., Wolf, C., Newsome, T. M., Hoffmann, M., Wirsing, A. J., McCauley, D. J. 2017. Extinction risk is most acute for the world's largest and smallest vertebrates. Proceedings of the National Academy of Sciences 114, 10678–10683.

Rogers, R. R., Swisher, C. C., Sereno, P. C., Monetta, A. M., Forster, C. A., Martínez, R. N. 1993. The Ischigualasto tetrapod assemblage (Late Triassic, Argentina) and 40Ar/39Ar dating of dinosaur origins. Science 260, 794–797.

Ross, C. F. 2005. Finite element analysis in vertebrate biomechanics. The Anatomical Record Part A: Discoveries in Molecular, Cellular, and Evolutionary Biology 283A:253–258.

Rowe, T. B., Luo, Z.-X., Ketcham, R. A., Maisano, J. A., Colbert, M. W. 2016. X-ray computed tomography datasets for forensic analysis of vertebrate fossils. Sci Data 3, 160040.

Rowe, A. J. & Snively, E. 2021. Biomechanics of juvenile tyrannosaurid mandibles and their implications for bite force: Evolutionary biology. The Anatomical Record 305: 373– 392.

Rowe, A. J. & Rayfield, E. J. 2022. The efficacy of computed tomography scanning versus surface scanning in 3D finite element analysis. PeerJ 10, e13760.

Russell, D. A. 1970. Tyrannosaurs from the Late Cretaceous of western Canada. National Museum of Natural Sciences Publications in Paleontology. 1: 1–34.

Ruxton, G. D. & Houston, D. C. 2003. Could *Tyrannosaurus rex* have been a scavenger rather than a predator? An energetics approach. Proceedings of the Royal Society Biological Sciences 270, 731–733.

Sakamoto, M. 2006. Scaling bite force in predatory animals: How does *T. rex* compare with living predators? Journal of Vertebrate Paleontology 26, 118A.

Sakamoto, M. 2021. Assessing bite force estimates in extinct mammals and archosaurs using phylogenetic predictions. Palaeontology 64, 743–753.

Sakamoto, M. 2022. Estimating bite force in extinct dinosaurs using phylogenetically predicted physiological cross-sectional areas of jaw adductor muscles. PeerJ 10, e13731.

Sampson, S. D. & Witmer, L. M. 2007. Craniofacial anatomy of *Majungasaurus crenatissimus* (Theropoda: Abelisauridae) from the Late Cretaceous of Madagascar. Journal of Vertebrate Paleontology 27, 32–104.

Sander, P. M., Christian, A., Clauss, M., Fechner, R., Gee, C. T., Griebeler, E.-M., Gunga, H.-C., Hummel, J., Mallison, H., Perry, S. F., Preuschoft, H., Rauhut, O. W. M., Remes, K., Tütken, T., Wings, O., Witzel, U. 2011. Biology of the sauropod dinosaurs: the evolution of gigantism. Biological Reviews of the Cambridge Philosophical Society 86, 117–155.

Schaeffer, J., Benton, M. J., Rayfield, E. J., Stubbs, T. L. 2020. Morphological disparity in theropod jaws: comparing discrete characters and geometric morphometrics. Palaeontology 63: 283-299.

Schwartz, H. L. & Gillette, D. D. 1994. Geology and taphonomy of the *Coelophysis* quarry, Upper Triassic Chinle Formation, Ghost Ranch, New Mexico. Journal of Paleontology. 68 (5): 1118–1130.

Seebacher, F. 2001. A new method to calculate allometric length-mass relationships of dinosaurs. Journal of Vertebrate Paleontology 21:1, 51-60.

Senter, P. & Robins, J. H. 2010. Hip heights of the gigantic theropod dinosaurs *Deinocheirus mirificus* and *Therizinosaurus cheloniformis*, and implications for museum mounting and paleoecology. Bulletin of Gunma Museum of Natural History 14:1-10.

Sereno, P. C. & Novas, F. E. 1992. The complete skull and skeleton of an early dinosaur. Science. 258 (5085): 1137–1140.

Sereno P. C., Wilson J. A., Larsson, H. C. E., Dutheil D. B., Sues, H. 1994. Early Cretaceous dinosaurs from the Sahara. Science. 266 (5183): 267–71.

Sereno, P. C., Dutheil, D. B., Iarochene, M., Larsson, H. C. E., Lyon, G. H., Magwene, P. M., Sidor, C. A., Varricchio, D. J., Wilson, J. A. 1996. Predatory dinosaurs from the Sahara and Late Cretaceous faunal differentiation. Science 272 (5264): 986–991.

Sereno, P. C., Beck, A. L., Dutheil, D. B., Gado, B., Larsson, H. C. E., Lyon, G. H., Marcot, J. D., Rauhut, O. W. M., Sadleir, R. W., Sidor, C. A., Varricchio, D. D., Wilson, G. P., Wilson, J. A. 1998. A long-snouted predatory dinosaur from Africa and the evolution of spinosaurids. Science 282, 1298–1302.

Sereno, P. C., Tan, L., Brusatte, S. L., Kriegstein, H. J., Zhao, X., Cloward, K. 2009. Tyrannosaurid skeletal design first evolved at small body size. Science 326, 418–422.

Shabana, A. A. 1997. Flexible multibody dynamics: Review of past and recent developments. Multibody System Dynamics 1, 189–222.

Sherman, M. A., Seth, A., Delp, S. L. 2011. Simbody: multibody dynamics for biomedical research. Procedia IUTAM 2, 241–261.

Smith, J. B. 2005. Heterodonty in *Tyrannosaurus rex*: Implications for the taxonomic and systematic utility of theropod dentitions. Journal of Vertebrate Paleontology 25, 865–887.

Snively, E., Henderson, D. M., Phillips, D. S. 2006. Fused and vaulted nasals of tyrannosaurid dinosaurs: Implications for cranial strength and feeding mechanics. Acta Palaeontologica Polonica 20.

Snively, E., Cotton, J., Witmer, L., Ridgely, R., Theodor, J. 2011. Finite element comparison of cranial sinus function in the dinosaur *Majungasaurus* and head-clubbing giraffes. ASME 2011 Summer Bioengineering Conference, SBC 2011.

Snively, E., Cotton, J. R., Ridgely, R., Witmer, L. M. 2013. Multibody dynamics model of head and neck function in *Allosaurus* (Dinosauria, Theropoda). Palaeontologia Electronica 16, 1–29.

Snively, E., O'Brien, H., Henderson, D. M., Mallison, H., Surring, L. A., Burns, M. E., Holtz, T. R., Russell, A. P., Witmer, L. M., Currie, P. J., Hartman, S. A., Cotton, J. R. 2019. Lower rotational inertia and larger leg muscles indicate more rapid turns in tyrannosaurids than in other large theropods. PeerJ 7.

Soodmand, E., Kluess, D., Varady, P. A., Cichon, R., Schwarze, M., Gehweiler, D., Niemeyer, F., Pahr, D., Woiczinski, M. 2018. Interlaboratory comparison of femur surface reconstruction from CT data compared to reference optical 3D scan. BioMedical Engineering OnLine 17:29.

Sookias, R. B., Butler, R. J., Benson, R. B. J. 2012. Rise of dinosaurs reveals major body-size transitions are driven by passive processes of trait evolution. Proc. R. Soc. B 279, 2180–2187.

Spiekman, S. N. F., Ezcurra, M. D., Butler, R. J., Fraser, N. C., Maidment, S. C. R. 2021. *Pendraig milnerae*, a new small-sized coelophysoid theropod from the Late Triassic of Wales. Royal Society Open Science 8, 210915.

Stanley, S. M. 1973. An explanation for Cope's rule. Evolution 27/1, 1-26.

Sues, H. D., Frey, E., Martill, D. M., Scott, D. M. 2002. *Irritator challengeri*, a spinosaurid (Dinosauria: Theropoda) from the Lower Cretaceous of Brazil. Journal of Vertebrate Paleontology 22: 535–547.

Sulej, T. & Niedźwiedzki, G. 2019. An elephant-sized Late Triassic synapsid with erect limbs. Science 363, 78–80.

Sutton, M. D., Briggs, D. E. G., Siveter, D. J., Siveter, D. J. 2001. Methodologies for the visualization and reconstruction of three-dimensional fossils from the Silurian Herefordshire Lagerstatte. Web publication/site. <http://palaeo-electronica.org/2001_1/s2/main.htm>

Taquet, P. & Russell, D. A. 1998. New data on spinosaurid dinosaurs from the early cretaceous of the Sahara. Comptes Rendus de l'Académie des Sciences - Series IIA - Earth and Planetary Science 327, 347–353.

Therrien, F. & Henderson, D. M. 2007. My theropod is bigger than yours … or not: estimating body size from skull length in theropods. Journal of Vertebrate Paleontology 27, 108–115.

Tseng, Z. J., Mcnitt-Gray, J. L., Flashner, H., Wang, X., Enciso, R. 2011. Model sensitivity and use of the comparative finite element method in mammalian jaw mechanics: Mandible performance in the Gray Wolf. PLOS ONE 6, e19171.

van Valkenburgh, B. 1996. Feeding behavior in free-ranging, large African carnivores. Journal of Mammalogy 77, 240–254.

Vermeij, G. J. 2016. Gigantism and its implications for the history of life. PLoS One 11, e0146092.

von Mises, R. 1913. Mechanik der festen Körper im plastisch-deformablen Zustand. Nachrichten von der Gesellschaft der Wissenschaften Zu Gottingen, Mathematisch-Physikalische Klasse, 1, 582– 592.

Waller, J. T. & Svensson, E. I. 2017. Body size evolution in an old insect order: No evidence for Cope's Rule in spite of fitness benefits of large size. Evolution 71, 2178–2193.

Waltenberger, L., Rebay-Salisbury, K., Mitteroecker, P. 2021. Three-dimensional surface scanning methods in osteology: A topographical and geometric morphometric comparison. American Journal of Physical Anthropology 174:846–858.

Weber, G. W. & Bookstein, F. L. 2011. Virtual anthropology: a guide to a new interdisciplinary field (p. 423). Wien: Springer.

Welles, S. P. 1984. *Dilophosaurus wetherilli* (Dinosauria, Theropoda), osteology and comparisons. Palaeontographica Abteilung A. 185: 85–180.

Witmer, L. M. 1995. The extant phylogenetic bracket and the importance of reconstructing soft tissues in fossils. In Thomason, J. J. (ed). Functional Morphology in Vertebrate Paleontology. New York. Cambridge University Press. pp: 19–33.

Witmer, L. M. 2001. Nostril position in dinosaurs and other vertebrates and its significance for nasal function. Science 293, 850–853.

Wojcieszek, J. M., Austin, P., Harvey, M. S., Simmons, L. W. 2012. Micro-CT scanning provides insight into the functional morphology of millipede genitalia. Journal of Zoology 287, 91–95.

Wosik, M. & Evans, D. C. 2022. Osteohistological and taphonomic life-history assessment of *Edmontosaurus annectens* (Ornithischia: Hadrosauridae) from the Late Cretaceous (Maastrichtian) Ruth Mason dinosaur quarry, South Dakota, United States, with implication

for ontogenetic segregation between juvenile and adult hadrosaurids. Journal of Anatomy. 241 (2): 272–296.

Xing, L., Wang, Y., Snively, E., Zhang, J., Dong, Z., Burns, M. E., Currie, P. J. 2015. Model-based identification of mechanical characteristics of *Sinosaurus* (Theropoda) crests. Acta Geologica Sinica - English Edition 89, 1–11.

Xu, X., Norell, M. A., Kuang, X., Wang, X., Zhao, Q., Jia, C. 2004. Basal tyrannosauroids from China and evidence for protofeathers in tyrannosauroids. Nature 431, 680–684.

Xu, X., Clark, J. M., Forster, C. A., Norell, M. A., Erickson, G. M., Eberth, D. A., Jia, C., Zhao, Q. 2006. A basal tyrannosauroid dinosaur from the Late Jurassic of China. Nature 439, 715–718.

Zaher, H., Pol, D., A. Navarro, B., Delcourt, R., Carvalho, A. 2020. An Early Cretaceous theropod dinosaur from Brazil sheds light on the cranial evolution of the Abelisauridae. Comptes Rendus Palevol 19, 101–115.

Zamora-Camacho, F. J., Reguera, S., Moreno-Rueda, G 2014. Bergmann's Rule rules body size in an ectotherm: heat conservation in a lizard along a 2200-metre elevational gradient. Journal of Evolutionary Biology 27, 2820–2828.

Zanno, L. E. 2010. Osteology of *Falcarius utahensis* (Dinosauria: Theropoda): characterizing the anatomy of basal therizinosaurs. Zoological Journal of the Linnean Society 158, 196–230.

Zapata, U., Metzger, K., Wang, Q., Elsey, R. M., Ross, C. F., Dechow, P. C. 2010. Material properties of mandibular cortical bone in the American alligator, *Alligator mississippiensis*. Bone 46:860–867.

Zelenitsky, D. K., Therrien, F., Kobayashi, Y. 2009. Olfactory acuity in theropods: palaeobiological and evolutionary implications. Proceedings of the Royal Society B: Biological Sciences 276, 667–673.

Zhu, Z., Jones, D.C., Liu, G. R., Soleimani, S., Huang, X., Shan, Z., Knorr, J., Caballero, M., van Aalst, J. A. 2019. Automated segmentation of swine skulls for finite element model creation using high resolution μ-CT images. International Journal of Computational Methods 16, 1842012.

Ziegler, M. J., Perez, V. J., Pirlo, J., Narducci, R. E., Moran, S. M., Selba, M. C., Hastings, A. K., Vargas-Vergara, C., Antonenko, P. D., MacFadden, B. J. 2020. Applications of 3D paleontological data at the Florida Museum of Natural History. Frontiers in Earth Science 8.

Zienkiewicz, O. C., Taylor, R. L, Zhu, J. Z. 2013. The Finite Element Method: Its Basis and Fundamentals. Butterworth-Heinemann. ISBN 978-0-08-095135-5.